

Contents

2A1 Electromagnetic Precursors of Earthquakes

2A2 High-Frequency Techniques

2A3a Highly Miniaturized on Chip Passive Components for MMIC/RFIC Applications

2A3b Innovation in Interconnects Modeling

2A4 Terahertz Technology

2P1a Polarimetric Radar Remote Sensing

2P1b Subsurface/GPR

2P2 Earth-Space Propagation

2P3 Medical Applications

2P6 Electromagnetic and Optical Wave Technologies for Communications and Sensing

Wave propagation mode of earth-origin EM Pulses as a precursor of Earthquakes

Minoru Tsutsui

Kyoto Sangyo University, Japan

Abstract - We developed a method of finding arrival directions of earth-origin electromagnetic (EM) pulses from detected electric E and magnetic H components of the pulses. The sensor system is composed of a vertical electric dipole antenna and horizontally- and orthogonally-arranged two search coils, which is inserted into a bore-hole of 10 cm in diameter and 100 m in depth. We detected electric and magnetic pulsed waveforms just when an earthquake occurred on Jan 6, 2004. From these waveforms, we first derive frequency dispersion characteristic curves of each field component. Next using amplitudes and phases of three EM components in all frequencies obtained in deriving their dispersion curves, we could provide frequency-dependent arrival directions by Poynting vector $E \times H$, and could determine a direction toward the source location of the EM pulse. Third, we could determine propagation distance of the EM pulse, by comparing the obtained dispersion curve to theoretical curves of tweek atmospherics, and we picked up one of the theoretical curves which matched with the measured one. As the result, the source location of the EM pulse was just in the epicenter of the earthquake. Therefore, we could find that the earth-origin EM pulses could have a possibility of a precursor of the earthquake.

In the analysis, however, we used theoretical dispersion curves for determining the propagation distances of the measured pulses. Therefore, hereafter, we need to determine source locations of EM pulses by direct measurements. For this purpose, we are preparing to establish a network observation system which is composed of plural observation sites equipped by the same system developed here. By the observations of the network sites we will be able to determine source locations of earth-origin EM pulses directly and on real time basis, by means of triangular measuring method in which each detection site provides own detected arrival directions toward source locations of EM pulses.

Furthermore, we needed to know wave propagation mode of the detected EM pulses and to explain the necessity of the bore hole for detecting earthquake related EM pulses. For this purpose, we here introduce a wave mode of the detected earth-origin EM pulses.

1. Introduction

In 1999, we began to observe electromagnetic (EM) waves in the earth, using electric sensor installed into a borehole made of electrically non-conductive pipe of 10 cm in diameter and 100 m in depth. From July to September in 2000 when seismic movements were abnormally active, we detected many electric pulses in both regions above and under the ground surface. We found, from the dynamic spectra (time-changes of frequency spectrum) of the detected electric pulses, that those pulses would be generated in the deep earth because the intensities of the pulses detected in the earth were stronger than those simultaneously detected above the ground [1]. In order to investigate the generation and propagation mechanisms of the EM pulses detected in the earth, we attempted to find their source locations. For this purpose, we manufactured a sensor system for finding arrival directions of EM pulses and developed a system for analyzing the detected EM pulses on real-time basis [2]. After accomplishing the system, we started to observe EM pulses in the earth at the end of

2003. In January 6, 2004, we detected an intense EM pulse just when an earthquake of M5.4 occurred at 34.2°N, 136.7°E in the Sea of Kumano of Kii-Peninsula, Kansai, Japan. The sensor system captured waveforms of a vertical electric component and horizontal and orthogonal two magnetic components of the EM pulse. From the analysis of these pulsed waveforms, we could find a direction to the EM pulse source. Furthermore, we could also obtain its propagation distance, by comparing the dispersion characteristic curve of the EM pulse to those of tweek atmospherics which are generally generated by lightning discharges and are propagating in the space between the ionosphere and the ground surface. As the result, we could determine the source location of the EM pulse, and identified that the source location of the EM pulse was in the epicenter region of the earthquake as shown in Fig. 1 [4]. This measured result has clearly proved a positive causality between movements of earth crust and generations of EM pulses.

However, we need to show reliable propagation mode of the earth-origin EM pulses. For this purpose, we propose a model of propagations from a relation between forms of frequency dynamic spectra ($f-t$ form) of detected EM pulses and their propagation paths.

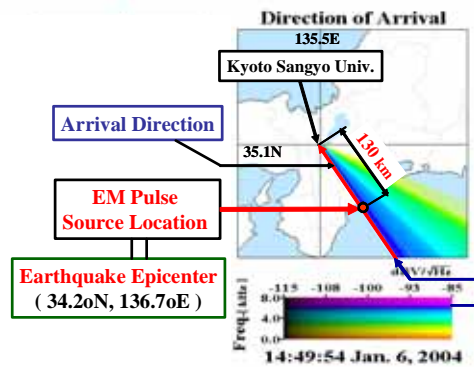


Fig. 1. Source location of an earth-origin EM pulse obtain from its arrival direction and estimated propagation distance [4].

2. Different $f-t$ forms of Earth-origin EM Pulses

In the analysis of EM pulses, we usually derive the time change of the frequency spectrum ($f-t$ form) from detected pulsed waveforms. Since waveforms of earth-origin EM pulses at their excitation are considered to be the δ -function which contains finite frequency components, the $f-t$ forms of detected pulses would show dispersion characteristic curves as those of “tweek atmospherics” when they have been propagating in a dispersive medium such as ionosphere plasma, and would show a trend of increase of time-delays in accordance with the decreasing frequency down to a cutoff [3]. Thus, if the $f-t$ forms of EM pulses showed such dispersion curves resemble to those of tweek atmospherics, they are regarded that they have been reflecting to the ionosphere. In this case, we can estimate propagation distances of the EM pulses by comparing their $f-t$ forms to theoretical dispersion characteristic curves of tweek atmospherics [5], and we can determine their source locations.

During the period of six days before and after the earthquake occurred on January 6, 2004, we detected about 500 EM pulses. However, we found

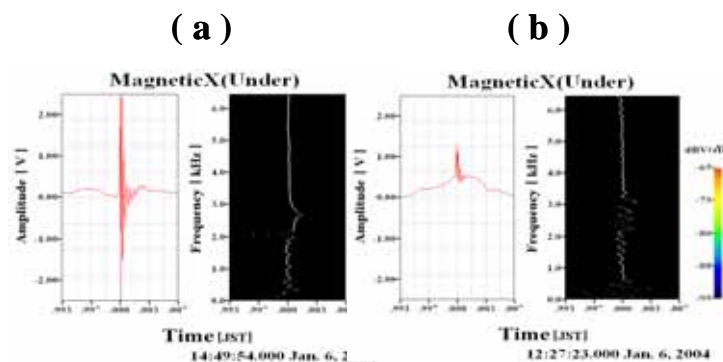


Fig. 2. Detected waveforms and their $f-t$ forms detected (a) at the occurrence of an earthquake, and (b) before the earthquake.

that most $f-t$ forms neither show clear dispersive curves nor clear frequency cutoff. Figure 2 shows two examples of $f-t$ forms of earth-origin EM pulses detected (a) at just the earthquake, and (b) before it. Figure 2(a) shows clear dispersion curve above the cutoff frequency at 2.7 kHz. For obtaining propagation distance of the EM pulses, we can apply the dispersive part which is resemble to those of “tweek atmospherics”. However, Fig. 2(b) shows no such the dispersive form but shows noisy spectral form. From pulse intensities of these two examples, we can imagine a reason of forming such the different spectral forms. Figure 2 (a) shows intense pulse waveform and a clear dispersion characteristic curve. On the other hand, Fig. 2 (b) shows the weak pulse and no such clear dispersion. This difference suggests that they might have been propagating along different paths in relation to their intensities. Therefore, we propose a following model of wave propagations.

3. A Model of Propagations of Earth-origin EM pulses

Figure 3 shows a schematic illustration of possible features of propagations of earth-origin EM pulses. When an earthquake occurred, EM pulses would be excited by piezo-electric effect in the earth crust by its own distortions, and the EM pulses would be emitted to all directions. Most energy of an EM pulse would be attenuated due to dissipations in rather conductive medium of the earth. However, a part of the pulse energy would spurt out of the ground surface of the earthquake epicenter.

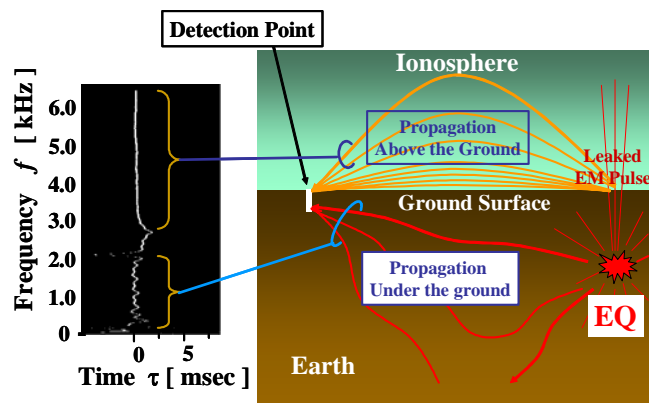


Fig. 3. Propagation paths of earth-origin EM pulses.

One part of the energy would

propagate into the space above the ground as a free space mode and would reflect to the ionosphere. Therefore, the $f-t$ forms of detected EM pulses of this mode would show clear dispersion curves as shown in Fig. 2 (a) which is similar to those of tweek atmospherics. However, we found, from the observed data, that most $f-t$ forms of EM pulses neither show clear dispersive curve and no clear frequency cutoff. As described above, the difference between those showing clear and non-clear dispersion characteristics in $f-t$ forms would be explained by the difference of intensities of the EM pulses after spouting out of the ground surface. If the intensity of the EM pulse is strong, one part of energy of the pulse would reach to the ionosphere. However, if its intensity is weak, the energy of the spouted out of the ground would be strongly refracted at the boundary. Thus the most detected pulses showing non-dispersive spectra would not have been coming to the ionosphere.

4. Refractions of the earth-origin EM pulse at ground surface

Zenneck proposed that electromagnetic waves which got into a conductive medium from a non-conductive medium (such as air) would change their mode after its refraction to a surface wave which would propagate along the boundary between the two media. He studied a property of radio waves propagating above the ground and getting into the ground. This effect could be applicable to the earth-origin EM pulses. They would also change their mode to the surface waves when they spurted out, because they are getting into the rather conductive sedimentary layer than the lower earth crusts. At the boundary of the sedimentary layer facing to the earth crust below it, some of EM

waves would refract and propagate along the boundary. Figure 4 shows a model of three-layers as the present situation. They are layers of the air, the rather conductive sedimentary layer and the earth-crust from top to bottom. In the figure, the propagation constants k_0 , k_1 and k_2 in these media and their related dielectric constant, magnetic permeability and electrical conductivity ϵ , μ , σ are also given as $k_0(\epsilon_0, \mu_0)$, $k_1(\epsilon_1, \mu_1, \sigma_1)$ and $k_2(\epsilon_2, \mu_2, \sigma_2)$, respectively. In a region including the boundary of the sedimentary layer

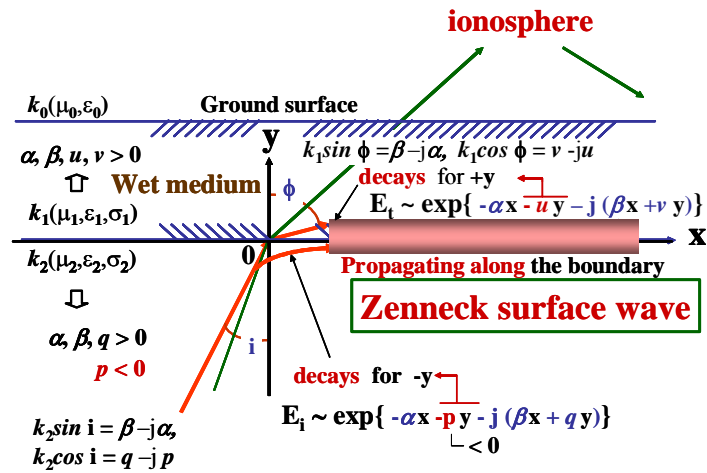


Fig. 4. A model layers and Zenneck surface wave changed from earth-origin EM pulse.

facing to the earth-crust, complex values of $k_2 \sin i (=k_1 \sin \phi) = \beta - j a$, $k_2 \cos i = q - j p$, $k_1 \cos \phi = v - j u$ are used as an incident and a refracted wave for the incident angle i and the refractive angle ϕ , respectively, under a condition that there exists no reflecting wave at the boundary. Therefore, amplitudes E_i of the incident wave and E_t of the refracted wave are given by

$$E_i \sim \exp\{-\alpha x - p y - j(\beta x - q y)\}$$

$$E_t \sim \exp\{-\alpha x - u y - j(\beta x - v y)\},$$

where y indicates the geographically vertical direction and x is the horizontal one along the boundary between the two media. In these formula, since $\alpha, \beta, u, v, q > 0$ and $p < 0$, the wave amplitudes of the incident wave from the bottom and the refracted wave will both decay for $-y$ and $+y$ directions due to the factors $\exp\{-p y\}$ and $\exp\{-u y\}$. By these effects, the propagation energy would concentrate along the boundary, then these waves would finally become a surface wave propagating along the boundary in the x direction although they would also decay with $\exp\{-\alpha x\}$. This refracted wave is called the Zenneck surface wave [6][7].

If the conductive sedimentary layer is thin, the earth-origin EM pulses as a Zenneck mode will easily penetrate the sedimentary layer and propagate along the ground surface. In such the case, the waves propagate without strong dissipation due to the parameter α in the free space, and they will be detected even by the EM sensor in the borehole.

Above the ground surface, however, there exist other pulsed waves generated by lightning. They would also become other Zenneck surface modes and would propagate along the ground surface. However, in the case that the conductive sedimentary layer is thick, the layer will take a role of an effective EM shielding for the EM sensor installed in the bore-hole from the lightning Zenneck mode. On the other hand, another Zenneck mode of earth-origin EM pulses propagating along the lower boundary of the sedimentary layer can be detected by the sensor at the deep earth without interferences of the lightning Zenneck mode.

5. Conclusion

We needed to explain the reason why the earth-origin EM pulses were detected as a free space mode. In the present consideration, we can understand that intense waves of the earth-origin EM pulses would spout out of the ground surface and propagate and reflected to the ionosphere.

However, weak EM pulses would be affected by refractions at the boundary of media with different conductivities. Thus we proposed that the earth-origin EM pulses would change its mode to a Zenneck wave which would propagate along the ground surface.

In the future, the propagation mode of these EM pulses will be more clear, if we accomplish a network of observation sites equipped with the same system including deep bore-hole and detect more earth-origin EM pulses. Furthermore, we are now preparing measurements of wave polarizations of the earth-origin EM pulses as the Zenneck waves by a new sensor system which is under manufacturing. They will provide us more clear understand about the propagation feature of the earth-origin EM pulses.

References

- [1] M. Tsutsui, Detection of earth-origin electric pulses, *Geophys. Res. Letters*, Vol. 29, No. 8, 10.1029/2001GL013713, 2002.
- [2] Minoru Tsutsui, Shigeo Konagaya and Tadayoshi Kagawa, A Method of Direction Finding for Dispersive Electromagnetic Pulses, *IEICE Trans.*, Vol. J89-B, No. 1, pp 1-9, (in Japanese) 2006.
- [3] M. Yamashita, Propagation of tweek atmospherics, *J. Atmos. Terr. Physics*, Vol. 40, pp. 151-156, 1978.
- [4] M. Tsutsui, Identification of earthquake epicenter from measurements of electromagnetic pulses in the Earth. *Geophys. Res. Letters*, Vol. 32, L20303, 2005
- [5] S. Yano, T. Ogawa and H. Hagino, Waveform analysis of tweek atmospherics, *Res. Lett. Atmos. Electr.* Vol. 9, pp. 31-42, 1989.
- [6] F. Vilbig and J. Zenneck, "Fortschritte der Hochfrequenztechnik, Becker and Erler 1941.
- [7] J. A. Stratton, "Electromagnetic Theory", McGraw-Hill, 1949

On non-linear plasma irregularities in the ionosphere due to electromagnetic precursory signals from earthquake

S. S. De, B. K. Sarkar, B. Bandyopadhyay, A. Guha

Centre of Advanced Study in Radiophysics & Electronics, University of Calcutta,
Kolkata 700 009, India

and

B. K. De

Tripura University, Suriyamaninagar 799 130, West Tripura, India

E-mail: de_syam_sundar@yahoo.co.in

Abstract Some effects on the ionosphere of the electromagnetic fields from earthquake have been studied in this presentation through some model calculations. The expressions of the variation of electron concentration and electron temperature as the ionospheric precursors of the earthquake have been deduced. The production of periodic inhomogeneities and their decay at different heights due to precursors at the active regions of the ionosphere as a whole have been considered through quasihydrodynamic formulations.

1. INTRODUCTION

There are different models for seismic waves and seismo-associated electromagnetic phenomena on the occasion of any earthquake [1-4]. The electromagnetic emissions are observed prior to the occurrence of earthquakes. Both precursory and post-seismic variations in ELF-VLF amplitude and in ionospheric parameters have been reported from satellite based observations surrounding earthquakes [5-10].

The study of seismic related phenomena shows the enhancement of DC electric field accompanied with the generation of periodic inhomogeneities in the electrical conductivity of the lower ionosphere and formation of geomagnetic field-aligned plasma layer in the upper atmosphere [11-14]. The lower ionosphere disturbances produced by the electromagnetic fields are due to large scale current systems in the terrestrial core at the final stage of earthquake generation [15, 16].

Preceding an earthquake, a strong variation in the electric field is observed which changes the direction of the field near the surface. As a result, significant changes in the electric field amplitude would be expected in the lower atmosphere that initiates the changes in the lower atmospheric parameters [17, 18].

The results of model calculations have been presented in this paper to estimate the changes in the electron concentration and electron temperature through energy balance equation, continuity equation and ionization balance equation for the ionospheric regions. The system of equations is solved for temperature and density irregularities for the stated situation. Ion-collision energy losses are more than those of electrons and the ion conductivity is less than those of electrons. For this, ion heating is relatively small. The electron-neutral molecule collision frequency and the electron energy loss per collision with molecule depend on temperature. As a result, the equation for electron temperature variation becomes non-linear. The equations for fluctuations of electron temperature and electron density are derived under the stated circumstances which can be used for numerical estimations.

2. MATHEMATICAL FORMULATIONS

In this model, the following momentum transport equation, energy balance equation and continuity equations are chosen to investigate the effects of electromagnetic field due to earthquake on the variation of ionospheric parameters:

$$N \frac{\partial \vec{v}}{\partial t} + N(\vec{v} \cdot \nabla) \vec{v} = -\frac{e}{m} N \vec{E}(t) - N \mathbf{n}_e(T_e) \vec{v} - \frac{\nabla p}{m} - \mathbf{h} \nabla^2 \vec{v} - \frac{eN}{m} (\vec{v} \times \vec{H}) \quad (1)$$

$$\frac{3}{2} \frac{\partial}{\partial t} (NkT_e) + eN\vec{v} \cdot \vec{E} + \frac{3}{2} \mathbf{d}\mathbf{n}_e(T_e) Nk(T_e - T) - \nabla \cdot \vec{W} + Q_i \frac{\partial N}{\partial t} = 0 \quad (2)$$

$$\frac{\partial N}{\partial t} = q_i + \mathbf{n}_{de} \mathbf{I} N - \mathbf{n}_a N - \mathbf{a}_r N^2 (1 + \mathbf{I}) + \frac{\partial}{\partial Z} \{ (D_t + D_a) \frac{\partial N}{\partial Z} \} \quad (3)$$

$$\frac{\partial N^+}{\partial t} = q_i - \mathbf{a}_r N^2 (1 + \mathbf{I}) - \mathbf{a}_i N^2 \mathbf{I} (1 + \mathbf{I}) + \frac{\partial}{\partial Z} \{ (D_t + D_a) \frac{\partial N^+}{\partial Z} \} \quad (4)$$

$$N^+ = N + N^-$$

where, $\vec{E}(t)$ is the external seismo-electric field; \vec{H} , the geomagnetic field; q_i , the ionization rate; \mathbf{n}_{de} , the effective electron detachment rate from the ions; \mathbf{n}_a , the rate of electron attachment to neutrals; D_t , the eddy diffusion coefficient; D_a , the molecular diffusion coefficient; \mathbf{a}_r , the effective coefficient of the dissociative recombination of electrons and positive ions; Z , the altitude; \mathbf{a}_i , the ion-ion recombination coefficient; k , the Boltzmann constant; \mathbf{n}_e , the effective electron collision frequency; Q_i , the ionization energy of the plasma medium; \vec{v} , the average electron velocity; N , electron number density; $\mathbf{d} = \frac{2m}{m'}$, m' , the mass of the heavy particle; T , the equilibrium temperature; T_e , the electron temperature; \mathbf{h} , the coefficient of viscosity and \vec{W} is the heat flow vector. It is expressed as

$$\vec{W} = -\mathbf{I}(T_e) \nabla T_e$$

where $\mathbf{I}(T_e)$ is the effective coefficient of electron energy conduction.

$$\mathbf{I} = k_T (1 - \mathbf{m} \mathbf{t}' / \mathbf{s}_0 k_T)$$

k_T is the coefficient of electron energy conduction at constant electron velocity; \mathbf{m} , the coefficient of electron energy conduction due to dc electric field; \mathbf{t}' , the current flow coefficient due to thermal gradients at constant pressure, $p = NkT_e$ and \mathbf{s}_0 is the dc electrical conductivity. The other symbols have their usual significance.

3. RESULTS

In the presence of external electric field due to earthquake, the expression for fluctuation of electron temperature within the upper atmosphere has been deduced in the approximation of small perturbation. It is given by

$$\begin{aligned} & \frac{\partial \Delta T_e}{\partial t} + \frac{1}{\mathbf{dn}_e T_e} [q_i + \Delta N (\mathbf{n}_{de} \mathbf{I} - \mathbf{n}_a) + N_0 \mathbf{dn}_e (T_e) - \mathbf{a}_r (i + \mathbf{I}) N_0^2] \Delta T_e = \Delta N \mathbf{dn}_e (T_e) - \\ & - \frac{2Q_i}{3kT \mathbf{dn}_e (T_e)} [q_i + (\mathbf{n}_{de} \mathbf{I} - \mathbf{n}_a) N_0 + (D_i + D_a) \frac{\partial^2 N}{\partial Z^2} - \mathbf{a}_r (1 + \mathbf{I}) N_0^2] + \\ & + \frac{2e^2 \Delta N}{3mkT \mathbf{dn}_e (T_e)} \vec{E} \cdot [\exp\{(-A) + \frac{e}{m_{i'}} \int X dt''\}] [\int_0^t \vec{E}(t') \exp\{1 + \frac{e}{m_{i'}} \int X dt''\} dt'] \end{aligned} \quad (5)$$

where

$$\mathbf{t} = \mathbf{dn}_e (T_e) t, \quad N = N_0 + \Delta N, \quad T_e = T_{e0} + \Delta T_e.$$

Following Belikovich et al. [13], the expression for density fluctuation under this situation is obtained as

$$\begin{aligned} & \frac{N_0 k (T_e - T)}{m} \frac{\partial^2 (\Delta N)}{\partial Z^2} + \frac{2Q_i}{3kT_e} [(D_i + D_a) + \mathbf{n}_e (T_e)] \frac{\partial (\Delta N)}{\partial Z} = \frac{\partial^2 (\Delta N)}{\partial t^2} - 2\mathbf{a}_r N_0 (1 + \mathbf{I}) \Delta N - \\ & - \frac{3}{2} \frac{N_0 k}{m} \mathbf{n}_{de} \frac{\partial^2}{\partial Z^2} (T_e - T) + 2\mathbf{n}_{de} \mathbf{I} \frac{\mathbf{d}(\Delta N)}{\partial t} \end{aligned} \quad (6)$$

From (5) and (6), the expected changes in the temperature and number density at different heights due to precursors at the active regions of the ionosphere can be estimated numerically.

Acknowledgement

This work is funded by Indian Space Research Organization (ISRO) through S. K. Mitra Centre for Research in Space Environment, University of Calcutta, Kolkata 700 009, India.

REFERENCES

1. Hayakaya, M. (ed), "Atmospheric and ionospheric electromagnetic phenomena associated with earthquakes," Terra Scientific Publishing Company, Tokyo, 1999.
2. Hayakaya, M., Molchanov, O. A. and NASDA/UEC team, "Achievements of NASDA's earthquake remote sensing frontier project," *Terr. Atmos. Oceanic Sci.*, Vol. 15, 311-327, 2004.
3. Pulinets, S. A., Legen'ka, A. D., Gaivoronskaya, T. V., Depuev, V. K., "Main phenomenological features of ionospheric precursors of strong earthquakes," *J. Atmos. Solar-Terr. Phys.*, Vol. 65, 1337-1347, 2003b.
4. Tronin, A. A., Hayakaya, M. and Molchanov, O. A., "Thermal IR satellite data application for earthquake research in Japan and China," *J. Geodynamics*, Vol. 33, 319-334, 2002.
5. Pulinets, S. A., Khagai, V. V., Boyarchuk, K., A. and Lomonosov, A. M., "Atmospheric electric field as source of ionospheric variability," *Phys.-Uspekhi*, Vol. 41, 515-522, 1998a.
6. Pulinets, S. A., "Seismic activity as a source of the ionospheric variability," *Adv. Space Res.*, Vol. 22, 903-906, 1998b.

7. Shvets, A. V., Hayakawa, M. and Molchanov, O. A., "Subionospheric VLF monitoring for earthquake-related ionospheric perturbations," *J. Atmos. Electricity*, Vol. 22, 87-99, 2002.
8. Molchanov, O. A. and Hayakawa, M., "Subionospheric VLF signal perturbations possibly related to earthquakes," *J. Geophys. Res.*, Vol. 103, 17489-17504, 1998.
9. Molchanov, O. A. and Hayakawa, M., Ondoh, T. and Kawai, E., "Precursory effects in the subionospheric VLF signals for Kobe earthquake," *Phys. Earth Planet. Inter.* Vol. 105, 239-248, 1998.
10. Chemirev, V. M., Isaev, N. V., Serebryakova, O. N., Sorokin, V. M. and Sobolev, Y. P., "Small-scale plasma inhomogeneities and correlated ELF emissions in the ionosphere over an earthquake region," *J. Atmos. Solar-Terr. Phys.*, Vol. 59, 967-974, 1997.
11. Martynenko, S. I., Fuks, I. M. and Shubova, R. S., "Ionospheric electric field influence on the parameters of VLF signals connected with nuclear accidents and earthquakes," *J. Atmos. Electricity*, Vol. 16, 259-269, 1996a.
12. Martynenko, S. I., Fuks, I. M. and Shubova, R. S., "The lower ionosphere response to conductivity variations in the nearsurface atmosphere," *Geomag. Aeronomy*, Vol. 34, 223-228, 1994.
13. Belikovich, V. V., Benediktov, E. A. and Terina, G. I., "On the formation of quasi-periodic artificial inhomogeneities in the ionosphere," *Radio Phys. Quantum Electronics*, Vol. 21, 985-988, 1978a.
14. Belikovich, V. V., Benediktov, E. A., Goncharov, N. P. and Tolmacheva, A. V., "Diagnostics of the ionosphere and neutral atmosphere at E-region heights using artificial periodic inhomogeneities," *J. Atmos. Solar-Terr. Phys.*, Vol. 59, 2447-2460, 1997.
15. Gokhberg, M. B., Gershenson, N. I., Gufeld, I. L., Kustov, A. V., Liperovsky, V. A. and Khusametdinov, S. S., "Possible effects of the action of electric fields of seismic origin on the ionosphere," *Geomag. Aeronomy*, Vol. 24, 183-186, 1984.
16. Martynenko, S. I., "Atmospheric electric field and disturbances of the lower ionosphere parameters," *J. Atmos. Electricity*, Vol. 19, 1-9, 1999a.
17. Martynenko, S. I., "Interrelations between temporal and spatial scales of perturbations from external electric fields in the lower ionosphere," *Geomag. Aeronomy*, Vol. 39, 249-253, 1999b.
18. Martynenko, S. I., "Coupling between temporal and spatial scales and modeling disturbances caused by external electric field in the lower ionosphere," *Ann. Geophys., Part III, Space Planetary Sci., Suppl. III*, to Vol. 16, C845, 1998.

A Study of Scattering Characteristics using Polygon Meshed PO

Navarat LERTSIRISOPON, Mir GHORAISHI,
Gilbert Siy CHING and Jun-ichi TAKADA

Department of International Development Engineering, Tokyo Institute of Technology, JAPAN

Abstract - The polygon meshes represented by several triangles are applied to implement the physical optics (PO) approximation method. The polygon meshes can now be easily generated by the intrinsic function of MATLAB. "Polygon Meshed PO" method was implemented and examined for modeling the scattering characteristics from 3D objects. Using Polygon Meshed PO, the calculation of the induced current and the scattered field can be systematically simplified by summing the contribution on each triangle. Furthermore, the parametric study and the analytical solutions including integral equation (IE) techniques were introduced in order to evaluate the performance of this method.

1. Introduction

Propagation mechanisms which degrade the performance of mobile communication system in urban areas are basically wall reflections, building edges and roof diffractions. From the experiment results [1], however, the scattering from other objects in the environment can have strong impact on the urban propagation channel. Careful analysis of these results reveals that these scattering objects, such as signboards, street lights, traffic lights and traffic signs, are involved in scattering transmitted signals to the receiver [2].

To study the impact of those scattering objects in the mobile communication channel, geometrical optics (GO) and geometrical theory of diffraction (GTD) which are currently used to simulate the propagation channel for mobile communications can not be applicable. Instead, we are going to use physical optics (PO) to simulate the scattering from small objects relative to the first Fresnel zone of the scattering paths. To simplify the calculation of the induced current and the scattered field, polygon meshes represented by several triangles are applied to implement a PO approximation method called "Polygon Meshed PO". Polygon meshes represented by triangles can be easily generated by using intrinsic functions in MATLAB for 2D cases. For 3D cases, a mapping to a 2D object is necessary to be able to use the MATLAB intrinsic functions. Then, the height is put back to the meshed 2D object to obtain the meshed 3D object. Furthermore, the parametric study and the analytical solutions including integral equation (IE) techniques were introduced in order to evaluate the performance of this method.

2. Physical Optics (PO) Approximation

PO is a type of high frequency approximation method, meaning the surface of the object is much bigger than the wavelength of the signal. In PO approximation [4], the induced electric current is approximated as the scatterer is replaced by an infinite ground plane, which is tangential to the surface of the scatterer at the point of interest. When the scatterer is a perfect electric conductor (PEC), then the simple image theory is applied. Only the tangential component of magnetic field is doubled, while the normal component is cancelled. The equivalent electric current \mathbf{I} is given by $2\hat{n} \times \mathbf{H}^i$ on the illuminated part of the surface \mathbf{S}_l while on the shadowed part \mathbf{S}_s of the scatterer, the current \mathbf{I} is zero, \mathbf{H}^i is the unperturbed incident magnetic field. For PEC, \mathbf{M} is always 0, as the tangential electric field vanishes on the PEC surface. Then

$$\mathbf{I}^{PO} = 2\hat{n} \times \mathbf{H}^i \text{ for illuminated part } \mathbf{S}_l; \quad (1)$$

$$\mathbf{M}^{PO} = 0 \quad (2)$$

In this case, the field at an observation point expressed in terms of electric and magnetic vector potentials, \mathbf{A} and \mathbf{B} respectively, is simplified.

$$\mathbf{E} = \mathbf{E}^i - j\omega\mu\mathbf{A} - j\frac{\nabla\nabla\cdot\mathbf{A}}{\omega\varepsilon} \quad (3)$$

Furthermore, if the observer P is in the far field region of the scatterer, the second term of the scattering field just eliminates the radial component of the first term and the electric field is expressed by using the unit vector $\hat{\mathbf{r}}_0$ towards the observer as follows:

$$\mathbf{E} = \mathbf{E}^i - j\omega\mu\mathbf{A} \times \hat{\mathbf{r}}_0 \times \hat{\mathbf{r}}_0 \quad (4)$$

3. Polygon Meshed PO

“Polygon Meshed PO” method is constructed by applying the polygon meshes represented by several triangles in PO. Since the scatterer is modeled by a polygon discussed in the next section, the complex calculation of \mathbf{A} can also be represented in the summation form of each polygon mesh instead of the surface integral in the case that each polygon mesh has a suitable size.

$$\mathbf{A} = \frac{1}{4\pi} \int_S \mathbf{J} \frac{e^{-jkr}}{r} dS \implies \mathbf{A} = \frac{1}{4\pi} \sum \mathbf{J} \frac{e^{-jkr}}{r} \Delta s \quad (5)$$

Moreover, to study about the convergence, a parameter called normalized polygon area is defined to determine the appropriate size of the polygon mesh as the following relationship.

$$\text{Normalized polygon area} = \frac{\text{avg}(\text{polygon area})}{\lambda^2} \quad (6)$$

3.1 Polygon Mesh Method

Although there are a variety of algorithms available to generate this kind of structure, the triangulation of a polygon is utilized since curved surfaces being subdivided into triangles can be handled efficiently. The triangulation algorithm is a fundamental operation in computational geometry under the assumption that the polygon is simple, i.e., that the vertices of the polygon are the only points of the plane that belong to two edges, and that no point of the plane belongs to more than two edges. Moreover, this well-known algorithm is provided as an intrinsic function of MATLAB and utilizes the Constructive Solid Geometry (CSG) model paradigm [5] to model the basic 2D geometrical objects consisting of circle, rectangle, ellipse and polygon and designs the mesh generation based on Delaunay triangulation [6].

For generating the triangulation in 3D geometrical objects, a mapping to a 2D object is necessary to be able to use the MATLAB intrinsic functions. Then, the height is put back to the meshed 2D object to obtain the meshed 3D object as shown in Fig. 1.

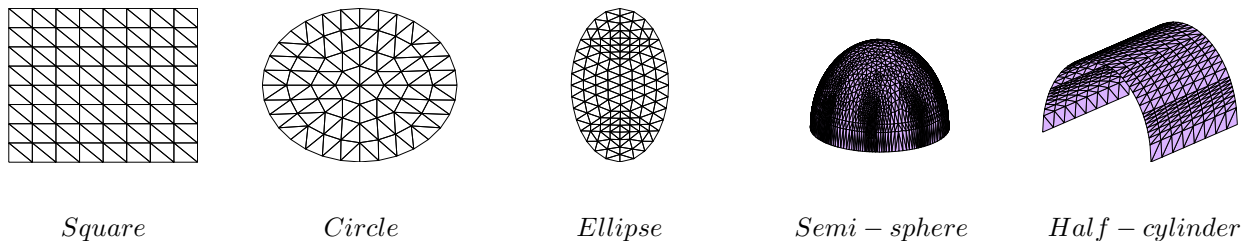


Figure 1: Varieties of scatterer shapes in 2D and 3D geometry

4. Simulation Results

To evaluate the performance of Polygon Meshed PO, the simulation parameters were chosen as in Table 1.

Table 1 : Simulation parameters

Scatterer shape	Square
Size	0.09 m. x 0.09 m.
Frequency	5.2 GHz
Observer distance	20 meters
Incident θ_i	60°
Incident ϕ_i	30°
Scatterer ϕ	210°
Polarization	Parallel

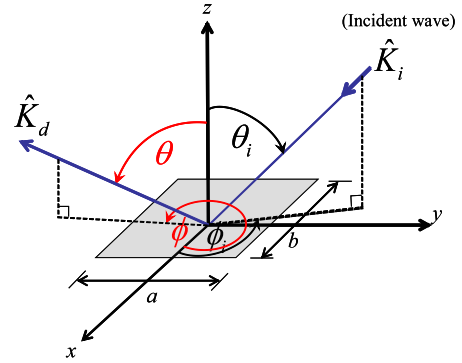


Figure 2 : Plane wave scattering from a plate

Figure 2 shows the scattering of a plane wave by a square plate sized $a \times b$ in the x - y plane. The $\hat{\mathbf{K}}_i$ represented by (θ_i, ϕ_i) in polar coordinates with the parallel polarization (θ_i component only) while the observer is in the direction of $\hat{\mathbf{K}}_d$ or (θ, ϕ) .

Figure 3 illustrates how the polygon mesh method can construct the scatterer when the size of each polygon mesh is varied by the normalized polygon area and Fig. 4 illustrates the magnitude of the scatterer fields from the square plate with respect to the elevation angle at the observer point. From these figures, it can be seen that when the normalized polygon area decreases, the sidelobe also decreases. Furthermore, the parametric studies show that the normalized polygon area of 0.1 is sufficient for the scattering field to achieve the convergence, therefore, the normalized polygon area below 0.1 will be utilized in the further simulations.

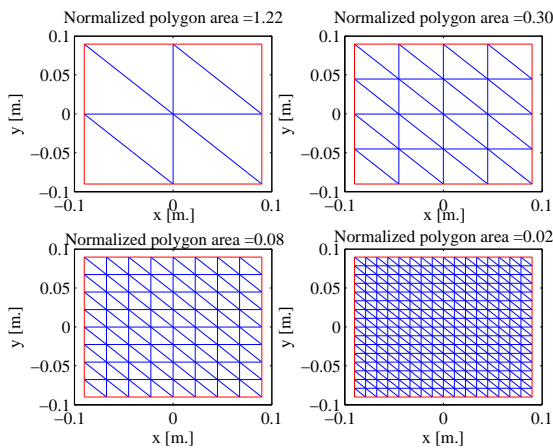


Figure 3 : Geometrical shape by varying polygon mesh ratio

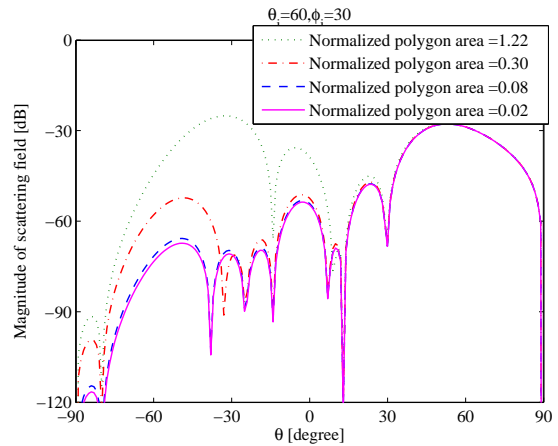


Figure 4 : Scattering field corresponding to polygon mesh ratio using Polygon Meshed PO

However, to justify whether the polygon mesh method can be applicable in PO approximation, we need to compare the results with the PO analytical model as derived in [4]. From this reason, the comparison between Polygon Meshed PO and PO analytical method is illustrated in Fig. 5. A high accuracy for both PO cases in the direction of main radiation ($\theta = 60^\circ$) is observed. This reveals that Polygon Meshed PO can perform as well as the PO analytical one. Since the characteristics of PO

treats only the portion of the scatterer that can be observed by the source (illuminated portion), the simulated scattering field will deviate from the numerically accurate method of moments (MoM) as the observer moves away from the illuminated portion and into the shadowed region. Moreover, Fig. 6 illustrated the magnitude of scattering field in the specific direction of observer for different θ and ϕ in order to observe the field outside the specular direction.

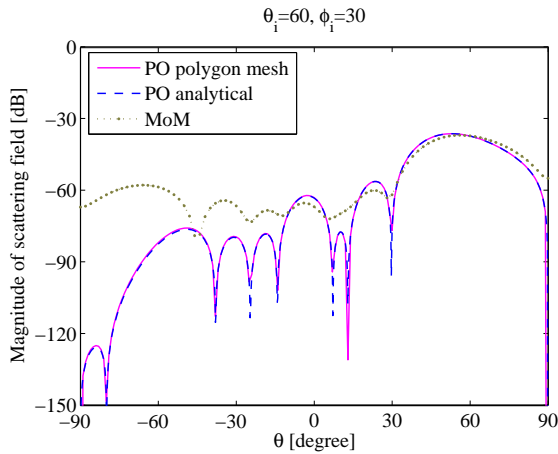


Figure 5 : Comparison with conventional models

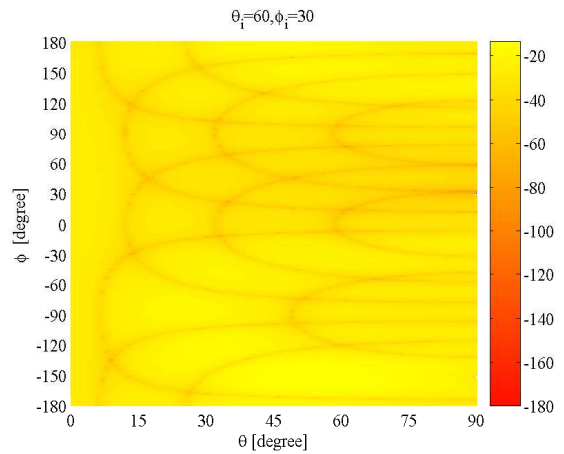


Figure 6 : Scattering field according to Fig. 2

In the real environment, the simple shape can not represent all the obstructions in the channel, for example, traffic light and its pole, car, etc., the 3D objects should also be simulated so that the simulation of a sphere, which is a typical 3D object, was conducted. It is known that the scattering from the sphere can be analytically calculated. Therefore, polygon meshed PO for 3D geometrical cases can be evaluated by comparing output with this analytical result.

Table 2 : Simulation parameters

Scatterer shape	Sphere
Radius	0.29 m. (5λ)
Frequency	5.2 GHz
Incident θ_i	180°
Incident ϕ_i	0°
Scatterer ϕ	0°

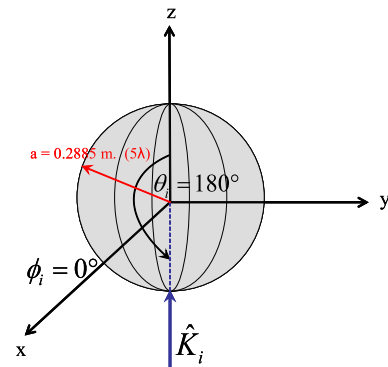


Figure 7 : Plane wave scattering from a sphere

The structure of the sphere is modeled whose radius is 5λ (0.2885 m.) as illustrated in Fig. 7 and simulated under the conditions as shown in Table 2. The observer is varying from $90^\circ < \theta < 180^\circ$ at $\phi = 0^\circ$. In the simulation, only lower-half of the sphere was utilized since in PO, induced current exists only on the illuminated part.

To evaluate the accuracy of this approach, the simulation is conducted and compared with the analytical model as shown in Fig. 8. The well-known characteristic of PO, in which the accuracy is expected in the region of main direction but degraded in the oblique incidence was observed in both 2D and 3D geometrical cases.

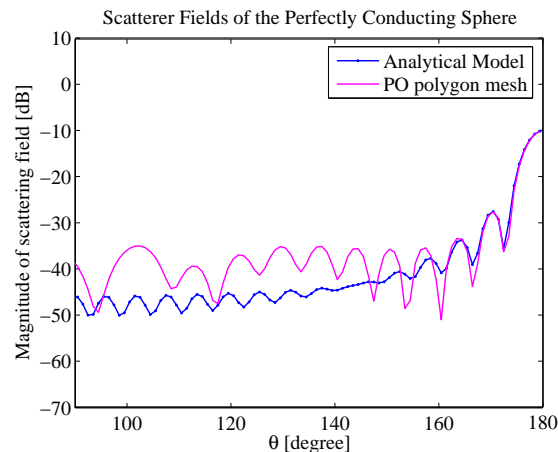


Figure 8 : Scattering field corresponding to Polygon Meshed PO and the analytical model

5. Conclusion

This study introduced the polygon mesh method applied in PO approximation to simplify the complex model and calculation of the scatterer and scattered field. This approach was called “Polygon Meshed PO”.

Simulations of the scattered field from 2D and 3D geometrical objects by either varying the incident directions or varying the observer directions were conducted to evaluate the performance of this approach. By defining the polygon mesh ratio, the convergence of the simulated scattered field can be found.

The verification of this approach was performed by comparing with the PO analytical model and MoM in the 2D geometrical case. The analytical solution of the perfectly conducting sphere was used in the 3D geometrical case to verify the accuracy. From the results of both 2D and 3D cases, PO analytical and PO using polygon mesh have great agreement with each other; however, they can perform high accuracy only in the region of main direction and is slowly degraded in the shadow region as a result of PO’s simplification.

REFERENCES

1. Mir Ghoraiishi, Jun-ichi Takada, and Tetsuro Imai, “Identification of the Scatterers in the Urban Microcell Environments,” *Technical report of IEICE, WBS2004-164, AP2004-345, RCS2004-432, MoMuC2004-215, MW2004-342 (2005-03)*.
2. Mir Ghoraiishi, Junichi Takada and Tetsuro Imai, “Investigating Dominant Scatterers in Urban Mobile Propagation Channel,” *IEEE International Symposium on Communications and Information Technologies 2004 (ISCIT 2004), Oct., 2004 (Sapporo, Japan)*.
3. Hary Budiarto, Kenshi Horihata, Katsuyuki Haneda, and Jun-ichi Takada, “Experimental Study of Non-specular Wave Scattering from Building Surface Roughness for the Mobile Propagation Modeling,” *IEICE Transactions on Communications, vol. E87-B, no.4, pp. 958-966, Apr. 2004*.
4. I. Yamashita, Eikichi, “*Analysis Methods for Electromagnetic Wave Problems. - 2Rev.ed.*,” Artech House Inc.1990.
5. Barber, C. B., D.P. Dobkin, and H.T. Huhdanpaa, “The Quickhull Algorithm for Convex Hulls,” *ACM Transactions on Mathematical Software, Vol. 22, No. 4, Dec. 1996*.
6. Roberto Lattuada and Jonathan Raper, “Application of 3D Delaunay Triangulation Algorithms in Geoscientific Modelling” <<http://www.ncgia.ucsb.edu/conf/>>
7. Nagayoshi Morita, Nobuaki Kumagai, Joseph R. Mautz, “*Integral Equation Method for Electromagnetics*” Artech House Inc, 1990.

Study of High Fundamental Frequency Crystal-based Voltage Control Oscillator for 10 Gbit Ethernet Application

Y. C. Chen

Department of Electrical Engineering, Lunghwa University of Science and Technology

Gueishan Shiang, Taoyuan County, Taiwan

Abstract - Nowadays, the operations of clock and data recovery (CDR), clock smoothing or frequency translation of optical fiber communication systems such as the SONET/SDH (Synchronous Optical Network / Synchronous Digital Hierarchy), are provided by voltage-tunable high frequency clock sources with, absolute pulling range exceeding ± 50 ppm in an operating temperature range of -40 to 85 OC, frequency-voltage linearity smaller than 10%, and phase jitter less than 1 pSec integrated from 12 KHz to 20 MHz of the offset frequency from the carrier. A voltage-controlled crystal oscillator (VCXO) is good for clocking up to about 100 MHz. For crystal to meet the requirements at high frequencies, high fundamental frequency (HFF) crystal blanks are required. In this paper, the developing procedures and test results for a HFF crystal-based 622.08 MHz voltage control oscillator are recorded. The VCXO is composed of a 155.52 MHz HFF crystal and a multiplier circuit is used to generate a 622.08 MHz clock. The test results include the variation of frequency over control voltage range, phase noise, and phase jitter. The pulling range, frequency-voltage linearity and phase jitter measured are + 155ppm/-133 ppm, 9.6 % and 0.21 pSec, respectively.

1. INTRODUCTION

Nowadays, the operations of clock and data recovery (CDR), clock smoothing or frequency translation of fiber-optic communication systems such as the SONET/SDH (Synchronous Optical Network / Synchronous Digital Hierarchy), are provided by voltage-tunable high frequency clock sources with, absolute pulling range exceeding ± 50 ppm in an operating temperature range of -40 to 85 °C, frequency-voltage linearity smaller than 10%, the phase jitter integrated from 12 KHz to 20 MHz must be less than 1 pSec.[1,2]

In the case of voltage control SAW oscillator (VCISO), the frequency temperature stability is ± 80 ppm from -40 °C to 85 °C. On the other hand, VCXO that uses AT-cut crystal, the frequency temperature stability is ± 20 ppm from -40 °C to 85 °C. The noise added in voltage control port will induce the phase noise of voltage control oscillator. Since a wider frequency tuning range is more needed for VCISO than that of VCXO to compensate the temperature variation. Thus the higher frequency sensitivity of VCISO is needed than that of VCXO at the same control voltage range. The phase noise of VCISO is worse than that of VCXO.[3-5]

For crystal to meet the requirements of 622.08 MHz clock, a 19.44 MHz VCXO composed of a 19.44 MHz crystal and with x32 phase lock loop can be used. But the phase jitter integrated from 12 KHz to 20 MHz will be larger than 1 pSec. The purpose of this paper is to develop a 622.08 MHz voltage control oscillator by a 155.52 MHz high fundamental frequency (HFF) crystal and x4 multiplier for SONET/SDH timing applications. The prototype can also be used in phase lock loop applications for clock smoothing and frequency translation. Testing results, including of the pulling range, linearity, phase noise and phase jitter are included.

II. DESIGN OF VCXO

The thickness shear AT cut crystal provides excellent temperature characteristic. The resonance frequency is inverse proportion to the thickness of the substrate. The substrate of AT cut crystal has to be approximately 10 micro-meter to achieve 155 MHz in the fundamental mode. Conventional mechanical fabricating method is not possible for mass production. But by a chemical etching method can be realized. As shown in figure 1, the equivalent circuit near resonant for such a 1-port crystal resonator has series resonant arm containing the motional elements C_m , L_m , and R_m shunted by a static capacitance C_0 .

The Pierce-type oscillator circuit of the VCXO is shown in figure 2. The capacitor at the base-to-GND and capacitor at the collector-GND along with the crystal resonator, which acts as an inductor, form a pi-network to provide the required phase shift so to fulfill the Barkhausen's oscillation criteria. From another viewpoint, oscillation can be sustained because the capacitor C_1 , together with the C_2 and the transistor, provides the negative resistance (gain) which cancels with the loss due to resistance of the resonator. C_1 and C_2 affect the center frequency and the frequency tuning bandwidth. The inductance L_1 can drag the load capacitance into the inductive domain such that frequency control range can be widened. In other words, the separation between the resonating frequency and anti-resonating frequency will increase when an inductor is added in series with the crystal resonator. Through this, the pulling range of the VCXO can be increased. By changing the load capacitance of the oscillation circuit with the characteristic of capacitance versus reverse direction voltage of the varactor diode D_1 (varicap), one can change the output frequency. Crystal, L_1 and D_1 together act as an effective resonator whose reactance can be changed by the control voltage. R_1 is a shunt feedback resistor from the collector to base for adjusting the feedback power into the effective resonator. The supply voltage for the VCXO is 3.3 V instead of the conventional 5.0 V so to achieve lower power consumption and faster signal processing.

III. TESTING RESULTS

The variation of the output frequency for the prototype 622.08 MHz VCXO with control voltage from 0.3 to 3.0 V with a 0.15 V step is as shown in figure 3. The center value of the control voltage is 1.65 V, which is the half value of the supply voltage. The frequency increases with the increase of the control voltage and pulling range is about +155 ppm/-133 ppm. The generally accepted definition of linearity is the ratio between frequency error and total deviation, expressed in percent, where frequency error is the maximum frequency excursion from the best straight line fit. The linearity calculated is 9.6 %.

The phase noise of the 622.08 MHz VCXO is measured with the three components comparison method using an Agilent phase noise testset. As seen from figure 4, the phase noise is -59, -93, -118, -138 and -142 dBc/Hz at 10 Hz, 100 Hz, 1 KHz, 10 KHz and 100 KHz offset from the carrier, respectively.

The phase jitter can be calculated by using equation as shown below which involves the integration the phase noise result from 12 KHz to 20 MHz:

$$\text{RMS Jitter in seconds} = (360/2/3.14) \times 10^{(\text{Value of definite integral}/20)} / 360 \times \text{Frequency}$$

The calculated phase jitter is about 0.21 pSec.

IV. CONCLUSION

This study is to develop a 622.08 MHz VCO composed of 155.52 MHz VCXO composed of a 155.52 MHz HFF crystal and x4 multiplier for the fiber-optic communication systems. The pulling range achieved is about +155 ppm/-133 ppm. The linearity is about 9.6 % with the control voltage range from 0.3 to 3.0 V. The phase noise at 10 Hz, 100 Hz, 1 KHz, 10 KHz and 100 KHz offset from carrier is -59, -93, -118, -138 and -142 dBc/Hz, respectively. The phase jitter is 0.21 pSec in the frequency range from 12 KHz to 20 MHz.

References

- [1]. M.C. Chow, "Understanding SONET/SDH", published by Andan, 2000.
- [2]. R. Colvin, "UHF Acoustic Oscillators", Microwave Journal, Vol. 23, 1980, pp. 22-23.
- [3]. I. D. Avramov, F. L. Walls, T. E. Parker, and G. K. Montress, "Extremely Low Thermal Noise Floor, High Power Oscillators Using Surface Transverse Wave Devices," IEEE Trans. On Ultrasonics, Ferroelectric and Frequency Control, Vol. 43, No. 1, January, 1996, pp. 20-28.
- [4]. G. K. Montress, and T. E. Parker , " Design Techniques for Achieving State-of-the-art Oscillator Performance," Proc. IEEE Freq. Contr. Symp., 1990, pp. 522-535.
- [5]. G. K. Montress, and T. E. Parker , " Design and performance of an Extremely Low Noise Surface Acoustic Wave Oscillator," Proc. IEEE Freq. Contr. Symp., 1994, pp. 365-373.

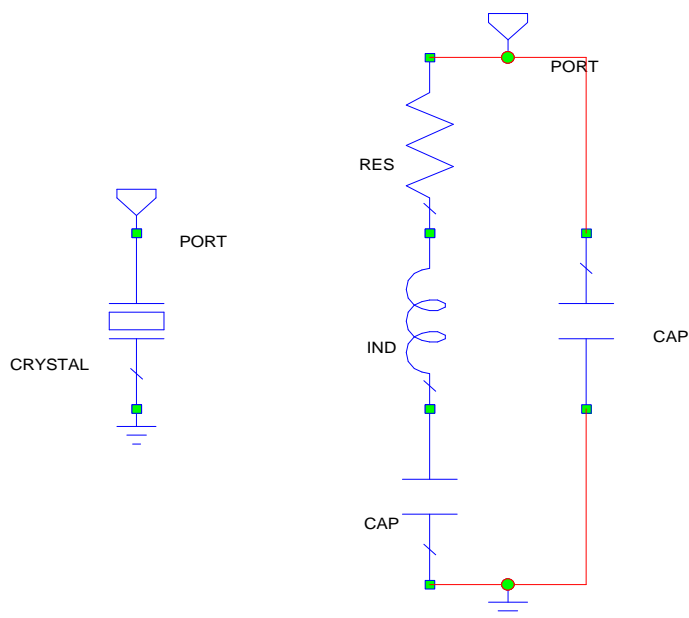


Figure 1. Equivalent Circuit of 1-port crystal.

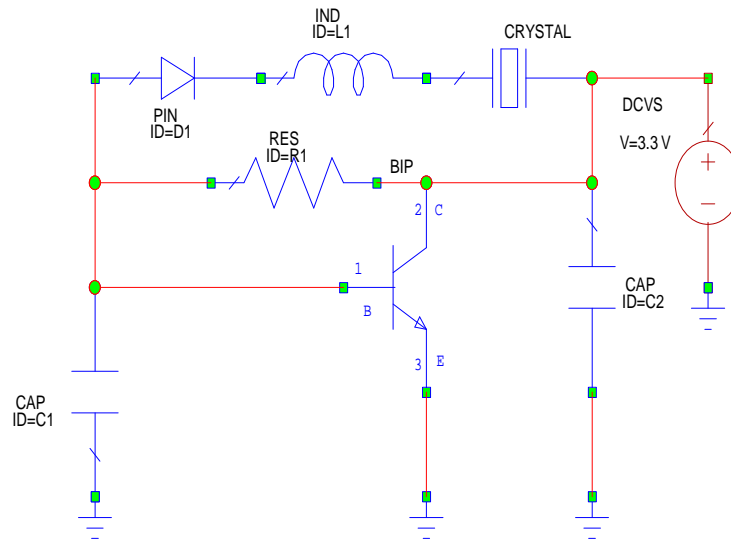


Figure 2. Basic circuit of the Pierce type VCXO.

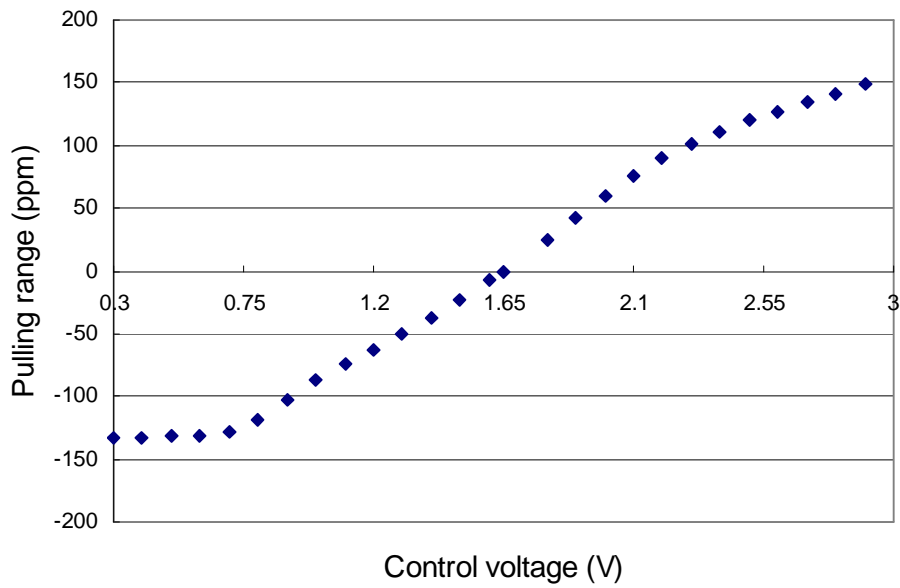


Figure 3. Variation of the Output Frequency with Control Voltage.

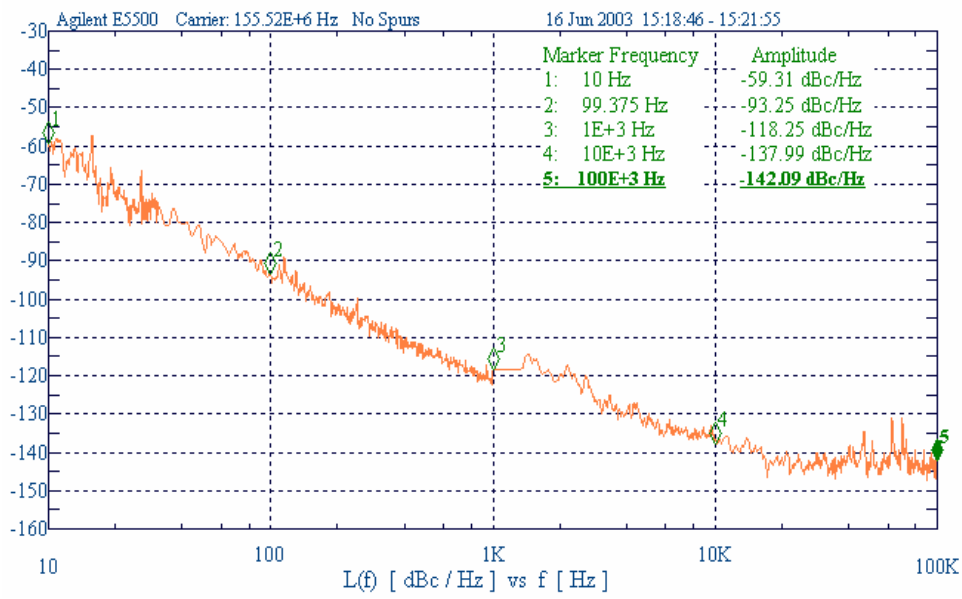


Figure 4. Phase Noise of the 622.08 MHz VCXO from 10 Hz to 100 KHz.

A Highly Miniaturized Broadband On-chip Impedance Transformer Employing PPGM on GaAs MMIC

YOUNG YUN, KYUNG-SIK LEE and CHUNG-RYUL KIM

Dept. of Radio Sciences and Engineering, Korea Maritime University

Abstract — In this work, using a microstrip line employing Periodically Perforated Ground Metal (PPGM) on GaAs MMIC, a highly miniaturized and broadband on-chip impedance transformer was developed for application to low impedance matching in broadband. Its size was 0.0425 mm^2 on GaAs substrate, which was 2.3 % of the one fabricated by conventional microstrip line. The transformer showed a good RF performance over a broadband including Ultra Wide Band (UWB).

1. Introduction

Recently, demands for broadband and fully integrated MMICs (Monolithic Microwave Integrated Circuits) have increased in the broadband wireless communication systems market [1]-[3]. In order to realize broadband and fully integrated MMICs, broadband low impedance transformer performing low impedance transformation between active devices is indispensable and it should be highly miniaturized for an integration on MMICs, because the real part of the input and output impedances of FETs are much lower than 50Ω in RF band[3]. However, conventional impedance transformers [4] have been fabricated outside of MMICs due to their large sizes, and used for application to the high impedance transformation (in the range of $40 - 70 \Omega$) because the line width of conventional microstrip line with low impedance is very large and it can't be realized on MMIC. For example, the line width W should be $500 \mu\text{m}$ to obtain a characteristic impedance Z_0 of 15Ω from the conventional microstrip line on GaAs substrate.

In this work, to realize on-chip low impedance transformer in a broadband system including UWB (Ultra Wide Band), we propose highly miniaturized on-chip transformer employing PPGM (Periodically Perforated Ground Metal) structure [5] that has a much lower characteristic impedance and shorter guided-wavelength than the conventional microstrip line structure, which allowed the integration of the transformer on MMIC via its miniaturization.

2. Microstrip Line Employing PPGM Structure

Figure 1 (a) shows a top view of the microstrip line employing PPGM, and Figure 1 (b) corresponds to a cross-sectional view according to Y-Y direction of Fig. 1 (a). As is well known, conventional microstrip line without PPGM has only a periodical capacitance C_a (C_a is shown in Fig. 1 (b)) per a unit length, while the microstrip line employing PPGM has additional capacitance C_b as well as C_a due to PPGM. From this figure, we can see that the microstrip line with PPGM exhibits much lower characteristic impedance (Z_0) and shorter guided-wavelength (λ_g) than conventional one, because Z_0 and λ_g are inversely proportional to the periodical capacitance, in other words, $Z_0 = (L/C)^{0.5}$ and $\lambda_g = 1/[f(LC)^{0.5}]$. The wavelength (λ_g) for conventional microstrip line and PPGM structure on GaAs substrate with a height of $100 \mu\text{m}$ is shown in Fig. 2, where the thickness of SiN film and T for PPGM structure are 700 nm and $20 \mu\text{m}$, respectively. As shown in this figure, the wavelength was highly reduced by using the PPGM structure. Figure 3 shows measured characteristic impedance Z_B , where T is the spacing between periodically perforated rectangular holes shown in Fig. 1 (a) and (b). Microstrip lines were fabricated by Au plating on GaAs substrate with a height of $100 \mu\text{m}$. The width L for the holes and line width W , which are shown in Fig. 1 (a) and (b), were set to $20 \mu\text{m}$, respectively. The thickness of the SiN layer was 700 nm . As shown in Fig. 3, characteristic impedance of the conventional microstrip line, which corresponds to the data at the spacing $T = 0$, is 80Ω , and low Z_B can be obtained by

increasing the spacing T because an increase of T causes an enhancement of periodic capacitance C_b . The value for Z_B can be easily controlled by only changing the spacing T . Above results mean that the PPGM structure can be used for application to low impedance and miniaturized on-chip components on MMIC.

We also investigated the loss of PPGM structure with double and single-sided via holes, which are shown in Fig. 4(a) and (b), respectively. The insertion loss of the PPGM structure with double and single-sided via holes are shown in Fig. 5, where the loss of the conventional microstrip line was also plotted for comparison. The insertion loss was measured at a port impedance of 50Ω , and it was normalized by characteristic impedance Z_0 of the microstrip lines.

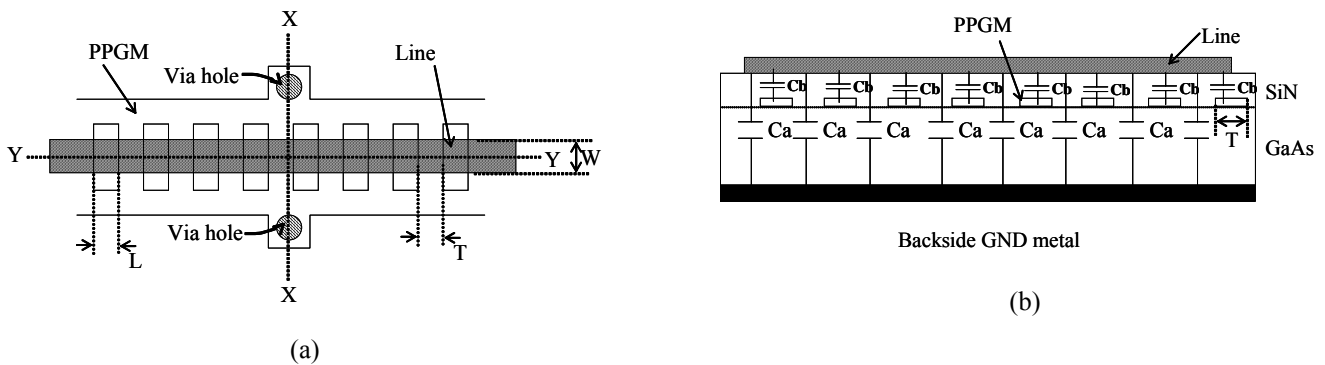


Fig. 1 (a): A top view of the microstrip line employing PPGM.

(b): A cross-sectional view according to Y-Y direction of Fig. 1 (a).

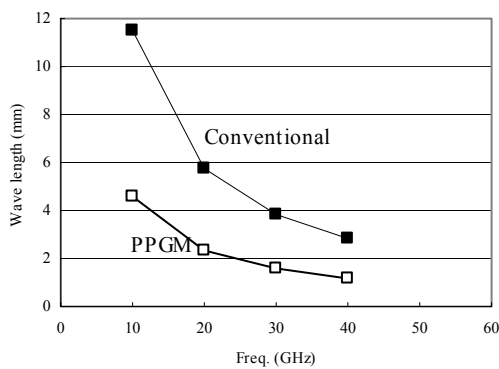


Fig.2: Wavelength for conventional microstrip line and PPGM structure.

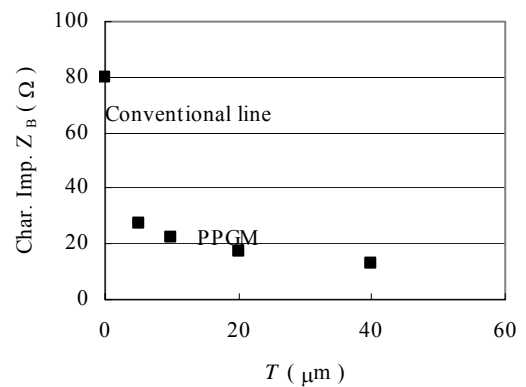


Fig.3: Characteristic impedance for conventional microstrip line and PPGM structure.



Fig. 4 (a): PPGM structure employing double-sided via holes.
 (b): PPGM structure employing single-sided via holes.

As shown in this figure, the microstrip line with PPGM structure shows higher insertion loss than the conventional one. Concretely, the loss with double-sided via holes is less than 2 dB up to 40 GHz. For application to highly miniaturized passive components, however, the PPGM structure seems very attractive in spite of its relatively high loss, because the loss (less than 2 dB up to 40 GHz) is not so serious for a development of on-chip passive components, and it can be easily compensated by increasing the gain of amplifiers of RF system. As shown in Fig. 5, we can see that the insertion loss of the PPGM structure is dependent on the ground condition, and therefore, the PPGM structure with double-sided via holes exhibits lower loss than the one with single-sided via holes. Up to 20 GHz, however, there is no difference between the two structures. Therefore, in this work, the PPGM structure with single-sided via holes was employed for a development of further miniaturized on-chip transformer, because the transformer was designed for application to frequency band lower than 20 GHz.

3. Highly Miniaturized and Low Impedance Transformer Employing PPGM Structure

In this work, we fabricated highly miniaturized on-chip transformers employing PPGM. We fabricated a single section $\lambda/4$ impedance transformer using the PPGM structure and measured its RF characteristics. Figure 6 and 7 shows a schematic diagram and photograph of the single section $\lambda/4$ impedance transformer employing PPGM structure on GaAs substrate. As shown in Fig. 6, the characteristic impedance Z_{0T} of the transformer is given by [6],

$$Z_{0T} = \sqrt{Z_0 Z_{LR}} \quad (1)$$

where Z_{LR} and Z_0 are the load and port impedance, respectively. In this work, the Z_{LR} and Z_0 are 20 and 10 Ω , respectively, and the Z_{0T} is 14.1 Ω . In this work, for the PPGM structure, we employed SIN film with a thickness of 100nm for a further miniaturization of transformer. Therefore, the length of the $\lambda/4$ transformer at 7 GHz is 0.425 mm for a line width W of 20 μm . Therefore, the size of the transformer including via holes is 0.0425 mm², which is 2.3% of the size of the transformer fabricated by conventional microstrip line. In other words, if $\lambda/4$ transformer with a Z_{0T} of 14.1 Ω is fabricated by conventional microstrip line on GaAs substrate, the line width W and length should be 550 μm and 3.3 mm, respectively, and its size is 1.82 mm²[6]. The sizes for the transformer are summarized in Table 1. Figure 8 shows measured return loss S_{11} (Γ of Fig. 6) and insertion loss S_{21} , respectively. As shown in this figure, we can observe return loss values lower than -9 dB from 3 GHz to 10.5 GHz, and insertion loss values lower than 1 dB in the above frequency range.

Table 1: Size of the single-section transformer employing conventional microstrip lines and PPGM.

	W	$\lambda_g/4$	Size
Conventional microstrip line	550 μm	3.3 mm	1.82 mm ²
PPGM	20 μm	0.425 mm	0.0425 mm ²

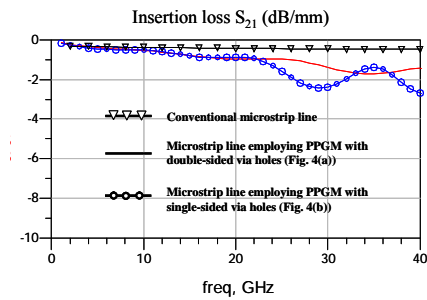


Fig. 5: The insertion loss of PPGM structure and conventional microstrip line.

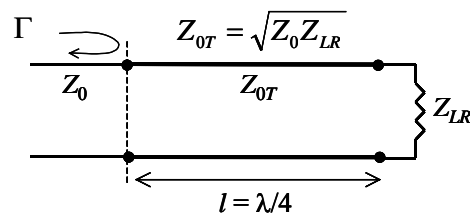


Fig.6: A schematic diagram of the single-section impedance transformer

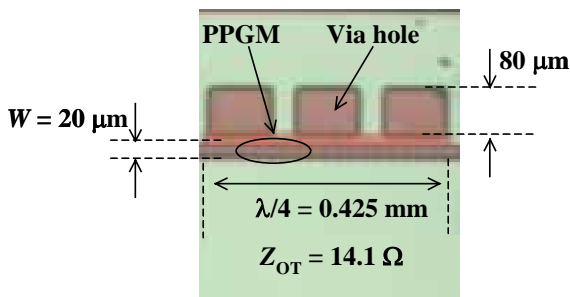


Fig.7: A photography of the single-section impedance transformer

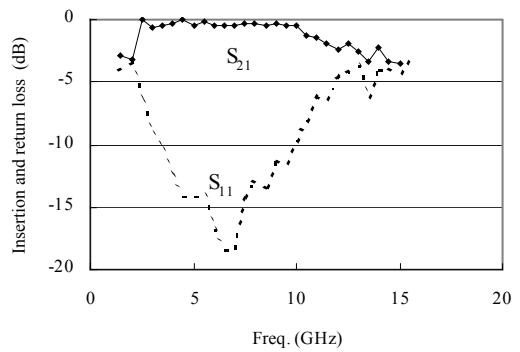


Fig. 8: Measured return and insertion loss of the single-section impedance transformer

4. Conclusion

In this work, using a microstrip line employing Periodically Perforated Ground Metal (PPGM) on GaAs MMIC, we fabricated a highly miniaturized and broadband on-chip impedance transformer for application to low impedance matching in broadband including UWB. Its size was 0.0425 mm^2 on GaAs substrate, which was 2.3 % of the one fabricated by conventional microstrip line. The transformer showed loss values lower than -9 dB from 3 GHz to 10.5 GHz, and insertion loss values lower than 1 dB in the above frequency range. Above results indicate that the on-chip impedance transformer employing PPGM is a promising candidate for application to the on-chip matching components in broadband system including UWB.

Acknowledgement

This work was supported by Korea Research Foundation Grant (R05-2004-000-12754-0).

REFERENCES

1. Matsunaga, K., Miura, I., and Iwata, N., "A CW 4-W Ka-Band Power Amplifier Utilizing MMIC Multichip Technology," *IEEE J. Solid State Circuits*, vol. 35, pp. 1293-1297, Sept. 2000.
2. Webster, D. R., Ataei, G., and Haigh, D. G., "Low-Distortion MMIC Power Amplifier Using a New Form of Derivative Superposition," *IEEE Trans. Microwave Theory and Tech.*, vol. 49, pp. 328-332, Feb. 2001.
3. Yun, Y., Nishijima, M., Katsuno, M., Ishida, H., Minagawa, K., Nobusada, T., and Tanaka, T., "A Fully-Integrated Broadband Amplifier MMIC Employing a Novel Chip Size Package," *IEEE Trans. Microwave Theory Tech.*, vol. 50, pp. 2930-2937, Dec. 2002.
4. Bahl, I., and Bhartia, P., *Microwave Solid State Circuit Design*, New York: John Wiley & Sons, 1988.
5. Yun, Y., "A Novel Microstrip Line Structure Employing a Periodically Perforated Ground Metal and Its Application to Highly Miniaturized and Low Impedance Passive Components Fabricated on GaAs MMIC," *IEEE Trans. Microwave Theory Tech.*, vol. 53, No. 6, pp. 1951-1959, June 2005.
6. D. M. Pozar, *Microwave Engineering*. Reading, MA: Addison-Wesley, 1990.

A highly miniaturized and low impedance on-chip Wilkinson power divider employing PPGM on MMIC

C.R. Kim and Y. Yun

Dept. of Radio Sciences and Engineering, Korea Maritime University, Korea

Abstract: In this work, we propose a low-impedance and highly miniaturized on-chip Wilkinson power divider on MMIC, which was fabricated by a microstrip line structure employing periodically perforated ground metal (PPGM) with single-sided via holes. Using the microstrip line with PPGM, a miniaturized 13 Ω power divider was fabricated. The size of the power divider was 0.110 mm², which was 6 % of conventional one.

1. Introduction

RF components dealing with high frequency signals are most important in wireless communication system and the performance of the system depends on them. In order to realize highly miniaturized and fully integrated MMICs, the development of miniaturized on-chip passive components is indispensable. The development of miniaturized on-chip passive components with low port impedances will especially greatly reduce the size of MMICs by removing bulky impedance transformation circuits between the passive components and low-impedance FETs; generally, the input and output impedances of the FETs are much lower than 50 Ω in the RF frequency. Therefore, impedance transformation circuits should be employed for impedance matching between 50 Ω - based passive components and low-impedance FETs [1]. However, in case of fabricating low impedance line using the conventional microstrip with ground metal on the backside of GaAs substrate, the width of the line becomes very large. For instance, when making 15 Ω line on the GaAs substrate with 100 μm height, the width of the line reaches 800 μm .

In this work, using Periodically Perforated Ground Metal (PPGM) structure with single-sided via holes, we developed a low-impedance and highly miniaturized on-chip Wilkinson power divider on MMIC.

2. A microstrip line employing PPGM

In this work, we employed Periodically Perforated Ground Metal (PPGM) structure with high capacitive element [2] in order to develop a low impedance on-chip Wilkinson power divider. Especially, the PPGM structure with single-sided via holes was used for size reduction, which highly miniaturized the Wilkinson power divider. Figure 1 (a) and (b) show a top view of the PPGM bend structure with double-sided and single-sided via holes, respectively, and Fig. 1 (c) corresponds to a cross-sectional view

according to Y-Y direction of Fig. 1 (a) and (b). As shown in Figure 1 (a)-(c), PPGM was inserted at the interface between SiN film and GaAs substrate, and it was electrically connected to backside ground metal through the via-holes.

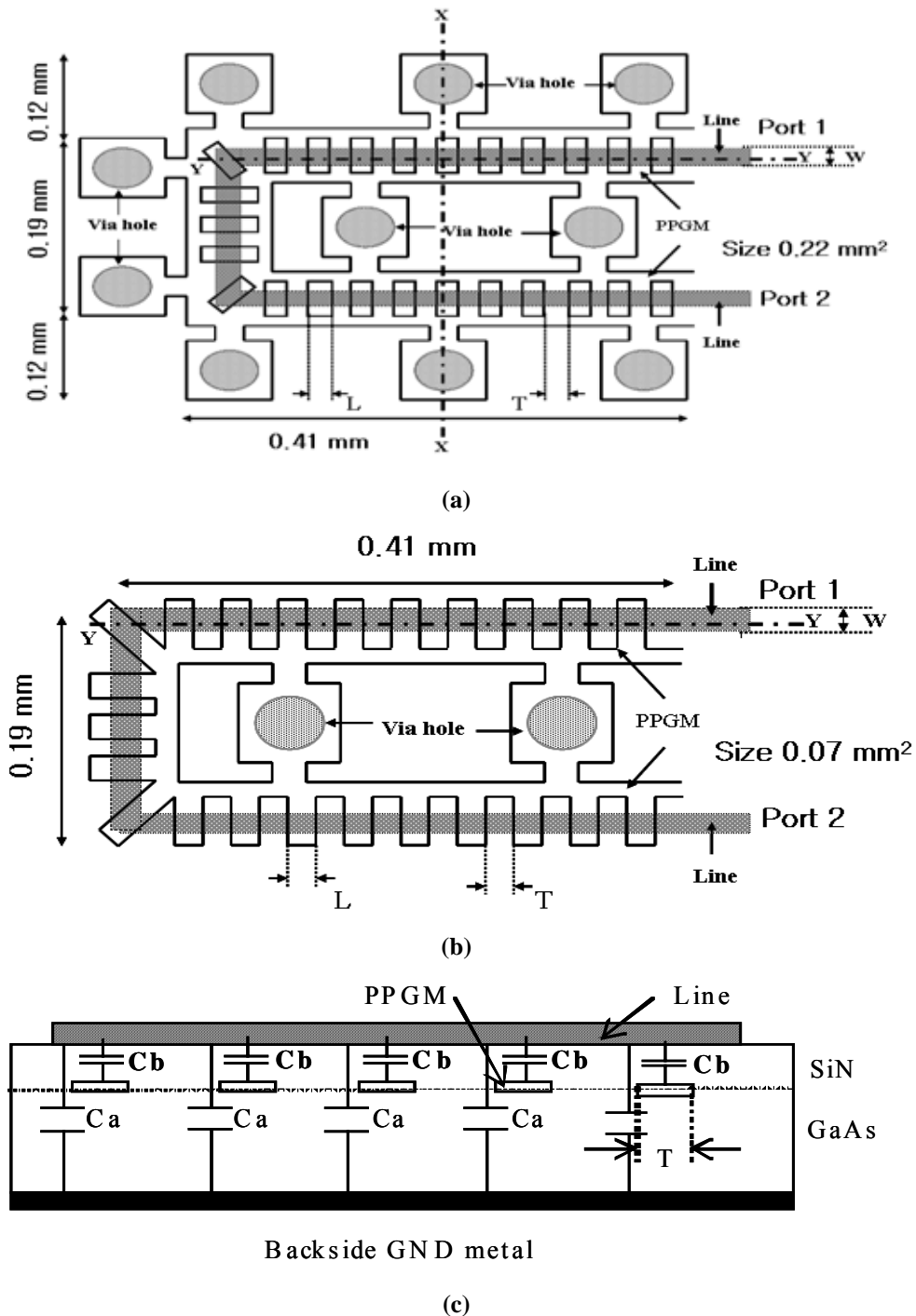


Figure 1 (a) PPGM bend structure with double-sided via holes
 (b) PPGM bend structure with single-sided via holes
 (c) A cross-sectional view according to Y-Y direction of Fig. 1 (a) and (b)

As is well known, conventional microstrip line without PPGM has only a periodical capacitance C_a (C_a is shown in Fig. 1 (c)) per a unit length, while the microstrip line employing PPGM has additional capacitance C_b as well as C_a due to PPGM. From this figure, we can see that the microstrip line with PPGM exhibits much lower characteristic impedance (Z_0) and shorter guided-wavelength (λ_g) than conventional one, because Z_0 and λ_g are inversely proportional to the periodical capacitance, in other words, $Z_0 = (L/C)^{0.5}$ and $\lambda_g = 1/[f \cdot (LC)^{0.5}]$. Table 1 shows the calculated wavelength for the conventional microstrip line and PPGM structure. As shown in Table I, line width and wavelength of the PPGM structure with a characteristic impedance of 13 Ω are 20 μm and 2.35 mm, while line width and wavelength of the conventional microstrip line with a characteristic impedance of 13 Ω are 640 μm and 18.5 mm. From the above results, we can conclude that low impedance and highly miniaturized passive components on MMIC can be realized by using the PPGM structure.

A number of via holes are required for perfect ground condition of the PPGM structure. In this work, however, the number of via holes was minimized in order to reduce the component size as much as possible, and the PPGM bend structure with single-sided via holes shown in Fig. 1 (b) was used for further reduction of the power divider. Figure 2 shows the insertion loss of the PPGM bend structures with double- and single-sided via holes shown in Fig.1 (a) and (b). As shown in this figure, a significant difference between the two structures is not observed up to 25 GHz, and the PPGM bend structure with single-sided via holes was employed for MMIC applications in lower frequencies than K band.

Table 1 The size comparison for the PPGM structure and the conventional microstrip line (at 5GHz)

	W	λ
Conventional microstrip line	640 (μm)	18.5 mm
PPGM structure	20 (μm)	2.35 mm

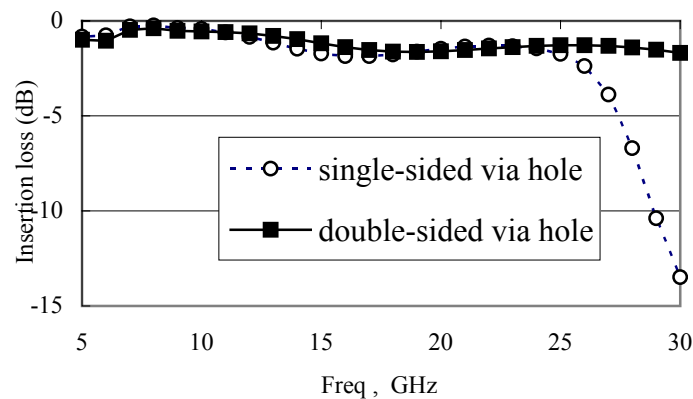


Figure 2 Insertion loss of the PPGM bend structure with single-sided and double-sided via holes

3. A miniaturized and low impedance on-chip Wilkinson power divider employing PPGM structure with single-sided via holes.

In this work, using the PPGM structure with single-sided via holes, a highly miniaturized on-chip Wilkinson power divider with a low port impedance of 13Ω was developed. The photograph for the power divide is shown in Fig.3. Real size of the power divider corresponds to the part surrounded by dotted line because GSG pad was connected for on-wafer measurement, and its size is 0.11 mm^2 , which is 6 % of the size of the one fabricated by conventional microstrip line (the size of the power divider employing conventional microstrip line is 1.82 mm^2 at a 5 GHz [3]). Figure 4 (a) and (b) shows measured power division (S_{12} and S_{13}) and isolation characteristics (S_{23}) for the Wilkinson power divider employing PPGM structure respectively. As shown in Fig. 4 (a), we can observe equal power division characteristics due to its symmetrical structure. From Fig. 4 (a) and (b), we can observe insertion loss values lower than 5.5 dB, and isolations values higher than 7.5 dB from 4.5 to 6 GHz. Isolation characteristics can be improved by increasing the number of via holes for the PPGM structures, however, the PPGM bend structures with only two via holes (see Fig. 3) was employed for size reduction.

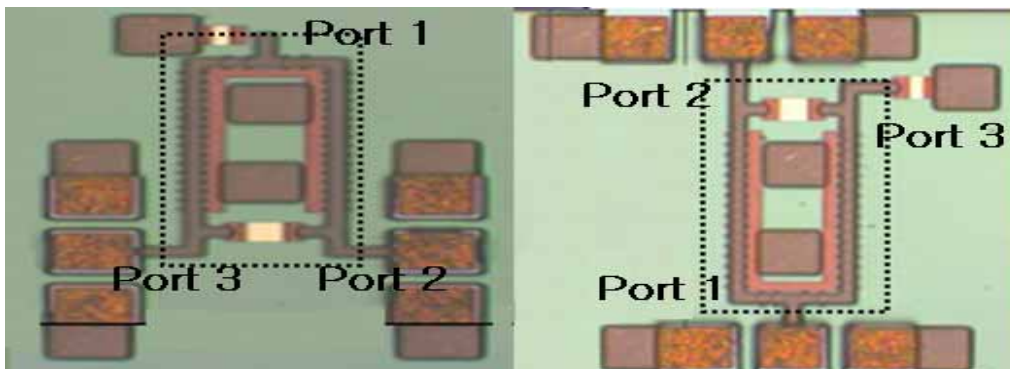


Figure 3 A photograph of the Wilkinson power divider employing PPGM bend structure with single sided via holes

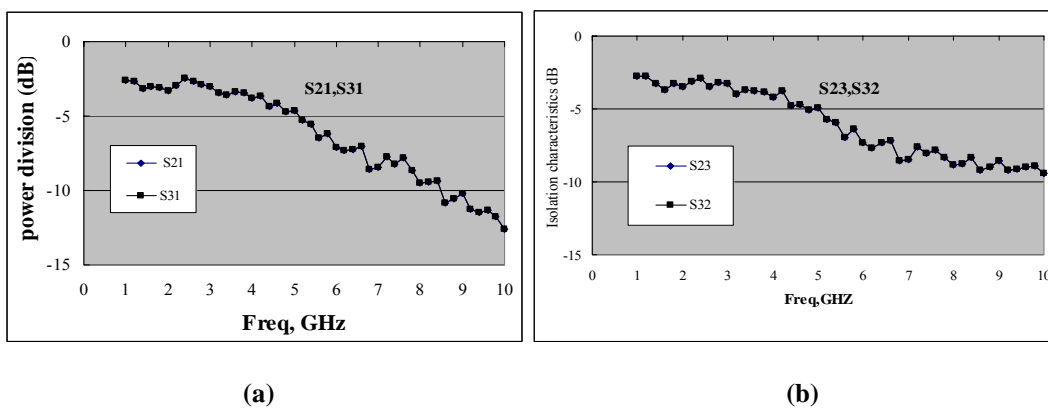


Figure 4 (a) Measured power division characteristic for the Wilkinson power divider
(b) Measured isolation characteristic for the Wilkinson power divider

4. Conclusion

In this work, highly miniaturized and low impedance on-chip Wilkinson power divider employing PPGM structure with single-sided via holes was fabricated on GaAs MMIC. Its size was 0.117 mm^2 , which was 6 % of the conventional one. Equal power division characteristics were observed from the power divider. The power divider showed insertion loss values lower than 5.5 dB and isolations values higher than 7.5 dB from 4.5 to 6 GHz.

Acknowledgement

This work was supported by Korea Research Foundation Grant funded by Korea Government (MOEHRD) (KRF-2005 -003-D00263)

References

- 1 Yun, Y., *et al.*: 'A Fully-integrated broadband amplifier MMIC employing a novel chip size package', *IEEE Trans. MTT.*, 2002, **50**, pp. 2930-2937
- 2 Yun, Y: 'A Low Impedance and Short-Guided Wavelength Microstrip Line', *Proc. 34 th European Microwave Conf.*, 2004, pp. 2930-2937
- 3 POZAR, D. M.: 'Microwave engineering', Second Ed., Chapter 6, (Addison-Wesley, 1990)

3-D 94 GHz Single Balanced Active Mixer using DAML-based Hybrid Ring Coupler

Jin-Koo Rhee, Sung-Chan Kim, Dan An, and Dong-Hoon Shin

Millimeter-wave INnovation Technology research center (MINT), Dongguk University
3-26 Pil-dong, Jung-gu, Seoul 100-715, Korea
Email: jkrhee@dongguk.edu

Abstract - The GaAs-based low loss transmission lines, dielectric-supported air-gapped microstrip lines (DAMLs), are developed using surface micromachining technology. The proposed DAMLs have major advantages such as easiness for fabrication and integration on MMICs compared to the established low loss transmission lines. The DAML-based hybrid ring coupler is successively developed and the novel single balanced active mixer using the hybrid ring coupler and 70 nm gate length MHEMTs is designed and fabricated. This mixer showed that the conversion loss and isolation characteristics were 2.5 dB ~ 2.8 dB and under -30 dB in the range of 93.65 GHz ~ 94.25 GHz, respectively. The low conversion loss of the mixer is mainly attributed to the high-performance of the MHEMTs exhibiting a maximum drain current density of 607 mA/mm, an extrinsic transconductance of 1015 mS/mm, a current gain cutoff frequency (f_T) of 330 GHz, and a maximum oscillation frequency (f_{max}) of 425 GHz. High isolation characteristics are due to the DAML-based hybrid ring coupler which shows isolation characteristics of -34 dB at center frequency of 94 GHz. To our knowledge, these results are the best performance demonstrated from 94 GHz single balanced mixer utilizing GaAs-based HEMTs in terms of conversion loss as well as isolation characteristics.

Keywords: single balanced active mixer, 70 nm, MHEMT, DAML, hybrid ring coupler

1. INTRODUCTION

Recently, the development of the millimeter-wave systems for both commercial and military applications leads to an increase in the demand for low cost and miniaturization characteristics by integrating passive components with active MMICs (micro-wave and millimeter-wave integrated circuits). For passive components, conventional planar transmission line structures such as microstrip line and coplanar waveguide (CPW) are widely used at present. However, the geometric structure of these conventional transmission lines has dielectric loss and dispersion characteristics due to the semiconductor substrate, which degrades the circuit performance at high frequency range. For the purpose of solving this problem, MEMS-based low loss transmission lines have been reported with various structures [1]-[6]. Specially, membrane-supported transmission lines have been proven to be one of the most promising candidates for millimeter-wave application [6]. Although these MEMS-based transmission lines can reduce the substrate loss, they have some critical drawbacks such as difficulty for fabrication, large size, and trouble of integration on MMICs, resulting in high costs per unit area.

In order to solve these problems, we proposed the novel dielectric-supported air-gapped microstrip lines (DAMLs) structure which the signal lines were elevated from ground plates, to reduce the substrate dielectric loss and obtain low losses in the range of millimeter-wave. Using our transmission lines, DAMLs, we developed hybrid ring couplers to demonstrate the possibility of application for the passive components in the range of millimeter-wave. The fabrication process of DAMLs is compatible with the standard MMIC techniques. Moreover the ground plate of the DAMLs is the same that of the MMIC fabricated by using CPW structure. Therefore, the developed hybrid ring coupler can be easily integrated into the MMICs. In addition, we can curtail the cost due to the reduced area by integrating the passive components on plane-structural MMICs vertically.

In this paper, we designed and fabricated a novel single balanced active mixer using the 70 nm gate length MHEMTs and the DAML-based hybrid ring coupler on the same GaAs substrate in order to prove the potential of integration between high performance passive components adopting DAML structure and MMICs. The low conversion loss of the mixer is mainly attributed to the high-performance

2. GAAS-BASED 70 NM MHEMT

GaAs-based epitaxial structures for MHEMTs were grown by molecular beam epitaxy (MBE) on 4-inch semi-insulating (S.I.) (100) GaAs substrates. To achieve low conversion loss of the mixer, a HEMT device should have high peak transconductance as well as low gate capacitance [7]. The epitaxial structure of the MHEMT device was designed with double silicon delta doping in a lower plane ($1.3 \times 10^{12}/\text{cm}^2$) and an upper plane ($4.5 \times 10^{12}/\text{cm}^2$) for high free electron sheet density lead to high peak transconductance [8]. We adopted a low linear grading rate for the $\text{In}_x\text{Al}_{1-x}\text{As}$ buffer layer with indium mole fraction, x , graded from 0 to 0.5 grown on the GaAs substrate to provide high band off-set $\text{In}_{0.52}\text{Ga}_{0.48}\text{As}/\text{In}_{0.53}\text{Al}_{0.47}\text{As}$ heterojunction structure with the high electron mobility and free electron sheet density. The

layer consisted of the following layers: a $1\ \mu\text{m}$ metamorphic buffer layers, a $400\ \text{nm}$ $\text{In}_{0.52}\text{Al}_{0.48}\text{As}$ buffer layer with a silicon delta doping layer, a $4\ \text{nm}$ $\text{In}_{0.52}\text{Al}_{0.48}\text{As}$ spacer layer, a $15\ \text{nm}$ $\text{In}_{0.53}\text{Ga}_{0.47}\text{As}$ channel layer, a $3\ \text{nm}$ $\text{In}_{0.52}\text{Al}_{0.48}\text{As}$ spacer layer, a $10\ \text{nm}$ $\text{In}_{0.52}\text{Al}_{0.48}\text{As}$ schottky layer with a silicon delta doping layer, and finally a $15\ \text{nm}$ $\text{n}^+\text{In}_{0.53}\text{Ga}_{0.48}\text{As}$ cap layer. Hall measurement of this structure, after moving the InGaAs Cap layer, showed a two-dimensional electron gas with a sheet density of $3.36 \times 10^{12}\ \text{cm}^{-2}$ and a mobility of $9070\ \text{cm}^2/\text{V}\cdot\text{s}$ at room temperature. The gate capacitance was minimized using an optimized narrow recess structure with short gate length. To obtain low gate capacitance, we fabricated the MHEMTs with a $70\ \text{nm}$ gate length using the in-house developed submicron technology [9].

The fabricated $70 \times 2\ \mu\text{m}$ (unit gate width of $70\ \mu\text{m}$ and two gate fingers) MHEMTs with a $70\ \text{nm}$ gate length were characterized by measuring the DC and RF. Fig. 1 shows the extrinsic transconductance (g_m) and drain current (I_{ds}) as functions of the gate voltage (V_{gs}) at $1.6\ \text{V}$ of drain voltage (V_{ds}). We obtained a good pinch-off property of $V_p = -0.8\ \text{V}$ and a maximum drain current density of $607\ \text{mA}/\text{mm}$. The measured maximum extrinsic transconductance (g_m) was $1015\ \text{mS}/\text{mm}$ at a drain voltage (V_d) of $1.6\ \text{V}$ and a gate voltage (V_g) of $-0.3\ \text{V}$. The RF measurements were performed in a frequency range of $1\ \text{GHz} \sim 75\ \text{GHz}$. As a consequence of extrapolating by a slope of $-6\ \text{dB}/\text{octave}$ from the measured current gain ($|h_{21}|^2$) and Mason's unilateral gain (U_{gain}), we obtained a current gain cutoff frequency (f_T) of $330\ \text{GHz}$ and maximum oscillation frequency (f_{max}) of $425\ \text{GHz}$ as shown Fig. 2.

3. DAML-BASED HYBRID RING COUPLER

3.1. DAML: Dielectric-supported Air-gapped Microstrip Line

The structure of the proposed DAML is shown in Fig. 3. The signal line is fabricated using GaAs-based surface micromachining techniques to rise in the air with the help of polyimide dielectric posts. This structure has the advantage of reduced dielectric losses because most of the electric field is confined in the air between the signal line and the ground plate, not in the GaAs substrate which has a typical thickness of $680\ \mu\text{m}$ and a relative dielectric constant of 12.9 . Also, the DAML relieves the burden of the complex backside process in the realization of a microstrip structure, because the signal line and the ground plate are on the same plane. Another interesting possibility of this technology is that we may achieve a compact, 3-D integration of active and passive devices, because active devices may be located under the elevated signal lines or passive devices based on these lines. Design parameters such as the characteristic impedance (Z_0), the insertion loss (dB/cm), and the dielectric constant were simulated by a commercial electromagnetic simulator, HFSS. The signal line width was varied from $10\ \mu\text{m}$ to $110\ \mu\text{m}$ by $10\ \mu\text{m}$ steps. The entire line length was $5\ \text{mm}$. The spacing between adjacent dielectric posts was $500\ \mu\text{m}$, and the size of the bottom plane of the post was $10\ \mu\text{m} \times 10\ \mu\text{m}$. The height of the post was varied from $2\ \mu\text{m}$ to $18\ \mu\text{m}$ by $1\ \mu\text{m}$ steps. From the electromagnetic (EM) simulation, we observed that the insertion losses saturated when the height was over $9\ \mu\text{m}$. The SEM photograph of the fabricated DAML is shown in Fig. 4. Sacrificial layers are completely removed between signal line and ground metal and signal line is stably elevated by dielectric post. From the SEM measurements, we verified that the maximum space between the dielectric posts to elevate the signal line on air with stability is $2\ \text{mm}$.

The process flow of DAML is as follows. Initially, Ti and Au are evaporated on a GaAs substrate as a ground metal, and then dielectric posts with height of $10\ \mu\text{m}$ are fabricated. Dielectric post is photo-definable and their size is $10\ \mu\text{m} \times 10\ \mu\text{m}$. After patterning sacrificial layer with height of $10\ \mu\text{m}$, Au thin film is evaporated to prevent the development of a

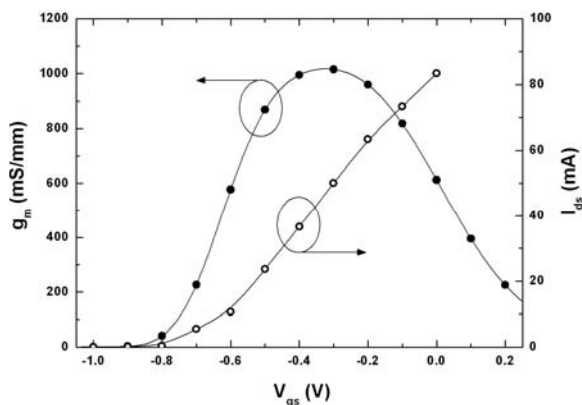


Fig. 1. Transconductance (g_m) and drain current (I_{ds}) as functions of the gate voltage (V_{gs}) at $1.6\ \text{V}$ of drain voltage (V_{ds})

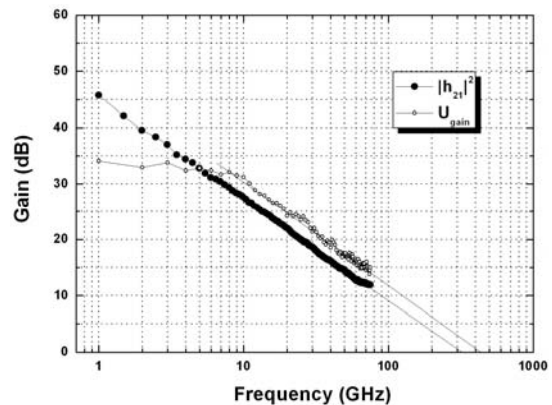


Fig. 2. Current gain ($|h_{21}|^2$) and Mason's unilateral gain (U_{gain}) characteristics as a function of frequency

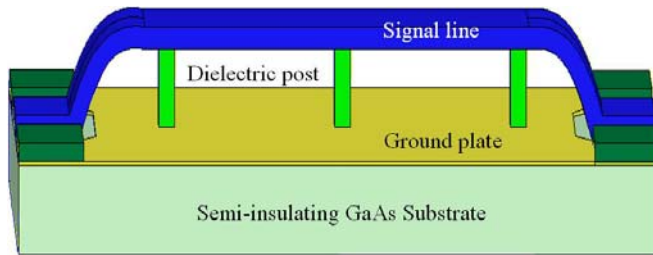


Fig. 3. Schematic view of the DAML structure

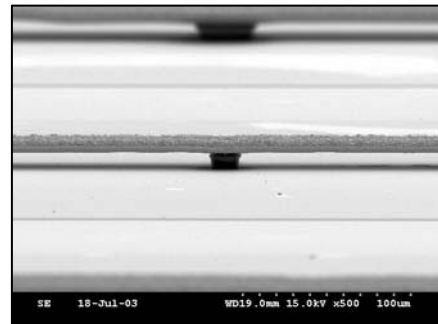


Fig. 4. SEM photograph of the fabricated DAML

sacrificial layer, which can occur during signal line patterning. This Au thin film is also used as a seed metal, to form the signal line with metal thickness of $5 \mu\text{m}$ by an electroplating. Finally, we carry out the PR-strip process and remove the sacrificial layer. Fig. 5 shows the simulation and measurement results of the characteristic impedance with a $10 \mu\text{m}$ height and a $5 \mu\text{m}$ metal thickness with reference to the signal line width. The characteristic impedance varied from 29Ω to 112Ω as the line width varied from $110 \mu\text{m}$ down to $10 \mu\text{m}$. This corresponds to an effective dielectric constant value of 1.04 and 1.026, respectively. For the signal line width of $30 \mu\text{m}$, $50 \mu\text{m}$, and $70 \mu\text{m}$, we obtained an insertion loss of 3.55 dB/cm, 2.75 dB/cm, and 1.88 dB/cm at 94 GHz, respectively, as shown in Fig. 6.

3.2. Hybrid Ring Coupler

The hybrid ring coupler was designed based on the characteristic impedance of signal line width and wavelength at 94 GHz. We obtained a characteristic impedance of 70Ω and 50Ω , when the width of transmission lines used for the design of the hybrid ring coupler are $29 \mu\text{m}$ and $49 \mu\text{m}$, respectively. A wavelength is 2.92 mm. Using these results, we designed the 3 dB hybrid ring coupler with a phase difference between port 2 and port 3 of 180° , which has the space between each port with the $\sqrt{2} Z_0$ transmission line of $\lambda/4$ and $3\lambda/4$. The hybrid ring coupler was fabricated on a $680 \mu\text{m}$ thick GaAs substrate as described from the previous section. These processes are compatible with the standard MMIC techniques, and the hybrid ring coupler can be easily integrated into active GaAs MMICs. The radius of the designed coupler is $730 \mu\text{m}$ and the height of the elevated structure is $10 \mu\text{m}$ from the ground plate. The SEM photograph of the fabricated ring coupler is shown in Fig. 7. To measure the full four-port characteristics of the fabricated ring coupler using two-port vector network analyzer measurement system, three identical couplers were designed and fabricated for different two-port measurement. The simulation and measurement results for the hybrid ring coupler are shown in Fig. 8.

Fig. 8 shows the insertion and reflection losses of the 3 dB hybrid ring coupler. The fabricated hybrid ring coupler shows wideband characteristics of the coupling loss of 3.57 ± 0.22 dB and the transmission loss of 3.80 ± 0.08 dB across the measured frequency range of 85 GHz to 105 GHz. The isolation characteristic is observed to be -34 dB at 94 GHz. From the figure, the center frequency of the coupler is shifted to a lower band of approximately a 1 GHz due to the process margin. We also found a phase difference between port 2 and port 3 of $180 \pm 1^\circ$ at 94 GHz.

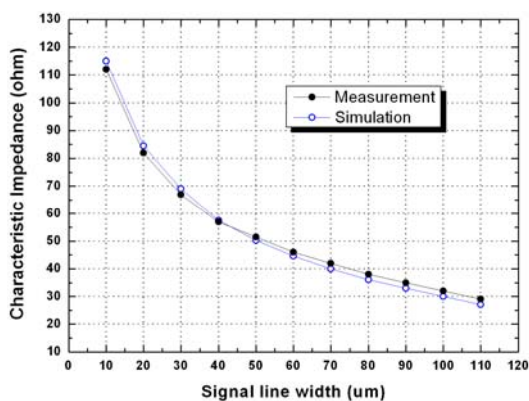


Fig. 5. Measured and simulated characteristic impedance versus signal line width of the DAML.

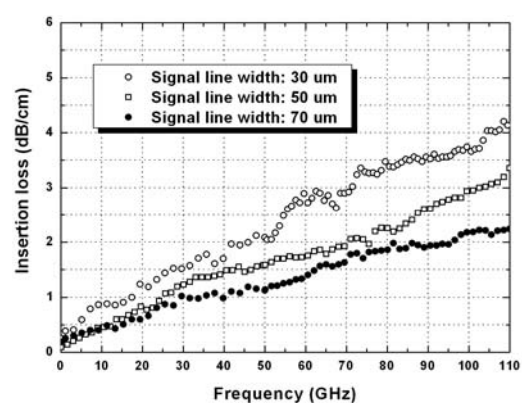


Fig. 6. Measured insertion loss versus frequency of the fabricated DAML.

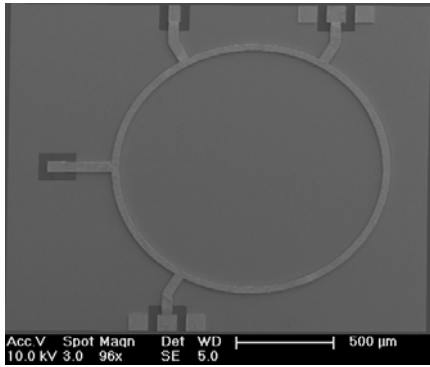


Fig. 7. SEM photograph of the fabricated hybrid ring coupler

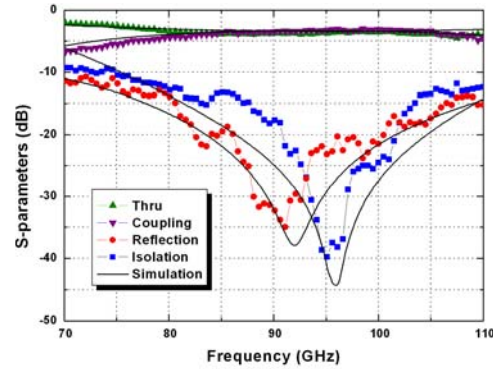


Fig. 8. Measured results compared with the simulated results of the fabricated hybrid ring coupler

4. SINGLE BALANCED ACTIVE MIXER

To demonstrate the possibility of a 3-D integration of active and passive elements using DAML technology, we designed and fabricated a 94 GHz monolithic single balanced active mixer using the developed hybrid ring coupler. The single balanced active mixer can suppress the leakage of LO signals. However, it is usually quite difficult to realize this mixer in single MMIC because the passive element such as a coupler, a transformer, or a balun either are too bulky or complicate the overall fabrication steps excessively. Using the hybrid ring coupler based on the DAML technology as described above may provide an elegant solution to this problem.

Design of the low conversion loss and high isolation single balanced active mixer is based on a systematic characterization of MHEMT devices and hybrid ring coupler with DAML. To design the mixer, we used Agilent ADS circuit design tool embedded the measured dataset of the fabricated hybrid ring coupler. The single balanced active mixer was designed using 70 nm MHEMT, metal-insulator-metal (MIM) capacitors, Ti-thin-film resistor, CPW, and DAML library. The RF, LO, and IF frequencies were designed to be 94 GHz, 94.2 GHz, and 200 MHz, respectively. The bias conditions were drain voltage of 1.5 V and gate voltage of -0.7 V and the drain current of the MHEMT in the mixer was 5 mA. Matching circuits, bias lines, and the IF ports were designed using CPW lines. On the other hand, the RF and LO ports were designed using the hybrid ring coupler with DAML structure in order to obtain higher RF-LO isolation characteristics. The MHEMT, bias lines, and matching circuits on the substrate were fabricated using the standard MMIC process of MINT [10]. The hybrid ring coupler was subsequently fabricated above the planar structures using the DAML technology. Since the DAML process is carried out at a low temperature below 120 °C and does not include any harsh step such as a dry etching process, the performance of the active devices is not degraded in any way. Fig. 9 shows the SEM photograph of the fabricated single balanced active mixer and the total chip size is 1.8 mm × 2.1 mm.

The fabricated mixer was measured using a cascade on-wafer probing system. For measurements, a RF and LO input signal at 94 GHz was generated by connecting Quinstar 94 GHz VCO and Millitech W-band variable attenuator for varying the power of input signals. The two separated, out-of-phase IF output signals from the mixer were combined using an external balun. The measured results of conversion losses versus RF and LO input power are shown in Fig. 10. A good conversion loss of 2.5 dB was obtained with an applied RF frequency of 94 GHz at a LO input power of 6 dBm and LO frequency of 94.2 GHz. Conversion loss and isolation characteristics versus frequencies were obtained at a RF power of

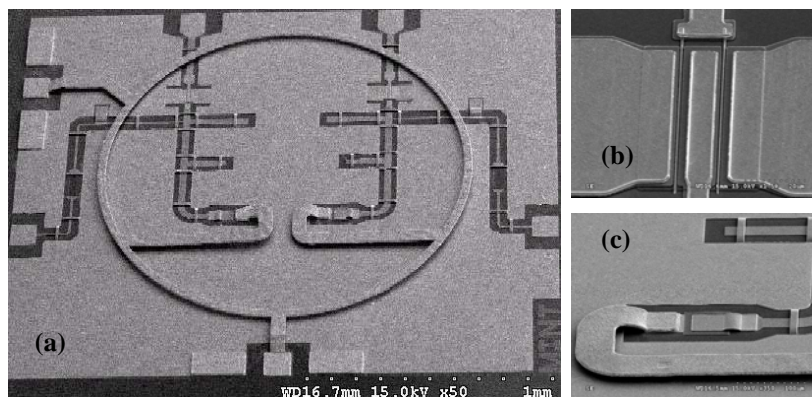


Fig. 9. SEM photographs of the fabricated single balanced active mixer; (a) Overview, (b) 70 nm MHEMT, (c) DAML-to-CPW transition part.

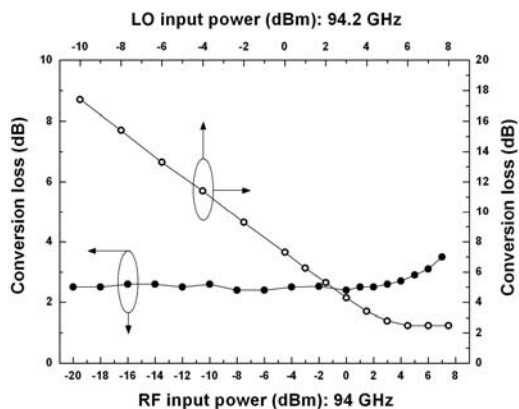


Fig. 10. Conversion loss characteristics versus RF and LO input power (at a LO frequency of 94.2 GHz, a RF frequency of 94 GHz)

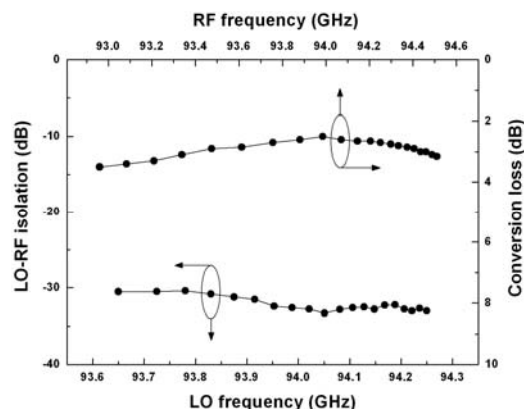


Fig. 11. Conversion loss and isolation characteristics versus frequencies (at a RF power of -10 dBm, a LO power of 0 dBm)

-10 dBm and LO power of 0 dBm. Conversion loss and isolation characteristics were 2.5 dB ~ 2.8 dB and under -30 dB, respectively, in the range of 93.65 GHz ~ 94.25 GHz as shown Fig. 11. The low conversion loss of the mixer is mainly attributed to the high-performance of the MHEMTs and high isolation characteristics are due to hybrid ring coupler.

5. SUMMARY

We successfully demonstrated the potential of integration between high performance passive components adopting DAMLs structure and MMICs by developing the novel single balanced active mixer. This mixer showed that the conversion loss and isolation characteristics were 2.5 dB ~ 2.8 dB and under -30 dB, respectively, in the range of 93.65 GHz ~ 94.25 GHz. At center frequency of 94 GHz, this mixer showed the minimum conversion loss of 2.5 dB at a LO power of 6 dBm. The low conversion loss of the mixer is mainly attributed to the high-performance of the MHEMTs and high isolation characteristics are due to hybrid ring coupler. To our knowledge, these results are the best performances demonstrated from 94 GHz single balanced mixer utilizing GaAs-based HEMTs in terms of conversion loss as well as isolation characteristics. We convince that this technology can lead to the fabrication of a fully integrated micro-system such as a single-chip transceiver for advanced millimeter-wave applications.

References

- [1] K. Nishikawa, S. Sugitani, K. Inoue, T. Ishii, K. Kamogawa, B. Piernas, and K. Araki, "Low-loss passive components on BCB-based 3D MMIC technology," in *IEEE MTT-S Int. Microwave Symp. Dig.*, vol. 3, 2001, pp. 1881-1884.
- [2] G. E. Ponchak, and A. N. Downey, "Characterization of thin film microstrip lines on polyimide," *IEEE Trans. Components, Packaging, and Manufacturing Technology-Part B*, vol. 21, no. 2, pp. 171-176, 1998.
- [3] Suidong Yang, Zhirun Hu, N. B. Buchanan, V. F. Fusco, J. A. C. Stewart, Yunhong Wu, B. M. Armstrong, G. A. Armstrong, and H. S. Gamble, "Characteristics of trenced coplanar waveguide for high-resistivity Si MMIC applications," *IEEE Trans. Microwave Theory Tech.*, vol. 46, no. 5, pp. 623-631, 1998.
- [4] Y. C. Shih, and T. Itoh, "Broadband characterization of conductor-backed coplanar waveguide using accurate on-wafer measurement techniques," *Microwave Journal*, pp. 95-105, April 1991.
- [5] Youngwoo Kwon, Hong-Teuk Kim, Jae-Hyoung Park, and Yong-Kweon Kim, "Low-loss micromachined inverted overlay CPW lines with wide impedance ranges and inherent airbridge connection capability," *IEEE Microwave and Wireless Compon. Lett.*, vol. 11, no. 2, pp. 59-61, 2001.
- [6] S. V. Robertson, A. R. Brown, L. P. B. Katehi, and G. M. Rebeiz, "A 10-60-GHz micromachined directional coupler," *IEEE Trans. Microwave Theory Tech.*, vol. 46, no. 11, pp. 1845-1849, 1998.
- [7] Stephen A. Maas, *Microwave Mixers*. Boston·London: Artech House, 1993.
- [8] S. M. Sze, *Physics of Semiconductor Devices*. NewYork·Chichester·Brisbane·Toronto·Singapore: JOHN WILEY & SON, 1981.
- [9] S. C. Kim, B. O. Lim, H. S. Lee, T. J. Beak, D.-H. Shin, and J. K. Rhee, "50 nm InGaAs/InAlAs/GaAs metamorphic high electron mobility transistors using double exposure at 50 kV electron-beam lithography without dielectric support," *J. Vac. Sci. Technol. B*, vol. 22, no. 4, pp. 1807-1810, Jul/Aug 2004.
- [10] Sung Chan Kim, Dan An, Woo Suk Sul, Han Shin Lee, Hyo Jong Han, Won Young Uhm, Hyung Moo Park, Sam Dong Kim, Dong-Hoon Shin and Jin Koo Rhee, "High conversion gain cascode quadruple subharmonic mixer for millimeter-wave applications," *Current Applied Physics*, vol. 5, no. 3, pp. 231-236, March 2005.

Application of Wavelets in Circuit Modeling and Simulation

¹Xuan Zeng*, ¹Fan Yang, ^{1,2}Dian Zhou and ^{1,3}Wei Cai

¹ASIC & System State Key Lab., Microelectronics Dept., Fudan University, P.R.China

²E. E. Dept., University of Texas at Dallas, U.S.A

³ Math. Dept., University of North Carolina at Charlotte, U.S.A.

Abstract—As SOC chips develop to higher and higher frequency, the singularity problem in high speed circuits has remarkably challenged the accuracy and computation time of the state-of-the-art circuit simulators. Taking advantage of the local support and multi-resolution properties of wavelets, the singularity problem in high speed circuits can be efficiently handled by wavelet collocation method with adaptive scheme. The last decade has seen the development of wavelet theory for solving ODE/PDE and its applications in simulation of high speed and large scale linear and nonlinear circuits. This survey will review a series of wavelet theories and fast computation techniques in the transient, steady state and noise analysis of nonlinear circuits, and model order reduction and fast simulation of linear interconnect circuits, as well as analog behavioral modeling. Compared with the traditional approaches using global support functions, the wavelet methods can significantly improve the simulation speed and accuracy, and consequently establish a new direction for high speed circuit simulation.

1. Introduction

The singularities existing in high speed circuits pose great challenges to today's circuit simulation and modeling techniques in both computational cost and accuracy. For instance, in model order reduction of interconnects, steady state analysis of nonlinear circuits, noise analysis and analog behavioral modeling, the global functions, such as Chebyshev function, harmonic function, sampling function and polynomial function, are employed by the traditional simulation approaches. These global functions require much more number of basis functions to achieve higher accuracy when dealing with singular waveforms. The augment of the number of global functions will drastically increase the computation cost while not evenly reduce the approximation errors. It is therefore desperately demanded to exploit new methodologies for simulation of high speed circuits.

The concept of wavelet approximation was firstly proposed in geophysics domain to analyze the earthquake wave propagation problems [1]. In electrical engineering, wavelet methods have been developed for function approximation involved in imaging compression and signal decomposition [1, 2]. In electromagnetics computations, wavelets have also been employed to compress the integral operator as reported in [3, 4].

Table 1: Wavelet Theory and its Applications in Circuit Modeling and Simulation

Wavelet Theory and Applications		Traditional Methods	Wavelet Based Method
Fundamental Theory	PDE Solving	-	SIAM NA, 1996 [5]
Basic Principles for Circuit Analysis	Transient Analysis	Time matching	TCAS-I, 1999 [6, 7]
	Linear Circuit Analysis	Time-domain MOR	Chebyshev basis [8]
Nonlinear Circuit Analysis	Frequency Domain	-	DATE'2006 [9]
	Clock Network	-	ISCAS'2003 [10], ASICON'2001 [11]
	Steady-state	-	ISCAS'2002 [12]
Circuit Modeling	Noise	Harmonic balance [13]	TCAS-I, 2002 [14]
	Behavioral Modeling	Sampling function [15]	ASP-DAC'2005 [16]
		Polynomial basis [17]	TCAS-II, 2003 [18]

In circuit modeling and simulation, when traditional methods based on global support functions suffered from accuracy and computation cost difficulties in high speed circuit simulation, wavelet theory [5] has been developed with solid mathematic fundamental and extensively applied to analyze not only high speed but also very large scale VLSI circuits. In Table 1, we outline the road map of the main research activities in this

This research is supported partly by NSFC research project 90307017, partly by the National Basic Research Program of China under the grant 2005CB321701, partly by Cross-Century Outstanding Schoolars fund of Ministry of Education of China, partly by the doctoral program foundation of Ministry of Education of China 20050246082, Shanghai Science and Technology committee Key project 04JC14015 and Shanghai AM R&D fund 0418, partly by NSF grants CCR-0306298, partly by the US National Science Foundation (grant numbers: DMS-0408309, CCF-0513179), Department of Energy (DEFG0205ER25678) and NERSC Computing Award.

area since last decade. In 1996, W. Cai et al. firstly established the fundamental wavelet theory for solving nonlinear PDEs with boundary conditions [5] in mathematics. The construction of wavelet basis functions for handling non-homogenous boundary conditions, the collocation method for solving PDEs and adaptive scheme etc. were completely developed in this work. In 1999, D. Zhou and W. Cai further established the basic wavelet circuit simulation theory by studying transient analysis of nonlinear ODE in time domain, while traditionally the classical time marching method has encountered with error accumulation difficulty in simulation of strong singularities in high speed circuits [6, 7]. A series of research of applying wavelets in large scale linear and nonlinear simulation have been extensively explored by X. Zeng, D. Zhou and W. Cai since 2001. For large scale linear circuit analysis, the wavelet approaches have been developed to clock network [12] and frequency domain analysis [10, 11] as well as model order reduction [9] etc.. Specifically, in model order reduction of high speed interconnect circuits, the wavelet functions [9] turn to be more efficient than the global support Chebyshev [8] polynomials to tackle with circuit singularities. Most importantly, for all of the spectrum approaches, like Chebyshev or wavelet method, a large scale coefficients matrix needs to be solved, which is very time consuming by vector equation solver [8] and becomes the bottleneck to prevent the spectrum methods from solving very large scale interconnect circuits with order up to 10^6 . We have proposed a fast Sylvester equation solver [9] which is two to three orders faster than the vector equation solver [8]. This fast numerical computation technique is so significant that it makes the wavelet method from circuit theory to solving really large scale interconnect circuits. For nonlinear circuit analysis, we have extended wavelet method to steady-state analysis and noise analysis in [14] and [16], respectively. The wavelet methods remarkably improve the simulation accuracy and efficiency compared to the global function based methods, such as harmonic balance method [13] and sampling function based method [15]. For behavioral modeling of analog circuits, we have proposed a wavelet collocation method with nonlinear companding technique to reduce model errors and control the error distribution continuously according to the system simulation requirements.

The rest of the paper is organized as follows. In Section 2, we give an introduction to basic principles of wavelet collocation method. We present wavelet applications in linear circuit analysis, nonlinear circuit analysis and behavioral modeling of analog circuits in Sections 3, 4 and 5, respectively. The fast Sylvester equation solver as a significant numerical method is presented in Section 6. We draw conclusions in Section 7.

2. Basic Principles of Wavelet Collocation Method

In this section, the basic principles of wavelet collocation method proposed in [5–7] are reviewed.

2.1 Wavelet Basis Functions

Let $H^2[0, L]$ be a Sobolev space, which basically contains all functions with square integrable second order derivatives. We first introduce spline wavelets function subspaces of $H^2[0, L]$ for a given $J \geq 0$, which are developed in [5], as follows.

$$\begin{aligned} V_b &= \text{span} \{ \eta_1(t), \eta_2(t), \eta_2(L-t), \eta_1(L-t) \} & V_0 &= \text{span} \{ \varphi_{0,-1}(t), \varphi_{0,0}(t), \dots, \varphi_{0,L-4}(t), \varphi_{0,L-3}(t) \} \\ W_j &= \text{span} \{ \psi_{j,k}(t), -1 \leq k \leq 2^j L - 2 \}, 0 \leq j \leq J-1 & V_j &= V_{j-1} \oplus W_{j-1}, 1 \leq j \leq J-1 & V_{bj} &= V_b \cup V_j \end{aligned} \quad (1)$$

where $\eta_1(t)$, $\eta_2(t)$, $\eta_2(L-t)$ and $\eta_1(L-t)$ are specially designed to handle the non-homogeneity of the boundary, functions $\varphi_{0,k}(t)$ and $\psi_{j,k}(t)$ denote scaling functions and wavelet functions, respectively. \oplus denotes direct sum.

Wavelet basis functions have the distinct property of local support, namely, having nonzero values only in a small time interval. The indexes j and k of wavelet functions $\psi_{j,k}(t)$ represent the operations of dilation and translation, respectively. The dilation generates high frequency wavelets and the translation moves wavelets to cover the whole physical time space. When using wavelets as the basis functions to approximate an arbitrary function, we can insert the wavelets at the needed physical time location by the translation operation and go to any high resolution by the dilation. Hence, we can achieve any high resolution at any physical location as we wish. In contrast, such a nice property is not shared by the global support function like Fourier series.

2.2 Wavelet Collocation Method

Collocation method is developed to solve the wavelet function coefficients when applying wavelet method to solve ODEs/PDEs [6]. In this subsection, we illustrate the wavelet collocation method by solving an ODE problem defined in time interval $[0, L]$, as described in (2).

$$\dot{X}(t) = f(X, t) \quad (2)$$

where $X(t) = [X_1(t), \dots, X_n(t)]^T$ are the n unknown state variables, and $f(X, t)$ is a given nonlinear vector function. Firstly, the state variables $X(t)$ are expanded by wavelets.

$$X(t) = \begin{bmatrix} X_1(t) \\ \vdots \\ X_n(t) \end{bmatrix} = \begin{bmatrix} H_{11} & \cdots & H_{1K} \\ \vdots & \ddots & \vdots \\ H_{n1} & \cdots & H_{nK} \end{bmatrix} \cdot \begin{bmatrix} \theta_1(t) \\ \vdots \\ \theta_K(t) \end{bmatrix} = H \cdot \theta(t) \quad (3)$$

where $H \in R^{n \times K}$ is the coefficient matrix, $\{\theta_i(t), i = 1, 2, \dots, K\}$ are wavelet basis functions defined in (1),

and K is the total number of basis functions that have been employed. By substituting (3) into (2) and let the expansion satisfy the original ODEs at the collocation points $\{t_1, t_2, \dots, t_K\}$, we get (4).

$$H \cdot [\dot{\theta}(t_1), \dot{\theta}(t_2), \dots, \dot{\theta}(t_K)] = [f(H\theta(t_1), t_1), f(H\theta(t_2), t_2), \dots, f(H\theta(t_K), t_K)] \quad (4)$$

The wavelet coefficients can be calculated by solving these nonlinear algebraic equations (4) by some iterative schemes [6].

2.3 Adaptive Scheme

One of the main advantages of the wavelet approximation is that there exists an adaptive scheme, which relies on the multi-resolution analysis in wavelet theory [5]. Using the adaptive technique, those wavelet basis functions, which are needed for approximating the given nonlinear function, can be employed automatically. It, in turn, improves the approximation efficiency significantly. The magnitude of the wavelet coefficients corresponding to basis functions in W_j will indicate whether a refinement, by increasing the wavelet space level, is needed or not [5]. More importantly, because of the local support of wavelet bases, not all wavelet basis functions in higher wavelet spaces $W_{j'}$ ($j' > j$) are needed in order to achieve more accuracy. In fact, only basis functions, whose positions near the singularities should be included.

3. Application of Wavelet Method in Linear Circuit Analysis

We have successfully applied wavelet method to linear circuit analysis problems, including time-domain model order reduction [9], frequency domain analysis [10, 11] and clock network analysis [12] etc.. In this section, we mainly present time-domain model order reduction of interconnect circuits by wavelet method [9].

With the continuous advance of semiconductor technology, interconnects have become the dominant factor to determine the performance of integrated circuits. The state-of-the-art technique for interconnect analysis is model order reduction. Generally, a linear circuit can be described by

$$\begin{aligned} \dot{x}(t) &= Ax(t) + Bu(t) \\ y(t) &= C^T x(t) \end{aligned} \quad (5)$$

where $x(t) = [x_1(t), x_2(t), \dots, x_N(t)]^T$ is the unknown N dimensional state vector and $u(t)$ is the input function. $y(t)$ is the outputs. $A \in R^{N \times N}$, $B \in R^{N \times p}$, $C \in R^{N \times q}$ are the system matrices. Here, p and q denote the number of inputs and outputs, respectively. Time domain model order reduction techniques approximate the time domain behavior of the linear circuit by sufficiently accurate lower order model. The existing global function based time-domain model order reduction techniques like Chebyshev polynomial method [8] have the following limitations. Firstly, these methods cannot handle large scale problems due to their high computational cost. Secondly, these methods cannot tackle fast changing waveforms because of the global support properties of the global functions. We propose to apply wavelet method to time domain model order reduction in [9]. For simplicity, the simulation interval in time domain is supposed to be $[0, L]$. Similarly, $x(t)$ is expanded by wavelets defined in (1), i.e. $x(t) = H\theta(t)$, where $H \in R^{N \times K}$ is the coefficient matrix, $\theta(t) = [\theta_1(t), \theta_2(t), \dots, \theta_K(t)]^T$ are wavelet basis functions, K is the number of wavelet basis functions. By substituting the expansion $x(t) = H\theta(t)$ into (5) and discretizing it at collocation points $\{t_1, t_2, \dots, t_K\}$, we get (6).

$$H[\dot{\theta}_1(t_1), \dot{\theta}_2(t_2), \dots, \dot{\theta}_K(t_K)] = AH[\theta_1(t_1), \theta_2(t_2), \dots, \theta_K(t_K)] + B[u(t_1), u(t_2), \dots, u(t_K)] \quad (6)$$

which can be formulated as a Sylvester equation. We have proposed a fast Sylvester equation solver in [9], as described in Section 6, to solve the coefficient matrix H . After coefficient matrix H is calculated and orthonormalized as V , the reduced order model is obtained by performing projection on V [9].

Compared with the global function based methods [8], wavelet based time domain model order reduction method can efficiently tackle high speed interconnect circuits with strong singularities, and is capable of reducing the original system into much smaller size.

4. Application of Wavelet Method in Nonlinear Circuit Analysis

In this section, wavelet methods for nonlinear circuit analysis, including steady-state analysis and noise analysis are reviewed.

4.1 Steady-State Analysis [14]

Taking a non-autonomous circuit as an example, the steady-state analysis of (2) is to find a $\bar{X}(t)$, which not only satisfies (2), but also satisfies the following two-point boundary constraint, $\bar{X}(0) = \bar{X}(T)$, where the steady-state response period T is determined by input excitations. We propose to solve the steady-state analysis problem by wavelet balance method [14]. Wavelet balance method follows the basic principles of the wavelet collocation method in (4) but with the difference that the two-point boundary constraint imposes one more vector equation for the coefficient matrix in wavelet balance method. Hence, optimization algorithms like Levenberg-Marquardt Method [14] are employed to obtain the least-square-error solution of coefficient matrix.

Compared with the conventional harmonic balance method [13], the proposed wavelet-balance method has

the following advantages. Firstly, the wavelet-balance method has a high-convergence rate, resulting in low computational complexity. Secondly, the wavelet-balance method works in the time domain, so that many critical problems in frequency domain, such as nonlinearity and high-order harmonics, can be handled efficiently. Thirdly, localized singularities exhibited in the response of nonlinear circuits can be easily captured by the wavelet approach through adaptivity.

4.2 Noise Analysis [16]

The noise analysis of a nonlinear circuit described by (2) is to calculate the continuous spectrum of the unknown state variables $X(t)$. The traditional frequency-domain simulation method like harmonic balance can only calculate the discrete frequency spectrum of $X(t)$. To obtain the continuous spectrum, the spectra of $X(t)$ is expanded by Fourier series over a finite frequency interval in [15]. The coefficients of the Fourier series are then calculated by sampling the time domain response of (2) i.e. $X(t)$, according to sampling theorem [15]. The noise analysis problem is then transformed to a transient analysis problem. In [15], the time domain response is obtained by expanding $X(t)$ with finite *sinc* series, which are the time domain series corresponding to the Fourier series in frequency domain, and then forcing the finite *sinc* series satisfy the ODEs at uniform sampling points. However, since *sinc* series are global support, the finite truncation of the expansion series will introduce inevitable simulation errors in calculating the time domain response, and correspondingly affect the accuracy of the coefficients of Fourier expansion in frequency domain.

In contrast, wavelet collocation method was proposed to obtain the time-domain solution of (2) in [16]. The coefficients of the Fourier series in frequency domain are calculated by sampling theorem in terms of the transient solution obtained by wavelet collocation method. Compared with *sinc* function based method [15], by taking advantage of the local compactness and multi-resolution properties of the wavelet bases, wavelet based method achieves high simulation speed and high accuracy in time domain transient analysis. Furthermore, an adaptive scheme exists to automatically select the wavelet basis functions for a desired accuracy. The high accuracy of the transient analysis, accordingly, enhance the accuracy of the coefficients of Fourier series in frequency domain.

5. Behavioral Modeling of Analog Circuits by Wavelet Method [18]

The most challenging task involved in behavioral modeling for bottom-up verification is how to accurately characterize the nonideal input-output relation with simple model representation. Furthermore, controlling error distribution of the behavioral model is an effective way to improve the overall simulation efficiency and to save memory space.

We propose to apply wavelet collocation method with nonlinear companding to accurately characterize the nonlinear input-output function of analog circuit. We take one-dimensional function approximation as example here. Denote the nonlinear function for approximation $y = g(x)$. For behavioral modeling, we expand function $g(x)$ by wavelet basis functions and employ collocation method to calculate the expansion coefficients. The companding algorithm is used to continuously control the modeling error distribution. The companding algorithm uses a companding function to map wavelet basis functions to basis functions with desired singularities. According to the wavelet approximation theory, the approximation error depends on the singularity of wavelet basis functions. Hence, the modeling error distribution can be continuously controlled by changing the singularity of wavelet bases with companding algorithm. The nonlinear companding function can be constructed by heuristic analysis [18] or automatic technique [19]. Experiments show that with adaptive and companding techniques, the number of wavelet basis functions required to approximate the input-output function and the approximation errors are remarkably reduced at the same time.

The above companding-oriented wavelet collocation method is able to reduce the modeling errors and control the modeling error distribution continuously based on system-level simulation requirements. Moreover, this companding scheme can efficiently reduce the number of basis functions, i.e. the number of coefficients needed to represent the model. It, in turn, improves the simulation efficiency significantly at the system level.

6. Fast Sylvester Equation Solver [9]

Solving large scale coefficient equation is a key problem to time domain model order reduction of large scale interconnect circuits. The coefficient equations no matter employed in wavelet based or Chebyshev polynomial based time domain model order reduction methods can be formulated in a matrix equation called Sylvester equation [9]. For instance, the matrix equation (6) can be rewritten as a Sylvester equation as $HZ - AH = G$, where $Z \in R^{K \times K}$, $A \in R^{N \times N}$, $H \in R^{N \times K}$ and $G \in R^{N \times K}$, if we denote $\Phi = [\theta_1(t_1), \theta_2(t_2), \dots, \theta_K(t_K)]$, $U = [u(t_1), u(t_2), \dots, u(t_K)]$, $Z = \frac{d\Phi}{dt}\Phi^{-1}$ and $G = BU\Phi^{-1}$.

The Sylvester equation can be solved in an equivalent vector equation formulation, or more directly and efficiently, in a matrix equation formulation [9]. The computational complexity of solving the equivalent vector equation is $O((N \times K)^3)$, which would be prohibitive as the original circuit order N and number of wavelet bases K increase. The traditional matrix equation solver like Complete Schur method requires Schur decompositions

of both A and Z . Since N could be 10^6 in real applications, the Schur decomposition of A with the complexity of $O(N^3)$ hampers Complete Schur method for large scale problems.

Based on the observations that $A \in R^{N \times N}$ is a large scale but sparse matrix while $Z \in R^{K \times K}$ is a much small scale matrix, we propose a fast Sylvester equation solver, i.e. Partial Schur decomposition method. In this solver, Schur decomposition is done only on the small matrix $Z \in R^{K \times K}$, and the equation involving A is solved efficiently with iterative schemes like GMRES etc., by taking advantage of the sparsity of A . Hence, the computational cost of the Partial Schur decomposition solver is much less than the Complete Schur decomposition one. Numerical experiments show that the Partial Schur decomposition Sylvester solver gains up to three orders and one order speedups compared with the vector equation solver and Complete Schur decomposition solver, respectively. This fast numerical computation technique is very crucial to make the wavelet method from circuit theory to solving really large scale interconnect circuits.

7. Conclusion

During the last decade, we have established the fundamental theory of wavelet collocation method and successfully applied wavelet collocation method to high speed and large scale circuit simulation and modeling. Taking advantage of the localization property, wavelets can accurately and efficiently catch singularities existing in high speed circuits. The series of work surveyed in this paper have opened a new direction for high speed circuit simulation.

REFERENCES

1. C.K.Chui. *An introduction to wavelets*. New York: Academic Press, 1992.
2. S. Mallat. A theory for multiresolution signal decomposition: The wavelet representation. *IEEE Trans. Pattern Recog. Machine Intell.*, 11(7):674–693, July 1989.
3. B. Alpert. A class of bases in L_2 for the sparse representation of integral operators. *SIAM J.Math. Anal.*, 24(1):246–262, Jan. 1993.
4. G. Oberschmidt and A. Jacob. Non-uniform wavelets on adapted grids for modeling edge singularities. In *Eur. Microwave Conf.*, pages 1258–1263, 1997.
5. W. Cai and J. Z. Wang. Adaptive multi-resolution collocation methods for initial boundary value problems of nonlinear PDEs. *SIAM J. Numer. Anal.*, 33(3):937–970, March 1996.
6. D. Zhou and W. Cai. A fast wavelet collocation method for high-speed circuit simulation. *IEEE Trans. Circuits Syst. I*, 46(8):920–930, Aug. 1999.
7. D. Zhou and W. Cai. An adaptive wavelet method for nonlinear circuit simulation. *IEEE Trans. Circuits Syst. I*, 46(8):931–938, Aug. 1999.
8. J. M. Wang, C.C. Chu, Q. Yu, and E. S. Kuh. On projection-based algorithms for model-order reduction of interconnects. *IEEE Trans. Circuits Syst. I*, 49(11), Nov. 2002.
9. X. Zeng, L. Feng, Y. Su, W. Cai, D. Zhou, and C. Chiang. Time domain model order reduction by wavelet collocation method. In *IEEE/ACM DATE*, pages 21–26, 2006.
10. J. Wang, X. Zeng, W. Cai, C. Chiang, J. Tong, and D. Zhou. Frequency domain wavelet method with GMRES for large scale linear circuit simulation. In *IEEE ISCAS*, pages 321–324, 2004.
11. X. Zeng, S. Huang, J. Wang, and D. Zhou. Frequency domain wavelet method for high-speed circuit simulation. In *IEEE ISCAS*, pages 233–236, 2002.
12. X. Li, X. Zeng, D. Zhou, and X. Ling. Wavelet method for high speed clock tree simulation. In *IEEE ISCAS*, pages 177–180, 2002.
13. K. S. Kundert and A. Sangiovanni-Vincentelli. Simulation of nonlinear circuits in the frequency domain. *IEEE Trans. CAD*, 5(10):521–535, Oct. 1986.
14. X. Li, B. Hu, X. Ling, and X. Zeng. A wavelet-balance approach for steady-state analysis of nonlinear circuits. *IEEE Trans. Circuits Syst. I*, 49(5):689–694, May 2002.
15. G. Casinovi. An algorithm for frequency-domain noise analysis in nonlinear systems. In *IEEE/ACM DAC*, pages 514–517, 2002.
16. X. Zeng, B. Liu, J. Tao, C. Chiang, and D. Zhou. A novel wavelet method for noise analysis of nonlinear circuits. In *IEEE/ACM ASP-DAC*, pages 471–476, 2005.
17. J. Shao and R. Harjani. Macromodeling of analog circuits for hierarchical circuit design. In *IEEE/ACM ICCAD*, pages 656–663, 1994.
18. X. Li, X. Zeng, D. Zhou, X. Ling, and W. Cai. Behavioral modeling for analog system-level simulation by wavelet collocation method. *IEEE Trans. Circuits Syst. II*, 50(6):299–314, June 2003.
19. J. Wang, J. Tao, X. Zeng, C. Chiang, and D. Zhou. Analog circuit behavioral modeling via wavelet collocation method with auto-companding. In *IEEE/ACM ASP-DAC*, pages 45–50, 2004.

A Time-domain Approach for Transforming Broadband SPICE-Compatible Models of Power Delivery Networks with Resonance Effect

Chen-Chao Wang, Chih-Wen Kuo, *Member, IEEE*, Chun-Chih Kuo*, Jian-Sheng Hsieh*, and
Tzong-Lin Wu**, *Senior Member, IEEE*

National Sun Yat-sen University, Kaohsiung 80424, Taiwan, cwkuo@mail.nsysu.edu.tw

*ASUS Corporation, Taipei 11259, Taiwan.

**National Taiwan University, Taipei 10617, Taiwan, wtl@cc.ee.ntu.edu.tw

Abstract - Resonance noise, or power/ground bounce noise, on the power and ground planes of high-speed circuit packages is one of main concerns of the signal integrity (SI) or power integrity (PI) issues. This paper proposes a time-domain approach to extract the equivalent models of power/ground planes with the resonant effect being considered. Employing the general pencil of matrix method (GPOM), the pole-residue representation of the time-domain responses of the planes structure is obtained. The broadband SPICE-compatible model then can be transformed based on the simple network transformation method. It is found that the extracted models accurately predict the power/ground bouncing or resonance behavior in wide-band range. The developed models can be efficiently incorporated to the HSPICE simulator with considering the power/ground bouncing noise in high-speed circuits.

Index Terms -finite-difference time-domain (FDTD), power integrity, SPICE model, time-domain reflectometry (TDR).

. INTRODUCTION

In recent high-speed digital circuits with pico-second rising/falling edges, it is reasonable to consider the power/ground planes as a dynamic electromagnetic system [1]. The simultaneous switching noise (SSN) or ground bounce noise, resulting from the transient currents which flow between power/ground planes during the state transitions of the logic gates, has become a critical factor to degrade the signal integrity (SI) and power integrity (PI) in PCB or package design [2]. In order to accurately perform overall system-level power integrity simulation, extracting the SPICE-compatible models with the resonant effect being considered in the power/ground planes and incorporating the model into the conventional circuit simulator, such as SPICE, is essential.

Several works had been contributed to the equivalent circuit extraction of the physics-based distributed lumped-circuit models approach based on physical structures of power/ground planes [3]-[4]. The lumped models are efficient in the simple prediction of the power/ground planes with resonance effect on the PI, but the cell size of the element array must be small to keep the good accuracy of the model. It will cost much computing time and many memory spaces. Several full-wave numerical techniques such as method of moment (MoM) and finite-element method (FEM) have also been developed to understand the propagation and resonance behavior of the power/ground planes [5]-[6]. Recently, based on time-domain responses either from simulations or measurements, the resonance effect of the power/ground planes was characterized using a complicated process [7].

In this paper, a time-domain approach is proposed for transforming the SPICE-compatible circuits of the power/ground planes based on a simple network model. According to either the measured or simulated time-domain reflected waveforms, the generalized pencil of matrix method (GPOM) [8] is employed to construct the time-domain step response of the power/ground planes by the rational functions. The equivalent model in terms of the rational functions pairs is obtained through a simple network transformation. The equivalent circuits of the model are finally transformed by a systematic lumped-model extraction technique (SLET) [9]-[10].

. MODELING METHOD

A. Simulation or Measurement Setup

Time-domain waveforms are employed to obtain the step response of the power/ground planes. The time domain waveforms are made available either through FDTD simulation or a TDR measurement. Fig. 1 shows an example of the power/ground planes for a two-layer board ($\epsilon_r = 4.3$). For the simulation setup, a resistive voltage source injects a step waveform into the power/ground planes, and a 50 Ω resistance is connected between the planes as a load. In addition, for measurement setup, we can use a general TDR, such as Tektronix CSA8000B or Agilent DCA86100C, to launch a step waveform into the power/ground planes. This setup is used for the power/ground planes model extraction both from the FDTD simulation or the TDR measurement.

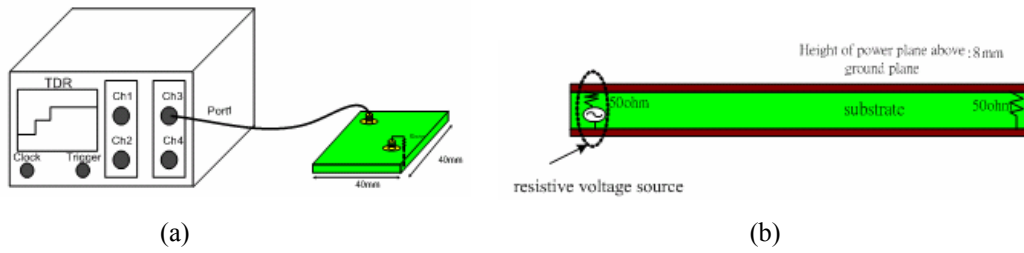


Figure. 1 (a) TDR setup for analyzing the characteristics of power/ground plane by measuring time-domain reflection signal of the DUT. (b) FDTD modeling of the TDR simulation with resistive voltage source.

B. Systematic Lumped-Model Extraction Technique (SLET)

As shown in Fig. 1, a step waveform with rise time τ is injected into port 1, and the reflected voltage waveform is recorded. The step response of the power/ground planes is obtained by normalizing the reflected waveform with respect to the incident wave amplitude, and is denoted as $y(t)$. By employing the general pencil of matrix method, the step response can be expressed as a summation of complex exponential terms (modes) as

$$y(t) = \sum_{i=1}^L r^i \exp(-p^i t), \tag{2.1}$$

where r^i and p^i are the residues and poles on the complex plane, and L is the number of exponential terms. After the best estimates of L , r^i , and p^i with $i=1, \dots, L$, are available through the GPOM method, the corresponding step response of the power/ground planes in frequency domain is obtained through the Laplace transform of (2.1) as

$$Y(s) = \sum_{i=1}^L \frac{r^i}{s + p^i}, \tag{2.2}$$

where $s=j2\pi f$ is the complex frequency. In order to characterize the power/ground planes with circuit model, the step response just obtained is transformed into an impedance representation, as shown in Fig. 2. The reflection coefficient at the incident end of the DUT which represents the power/ground planes can be derived as

$$\Gamma(s) = 2 \left[\frac{Z_{in}(s)}{Z_{in}(s) + Z_1} - \frac{Z_2}{Z_1 + Z_2} \right], \tag{2.3}$$

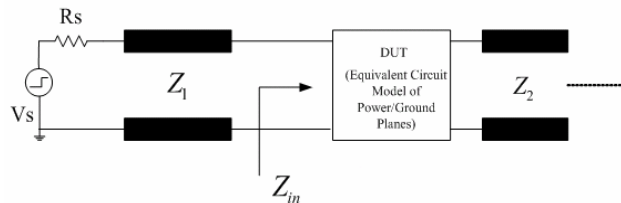


Figure. 2 Relation of the reflection coefficient with the input impedance at the input end of the DUT.

where $Z_{in}(s)$ is the input impedance looking into the DUT. When the input source is an impulse function, then the reflection coefficient thus obtained is also the impulse response. The relation between step response and impulse response is a simple differentiation:

$$Y(s) = \frac{1}{s} \Gamma(s). \tag{2.4}$$

Combining (2.3) and (2.4), the input impedance can be written in a form relating to $Y(s)$ as

$$Z_{in}(s) = Z_1 \frac{\frac{Z_1}{Z_1 + Z_2} + \frac{sY(s)}{2}}{\frac{Z_1}{Z_1 + Z_2} - \frac{sY(s)}{2}} \quad (2.5)$$

After substituting (2.2) into (2.5), the partial fraction expansion of (2.5) can be expressed as

$$Z_{in}(s) = s \sum_{\substack{i=1 \\ b_i > 0}}^{N_0} \frac{b_i}{s + a_i} + s \sum_{\substack{i=1 \\ c_i > 0}}^{N_1} \frac{f_i s + c_i}{s^2 + d_i s + e_i} + Q(s), \quad (2.6)$$

where $a_i, b_i, c_i, d_i, e_i, f_i$ are all real numbers. The corresponding circuit models for the first-order and second-order terms in (2.6) are shown in Fig. 3(a) and 3(b), respectively. Corresponding values of the circuit elements are easily recognizable as $R_L = b_i$ and $L = R_L/a_i$ for first-order terms, and $L = c_i/e_i, R_L = c_i/(d_i f_i/L), R_c = f_i \times R_L/(R_L - f_i)$, and $C = R_L/(c_i \times (R_L + R_c))$, for second-order terms. The remaining term $Q(s)$ is then realized by converting to the admittance as

$$Y(s) = 1/Q(s) = s \sum_{\substack{i=1 \\ q_i > 0}}^{K_0} \frac{q_i}{s + h_i} + s \sum_{\substack{i=1 \\ v_i > 0}}^{K_1} \frac{r_i s + v_i}{s^2 + u_i s + m_i} + R(s), \quad (2.7)$$

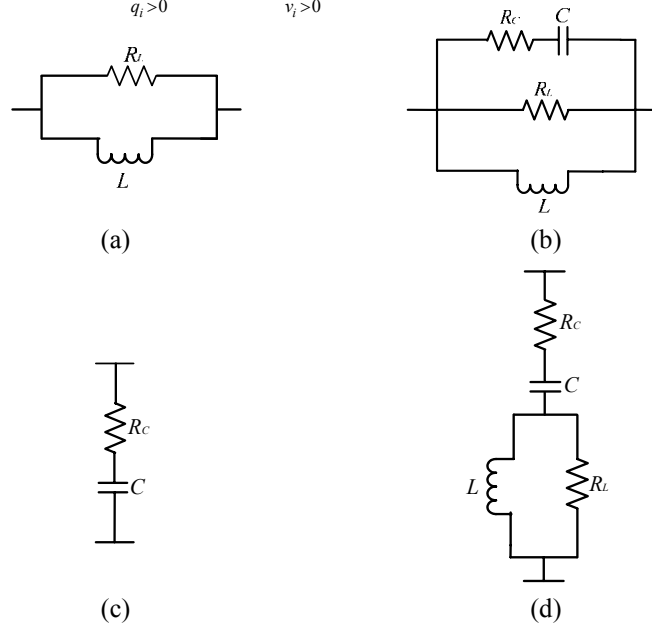


Figure. 3 Four types of equivalent model extracted from the pole-residual representations of the input impedance.

where $q_i, h_i, r_i, v_i, u_i, m_i$ are also real numbers. Similarly, the corresponding circuit models for the first-order and second-order terms in (2.7) are shown in Fig. 3(c) and 3(d), respectively. The corresponding values can be derived as $R_c = 1/q_i$ and $C = 1/h_i R_c$ for the first-order term and $C = v_i/m_i, R_c = (u_i r_i/C)/v_i, R_L = 1/r_i - R_c$, and $L = R_L \times r_i/(C \times m_i)$ for the second-order terms. The remaining term $R(s)$ in (2.7) is the summation of the first-order and second-order terms with negative value q_i and v_i , respectively. By employing the voltage-control-voltage-source (VCVS), they can be synthesized as the model shown in Fig. 4, respectively, for the first-order and second-order terms. The corresponding values can be derived as $R_c = 1/q_i$ and $C = -1/h_i R_c$ for the first-order term and $C = -v_i/m_i, R_c = (u_i + r_i/C)/v_i, R_L = 1/r_i - R_c$, and $L = R_L \times r_i/(C \times m_i)$. $V_C(s)$ and $V_L(s)$ are the voltage crossing on the corresponding capacitor and inductor, respectively.

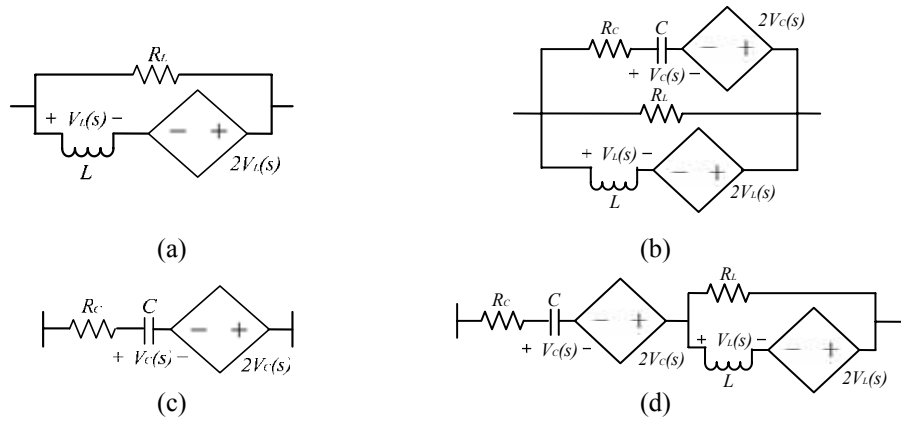


Figure. 4 Four types of voltage-control-voltage-source (VCVS) equivalent model.

RESULT

An FDTD simulation with a 0.4V step source of 10ps rise-time was launched to port 1 to obtain the time domain response. Using the proposed approach, the equivalent model of the power/ground planes can be extracted successful. The accuracy of the equivalent lumped model is verified both in time- and frequency-domain. Fig. 5 shows the reconstructed waveforms using the extracted model in ADS and the original waveform computed by the FDTD method. Difference between the two results is almost indistinguishable. For comparing the results in the frequency-domain, S_{11} calculated by the extracted model and Ansoft HFSS is shown in Fig. 6. Both the magnitude and phase agree reasonably well. Good agreement both in magnitude and phase is also seen in frequency range from DC to 6GHz.

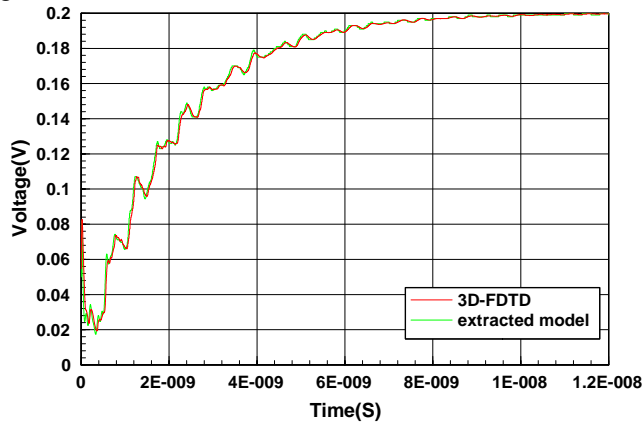


Figure. 5 The reconstructed waveforms using the extracted model in ADS and the original waveform computed by the FDTD method.

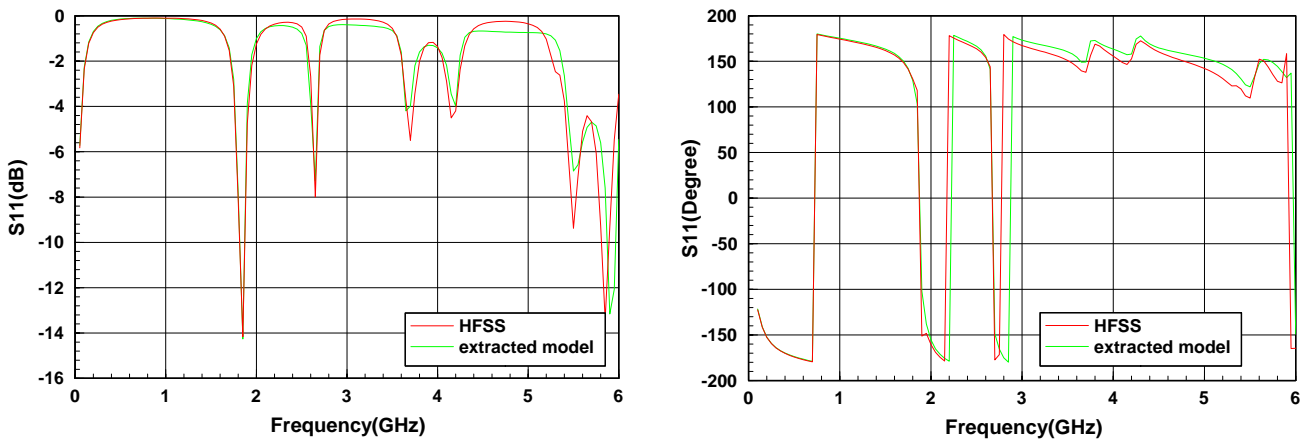


Figure. 6 Comparison of S_{11} with extracted model in HSPICE and HFSS simulations(a) magnitude and (b) phase.

CONCLUSION

Based on the TDR-measured or FDTD-computed time-domain data, an efficient systematic approach has been proposed to extract the SPICE-compatible models of the power delivery networks. According to either the measured or simulated time-domain waveforms, the GPOM is employed to construct the time-domain step response of the power/ground planes by the rational functions. The rational functions are then used to extract the lumped circuits of DUT by SLET. The good accuracy of the proposed approach both in time- and frequency-domain has been presented.

REFERENCES

- [1] S. Van den Berghe, F. Olyslager, D. De Zutter, J. De Moerloose, and W. Temmerman, "Study of the ground bounce caused by power plane resonances," *IEEE Trans. Electromagn. Compat.*, vol. 40, May 1998.
- [2] J. Nuebel, T. Roy, and S. Das, "An investigation on power plane decoupling for high speed multiprocessor boards," in *Proc. IEEE Int. Symp. Electromagn. Compat.*, 1999, pp. 355-360.
- [3] H. H. Wu, J. W. Meyer, and K. Y. Lee, and A. Barber, "Accurate power supply and ground plane pair models [for MCMs]," *IEEE Trans. Advanced Packaging*, vol. 22, pp. 259-266, Aug. 1999.
- [4] E. Diaz-Alvarez, J. P. Krusius, and F. Kroeger, "Modeling and simulation of integrated capacitors for high frequency chip power decoupling," *IEEE Trans. Advanced Packaging*, vol. 23, pp. 611-619, Dec. 2000.
- [5] Ji Yun, and T. H. Hubing, "On the interior resonance problem when applying a hybrid FEM/MoM approach to model printed circuit boards," *IEEE Trans. On Electromagnetic Compatibility*, vol. 44, pp. 318-323, May. 2002.
- [6] Ji Yun, and T. H. Hubing, "On the modeling of a gapped power-bus structure using a hybrid FEM/MoM approach," *IEEE Trans. On Electromagnetic Compatibility*, vol. 44, pp. 566-569, Nov. 2002.
- [7] S. Pannala, J. Bandyopadhyay, and M. Swaminathan, "Contribution of resonance to ground bounce in lossy thin film planes," *IEEE Trans. Advanced Packaging*, vol. 22, pp. 248-258, Aug. 1999.
- [8] T. K. Sarkar, and O. Pereira, "Using the Matrix Pencil to Estimate the Parameters of a Sum of Complex Exponentials," *IEEE Antenna and Propagation Magazine*, vol. 37, pp. 48-55, 1995.
- [9] T. L. Wu, C. C. Wang, C. C. Kuo, and J. S. Hsieh, "A novel time-domain method for synthesizing broadband macro-pi models of differential via," *IEEE Microwave and Wireless Components Letters*, vol. 15, pp. 378-380, May 2005.
- [10] M. H. Wang, and R. B. Wu, "Equivalent circuit Extraction Using Time-Domain Reflectometry (TDR)", Master Thesis of National Taiwan University, 1997.

New Models for Controlling Signal Dispersion, Attenuation and Total Delay in the Design of Long High Performance Lossy Interconnects

Prof. Robert H. Flake

The University of Texas at AUSTIN, USA

Abstract- A primary challenge faced in the design of high performance lossy metal interconnect (HPLI) circuits in digital and communication systems is to obtain and maintain signal integrity (SI) requirements on these lines while operating under significant signal dispersion and attenuation. The recent discovery of a special signal waveform, called Speedy Delivery (SD), with controlled signal dispersion, attenuation and delay promises to reduce the challenge in extending the data rate above the current state-of-the-art HPLI circuits.

1. Introduction

A primary challenge faced in the design of high performance lossy metal interconnect (HPLI) circuits in digital and communication systems is to obtain and maintain signal integrity (SI) requirements on these lines while operating under significant signal dispersion and attenuation.

As an example, designing 6 GHz half-meter serialized high-speed back plane digital interconnects currently demand overcoming high signal dispersion and 30db attenuation while maintaining adequate SI specifications. Further improving the data rate in these interconnects has been a challenge.

2. Applications of the SD signal to increase data rate on metal digital and communication circuits

A simple HPLI design improvement process utilizing the SD signal (i.e. positive exponential^{[1][2][3]}) is proposed in this paper whose goal is to obtain a higher data rate from an existing interconnect originally designed for conventional amplitude modulated digital signals. The key to improved data rate in this approach is to modify the conventional data pulse by altering the leading edge of the amplitude modulated digital pulses. This is accomplished by incorporating the shape preserving^{[1][2][3]} SD signal in the leading edge of the digital pulse and coding^{[4][5]} the SD shape parameter (exponent coefficient, “ α ”) in the edge. Coding additional bits by varying the SD signal shape parameter (α) yields a significantly higher HPLI data rate without requiring any tangible increase in the bandwidth of the conventional interconnect design.

The SD waveform and its accompanying propagation properties can thereby be incorporated into the signal waveforms of digital and communication systems^{[4][5]}. The new coding modalities unique to the SD waveform can be utilized that complement current waveform coding techniques^{[4][5]}. For example, since the SD waveform does not change shape during propagation in dispersive and lossy media, the SD shape parameter α (exponential coefficient) may be varied from one transmitted SD pulse to another with the pattern of discrete changes in α detected at the receiver. In this manner, the value of α may be coded to convey information transmission in the channel^{[4][5]}. Experimental measurements are discussed below showing that this process of modulation on a long metal cable, produces essentially no increase in the spectral width of the transmitted data pulses. Thus, an increase in transmission data rate is obtained while the interconnect bandwidth requirements are essentially unchanged.

In addition, this process of encoding also allows multiple distinct values of α to be simultaneously incorporated into SD portions of the leading edge of each of the data pulses. An example using a long interconnect (200m cable) is illustrated in the figures that follow.

Figure1 shows the faceplate of a software controlled arbitrary waveform generator producing a signal waveform with two distinct shapes of SD signals comprising the leading edge of the pulse. The lower voltage range of the edge consists of an SD signal with a shape parameter $\alpha_1 = 2 \times 10^7$ (1/sec) and the higher voltage range of the leading edge consists of a second SD waveform shape with $\alpha_2 = 3 \times 10^7$ (1/sec). These distinct shapes incorporated in the leading edge of the voltage pulse applied to a RG 58/U coaxial cable are preserved while propagating 200m distance. Figure2 illustrates the preservation of the first SD signal section of the pulse with shape parameter $\alpha_1 (= 2 \times 10^7$ 1/sec) with the input pulse shown on the left of the figure and the output pulse after traveling 200m on the

right. Figure 3 illustrates the natural log of the voltage amplitudes of these input and output signals with slopes of both consistent with $\alpha_1 = 2 \times 10^7$ (1/sec). Figures 4 and 5 illustrate the shape preservation of the second SD signal portion of the leading edge with $\alpha_2 = 3 \times 10^7$ (1/sec).

Figure 6 shows a pulse with these two sections of SD signals interchanged with $\alpha_1 = 3 \times 10^7$ (1/sec) for the first section and $\alpha_2 = 2 \times 10^7$ (1/sec) for the second section. Figures 7 and 8 show the preservation of the shapes for the $\alpha_1 (= 3 \times 10^7$ 1/sec) section of the input and output pulse edges and figures 9 and 10 for the second $\alpha_2 (= 2 \times 10^7$ 1/sec) section of the input and output pulse edges.

These two pulses with composite SD shapes in their leading edge, together with two pulses with distinct single SD shapes corresponding to either α_1 or α_2 in their leading edge, provide a modulation scheme capable of conveying additional two bits per symbol in the channel. The standard pulse amplitude modulation process may be combined with this modulation of SD shapes creating a composite modulation technique enhancing the signal data rate by two bits per symbol period with essentially no increase in bandwidth of the transmitted waveforms. The values of α in the SD sections of these pulses may be detected (decoded^{[4][5]}) by DSP filters using standard slope detection algorithms processing the linear log amplified edges.

3. High frequency CMOS SD pulse driver circuits

These experimental results illustrating how to apply the SD signal to increase an interconnect data rate discussed above employed 200m cable and was therefore using an appropriately low data symbol frequency. Applications of this approach to other interconnect designs such as high speed backplanes would entail a much higher pulse frequency requiring high frequency drivers for SD signal generation.

A high frequency SD driver circuit can be implemented in CMOS. In fact, conventional high speed latched comparator circuits in CMOS contain a middle stage (unstable feedback loop) that produces the positive exponential waveform^{[6][7]}.

4. Conclusion

A simple HPLI design improvement process utilizing the SD signal is proposed in this paper whose goal is to obtain a higher data rate from an existing interconnect originally designed for conventional digital signals. The key to improved data rate in this approach is to modify the conventional data pulse by altering the leading edge of conventional amplitude modulated data pulses. That is, by including the shape preserving^[1] SD signal as the leading edge and coding^{[4][5]} the SD shape (exponent coefficient, " α ") parameter of the edge. Coding additional bits by varying the SD signal shape parameter (α) yields a significantly higher HPLI data rate without requiring any tangible increase in the conventional interconnect bandwidth design.

REFERENCE

1. R. H. Flake and J. F. Biskup, "Signal propagation without distortion in dispersive lossy media", 11th IEEE International Conference on Electronics, Circuits and System Proceedings, pp. 407-410, Dec 2004, Tel-Aviv, Israel. ISBN 0-7803-8715-5.
2. R. H. Flake, "Part I (Theory) Signal Propagation without Distortion on Lossy Transmission Lines Having Frequency Dependent Parameters", 9th IEEE workshop on signal propagation on interconnects, pp. 43-45, May 2005, Garmish-Partenkirchen, Germany. ISBN 0-7803-9054-7.
3. Robert H. Flake and John Biskup, "Part II (Experiments) Signal Propagation without Distortion on Lossy Transmission Lines Having Frequency Dependent Parameters", 9th IEEE workshop on signal propagation on interconnects, pp. 51-54, May 2005, Garmish-Partenkirchen, Germany. ISBN 0-7803-9054-7.
4. "Methods For Transmitting a Waveform Having a Controllable Attenuation and Propagation Velocity", US Patent Number 6,441,695
5. "Methods For Transmitting a Waveform Having a Controllable Attenuation and Propagation Velocity", US Patent Number 6,847,267
6. B. Razavi and B. W. Wooley, "Design techniques for high-speed, high-resolution comparators." *IEEE J. Solid-state Circuits*, vol. 27, pp. 1916-1992, Dec. 1992.
7. D. Johns and K. Martin, *Analog integrated circuit design*. New York: Wiley, p317-326, 1997.

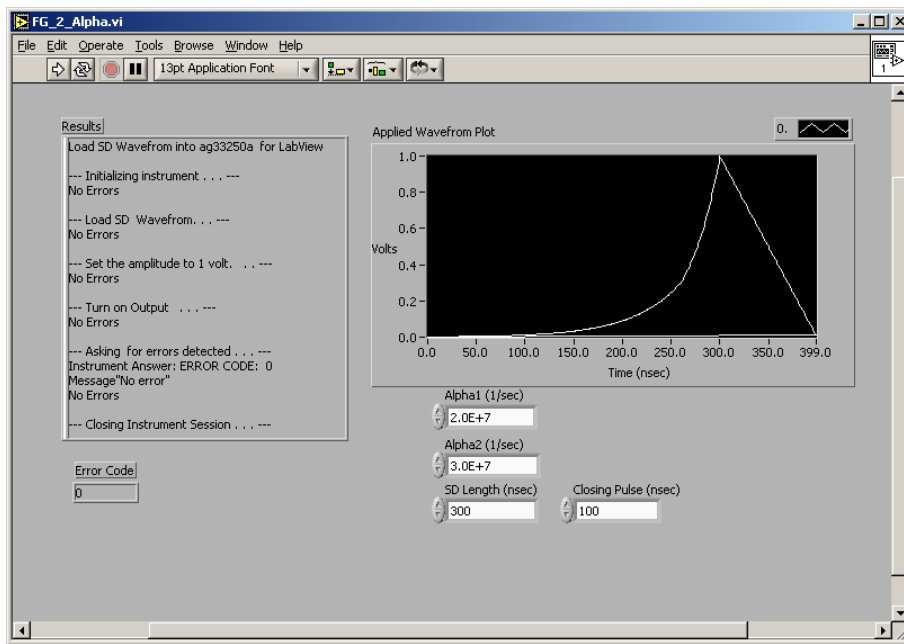


Figure 1: Faceplate of a software controlled arbitrary waveform generator ($\alpha_1 < \alpha_2$)

Input and Output Signals for 200m of RG 58 U Coax

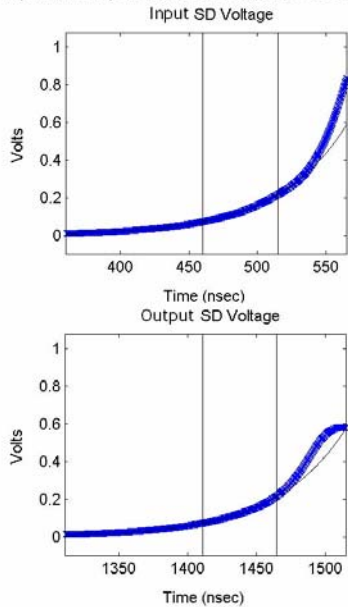


Figure 2: Preserves Shape: 200m Propagation of Speedy Delivery Waveform on Coaxial Cable (Portion of SD Leading Edge with $\alpha_1 = 2 \times 10^7$ 1/sec, $\alpha_1 < \alpha_2$)

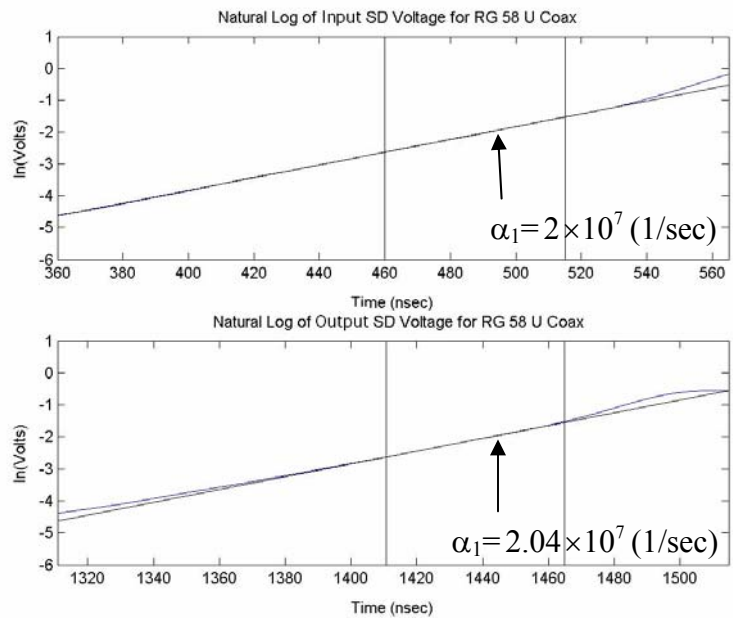


Figure 3: Natural Log of the Voltage Amplitudes of These Input and Output Signals (Portion of SD Leading Edge with $\alpha_1 = 2 \times 10^7$ 1/sec, $\alpha_1 < \alpha_2$)

Input and Output Signals for 200m of RG 58 U Coax

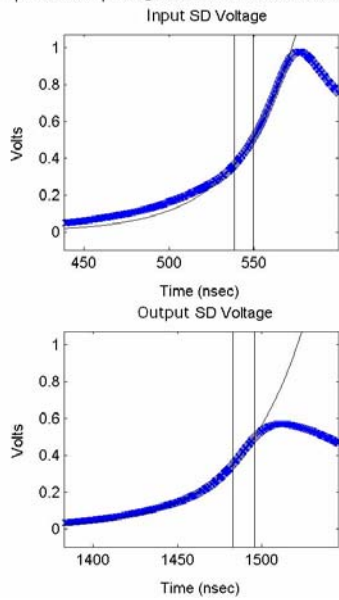


Figure 4: Preserves Shape: 200m Propagation of Speedy Delivery Waveform on Coaxial Cable (Portion of SD Leading Edge of SD Leading Edge with $\alpha_2 = 3 \times 10^7$ 1/sec, $\alpha_1 < \alpha_2$)

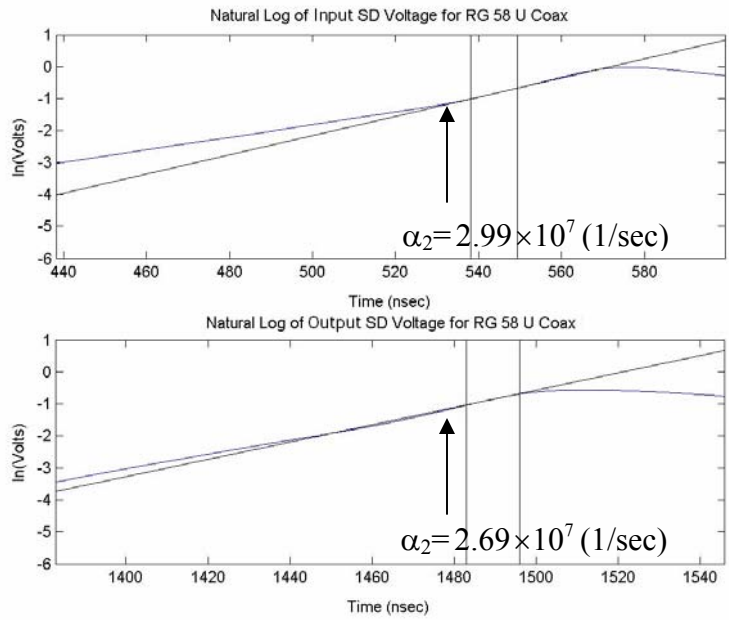


Figure 5: Natural Log of the Voltage Amplitudes of These Input and Output Signals (Portion of SD Leading Edge with $\alpha_2 = 3 \times 10^7$ 1/sec, $\alpha_1 < \alpha_2$)

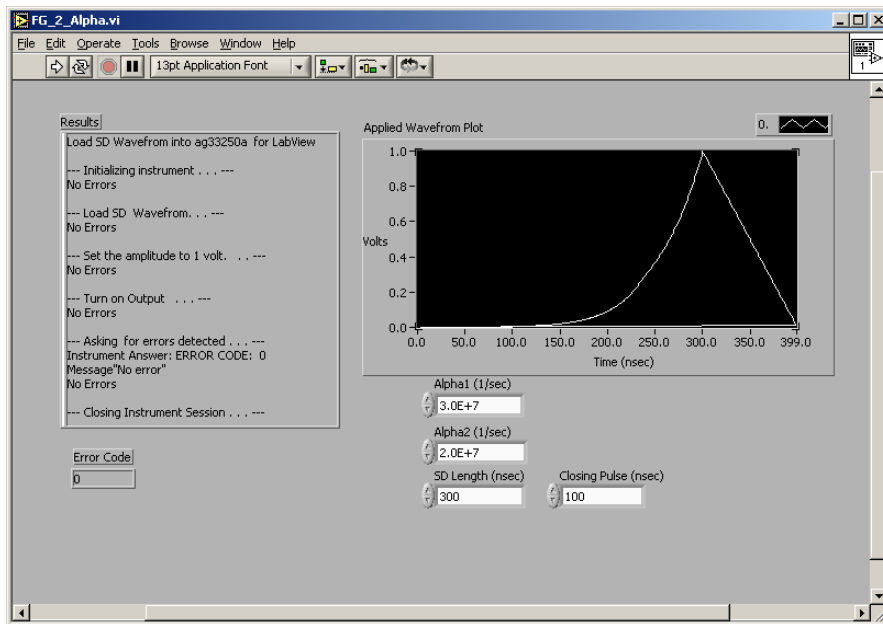


Figure 6: Faceplate of a software controlled arbitrary waveform generator ($\alpha_1 > \alpha_2$)

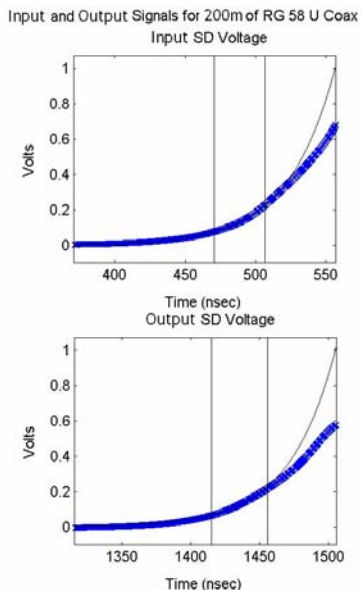


Figure 7: Preserves Shape: 200m Propagation of Speedy Delivery Waveform on Coaxial Cable (Portion of SD Leading Edge with $\alpha_1 = 3 \times 10^7$ 1/sec, $\alpha_1 > \alpha_2$)

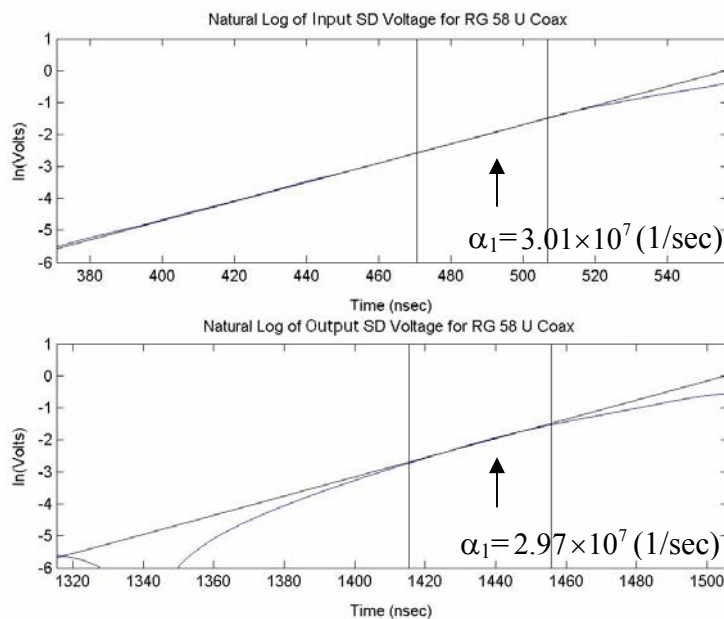


Figure 8: Natural Log of the Voltage Amplitudes of These Input and Output Signals (Portion of SD Leading Edge with $\alpha_1 = 3 \times 10^7$ 1/sec, $\alpha_1 > \alpha_2$)

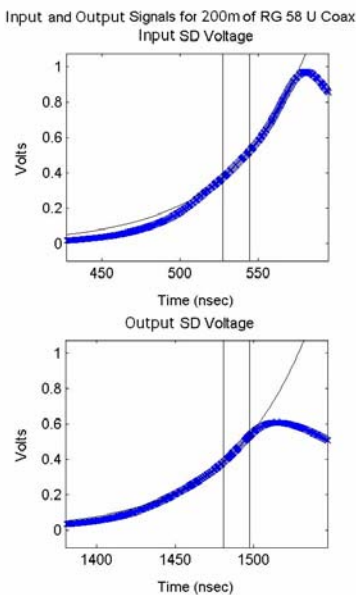


Figure 9: Preserves Shape: 200m Propagation of Speedy Delivery Waveform on Coaxial Cable (Portion of SD Leading Edge with $\alpha_2 = 2 \times 10^7$ 1/sec, $\alpha_1 > \alpha_2$)

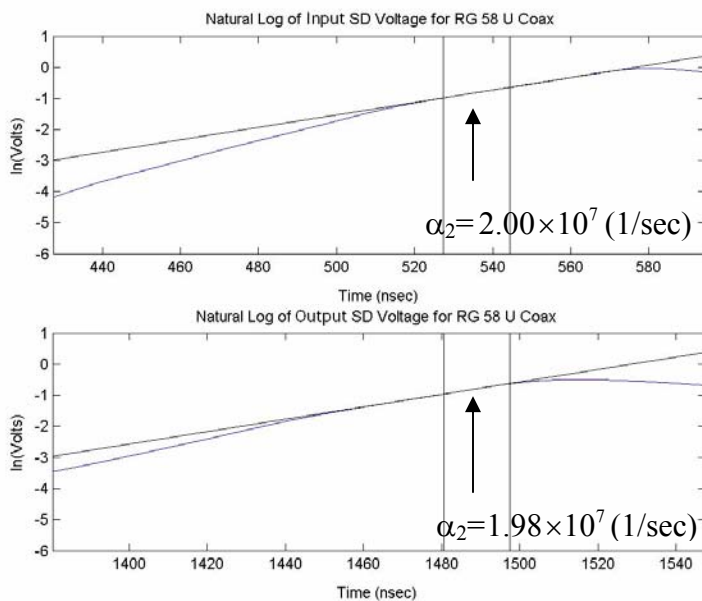


Figure 10: Natural Log of the Voltage Amplitudes of These Input and Output Signals (Portion of SD Leading Edge with $\alpha_2 = 2 \times 10^7$ 1/sec, $\alpha_1 > \alpha_2$)

A Quick Parasitics Extraction Tool for IC Interconnections

Yang Yang **Gaofeng Wang**
Computer School of Wuhan University, China
Jintao Xue
Fudan University, China

Abstract—This paper presents a software tool capable of automatic interconnect parasitic resistance, inductance and capacitance (RLC) extraction. Employing a multipole accelerated Generalized Minimal Residual (GMRES) algorithm based fast three-dimensional (3-D) field solver, the tool extracts parasitics very quickly and accurately for arbitrary interconnects embedded in piece-wise constant dielectrics. A grid-type parallel capacitance extraction solver is also integrated into this tool for large-scale layout and complex net extraction. The interconnect extraction tool also assembles a quick 2-D RLC extraction tool which is useful for some special applications. Architecture of the tool and numerical techniques of parasitics extraction solvers are discussed in this paper. Some experimental results to demonstrate the accuracy and performance of the extraction solvers are also presented.

1. Introduction

For sub-micron, deep sub-micron, and nanometer IC designs, electrical performance of on-chip interconnects is increasingly important. The success of interconnect-centric design flows depends heavily on the availability of sophisticated electromagnetic modeling methodologies and computer-aided-design tools. Accurate and quick field based parasitic RLC extraction tools can be used not only for critical nets, block IP, standard and custom cell analysis, but also for characterization of interconnect models or library patterns which constitute kernels of model-based or library-based full-chip extraction solvers. This paper will describe the architecture of the parasitic extraction tool, multipole accelerated GMRES based fast 3-D field solvers, and Message Passing Interface (MPI) based parallel algorithm for interconnect capacitance extraction. The tool also assembles a quick field based 2-D solver that is useful for some special applications such as buses where several wires go for a long way in parallel. Different solvers can be invoked according to different conditions to maintain accuracy yet quick extraction speed. Some examples are presented to demonstrate the accuracy and performance of these solvers, and some advice for future work will be given.

2. Tool Architecture

Figure 1 depicts the architecture of the parasitics extraction tool. The user is IC designer, and the software includes the following use cases:

(1) Input layout file

IC designer input layout file. This software supports standard layout format like GDSII, which is a binary stream file format.

(2) Input technology file

IC designer input interconnect technology file [1]. The interconnect technology file describes the manufactory information, including geometric and electric information of interconnect layers.

(3) Input netlist file

IC designer input netlist file. This netlist file is a schematic netlist file, and its corresponding circuit is the same as the one which layout file describes. The netlist is used to back-annotate the net ID information to parasitics when output parasitic parameters file. This software supports standard netlist format like SPICE.

(4) View interconnections

IC designer can view interconnections. After inputting layout file and interconnect technology file, IC designers can view the interconnections of a layout, including 2-D view and 3-D view.

(5) Extract parasitics

IC designer extract interconnect parasitic resistance, inductance and capacitance. Because the tool includes different solvers, the user can choose to extract what kind of interconnect parasitic parameter separately, and can choose to use 2-D solver or 3-D solver under different conditions. For capacitance extraction, the user can choose to use Message Passing Interface (MPI) method.

(6) Output parasitic parameters

IC designer output interconnect parasitic parameters. This software outputs standard parasitic parameters file format including SPF and DSPF format.

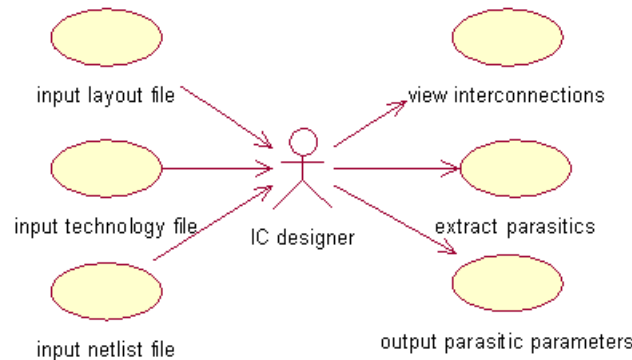


Figure 1: Architecture of parasitics extraction tool

3. RLC extractors

3.1 field based 3-D capacitance extractor

The capacitance of an m -conductor geometry is summarized by an $m \times m$ capacitance matrix C . To determine the j -th column of the capacitance matrix, we compute the surface charges on each conductor by raising conductor j to unit potential 1 while grounding the other conductors. C_{ij} is numerically equal to the charges on conductor i . This procedure is repeated m times to compute all columns of C .

Each of the m potential problems can be solved using an equivalent free-space formulation where dielectric-dielectric interface is replaced by a charge layer of density σ_d . The potential is given by

$$\psi(\vec{r}) = \int_{S_{cd}} \sigma_{cd}(\vec{r}') \frac{1}{4\pi\epsilon_0 \|\vec{r} - \vec{r}'\|} da' + \int_{S_{dd}} \sigma_{dd}(\vec{r}') \frac{1}{4\pi\epsilon_0 \|\vec{r} - \vec{r}'\|} da' \quad (1)$$

where $\psi(\vec{r})$ is the known conductor surface potential, and σ_c is the charge density on conductor surfaces. In this approach, a 3-D free space Green's function in junction with total charges on the conductor-dielectric interfaces and polarization charges on the dielectric-dielectric interfaces is used. This formation has the advantage that there is no theoretical limit to the number of dielectric layers. The dielectric interface condition

$$\epsilon_a \frac{\partial \psi_a(\vec{r})}{\partial n_a} - \epsilon_b \frac{\partial \psi_b(\vec{r})}{\partial n_a} = 0 \quad (2)$$

should be satisfied at any point \vec{r} on the dielectric-dielectric interfaces. ϵ_a and ϵ_b are the permittivities of two adjacent dielectrics a and b , n_a is the normal to the dielectric-dielectric interface at \vec{r} pointing to dielectric a . $\psi_a(\vec{r})$ and $\psi_b(\vec{r})$ are the potentials approaching \vec{r} from dielectric a and b respectively.

A Galerkin scheme is used to numerically solve (1) and (2) for σ_c . In this approach, conductor surfaces and dielectric-dielectric interfaces are divided into n_c and n_d small panels. Assuming uniform charge distribution on each panel, we can transform (1) and (2) into a dense linear system [2]. The dense linear system is efficiently solved with preconditioned generalized minimal residual algorithm (GMRES)[3], in which each iteration is accelerated significantly with adaptive hierarchical multipole accelerated method [4] and number of iterations is decreased considerably using an electrostatic screening based preconditioner.

3.2 field based 2-D capacitance extractor

The capacitance problem of m transmission-lines embedded in piecewise-constant dielectric medium is similar to that of the m conductor geometry discussed above, except that the 3-D free space Green's function in (1) is substituted by a 2-D one [5]. Then a boundary element method (BEM) [6] is applied to solve the integral equation.

3.3 MPI based 3-D capacitance parallel extractor

Large scale layout or complex net parasitic capacitance extraction problem are mainly solved by window techniques [7] and divide techniques [8]. At first, scan the layout and use quick parasitic analytical formulae to evaluate all the interconnect capacitance, and then mark the net where capacitance is above the threshold the critical net. Only consider the critical net and the near conductor can get enough extraction result accuracy. The article [8] refers to a dividing algorithm for critical net, thus divides a complex critical net and its neighboring conductors into many small sub-windows and then parasitics can be extracted separately in parallel mode.

Because we need a process to control the critical net selection and dividing, and to collect extraction result of all sub-windows, the master-slave mode Message Passing Interface (MPI) based parallel algorithm is suitable for the complex interconnect parasitics extraction. Master process controls the critical net window selection and dividing, and sends the geometric information of conductor and dielectric surface to slave processes. Each slave process accepts these data, meshes the conductor and dielectric surfaces, invokes the multipole accelerated GMRES based fast 3-D field solver as describes in section 3.1, and sends result to master process for capacitance synthesis. The architecture of the parallel program can be extended to inductance extraction with careful interconnect dividing.

3.4 3-D inductance and resistance extractor

The numerical technique of 3-D inductance and resistance extraction is something like the capacitance extraction. The impedance of an m -port interconnects is summarized by an $m \times m$ impedance matrix Z . To determine the j -th column of the impedance matrix, we compute the voltage on each port by putting the current of port j to 1 while the other ports current are 0. Z_{ij} is numerically equal to the voltage on port i . This procedure is repeated m times to compute all columns of Z .

To solve each of the m voltage problems, we use mesh analysis method [9]. After discretize the conductor into a number of filaments, use mesh analysis method to build mesh matrix, and use a multipole accelerated GMRES matrix solution to solve the matrix quickly.

4. Experimental Results

4.1 3-D capacitance extraction

(1) Calculation accuracy

In this experiment, we extract capacitance of 3x3 Cross Buses in different dielectric media. The upper three buses are located in a dielectric with permittivity $\epsilon_2 = 6.8\epsilon_0$, while the lower three buses in a dielectric with permittivity $\epsilon_2 = 3.9\epsilon_0$ where ϵ_0 is vacuum permittivity. Each one of buses is 1.2 μm wide, 1.2 μm thick and 8.4 μm long and the space between any two buses is also 1.2 μm . The field based 3-D solver is invoked to extract the capacitance matrix of the 3x3 cross bus geometry. Table 1 and Table 2 compare capacitance matrix computed by our method with that by Fastcap [10].

Conductor 2 and 5 are not listed for the symmetry of the 3x3 bus structure.

Table 1
Capacitance results of quick solver for 3x3 buses (In fF)

	Cond 0	Cond 1	Cond 3	Cond 4
Cond 0	1.694	-0.475	-0.301	-0.247
Cond 1	-0.475	1.881	-0.258	-0.208
Cond 2	-0.051	-0.475	-0.301	-0.246
Cond 3	-0.304	-0.260	2.737	-1.093
Cond 4	-0.248	-0.208	-1.093	3.277
Cond 5	-0.304	-0.260	-0.136	-1.093

Table 2
Capacitance results of Fastcap for 3x3 buses (In fF)

	Cond 0	Cond 1	Cond 3	Cond 4
Cond 0	1.696	-0.4762	-0.3036	-0.2475
Cond 1	-0.4762	1.882	-0.2593	-0.2072
Cond 2	-0.05083	-0.4758	-0.3038	-0.2476
Cond 3	-0.3036	-0.2593	2.743	-1.095
Cond 4	-0.2475	-0.2072	-1.095	3.28
Cond 5	-0.3041	-0.2597	-0.1358	-1.094

(2) Calculation speed

In this experiment, we extract capacitance from the $k \times k$ cross buses for $k=2,4,8$. Each bus is $5\mu m \times 5\mu m \times 100\mu m$. The distance between buses on the same layer is $5\mu m$, and the distance between layers is $10\mu m$. Table 3 compares the time needed for the $k \times k$ examples by multipole accelerated GMRES based solver and a direct solver without multipole accelerated GMRES processing. We can see the quick solver represents significant performances leap in 3-D interconnect capacitance extraction.

Table 3: Capacitance extraction time needed for $k \times k$ cross buses (In second)

k	2	4	8
Solver Type			
MA GMRES	25.1	78.4	338.7
Direct	130.0	1179.2	15120.1

4.2 capacitance parallel extraction

In this experiment, we extract capacitance from 100 of 4×4 cross buses. Each bus in the examples is $5\mu m \times 5\mu m \times 100\mu m$. The distance between buses on the same layer is $5\mu m$, and the distance between layers is $10\mu m$. Figure 2 depicts the relationship of extraction time and the number of parallel running machines. And another result of this experiment indicates the acceleration rate of parallel extraction is almost linear increase with the number of machines increase. But this performance experiment result may not denote the real layout extraction performance very accurately, because the real interconnects structure are more complex and the communication cost in parallel processes perhaps will take more time.

4.3 resistance and inductance extraction

In this experiment, we extract inductance from k parallel buses for $k=2,4,8,16$. Each bus is $5\mu m \times 5\mu m \times 100\mu m$. The distance between buses is $5\mu m$. Figure 3 depicts the relationship of the extraction time with the number of mesh m : direct extraction time increases approximately with m^2 , and multipole accelerated GMRES based inductance extraction time increases approximately with m .

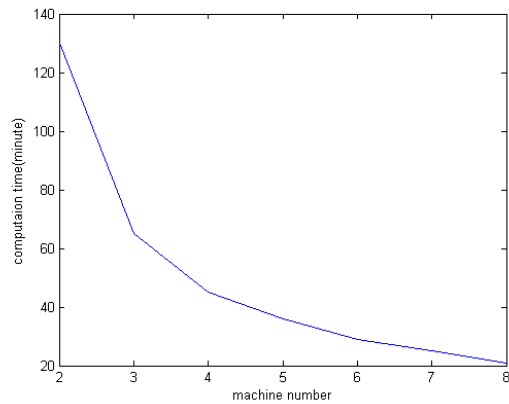


Figure 2: parallel extraction time for 100 of 4x4 buses

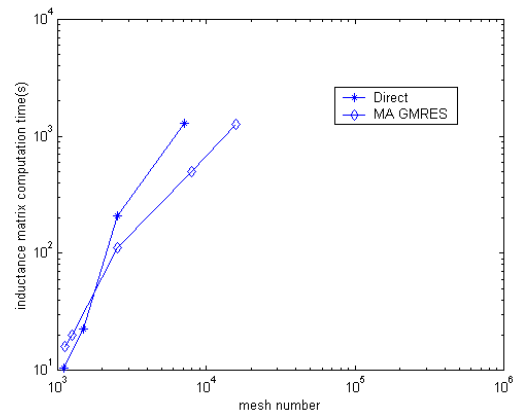


Figure 3: inductance extraction

5. Conclusion

In this paper, a quick parasitics extraction tool is introduced. Compare to direct solvers, the quick 3-D capacitance, inductance and resistance solvers use multipole accelerated GMRES method to improve extraction performance significantly. All experiments environment is Redhat 9.0 Operation System, on the computer with 512M memory and Celeron 2.0GHZ CPU. In future work, we will improve conductor geometry modeling and mesh algorithm to process interconnect having more complex geometric structures. And we will build a database to manage all the data produced during extraction period.

REFERECES

1. Q. K. Zhu, Interconnect RC and Layout Extraction for VLSI, Canada: Trafford Publishing, 2002.
2. K. Nabors, J. White, "Multipole-accelerated capacitance extraction algorithms for 3-D structures with multiple dielectrics," IEEE Trans. Circuit and Systems-1: Fundamental Theory and Applications, Vol. 39, pp. 946-954, 1992.
3. Y. Saad, M. H. Schultz, "GMRES: A generalized minimal residual algorithm for solving nonsymmetric linear systems," SIAM J. Scientific and Statistical Computing, Vol.7, pp. 856-869, 1986.
4. L. Greengard, The Rapid Evaluation of Potential Fields in Particle Systems. Cambridge, MA: MIT Press, 1988.
5. C. Wei, R. F. Harrington, J. R. Mautz, T. K. Sarkar, "Multiconductor transmission lines in multilayered dielectric media," IEEE Trans. Microwave Theory and Techniques, Vol. 32, pp. 439-450, 1984.
6. G. W. Pan, G. Wang, B. K. Gilbert, "Edgy effect enforced boundary analysis of multilayered transmission lines," IEEE Trans. Circuits and Systems-1: Fundamental Theory and Applications, Vol. 39, pp. 955-963, 1992.
7. M. Bächtold, M. Spasojevic, C. Lage and P. B. Ljung. "A system for full-chip and critical net parasitic extraction for ULSI interconnects using a fast 3-D field solver," IEEE Trans. Computer-Aided Design of Integrated Circuits and Systems, Vol. 19, pp. 325-338, 2000.
8. F. Yu and W. Shi, "A divide-and-conquer algorithm for 3D capacitance extraction," ISQED 2004, pp. 253-258, 2004
9. C. A. Desoer and E. S. Kuh, Basic Circuit Theory. New York: McGraw-Hill, 1969.
10. K. Nabors, J. White, "Fastcap: A multipole accelerated 3-D capacitance extraction program," IEEE Trans. Computer-Aided Design of Integrated Circuit and System, Vol. 10, pp. 1447-1459, 1991.

Terahertz label-free biochip sensor with thin metal mesh

Yuichi Ogawa¹, Shin'ichiro Hayashi^{1,2}, Eiji Kato³, Hisa Yoshida¹, Fumiaki Miyamaru²,
Chiko Otani², Kodo Kawase^{1,2,4}

¹Tohoku University, ²RIKEN, ³Advantest Laboratories Ltd., ⁴Nagoya University

Abstract— We demonstrated a biological sensing application using thin metallic mesh — a two-dimensional array of sub-wavelength holes. The band-pass filter property of the thin metal mesh depends not only on its geometrical parameters, but also on the refractive index of the medium in the vicinity of the mesh openings. In order to demonstrate the applicability of this principle in THz biosensing, we used electrospray deposition for realizing a uniform and controllable layer of avidin on a metal mesh substrate. We found out that a quantity of 200 ng/mm² electrosprayed avidin produced a distinct shift in the mesh transmission spectrum towards lower frequencies. This observation suggests that it is possible to achieve label-free sensors in the THz range using thin metal mesh sample substrates.

1. Introduction

Many researchers have been investigating various methods for analyzing biomolecules using terahertz (THz) waves [1-6]. This interest is explained by the fact that large molecules exhibiting complex structures have absorption peaks lying in the THz band; for example, the hybridization of DNA and the antigen-antibody reaction can be distinguished without labeling them with fluorescent agents. At present, the THz time-domain spectroscopy (THz-TDS) technique is used for most of the research on biomolecules in the terahertz region. Although THz-TDS is a sensitive detection method, it involves building complex and expensive systems. Consequently, a simpler and cheaper analysis method would be very beneficial.

In parallel, research in the far-infrared using metallic meshes to build band-pass filters has started from around the 1960s. It became clear that the frequency characteristics are determined by geometrical parameters such as the grid's spatial period and aperture size, and application in spectroscopic analysis was suggested [7, 8].

We have been developing a novel sensing method which uses the band-pass characteristics of a thin conductive metal mesh. This sensing method relies on the change in the transmittance of the THz radiation through a metal mesh when a sample substance is inserted in its openings; the transmittance changes not as much because of the absorption in the sample, but mostly because of the different refractive index of the propagation medium near the openings. Our target is to develop a simple and cheap label-free biochip by using a monochromatic light source and a metal mesh.

2. Characteristics of thin metal mesh

Figure 1 shows pattern diagrams of a thin metal mesh (also called an inductive two-dimensional grid) and the equivalent electrical circuit to illustrate its transmission properties. The circuit parameters are determined as functions of the grid geometric parameters [7] and can be calculated approximately from the grating period (g), its thickness (t) and the wire strip width ($2a$).

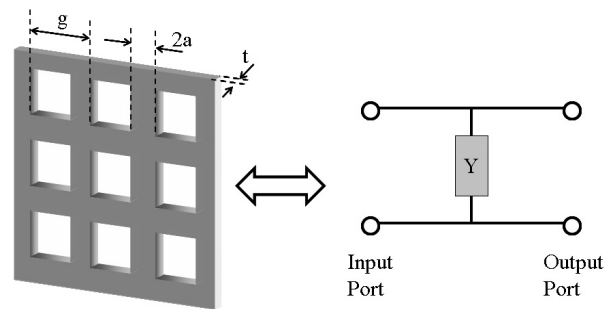


Figure 1. Schematic of the thin metal mesh and the equivalent circuit.

Ulrich's theory shows that at long wavelengths ($g/\lambda < 1$) and for very small thickness ($t \ll \lambda$) the optical properties of the thin metal mesh are conveniently represented as an equivalent electrical circuit by a single admittance (Y) shunting the input. The complex amplitude reflection coefficient of this circuit is

$$\Gamma = -\frac{Y/2}{1+Y/2} \quad (1)$$

In our experiment, the material of metal mesh is electroformed nickel. The thickness of this metal mesh is $5 \mu\text{m}$, the grating constant (mesh period) is $63.5 \mu\text{m}$, and the side of the square apertures is $45 \mu\text{m}$. The transmission spectrum, shown in Figure 2, was measured by FTIR spectroscopy. Figure 2 also shows the calculated transmission spectrum resulting from the geometric parameters of thin metal mesh, based on Ulrich's theory.

This metal mesh behaves as a high-pass filter and the transmittance is approximately 7% at 1 THz. The difference between the experimental curve and the calculated values are relatively small at low frequencies, approximately up to where g/λ is 0.6. Large differences around the peak transmittance are explained by the propagation of diffracted modes [9].

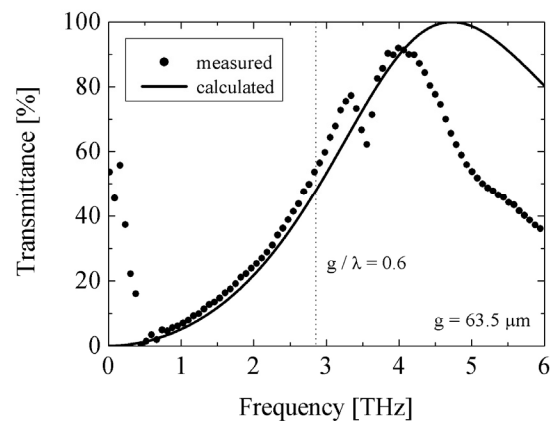


Figure 2. A measured transmission spectrum of the thin metal mesh (●) and its theoretical version calculated using Ulrich's theory (solid line). The dashed line indicates where $g/\lambda = 0.6$.

We first investigated the transmission characteristics of this metal mesh and the way they change depending on the refractive medium in the vicinity of the mesh. For this purpose we coated the mesh with vegetable oil ($n = 1.5$, $k = 0.01$) as a sample. The sample quantity was about 1.0 mg/cm^2 on the mesh. The oil extended uniformly so that its thickness was approximately the same as the metallic mesh, that is, $5 \text{ }\mu\text{m}$.

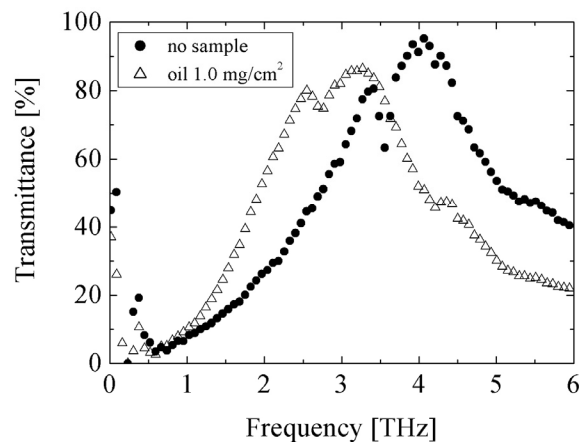


Figure 3. Measured transmission spectra of the thin metal mesh without sample (●) and with vegetable oil as sample (△).

The amplitude of the transmission peak in the spectrum decreases by about 10% when the oil covers the mesh apertures; at the same time the peak frequency drops from 4.1 THz to 3.3 THz. This result demonstrates that the thin metal mesh is sensitive to the refractive index of the sample. Noting that in the frequency range below the peak of the thin metal mesh without sample the transmittance of the thin metal mesh with sample is higher, we conclude that it should also be possible to perform an imaging of the refractive index change at a single frequency.

3. Electrospayed protein sample

Considering the results presented in the previous section, it is natural to infer that the transmission of the thin metal mesh is also sensitive to biomolecular samples, such as avidin and biotin. The affinity between biotin and avidin is nearly as strong as covalent bonding. To disrupt the complex, extreme denaturing conditions are required. The highly specific and strong binding of the avidin-biotin system has led to its wide usage in a variety of biotechnological applications [4].

In order to apply an avidin sample uniformly and in a controllable quantity, we used the electrospay deposition (ESD) technique [10]. ESD is a versatile method for forming thin films, applicable for solute molecules with a wide range of molecular weights, such as DNA, proteins, and polymers. In the ESD technique, solutions of these materials are transformed into droplet jets; charged electrospay products are deposited onto specific areas of a conductive substrate under control of electrostatic forces. One major advantage of the ESD is that it preserves the functional properties of the electrospayed biological molecules, such as antigenic and catalytic properties of proteins and hybridization ability of DNA molecules.

In our experiments, electrospaying was carried out using an electrospay deposition device (Esprayer, Fuce Co., Ltd., Japan); the sprayed area was 8 mm in diameter, and the surface density of avidin was 200 ng/mm². We investigated the basic sensor property of a thin metal mesh made of nickel (thickness: 6 μm, grid period: 76.2 μm, aperture size: 58 μm). Figure 4 shows the result of transmittance measurements of the thin metal mesh with and without avidin, obtained using an FTIR spectrometer.

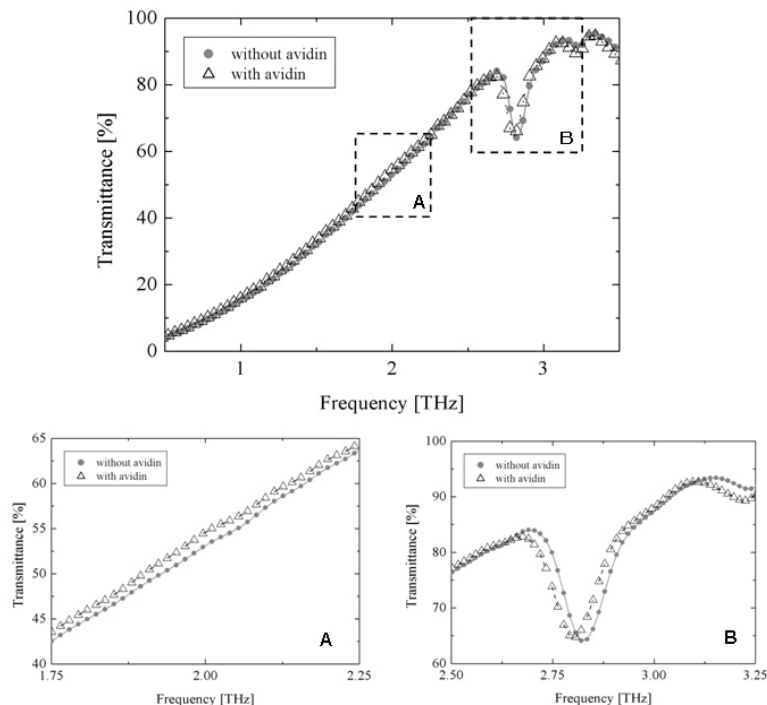


Figure 4. Measured transmission spectra of the thin metal mesh without any sample (●) and with avidin (Δ). Expanded parts of the plot are shown in (A) and (B).

The transmission spectrum of the avidin-sprayed mesh was found to shift towards lower frequencies relative to the bare mesh. As a result, at 2 THz the transmission of the mesh with avidin is approximately 0.8% higher than without avidin. Simultaneously, the resonance absorption peak at 2.82 THz was shifted to 2.79 THz. This shift is believed to be caused by the different refractive index in the vicinity of the metal mesh surface when the small amount of avidin is sprayed on the mesh [11].

4. Conclusion

We demonstrated a sensor application using thin metal mesh, based on the change in the transmission characteristics produced by a variation of the refractive index near the mesh. This result suggests the possibility of realizing a label-free biosensor that may be used, for example, in investigating the biological affinity, such as DNA hybridization and protein interaction. In this report, we will present some detailed results of a sensitivity evaluation of the mesh sensor. Additionally, to confirm the feasibility of biochip sensors, we performed a series of imaging experiments using a monochromatic source at 1 THz.

Acknowledgment

The authors would like to thank Dr. Horoshi Kase and Dr. Kaname Mogami from Fuenche Co., Ltd. for allowing us to use their electrospray deposition system.

References

- [1] M. Brucherseifer, M. Nagel, P. H. Bolivar, H. Kurz, A. Bosserhoff and R. Büttner: *Appl. Phys. Lett.*, **77**, 4049 (2000)
- [2] M. Nagel, P. H. Bolivar, M. Brucherseifer, H. Kurz, A. Bosserhoff and R. Büttner: *Appl. Phys. Lett.*, **80**, 154 (2002).
- [3] P. H. Bolivar, M. Brucherseifer, M. Nagel, A. Bosserhoff and R. Büttner: *Phys. Med. and Biol.*, **47**, 3815 (2002).
- [4] S. P. Micken, A. Menikh, H. Liu, C. A. Mannella, R. MacColl, D. Abbott, J. Munch, and X.-C. Zhang, *Phys. Med. Biol.*, **47**, 3789 (2002).
- [5] B. Ferguson and X.-C. Zhang, *Nature materials*, **1**, 26 (2002).
- [6] A. Menikh, S. P. Micken, H. Liu, R. MacColl, X.-C. Zhang, *Biosensor and Bioelectronics*, **20**, 658 (2004).
- [7] R. Ulrich, *Infrared Phys.*, **7**, 37 (1967).
- [8] K. Sakai, T. Fukui, Y. Tsunawaki and H. Yoshinaga, *Jpn. J. Appl. Phys.*, **8**, 1046 (2003).
- [9] J. M. Laarre, N. Coron, R. Courtin, G. Dambier and M. Charra, *Int. J. Infrared and Millimeter Waves*, **2**, 273 (1981).
- [10] V. N. Morozov and T. Ya. Morozova, *Anal. Chem.* **71**, 3110 (1999).
- [11] F. Miyamaru, S. Hayashi, C. Otani, K. Kawase, Y. Ogawa, H. Yoshida, E. Kato, *Opt. Lett.*, **31**, 1118 (2006).

Compact Terahertz Time Domain Spectroscopy System with 1.5- μm -Wavelength Femtosecond-Fiber-Laser

Masato Suzuki, and Masayoshi Tonouchi

Institute of Laser Engineering, Osaka University, 2-6 Yamadaoka, Suita, Osaka 565-0871, Japan

Abstract—We have investigated performances of a compact terahertz (THz) time-domain spectroscopy system using 1.5 μm Er-doped fiber laser. 1.5 μm excitation of InSb realizes the most efficient THz emission in our emitters with a maximum available frequency of 4 THz. Defocus excitation of p-InAs emitter provides stronger THz signals due to phased array effect with reduced bandwidth.

1. Introduction

Terahertz time domain spectroscopy (THz-TDS) systems are expected to be one of powerful tool to open the new research field in THz science and technology. [1-3] Many researchers are utilizing the pulsed THz systems based on Ti: sapphire lasers, which have the center wavelength of 800 nm. The standard THz systems show the power dynamic range of 1×10^6 and maximum available frequency of 4 THz. However, development of practical THz systems requires more stable and more compact lasers than the Ti: sapphire lasers, because Ti: sapphire lasers are bulky and unstable against changes in lasing environment as temperature, humidity and air turbulence. A fiber laser is one of the candidates for the practical compact system. The fiber lasers offer high performances in portability and stability. However, the typical wavelength of the fiber laser is 1.5 μm . Therefore, it is technological importance to develop efficient THz emitters and detectors for 1.5 μm laser operation.

Since Howells *et al.* have reported excitation wavelength dependences of THz emission from InSb, THz devices for 1.5 μm laser operation have been studied and developed. [4-11] Current development of 1.5- μm -optimized THz emitters based on surface radiation is in the stage of characterizing various emitters as InAs and InSb, which show high THz emission efficiencies. [5,6] Development for 1.5- μm -excited THz detectors is far behind that of the emitters. Detection efficiency of the 1.5- μm -triggered PC antenna based on low-temperature grown GaAs is roughly one-tenth of the detector excited by 800 nm pulses. [7,8] Very recently, the research progress in 1.5- μm -optimized THz devices has gone a step further. Nagai *et al.* have demonstrated THz wave generation by optical rectification and electro-optical detection with GaAs using a 1.5 μm fiber laser. [9] We also have reported THz wave generation and detection by Fe-implanted InGaAs PC antennas excited by 1.5 μm light. [10,11] Therefore, these 1.5- μm -excited THz devices achieve a high level of performance for the prototype of THz systems with 1.5 μm fiber lasers. In this letter, we investigate basic performances of a compact THz-TDS system with a 1.5 μm fiber laser.

2. Experimental setup

A compact mode-locked laser based on Er-doped fiber oscillator (IMRA Femtolite) operating at a repetition rate of 50 MHz is used as an optical pulse source of our THz spectroscopy systems. The output beam has the center wavelength of 1560 nm and the pulse width of 70 fs. The total output power is 70 mW. The fiber laser system with a

palm-size laser head can be operated at room temperature without external cooling.

In the THz systems, the output beam from the fiber laser is split into the pump and the trigger pulses by a beamsplitter. The pump beam at incidence angle of 45 degrees is focused onto an emitter surface by a lens. We examine n- and p-type InAs, and InSb emitters to compare emission properties. The pump pulse is also modulated by an optical chopper at 2 kHz. THz emission from the emitter is collected and guided into an LT-GaAs dipole antenna detector on a semispherical silicon lens by off-axis parabolic mirrors. The probe beam through a scan delay stage is focused onto the 5 μm gap of the antenna detector by an objective lens. To maximize a THz signal, crystalline axis of an emitter and polarization planes of pump and trigger pulses are adjusted by rotation of an emitter holder and half wave plates, respectively. A THz waveform is obtained by delaying the timing of the trigger pulse to the pump pulse and lock-in detection referenced to the chopper modulation at the time constant of 300 ms.

3. Results and discussion

Figures 1 (a) and (b) show pump power dependences of the peak THz amplitude signals of focus- and defocus-excited emitters, respectively. The spot sizes for the focus and defocus excitations are estimated to be about 140 and 600 μm , respectively. At a focus excitation condition, InSb becomes the most efficient emitter at a pump power of more than 12 mW. The peak amplitude of focus-excited InSb at the pump power of 35 mW is two times larger than that of p-InAs owing to the linear power dependence of InSb. On the other hand, the peak amplitudes of n- and p-type InAs emitters saturate with increase in the pump power. Our results show that in high power excitation case, 1.5 μm -excited InSb is a more efficient emitter than the 1.5 μm -excited InAs.

Defocus excitation enhances THz radiation in the reflected direction due to phased array effect. The directional THz radiation is easily collected by an off-axis parabolic mirror to increase the magnitude of THz signals. In fact, the detected amplitude of the defocus-excited p-InAs is larger than that of the focus-excited InSb due to the directional THz wave. Additionally, the power dependences of all defocus-excited emitters become linear because of low optical densities as shown in Fig. 1 (b). Optical densities at the defocus excitation are one twentieth of these at the focus excitation. Thus, Fig. 1 (b) corresponds to a magnified view of Fig. 1 (a) in the power range of 0-1.9 mW. This is the reason for defocus-excited p-InAs becoming the most efficient emitter.

The power and the spot size of the pump pulses play important parts in choosing the best emitter for a THz system. In general, the directional THz wave induced by defocus excitation can suppress loss caused by the solid angle of THz radiation. The amplitude of THz radiated field also increases with the optical density of pump pulses. To enhance THz signals, however, we must adjust the spot size to obtain large phased array effect and high optical density excitation. In our case, defocus-excited p-InAs becomes one of candidates for the emitter of THz systems using 1.5 μm pulses, although InSb is a more efficient 1.5- μm -excited THz emitter than InAs at high optical density excitation.

Frequency bandwidth of the THz systems is one of important features from the viewpoint of application to spectroscopy. Figures 2 (a) and (b) show normalized waveforms and Fourier power spectra of our THz system with various emitters at excitation by 1.5 μm pulses. The pump and trigger powers of the waveforms in Fig. 2 are 32 and 30 mW, respectively. As shown in Fig. 2 (b), maximum frequency available from the focus-excited InSb and InAs are achieved to be 4 THz, a typical value of the bandwidth for standard THz systems. From these results, THz systems operated by 1.5 μm pulses can be utilized instead of standard THz systems for 800 nm laser operation. In contrast with increasing the THz amplitude, frequency bandwidth of defocus-excited p-InAs is limited to 2.5 THz because of low optical density excitation. One of reasons for this is that THz pulses from p-InAs at low optical

density becomes broader than that at high optical density due to the difference of THz radiation mechanism between high and low optical density excitation.

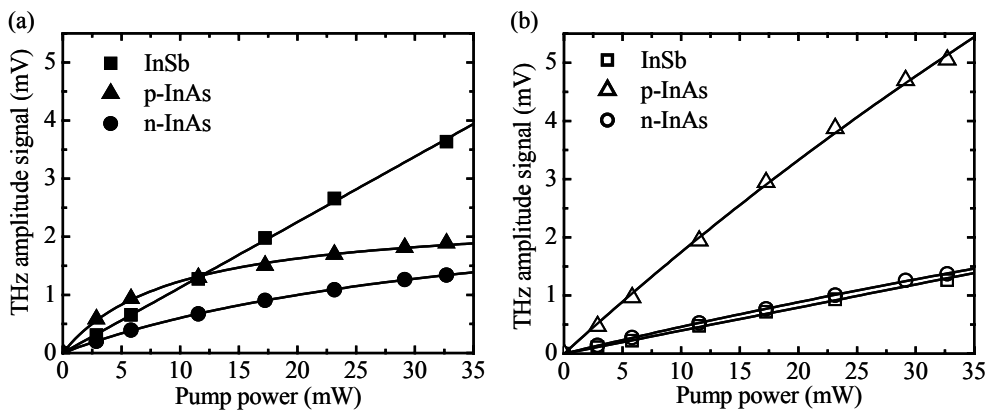


Fig. 1. Pump power dependence of the THz radiation from n- and p-type InAs and InSb in the cases of focus (a) and defocus (b) excitation

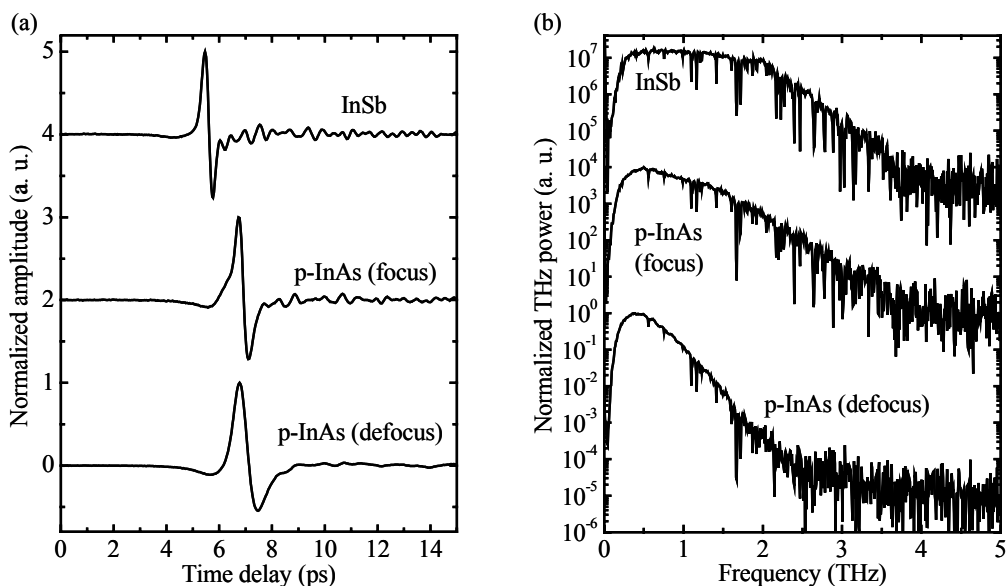


Fig. 2. The temporal waveform (a) and Fourier spectra (b) of the THz radiation from focus- and defocus-excited p-type InAs and focus-excited InSb. The waveforms and spectra of focus-excited InSb and p-InAs are shifted.

4. Conclusion

We have demonstrated performances of a compact THz spectroscopy system with a 1.5 μm compact fiber laser. The emitters and the detector for the THz system are selected to be a narrow gap semiconductors as InSb and InAs, and an LT-GaAs-based dipole antenna detector, respectively. At focus excitation, InSb has higher radiation efficiency compared to that of InAs and linear power dependence of THz power. At defocus excitation, p-InAs becomes one of candidates for the emitter of our THz system due to phased array effect. The maximum frequency components of THz radiated fields from the focus-excited emitters are achieved to be 4 THz. Therefore, the bandwidth of the THz system operated by 1.5 μm lights corresponds to that of standard THz systems for 800 nm lights.

Acknowledgment

This work was supported in part by the Strategic Information and Communications Research and Development Promotion Fund of Ministry of Internal Affairs and Communications (MIC), Special Coordination Fund for Promoting Science and Technology of the Ministry of Education, Sports, Culture, Science and Technology (MEXT). The authors thank Professor X.-C. Zhang for the p-InAs emitters used in this work.

REFERENCES

1. B. Ferguson and X.-C. Zhang, *Nat. Mat.* **1**, 26 (2002).
2. *Sensing with Terahertz Radiation* edited by D. Mittleman (Springer, Berlin, 2003).
3. *Terahertz Optoelectronics* edited by K. Sakai (Springer, Berlin, 2005).
4. S. C. Howells, S. D. Herrera and L. A. Schlie, *Appl. Phys. Lett.* **65**, 2946 (1994).
5. T. Kondo, M. Sakamoto, M. Tonouchi, and M. Hangyo, *Jpn. J. Appl. Phys.* **38**, L1035 (1999).
6. H. Takahashi, Y. Suzuki, M. Sakai, S. Ono, N. Sarukura, T. Sugiura, T. Hirosumi, and M. Yoshida, *Appl. Phys. Lett.* **82**, 2005 (2003).
7. H. Erlig, S. Wang, T. Azfar, A. Udupa, H. R. Fetterman, and D. C. Streit, *Electron. Lett.* **35**, 173 (1999).
8. M. Tani, K.-S. Lee, and X.-C. Zhang, *Appl. Phys. Lett.* **77**, 1396 (2000).
9. M. Nagai, K. Tanaka, H. Ohtake, T. Bessho, T. Sugiura, T. Hirosumi, and M. Yoshida, *Appl. Phys. Lett.* **85**, 3974 (2004).
10. M. Suzuki and M. Tonouchi, *Appl. Phys. Lett.* **86**, 051104 (2005).
11. M. Suzuki and M. Tonouchi, *Appl. Phys. Lett.* **86**, 163504 (2005).

Target Enhancement Oriented Fusion Method using Polarimetric SAR Data

Yilun Chen, Jian Yang

Department of Electronic Engineering, Tsinghua University
Beijing, 100084, P.R.China
chenyl@mails.tsinghua.edu.cn

Abstract—Polarimetric Synthetic Aperture Radar (SAR) can provide multi-dimensional radar images with different transmitting and receiving polarization states of antennas. For the application of target detection, an essential problem is to combine multi-dimensional images into a single one to enhance the contrast between the target and the clutters. In this paper, a novel fusion method is proposed for the enhancement of local contrast. The optimal local contrast of each pixel is first defined based on the ratio between neighboring pixels. Then the problem is formulated in a least square minimization framework. It is proved that the solution can be obtained by solving a discrete Poisson equation via the Fast Fourier Transform (FFT) implementation. With polarimetric synthetic aperture radar data, we demonstrate the effectiveness of our method for target enhancement, where road detection is used as an example.

1. Introduction

Synthetic Aperture Radar (SAR) has attracted more and more attention in recent years for its all-day and all-weather capability of earth observation. Polarimetric synthetic aperture radar can provide multi-dimensional data by transmitting and receiving electromagnetic waves with different polarizations, which can be especially helpful in the application of target detection. An important problem for target detection using polarimetric SAR data is how to fuse information from different channels to make the target more salient from the background, i.e., to enhance the target/clutter contrast by combining data from different channels in a proper way.

For years researchers have devised several methods to utilize the polarimetric information for target enhancement. Optimal polarimetric contrast enhancement (OPCE) is to choose optimal polarization states for enhancing a desired target versus an undesired target/clutter [1]- [5]. By incorporating more parameters, Yang et al. extends the OPCE into a more general form with more encouraging results [6].

However, traditional methods tend to enhance the contrast between single target and single clutter and require the statistics of these targets first, which limits their use. Because in practice the statistical characteristics of different targets may vary significantly, and so do the clutters. For the problem of multi-targets/multi-clutters enhancement, traditional methods might not work well.

In this paper, a new fusion method is proposed to solve this problem. The optimal local contrast for polarimetric SAR data is first defined. A fused image is then reconstructed from the obtained optimal local contrast. The problem is formulated in a least square minimization framework. The fused image can be obtained by solving a discrete Poisson equation with the Fast Fourier Transform (FFT) implementation. We use polarimetric SAR data from the NASA/JPL L-band AirSAR to demonstrate the effectiveness of the proposed method.

2. Poisson reconstruction based fusion method for polarimetric SAR images

2.1 The definition of local contrast

The local contrast is defined to measure the difference of neighboring pixels. For a SAR image with intensity value I , the horizontal contrast and the vertical contrast of the pixel(i, j) are defined as

$$r_{i,j}^x = \frac{I_{i,j}}{I_{i-1,j}}, r_{i,j}^y = \frac{I_{i,j}}{I_{i,j-1}}, \quad (1)$$

respectively. The ratio form in eq.(1) is adopted due to the multiplicative speckle noise of SAR images.

For polarimetric SAR data, a Sinclair scattering matrix [S] can be obtained from each pixel:

$$[S] = \begin{bmatrix} s_{HH} & s_{HV} \\ s_{VH} & s_{VV} \end{bmatrix}. \quad (2)$$

In a reciprocal isotropic medium for the monostatic case, the reciprocity theorem holds and thus the Sinclair scattering matrix is symmetric, i.e., $s_{HV} = s_{VH}$. Therefore, we have three images from independent channel denoted as HH , HV and VV , respectively. With these images from three different channels, the optimal horizontal local contrast R^x is defined as

$$R_{i,j}^x = \begin{cases} M_{i,j}^x & \text{if } M_{i,j}^x > 1/m_{i,j}^x \\ m_{i,j}^x & \text{else} \end{cases}, \quad (3)$$

where

$$M_{i,j}^x = \max \left\{ \left| \frac{HH_{i,j}}{HH_{i-1,j}} \right|, \left| \frac{HV_{i,j}}{HV_{i-1,j}} \right|, \left| \frac{VV_{i,j}}{VV_{i-1,j}} \right| \right\} \quad (4)$$

and

$$m_{i,j}^x = \min \left\{ \left| \frac{HH_{i,j}}{HH_{i-1,j}} \right|, \left| \frac{HV_{i,j}}{HV_{i-1,j}} \right|, \left| \frac{VV_{i,j}}{VV_{i-1,j}} \right| \right\}. \quad (5)$$

Similarly, the optimal horizontal local contrast R^y is defined as

$$R_{i,j}^y = \begin{cases} M_{i,j}^y & \text{if } M_{i,j}^y > 1/m_{i,j}^y \\ m_{i,j}^y & \text{else} \end{cases}, \quad (6)$$

where

$$M_{i,j}^y = \max \left\{ \left| \frac{HH_{i,j}}{HH_{i,j-1}} \right|, \left| \frac{HV_{i,j}}{HV_{i,j-1}} \right|, \left| \frac{VV_{i,j}}{VV_{i,j-1}} \right| \right\} \quad (7)$$

and

$$m_{i,j}^y = \min \left\{ \left| \frac{HH_{i,j}}{HH_{i,j-1}} \right|, \left| \frac{HV_{i,j}}{HV_{i,j-1}} \right|, \left| \frac{VV_{i,j}}{VV_{i,j-1}} \right| \right\}. \quad (8)$$

2.2 The reconstruction framework

Based on the optimal local contrast R^x and R^y defined in the above subsection, the fusion problem is to reconstruct the fused image P from R^x and R^y , i.e., to find an image P with its local contrast (defined in eq.(1)) closest to R^x and R^y :

$$\frac{P_{i,j}}{P_{i-1,j}} \rightarrow R_{i,j}^x, \frac{P_{i,j}}{P_{i,j-1}} \rightarrow R_{i,j}^y. \quad (9)$$

Let $f = \ln P$, $g^x = \ln R^x$ and $g^y = \ln R^y$, we use the following form to approximate eq.(9) for the convenience of calculation,

$$f_{i,j} - f_{i-1,j} \rightarrow g_{i,j}^x, f_{i,j} - f_{i,j-1} \rightarrow g_{i,j}^y. \quad (10)$$

The approximation is implemented by minimizing the following energy function

$$\min E = \sum_{i,j} \left((f_{i,j} - f_{i-1,j} - g_{i,j}^x)^2 + (f_{i,j} - f_{i,j-1} - g_{i,j}^y)^2 \right). \quad (11)$$

Let $\frac{\partial E}{\partial f_{i,j}} = 0$, it can be proved that the optimization of eq.(11) is equivalent to the solution of the following linear equations

$$4f_{i,j} - f_{i-1,j} - f_{i,j-1} - f_{i+1,j} - f_{i,j+1} = g_{i+1,j}^x - g_{i,j}^x + g_{i,j+1}^y - g_{i,j}^y, \quad (12)$$

which turns to be the discrete form of Poisson equation [7].

The log image f can be solved by Poisson reconstruction using the Fast Fourier Transform (FFT). Define a set of image operators as follows

$$h = \begin{bmatrix} & -1 & \\ -1 & 4 & -1 \\ & -1 & \end{bmatrix}, h^x = \begin{bmatrix} & & \\ 0 & -1 & 1 \\ & & \end{bmatrix}, h^y = \begin{bmatrix} & 0 & \\ & -1 & \\ & & 1 \end{bmatrix}. \quad (13)$$

Expressing eq.(12) in the convolution form

$$h * f = h^x * g^x + h^y * g^y, \quad (14)$$

and applying the Fourier Transform on both sides, there is

$$H \cdot F = H^x \cdot G^x + H^y \cdot G^y, \quad (15)$$

where H, H^x, H^y, G^x and G^y are the Fourier Transformation of h, h^x, h^y, g^x and g^y , respectively. f is then reconstructed by

$$f = \text{ifft}(H^{-1}(H^x \cdot G^x + H^y \cdot G^y)), \quad (16)$$

and the fused image P can thus be obtained:

$$P = \exp(f). \quad (17)$$

3. Experimental results

A National Aeronautics and Space Administration SIR-C/X-SAR L-band image of a forest area is used for validating the effectiveness of the proposed method. In this area, several roads pass through the forest area. Fig.1(a) - Fig.1(d) show HH image, HV image, VV image and the span image of this area, respectively. The fusion result obtained from the proposed method is shown in Fig.1(f). From this image, one can easily find the roads in the forest area which are more clear than those in Fig.1(a) to Fig.1(d). For comparison, we also use the OPCE to enhance the contrast between forest area and non-forest area, and the result is shown in Fig.1(e). We can see that difference of the OPCE and the proposed method: only a limited number of roads are enhanced from the background in OPCE results. That is because the statistics of targets vary from region to region, OPCE tries to enhance the contrast of only two types of targets which fails in the multiple targets/multiple clutters enhancement scenarios, as the experiment shows.

To see the results more clearly, we zoom a selected sub-region, as shown in Fig.2. Two roads are marked with arrows. The first road is clear to see in the HH image but blurred in the HV image, while the second road is easy to be found in the HV image but is not distinct in the HH image. For the scattering characteristics of the two roads are different with each other, OPCE could enhance only one of them from the background (see Fig.2(c)). By taking advantage of local contrast from all the polarizations, the proposed method achieves the best contrast-preserving fusion result, where all the roads are easy to be found in Fig.2(d).

4. Conclusion

In this paper, we have presented a new fusion method for target enhancement in polarimetric SAR images. The basic idea is to fuse the local contrast of image from each channel to obtain an optimal contrast image. A fused image is then reconstructed from the optimal contrast image, by solving a discrete Poisson equation. The proposed method focuses its attention on enhancing local contrast between the target and its neighboring pixels and does not require prior statistical knowledge of the targets to be enhanced. The effectiveness of the proposed method is demonstrated by experimental results using polarimetric SAR data. The algorithm is applied to polarimetric SAR images in this paper, however, it can be naturally extended to general multi-channel SAR data processing, such as multi-frequency and etc.

Acknowledgment

This work was supported by the National Important Fundamental Research Plan of China (2001CB309401) and by the Fundamental Research Foundation of Tsinghua University.

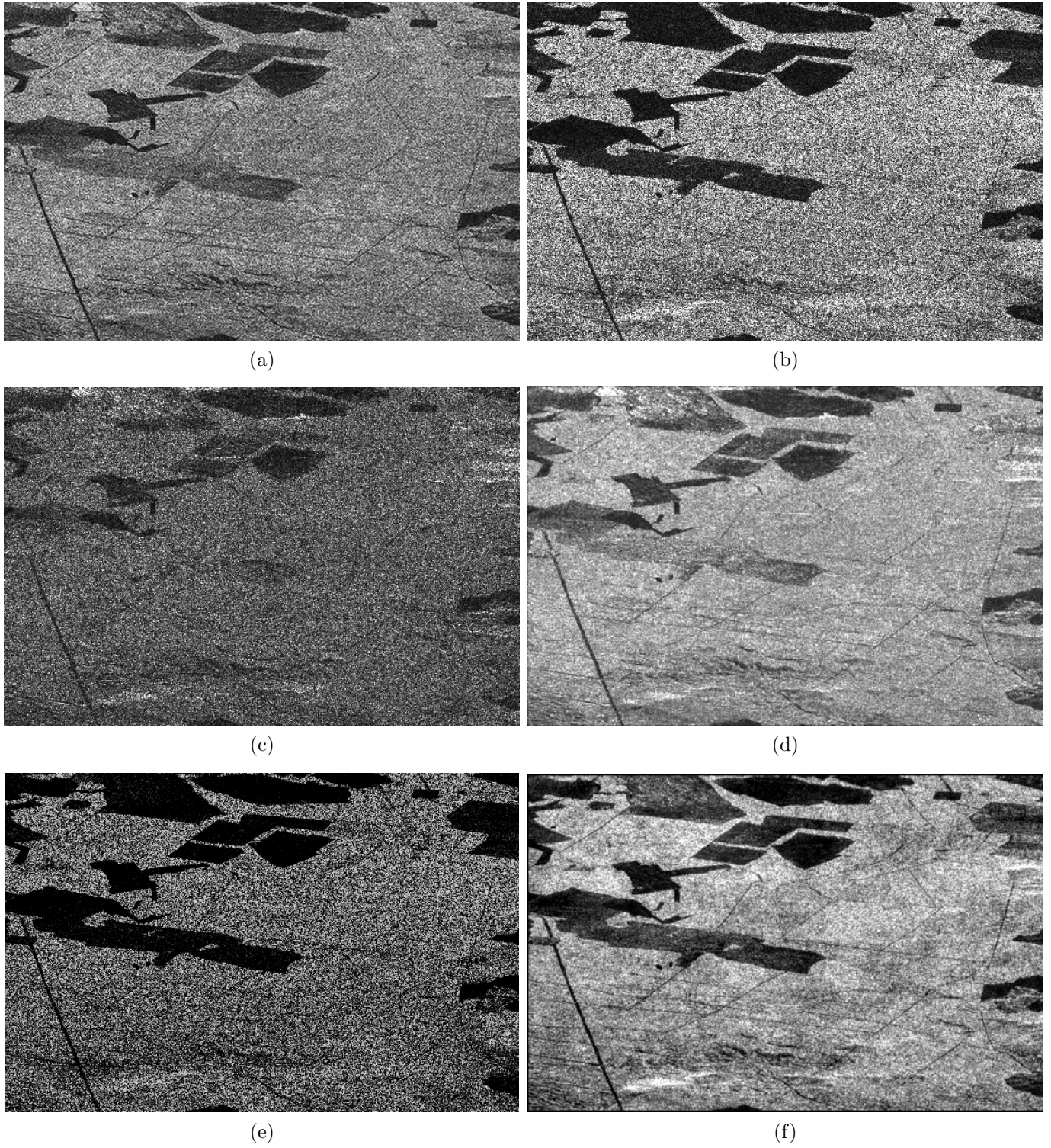


Figure 1: Experimental results.(a) The HH image.(b)The HV image.(c) The VV image. (d) The span image. (e) Result obtained by OPCE. (f) Result from the proposed method.

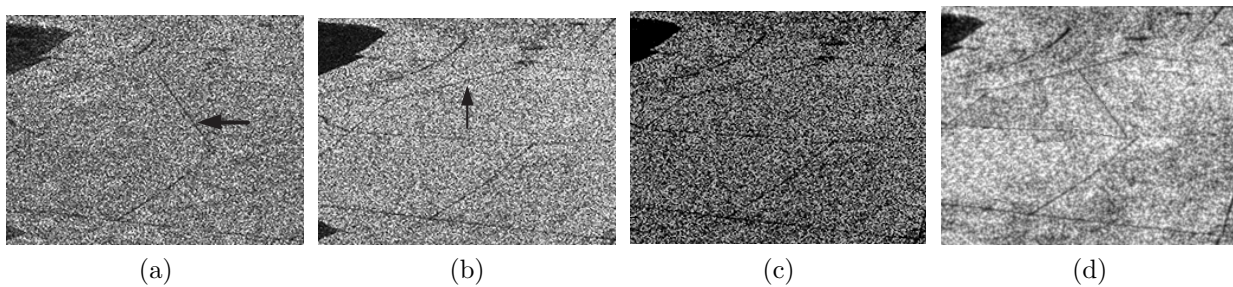


Figure 2: Results from a selected region of the area. (a) The HH image .(b)The HV image. (c) Result by OPCE. (d) Result by the proposed method.

REFERENCES

1. Kostinski A. B. and Boerner W.-M., "On the polarimetric contrast optimization," *IEEE Trans. Antennas Propagat.*, vol. AP-35, pp. 988-991, Aug. 1987.
2. Kostinski A. B. and Boerner W.-M., "On the polarimetric contrast optimization," *IEEE Trans. Antennas Propagat.*, vol. AP-35, pp. 988-991, Aug. 1987.
3. Mott H. and Boerner W.-M., "Polarimetric contrast enhancement coefficients for perfecting high resolution POL-SAR/SAL image feature extraction," *Proc. SPIE*, vol. 3120, pp. 106-117, July 1997.
4. Ioannidis G. A. and Hammers D. E., "Optimum antenna polarizations for target discrimination in clutter," *IEEE Trans. Antennas Propagat.*, vol. AP-27, pp. 357-363, Mar. 1979.
5. Yang J., Yamaguchi Y., Boerner W.-M., and Lin S. M., "Numerical methods for solving the optimal problem of contrast enhancement," *IEEE Trans. Geosci. Remote Sensing*, vol. 38, pp. 965-971, Mar. 2000.
6. Yang J., Dong G., Peng Y. and et al., "Generalized polarimetric contrast enhancement", *IEEE Geosci. Remote Sensing Lett.*, 2004, vol.1, no.3, pp. 171-174
7. Strikwerda J.C., "Finite difference schemes and partial differential equations", Wadsworth Publ. Co. Belmont, CA, USA, 1989

Novel Target Decomposition Method based on Polarimetric Signatures

Yilun Chen, Jian Yang

Department of Electronic Engineering, Tsinghua University
Beijing, 100084, P.R.China
chenyl@mails.tsinghua.edu.cn

Abstract—Polarimetric signatures have been used successfully to present the scattering characteristics of a wide range of target types. However, most of previous researchers tend to provide a qualitative description rather than a quantitative analysis. In this paper, we propose a mathematical framework for analyzing the polarimetric signatures. The inner product between two polarimetric signatures is first defined, which is proved to have a simple form from elements of the Kennaugh matrices. The distance measurements are then introduced to quantify the difference between two polarimetric signatures. All these parameters are shown to have a compact form which is convenient for calculation. Based on these parameters, a novel target decomposition method is proposed which divides the target into several typical scattering mechanisms. With the least square rule, the proposed decomposition method can be carried out by the constrained quadratic programming. By using polarimetric Synthetic Aperture Radar (SAR) data, we demonstrate that the signature based decomposition method's ability to reflect the target's scattering mechanism, such as the components of single- and double-bounce, which can be employed for weak target detection.

1. Introduction

For target detection and target recognition in radar polarimetry, an important problem is how to analyze characteristics of a radar target. According to the features of some typical targets, Huynen [3] proposed a set of parameters for describing the symmetry, structure, torsion and helicity of a target. Krogager [4] decomposed a target into three components corresponding to a sphere, a diplane and a helix. Cloude and Pottier [5, 6] introduced the concept of entropy for target decomposition and classification. Yang et al. extracted characteristics of a target based on the similarity parameter between two scattering matrices, which is convenient for analyzing some characteristics of a target. In this paper, a new target decomposition method is proposed based on the analysis of target's polarimetric signatures.

Polarimetric signatures, first introduced by van Zyl [1], are an effective way to characterize the polarization properties of microwave backscatter. These signatures have been used successfully in the past to present the scattering characteristics of a wide range of target types [2]. The signatures are significant because they utilize full amplitude and phase information from targets, which display backscattered intensity as a function of the polarization state of the backscattered TEM wave. The concept of a polarization ellipse is useful to provide a geometric interpretation of the polarization state of each point in the signature. This ellipse may be described in terms of two angles $[\chi, \psi]$: the angle χ gives the ellipticity, or "fullness" of the scatter, while ψ gives the orientation with respect to the horizontal.

For the col-pol case, the polarimetric signature $P(\chi, \psi)$ is determined for any arbitrary polarization state by calculating the Kennaugh matrix $[K]$ and the transmit-receive polarization vectors

$$P(\chi, \psi) = \mathbf{g}^T [K] \mathbf{g}, \quad (1)$$

where $\mathbf{g} = (1, \cos 2\chi \cos 2\psi, \cos 2\chi \sin 2\psi, \sin 2\chi)^T$ and T indicates the transpose. The cross-pol case may be realized by letting receive antenna ellipticity χ be the negative of the transmit antenna ellipticity and by letting the receive orientation angle ψ be orthogonal to that of the transmit antenna, i.e., $\psi + 90^\circ$.

The rest of this paper is organized as follows: in section 2, we provide quantitative descriptions to analyze the relation between two polarimetric signatures, including the concept of inner product as well as their distance measurement. Based on these descriptions, the polarimetric signature based decomposition method is proposed in section 3 and validated by using polarimetric synthetic aperture radar data in section 4. Conclusions are summarized in section 5.

2. Quantitative descriptions of two polarimetric signatures

2.1 The inner product of polarimetric signatures

Here we take the col-pol case first, the inner product between two signatures is defined as

$$\langle P_1(\chi, \psi), P_2(\chi, \psi) \rangle_c = \int_{-\pi/4}^{-\pi/4} \int_{-\pi/2}^{-\pi/2} P_1(\chi, \psi) P_2(\chi, \psi) d\chi d\psi, \quad (2)$$

where $P_1(\chi, \psi)$ and $P_2(\chi, \psi)$ denote the col-pol polarimetric signatures of target 1 and target 2, respectively; the subscript c stands for the col-pol case. By substituting eq.(1) into eq.(2), we can prove that

$$\langle P_1(\chi, \psi), P_2(\chi, \psi) \rangle_c = \mathbf{q}_1^T W_c \mathbf{q}_2. \quad (3)$$

Here \mathbf{q} is defined as the target's characteristic vector, which is composed of elements from the Kennaugh matrix $[K] = (k_{ij})_{i,j=0\dots3}$:

$$\mathbf{q} = (k_{00}, k_{01}, k_{02}, k_{03}, k_{11}, k_{12}, k_{13}, k_{22}, k_{23})^T. \quad (4)$$

The weighted matrix W_c is calculated to be

$$W_c = \begin{pmatrix} 19/16 & 0 & 0 & 0 & -9/32 & 0 & 0 & -9/32 & 0 \\ 0 & 1/2 & 0 & 0 & 0 & 0 & 0 & 0 & 0 \\ 0 & 0 & 1/2 & 0 & 0 & 0 & 0 & 0 & 0 \\ 0 & 0 & 0 & 1 & 0 & 0 & 0 & 0 & 0 \\ -9/32 & 0 & 0 & 0 & 25/128 & 0 & 0 & 19/128 & 0 \\ 0 & 0 & 0 & 0 & 0 & 3/32 & 0 & 0 & 0 \\ 0 & 0 & 0 & 0 & 0 & 0 & 1/8 & 0 & 0 \\ -9/32 & 0 & 0 & 0 & 19/128 & 0 & 0 & 25/128 & 0 \\ 0 & 0 & 0 & 0 & 0 & 0 & 0 & 0 & 1/8 \end{pmatrix} \pi^2. \quad (5)$$

From eq.(3) one can see that the defined inner product of polarimetric signatures turns to be the weighted inner product of two vectors \mathbf{q}_1 and \mathbf{q}_2 , which provides a simple form for computation.

Similar results can be obtained for cross-pol case, where we replace W_c by W_x in eq.(3)

$$W_x = \begin{pmatrix} 3/16 & 0 & 0 & 0 & -1/32 & 0 & 0 & -1/32 & 0 \\ 0 & 0 & 0 & 0 & 0 & 0 & 0 & 0 & 0 \\ 0 & 0 & 0 & 0 & 0 & 0 & 0 & 0 & 0 \\ 0 & 0 & 0 & 0 & 0 & 0 & 0 & 0 & 0 \\ -1/32 & 0 & 0 & 0 & 25/128 & 0 & 0 & 19/128 & 0 \\ 0 & 0 & 0 & 0 & 0 & 3/32 & 0 & 0 & 0 \\ 0 & 0 & 0 & 0 & 0 & 0 & 1/8 & 0 & 0 \\ -1/32 & 0 & 0 & 0 & 19/128 & 0 & 0 & 25/128 & 0 \\ 0 & 0 & 0 & 0 & 0 & 0 & 0 & 0 & 1/8 \end{pmatrix} \pi^2 \quad (6)$$

obtaining

$$\langle P_1(\chi, \psi), P_2(\chi, \psi) \rangle_x = \mathbf{q}_1^T W_x \mathbf{q}_2, \quad (7)$$

where the subscript x denotes the cross-pol case.

2.2 The distance measurement of polarimetric signatures

The distance measurement of two signatures is defined as

$$\|P_1(\chi, \psi) - P_2(\chi, \psi)\|_c = \int_{-\pi/4}^{-\pi/4} \int_{-\pi/2}^{-\pi/2} (P_1(\chi, \psi) - P_2(\chi, \psi))^2 d\chi d\psi. \quad (8)$$

Expanding the right term in eq.(8), there is

$$\|P_1(\chi, \psi) - P_2(\chi, \psi)\|_c = \langle P_1(\chi, \psi), P_1(\chi, \psi) \rangle_c - 2 \langle P_1(\chi, \psi), P_2(\chi, \psi) \rangle_c + \langle P_2(\chi, \psi), P_2(\chi, \psi) \rangle_c \quad (9)$$

Based on the results of the inner product which has been derived, we obtain the quadratic form

$$\|P_1(\chi, \psi) - P_2(\chi, \psi)\|_c = (\mathbf{q}_1 - \mathbf{q}_2)^T W_c (\mathbf{q}_1 - \mathbf{q}_2). \quad (10)$$

For the cross-pol case, we just replace W_c by W_x .

3. Polarimetric signature based target decomposition

The problem of target decomposition is to find the combination of several typical scattering mechanisms to represent a given target. For the signature value stands for the received power, one can expect a target's polarimetric signature to be decomposed as N typical scattering mechanisms with distributed scatters in a resolution cell:

$$P(\chi, \psi) = \sum_{i=1}^N a_i P_i(\chi, \psi), \quad (11)$$

where $P_i(\chi, \psi)$ denotes a specific scattering component's signature, and a_i is its corresponding coefficient which should be a non-negative value.

Due to the presence of speckle noise, we obtain the component coefficients $\{a_i\}_{i=1\dots N}$ by solving the following constrained least square problem

$$\begin{aligned} \min \quad & \|P(\chi, \psi) - \sum_{i=1}^N a_i P_i(\chi, \psi)\|_\gamma \\ \text{s.t.} \quad & a_i \geq 0, \quad i = 1\dots N, \end{aligned} \quad (12)$$

where $\gamma = c$ or x , denoting the col-pol case or the cross-pol case, respectively. Eq.(12) can be proved to be equivalent to

$$\begin{aligned} \min \quad & \frac{1}{2} \mathbf{a}^T R \mathbf{a} - \mathbf{c}^T \mathbf{a} \\ \text{s.t.} \quad & \mathbf{a} \geq 0. \end{aligned} \quad (13)$$

\mathbf{a} is the unknown vector $(a_1, a_2, \dots, a_N)^T$, R is a $N \times N$ matrix where $R_{ij} = \langle P_i(\chi, \psi), P_j(\chi, \psi) \rangle_\gamma$, and $\mathbf{c} = (c_1, c_2, \dots, c_N)^T$ is a $N \times 1$ column vector where $c_i = \langle P_i(\chi, \psi), P(\chi, \psi) \rangle_\gamma$, the subscript $\gamma = c$ or x . Eq.(13) can be solved via the standard quadratic programming method [9].

Given the coefficients $\{a_i\}_{i=1\dots N}$, we define the normalized component coefficients $\{r_i\}_{i=1\dots N}$ as

$$r_i = \frac{a_i}{\sum_{i=1}^N a_i}, \quad i = 1, \dots, N. \quad (14)$$

r_i reflects the percentage of the i th scattering component's contribution to the whole scattering mechanism. Since $\{r_i\}_{i=1\dots N}$ are normalized, they are determined by the shape of the polarimetric signature (i.e., the scattering mechanism) rather than the absolute received scattering intensity.

According to Huyen's theory, one knows that $[K^0]$ denotes the Kennaugh matrix of a target in a special position, where the orientation angle of the target equals to zero. If $[K]$ is known, $[K^0]$ can be obtained [3], therefore polarimetric signatures with zero target's orientation angle can also be obtained. In practice, we first "shift" a polarimetric signature to the zero orientation angle and then apply the proposed decomposition method. In this way, the decomposition results are invariable with target's orientation angle.

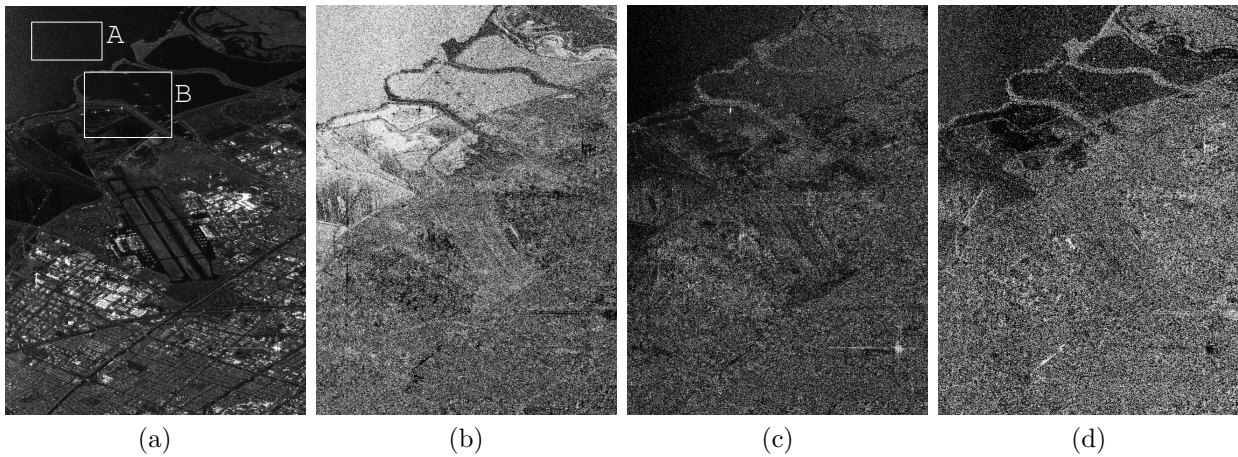


Figure 1: The span image of NASA ARC with decomposition results. (a) The span image (b) r_1 (c) r_2 (d) r_3 .

4. Experimental results

A NASA/JPL AIRSAR L-band image of the NASA ARC is used to test the proposed target decomposition method. The span image is shown in Fig.1(a). In this experiment, we use a plate, a diplane and a wire as three kinds of basic scattering mechanism. Their Kennaugh matrices are supposed to be $[K_1]$, $[K_2]$ and $[K_3]$, respectively, where

$$[K_1] = \begin{pmatrix} 1 & & & \\ & 1 & & \\ & & 1 & \\ & & & -1 \end{pmatrix}, \quad [K_2] = \begin{pmatrix} 1 & & & \\ & 1 & & \\ & & -1 & \\ & & & 1 \end{pmatrix}, \quad [K_3] = \begin{pmatrix} 0.5 & 0.5 & & \\ 0.5 & 0.5 & & \\ & & 0 & \\ & & & 0 \end{pmatrix}. \quad (15)$$

The Kennaugh matrix of each pixel is first pre-processed to rotate the target's orientation angle to zero and then applied with the proposed decomposition method, here we use the col-pol signatures. The normalized component results $r_1 - r_3$ are shown in Fig. 1(b) - Fig.1(d), respectively. From these figures we can find that r_1 has large value in the sea region (region A), which hints the main scattering mechanism of sea region is single-bounce. For the man-made objects, r_1 turns to be small value and r_2, r_3 begin to rise up. For instance, the linear-structured targets on the sea (region B) tend to have larger value of r_3 , i.e., the wire-like targets.

If we zoom in region B in Fig.1, we can find some linear objects, as the arrow points out (Fig.1(b)). These objects are weak scatters which are not easy to observe from the power image (Fig.3(a)), however, they are more salient from the proposed signature based decomposition results. The dark line on the sea hints the possibility of man-made objects. The picture from optical satellite of this region is also shown in Fig.3(c), where we can see that these objects do exist.

We also use other decomposition methods for comparison. The polarization entropy and alpha angle [5, 6] are shown in Fig.2(a) and Fig.2(b), respectively. Fig.2(c) and Fig.2(d) show the similarity parameter [8] of single-bounce and double-bounce. From the comparison, it can be seen that the signature based decomposition results' potential to detect weak targets.

5. Conclusion

A new target decomposition method is presented in this paper which is based on the quantitative analysis of polarimetric signatures. The inner product and the distance measurement of two signatures are defined and then shown to have a simple form for calculation. Based on these quantitative descriptions, the signature based target decomposition method is proposed, where a target's signature is divided into components from several typical targets. The normalized component coefficients can be used to reflect the scattering mechanism of the given target. Experimental results demonstrate the proposed method's potential to discover weak man-made scatters, which is an important problem for target detection.

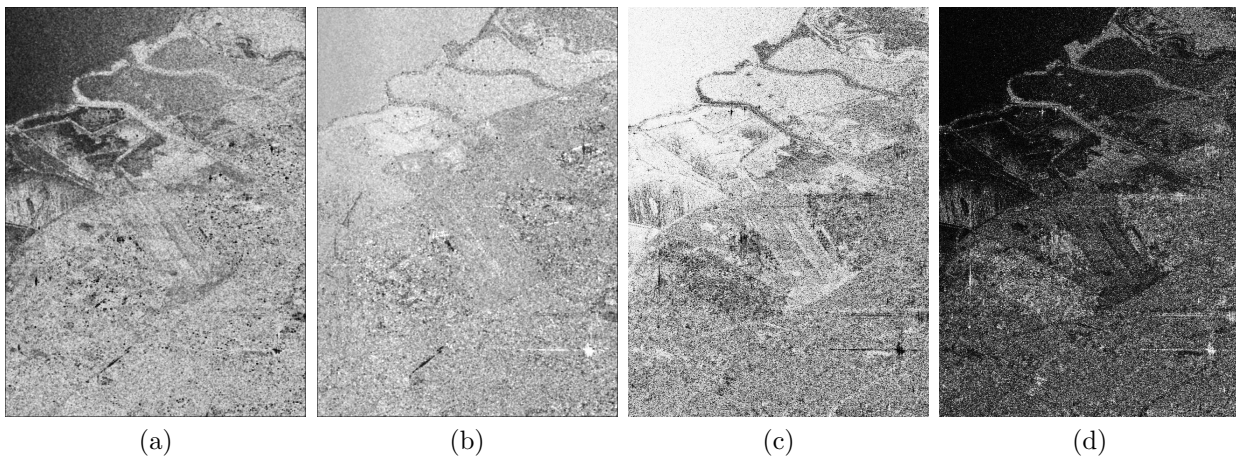


Figure 2: (a) The polarization entropy H . (b) The alpha angle α . (c) The similarity parameter of single-bounce s_1 . (d) The similarity parameter of double-bounce s_2 .

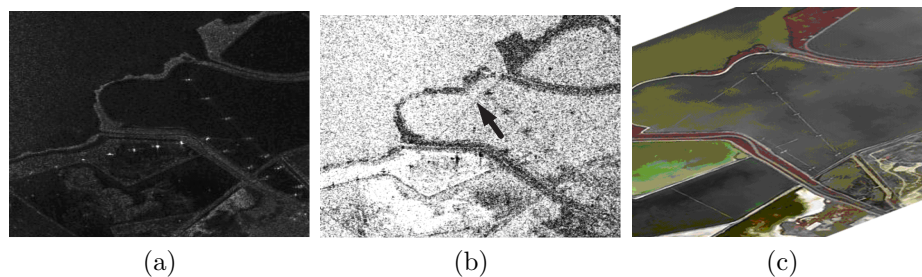


Figure 3: The decomposition results of weak targets. (a) The span image. (b) The decomposition result r_1 . (c) The ground truth (optical image from satellite).

Acknowledgment

This work was supported by the National Important Fundamental Research Plan of China (2001CB309401) and by the Fundamental Research Foundation of Tsinghua University.

REFERENCES

1. Van Zyl J. J. , "On the importance of polarization in radar scattering problems", Ph.D. dissertation, California Institute of Technology, Pasadena, 1985.
2. Evans D. L., Farr T. G., Van Zyl J. J. and Zebker H. A., "Radar polarimetry: Analysis tools and applications", IEEE Transaction on Geoscience and Remote Sensing, vol. 26, pp. 774-789, 1988.
3. Huynen J. R., "Phenomenological Theory of Radar Targets", Ph. D. Dissertation, 1970
4. Krogager E., "A New Decomposition of the Radar Target Scattering Matrix", Electron. Lett., 1990, 26(18): 1525-1526
5. Cloude S. R., Pottier E., "An entropy based classification scheme for land applications of polarimetric SAR", IEEE Tans. on Geoscience and Remote Sensing, 1997, 35(1): 68-78
6. Cloude S. R., Pottier E., "A Review of Target Decomposition Theorems in Radar Polarimetry", IEEE Trans. Geosci. Remote Sensing, 1996, 34(2): 498-518
7. Freeman A., Durden S. L., "A Three-Component Scattering Model for Polarimetric SAR Data", IEEE Trans. Geosci. Remote Sensing, 1998, 36(3): 963-973
8. Yang J., Peng Y. N. and et al., "Similarity between two scattering matrices", IEE Electron. Lett. 2001, vol.37, no.3, pp. 193-194.
9. Coleman T.F. and Li Y., "A Reflective Newton Method for Minimizing a Quadratic Function Subject to Bounds on some of the Variables," SIAM Journal on Optimization, Vol. 6, Number 4, pp 1040-1058, 1996.

GPR with an Electronically Steered Footprint

A. G. Yarovoy, P. J. Aubry, L. P. Ligthart

International Research Centre for Telecom and Radar
Delft University of Technology, the Netherlands

M. Tanigawa, A.-J. Boonstra,

W. van Cappellen, H. J. Boer
ASTRON, the Netherlands

Abstract –To investigate the possibilities of electronic steering of an antenna footprint in the near field, an array-based GPR has been built. The antenna system of this GPR consists of a single transmit antenna and 6 receive ones. For the transmit antenna a Vivaldi antenna has been used, while shielded loop antennas have been used as receives one. The antenna array has been optimized to provide high-resolution images of the shallow subsurface. Footprint steering has been implemented in the digital signal processing via true time delay of the received signals. The performance of the radar has been investigated experimentally. Electrical scanning along the array has been achieved, and 2D localization of buried objects without mechanical scanning has been demonstrated.

1. Introduction

Ground Penetrating Radar (GPR) is a useful tool for detection of all kinds of electrical inhomogeneities in the ground, and is widely used in geological, geotechnical, archeological and forensic investigations [1]. The exact localization of detected inhomogeneities and their characterization requires mechanical 2D scanning of the area under investigation with GPR and off-line processing of the acquired data (see e.g. [2]). This state-of-the-art procedure can be improved by replacing the mechanical scanning over the area by an electrical scanning of the subsurface, similarly to far-field scanning in phased arrays. The principal difference between the conventional phase-array approach and GPR lies in a need to focus and steer not a far-field radiation pattern but a near-field footprint.

To investigate the possibilities of electronic steering of the antenna footprint in the near-field we have built a proof-of-principle demonstrator, which includes an antenna array and RF electronics. To demonstrate the electronic footprint steering we built a linear array of receive antennas. Such an array together with a dedicated signal processing implemented via a true time delay should result in 1D footprint steering. Object localization in the second dimension (e.g., depth) is realized via short down-range resolution of the transmitted signal. As for archeological applications and utility detection penetration up to 1m into the ground should be combined with a reasonably high down-and cross-range resolution, we have selected the operational bandwidth of the system between 500MHz and 3GHz. This demonstrator is described in the current paper. The antenna system is described in Chapter 2, while the footprint steering algorithm is described in Chapter 3. The first experimental results are described in Chapter 4.

2. Antenna Array Design

Based on previous experience of IRCTR with GPP antenna systems [3-4] we have developed and manufactured an antenna system, which consists of a transmit antenna and a linear array of receive ones. For the transmit antenna we have selected the Vivaldi antenna, previously developed for radioastronomic application, and we have built the linear array from 6 shielded loop antennas [5] (Figure 1). To mount the antenna system on the scanner, a special junction between the transmit antenna and the vertical axis of the scanner has been made.

The transmit antenna has been fed by a step generator with a rise time of about 100ps. The spectrum of the transmitted pulse as it was measured by a probe buried at the depth of 17cm [6] is shown in Figure 2. The dip in the spectrum at approximately 500MHz is due to the balun of the transmit antenna, while the dip around 3GHz is due to a resonance in the probe. The bandwidth of the probing signal at -10dB level starts at approximately 600MHz and stops as 2.5GHz. At the higher frequencies the probing signal spectrum monotonically decreases until 5GHz.

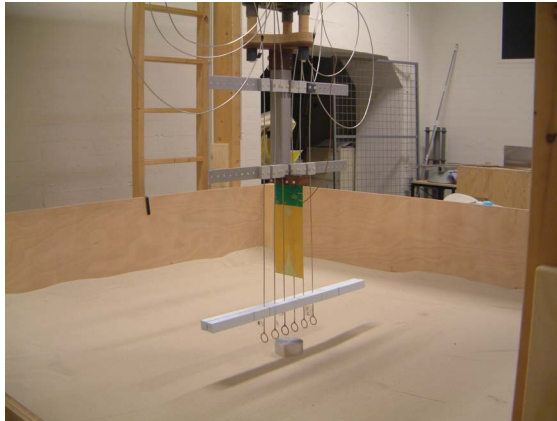


Figure 1: Photo of the developed antenna array.

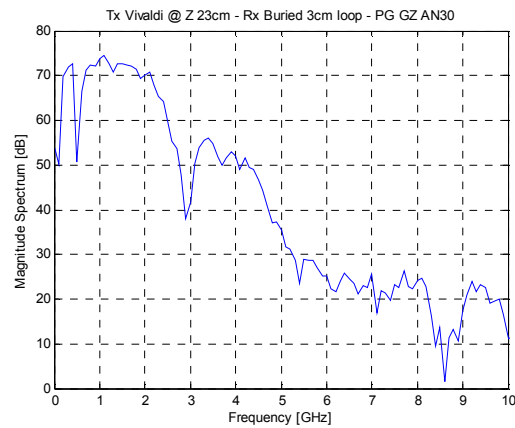


Figure 2: Spectrum of the probing signal in the ground.

The peak-to-peak footprint of the transmit antenna in the ground is shown in Figure 3. On -10dB level it measures 1m in E-plane by 1.2m in H-plane. Within this footprint we can demonstrate the electronic footprint steering of the receive array. The footprints of the elements of the receive antenna array have been also measured for different array elevations above the ground. The footprint of a single receive antenna is shown in Figure 4.

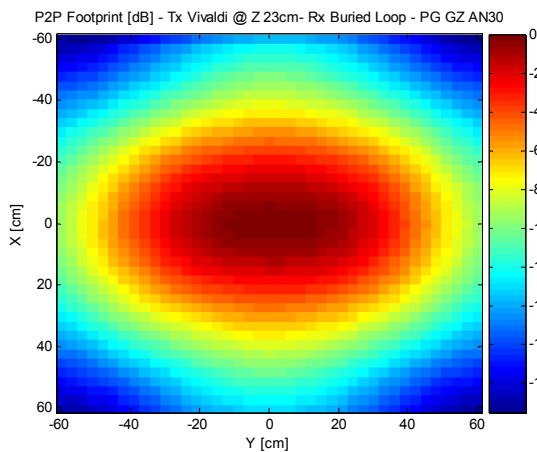


Figure 3: Peak-to-peak footprint of the transmit antenna. Signal magnitude is shown in dB.

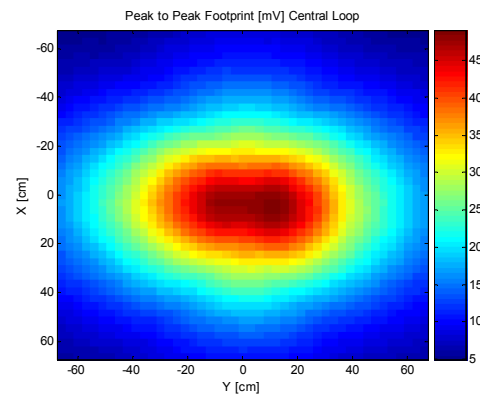


Figure 4: Peak-to-peak footprint of a single receive antenna. Signal magnitude is shown in linear scale.

To determine the optimal separation between the receive antennas the array of 6 shielded loop antennas with a diameter of 3.41cm has been simulated. From this simulation it has been found that the coupling between loops has a narrow-band nature and results in a sharp peak of the loop sensitivity. The frequency at which this peak happens depends on the loop separation. For a loop separation of 5cm, the peak takes place at around 3.7GHz (see Figure 5). As, at this frequency, the spectral content of the transmitted pulse is of about 20dB lower than in the maximum, the mutual coupling between the loops cannot cause substantial impact of the receive signal. So the distance between the loop antennas has been selected to be 5cm, resulting in the total length of the array of 25cm.

To cover the necessary bandwidth we use in the radar a step generator with a rise time of about 100ps. To acquire the data from the terminals of the receive antennas we use a seven-channel signal conditioner and an eight-channel sampling converter (built by GeoZondas Ltd., Lithuania). The receiver chain has an analog

bandwidth from 300MHz up to 6GHz and a linear dynamic range of 69dB (with averaging over 128 samples). The sampling converter operates with the sampling rate of 500kHz per channel. The observation time window can be varied from 32ps till 20ns with a number of acquisition points available from 16 till 4096. The large flexibility in the duration of the observation time window and the sampling time allows us to adjust the system to different ground types and data acquisition scenarios. A very important feature of the sampling converter is its high measurement accuracy. The maximal error in the amplitude scale and the time scale linearity of the sampling converter is of about 1%.

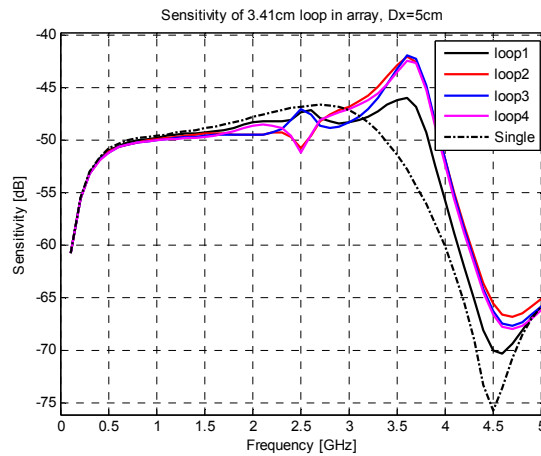


Figure 5: Computed sensitivity of the receive antennas within the antenna array.

3. Signal Processing

The electronic steering of the receive antenna footprint is done via true time delay of the received signals realized via digital signal processing. The propagation delay for each antenna has been calculated in the receive antenna plane based on the following equation

$$t = \frac{d_1}{v_1} + \frac{d_2}{v_2} = \frac{\sqrt{(y-L)^2 + H^2}}{v_1} + \frac{\sqrt{L^2 + D^2}}{v_2} \tag{1}$$

In (1) the speed of propagation in air and ground are designated as v_1 and v_2 ; H is elevation of the receive antenna above the ground; D is the depth of the imaging point; L is point of refraction (see Figure 6).

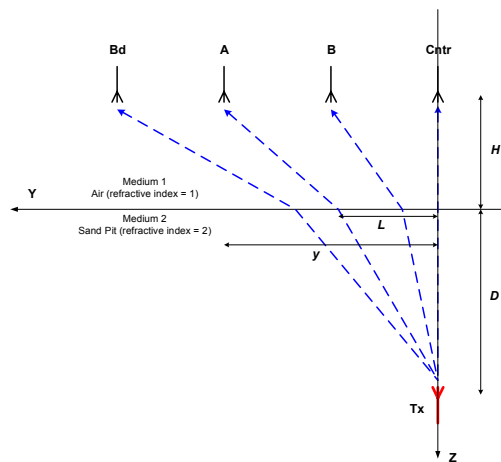


Figure 6: Receive antenna geometry and focusing point position.

4. Experimental Results

The performance of the system has been tested in IRCTR test site for GPR antennas [6]. A typical target response is shown in Figure 7. The short duration of the scattered signal proves high down-range resolution of the radar. The spectrum of the target response keeps its shape while measured by different loops in the array. This feature is very important for the application of the focusing algorithms to the measured data.

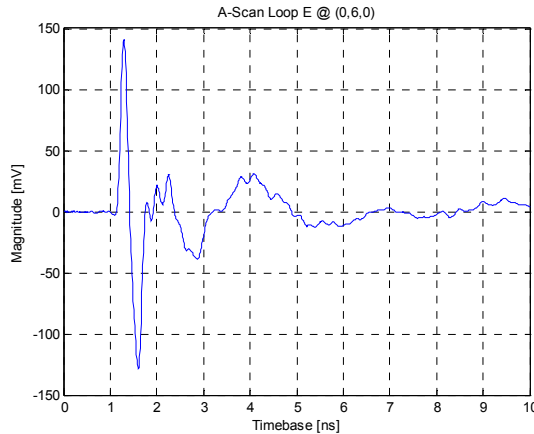
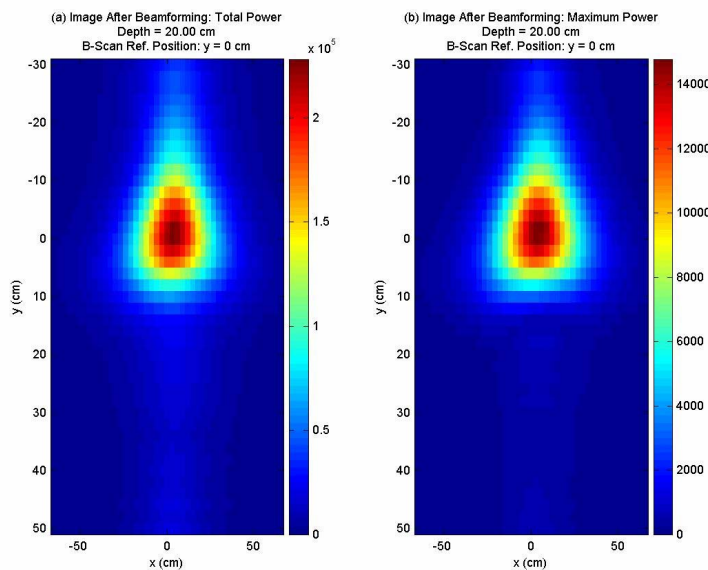


Figure 7: Typical waveform of a received signal.

Imaging of a scatterer buried 17cm beneath the ground is shown in Figure 8. The figure shown on the left side is the total energy of the signal processing output, while the figure on the right reflects the peak power of the output. The “hot spot” in the images correspond to the location from which the most amount of energy was received after processing. Due to receive array data processing along the Y-axis the size of the image in this direction is considerably smaller than along the X-axis, where no focusing has been implemented. At the later stage a migration algorithm can be implemented along this direction as well. The asymmetry of the image along the Y-axis can be explained by an asymmetric position of the scatterer with respect to the transmit antenna.



gpr_4x_bproc_ref_h_13_bscan_23_image_track_23_z_16.jpg

Figure 7: Output of the focusing procedure at the depth of 20cm.

5. Conclusions

We have developed a proof-of-principle phased-array antenna system for GPR. This includes both hardware and dedicated software for footprint steering. The hardware consists of an antenna array and RF electronics. The antenna array consists of a single transmit antenna and 6 receive ones. For the transmit antenna a Vivaldi antenna has been used, while shielded loop antennas have been used as receive ones. The antenna array has been optimized to provide high-resolution images of the shallow subsurface. The RF electronics block consists of a pulse generator, signal conditioner and 8 channels stroboscopic receiver.

Via processing based on a true time delay realized in digital processing, we have demonstrated both the focusing of the energy radiated by the array and the shift of the footprint by applying a progressive time delay to the received signals. Combination of the footprint steering in the array plane and high down-range resolution due to short duration of the probing pulse results in 2D localization of buried objects without mechanical scanning.

Acknowledgment

The authors would like to thank Dr. B. Levitas from GeoZondas Ltd. for fruitful cooperation and help during the development of the radar electronics and J.H. Zijderfeld, P. Hakkaart, M. v.d. Wel and J. Idserda for their technical assistance during antenna measurements, system assembling and testing.

This research is supported by SenterNovem within the framework of the project "Phased Array Grondradar".

REFERENCES

- [1] Daniels, D. J., *Ground-Penetrating Radar*, 2nd Edition, IEE-UK, 2004.
- [2] Zarkhidze, A, Lemenager, E. , "Case study – use of 3D GPR technologies for utility mapping in Paris", *Proceedings of the Tenth International Conference on Ground Penetrating Radar*, Delft, The Netherlands, vol. 1, 375-378, 2004.
- [3] Yarovoy, A.G., et al., "Ground penetrating impulse radar for detection of small and shallow-buried objects," *IGARSS'99 Proceedings*, Hamburg, Germany, vol.5, 2468-2470, 1999.
- [4] Yarovoy, A.G., Ligthart, L.P., Schukin, A., and Kaploun, I., "Polarimetric Video Impulse Radar for Landmine Detection," *Subsurface Sensing Technologies and Applications*, vol.3, no.4, 271-293, 2002.
- [5] Yarovoy, A.G., de Jongh, R.V., and Ligthart, L.P., "Ultra-wideband Sensor for Electromagnetic Field Measurements in Time Domain," *Electronics Letters*, vol. 36, no. 20, 1679-1680, 2000.
- [6] Yarovoy, A.G., "Comprehensive Experimental Analysis of GPR Antennas," *Proceedings of the Tenth International Conference on Ground Penetrating Radar*, Delft, The Netherlands, vol. 1, 153-156, 2004.

Design, Implementation and Calibration of Low Cost 1-2 GHz Stepped Frequency GPR for Metal Object Detection Under the Ground

Joko Suryana AB Suksmono Sugihartono A Kurniawan Kenji Tanaka K Igarashi Mitsuyoshi Iida
 STEI ITB, Indonesia NICT Japan ARIB Japan
 e-mail: joko@ltrgm.ee.itb.ac.id

Abstract— Stepped Frequency Ground Penetrating Radar (SFGPR) is a promising alternative technique for realizing the GPR transceiver which has more features than Pulse GPR technique. Moreover, with the decreasing of RF component costs in the market, the realization of GPR equipment would be cheaper than ten years ago. In this paper, we will describe the design and realization steps of 1 – 2 GHz SFGPR transceiver for metal detection under the ground. Before using prototyped GPR for detecting the metal under the ground, several calibration processes must be performed, namely phase calibration and monocycle pulse waveform calibration. After completing the calibrations, this prototyped GPR would be ready for detecting the hidden object such as a metal plate 5 cm under the ground in our small test range size 25 cm x 75 cm x 10 cm. From the calibration and detection results, we concluded that the prototyped SFGPR passed the technical specifications of the design and could perform the metal detection under the ground with high SNR.

1. Introduction

Stepped frequency radar (SFR) is a microwave imaging technique that can be used as an alternative imaging technique with impulse radar (IR) to get scattering parameter data in wideband time domain [1] [3]. By using the Inverse Fourier Transform, SFR data consist of magnitude and phase can be changed to synthetic time domain pulse. Therefore, by combining time domain imaging technique with data collection via SFR, a B-scan image from objects buried underground can be well-visualized. SFR is used not only for underground measurement (GPR), it can also be applied for non-destructive evaluation to detect the road pavements and imperfect structure in building , bridges, tunnels, highway and runway. Beside that, SFR is developed to detect human existence in a building or in beneath, even in medical care, SFR is developed to monitor heartbeat and lung-breathe without using electrodes touching to the patients' body like what the usual conventional technique applies. The advantages of SFR are its higher SNR comparing to IR, so that it has better accuracy and stability, and its simplicity to implement the receiver tool since it does not need high sampling rate [1] [3]. The disadvantage of SFR is its longer time needed for data collection comparing to IR. But with the electronic technological advances, this problem can be solved.

In this report, we will describe the *Stepped Frequency Radar* microwave imaging system for GPR (SFGPR) and other non-destructive evaluation (NDE) applications. This system consists in microwave sensors with 1 – 2 GHz working frequency, data acquisition subsystem and computer with signal processing software for target imaging. By using the Inverse Fourier Transform algorithm, SFGPR data can be changed into synthetic time domain pulse to get the intended target image. We also use the calibration procedures to eliminate distortion in synthetic pulses because of phase instability or non-linearity from transmitter, distortion by connector and transmission line, and antenna ringing. After doing the calibration procedures, SFGPR is used for single target imaging under the ground with low homogeneity to examine the real target imaging ability. From calibration and target imaging trial result, we conclude that SFGPR is able to detect objects under the ground well according to design specifications.

2. SFR Description

The working flow of SFR system can be described as follows : Signal with bandwidth B , lowest frequency f_r , and highest frequency f_t is discretized into N frequencies separated by frequency space Δf . Scanning process is done by transmitting signal with initial frequency f_r from t_0 until $t_0 + \Delta t$. At $t_0 + \Delta t$, transmitter re-transmit signal with new frequency $f_r + \Delta f$ which can be described as :

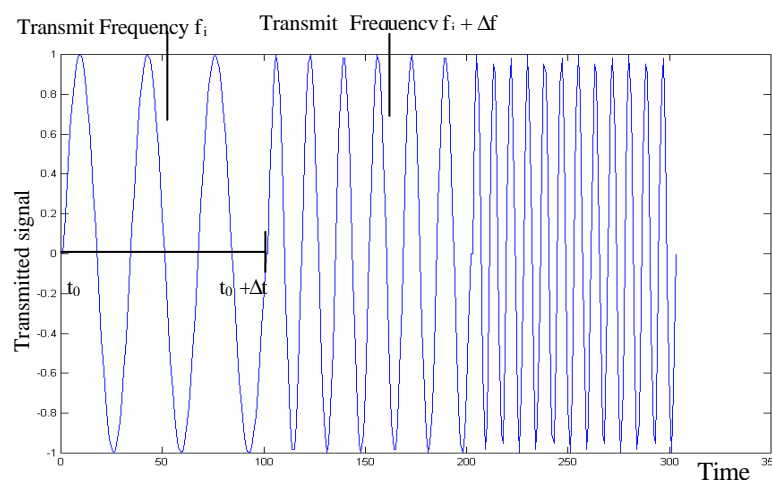


Figure 1. Stepped Frequency Radar Signal

This process continues until the highest frequency f_r is transmitted. Total time to complete the scanning process at this N frequencies is NDr . If the signal from f_r until f_t touches the linear material such as soil and plastic, the reflected signal will have the same frequency but the phase and the amplitude have changed. If SFR is designed at working frequency from 1 – 2 GHz ($f_r = 1\text{GHz}$ and $f_t = 2\text{GHz}$), we will get about 10 cm resolution, and by advanced post-processing the resolution can be enhanced into 5 cm. SFR block diagram is shown in figure 2.

Subsystems that build an SFR system are :

1. Antenna subsystem : transmit signal to the target and receive the reflected signal.
2. RF transceiver subsystem : stepped frequency signal source and detect received signal.
3. Hardware controller subsystem : hardware controlling from microwave sensor and also functions for PC communications.
4. Software controller subsystem : data acquisition and raw data storage into file text.
5. Software imaging subsystem : application to visualize target imaging data.

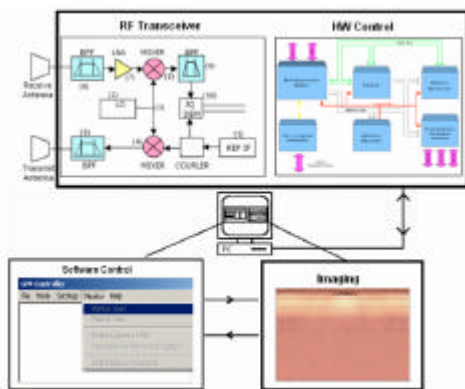


Figure 2. SFR Block Diagram



Figure 3. 1 – 2 GHz Circular end Bowtie Antenna

2.1. Antenna Subsystem

In this experiment, we will implement circular-end bowtie antenna with 70° flare angle, as shown in figure 3. Bowtie antenna is included in 2D planar bicone antenna family [2] which has very wide working frequency bandwidth. The reason for choosing bowtie antenna in this SFR system is beside its working frequency bandwidth characteristics, also because of the simplicity in its implementation. In bowtie antenna design and implementation, some parameters that influence the antenna performance are :

1. Physical dimension : effective length and width of the antenna
2. Flare angle of antenna arm
3. Antenna edge profile

For SFR with 1 – 2 GHz working frequency, bowtie antenna with circular end profile, 70° flare angle and 25 cm effective length has fulfilled the specifications.

2.2. RF Transceiver Subsystem

RF transceiver diagram block which is implemented in this SFR research can be described in figure 4 :

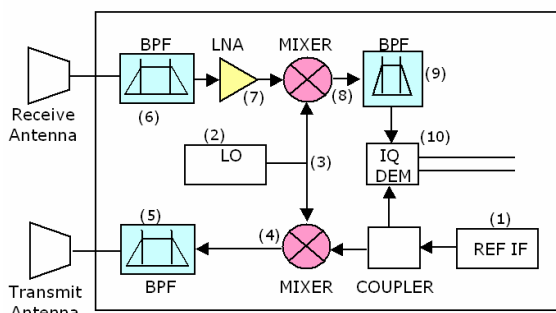


Figure 4. RF Transceiver Subsystem



Figure 5. The Implemented Transceiver Prototype

This RF transceiver consists of transmitter which generates stepped sinusoidal signal at 1 - 2 GHz frequency and receiver which detects quadrature of reflected signal. The working flow of this subsystem can be described as follows : IF signal source for reference is generated by RIF (1) and through coupler went to mixer (4) to be mixed with stepped-frequency local oscillator (LO) (2). This reference IF signal is also used by IQ demodulator (10) to get information on reflected signal amplitude and phase. The mixing result of RIF signal with LO by bandpass filter (5) mixer (4) is then sent to the target through transmitter antenna. After reflected by target, receiving antenna receives reflected signal then bandpass filtered (6) and amplified by an LNA (7) to be mixed with local oscillator (LO) signal. Before entering IQ demodulator, signal coming out from mixer (8) is re-filtered by IF bandpass filter (9) and then fed to IQ modulator (10) to get information on amplitude and phase.

2.3. IQ Demodulation

The performance of SFR depends on some important factors, such as discrete frequency generation stability, nondispersive antenna system, and IQ demodulation reliability. IQ demodulation relates to the information extraction of amplitude and phase of reflected signal from the transmitting signal. Herewith, we will describe mathematically the principles of IQ demodulation. For example, a reference IF signal RIF with unit amplitude and zero phase angle follows the equation :

$$RIF(t) = \cos (\omega_{RIF} t) \tag{1}$$

Then, we assume the IF receiving reflected signal is :

$$IF(t) = A \cos (\omega_{IF} t + \theta) \tag{2}$$

where : $\omega_{IF} = \omega_{RIF} = \omega$

By using trigonometry :

$$\cos A . \cos B = \frac{1}{2} \cos (A+B) + \frac{1}{2} \cos (A-B) \tag{3}$$

The mixture between RIF and IF signal will result in equation :

$$\cos (\omega t) . A \cos (\omega t + \theta) = \frac{1}{2} A \cos (2 \omega + \theta) + \frac{1}{2} A \cos (\theta) \tag{4}$$

by doing lowpass filtering, we will get :

$$I = \frac{1}{2} A \cos (\theta) \tag{5}$$

Meanwhile, if the mixture is between IF signal and 90° phase-shifted RIF signal, by using the same method we will get the signal equation :

$$Q = \frac{1}{2} A \sin (\theta). \tag{6}$$

Then, to get the value of A and θ , we have to calculate using the equation :

$$A = \sqrt{I^2 + Q^2} \text{ dan } \theta = \tan^{-1} (Q/I) \tag{7}$$

2.4. Hardware Controlling Subsystem

To do the stepped-frequency measurement, we need RF transceiver controlling to control the sequence and frequency distance from the generated sinusoidal signals. Beside that, hardware control is also needed to coordinate the IQ data recording as an output of RF transceiver to the PC. In this research, microcontroller mini board is using the ADC (*Analog to Digital Converter*) dan DAC (*Digital to Analog Converter*) [6] as shown in figure 6.

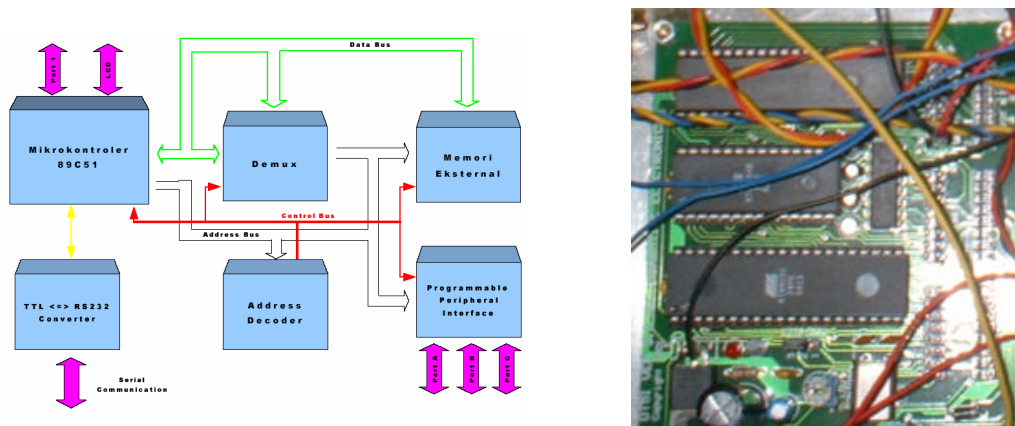


Figure 6. Block diagram and Photograph of microcontroller mini board to control SFGPR hardware [5]

To generate stepped frequency signal, mikrocontroller board is programmed to generate numerical sawtooth signal at every VCO (Voltage Contolled Oscillator) . Figure 7 shows part of listing program to control SFGPR :

4.1. Signal Processing for SFGPR Data

Signal processing on raw data from conventional GPR has 2 main objectives : first, signal processing is applied to eliminate disturbing signals coming from clutter, and second, signal processing is needed to improve S/N in image data to enable human operator interpretation.

4.2. Clutter Disturbance Elimination

Clutter can be defined as scattered and reflected signal from non-target objects that appear at the same time window and with similar spectral characteristics with the target. In GPR application, clutter can be reflections coming from air-ground interface, repeated reflection between antenna and the surface, sidelobe reflection, and discontinuities coming from stones or grasses.

4.3. S/N Data Image Enhancement

Noise can be defined as disturbance signal which has different spectral characteristics than target reflection or clutter. Noise will reduce image quality that makes visual interpretation difficult. There are some noise reducing techniques known, namely : focusing technique to improve disturbance coming from antenna beamwidth, and filtering technique such as median filter or wiener filter [4] to reduce AWGN. Figure 10 shows A-scan images of 45 signals, where each signals is time domain signal, results from Inverse Fourier Transformation from SFGPR raw data. Figure 10 (upper) shows A-scan signal set before eliminating clutter, while figure 10 (below) shows A-scan signal set after eliminating clutter.

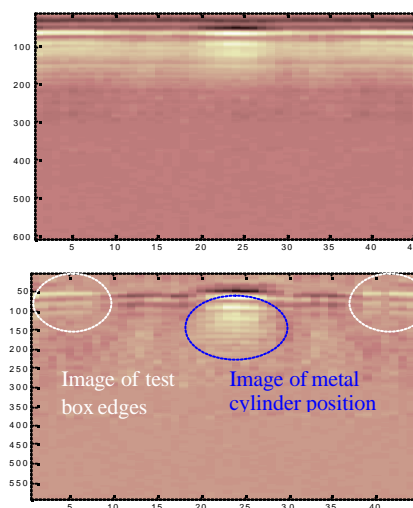
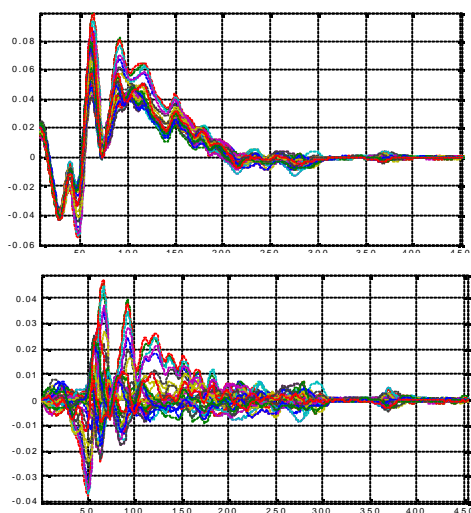


Figure 10. A-scan signal for 45 sweeping positions (upper : before eliminating clutter, lower: after eliminating clutter using software)

Figure 11. B-scan image from metal cylinder imaging which was buried in a test box at 5 cm depth (upper : before eliminating clutter lower : after eliminating clutter using software)

5. Conclusion

The result of calibration and metal cylinder detection test shows that the implemented SFGPR prototype works well as the intended specifications. This shows that the implemented SFGPR hardware is able to generate quite stable frequency source and the prototype is able to IQ demodulate the transmitting signal with echo signal well. Raw data processing software also has important role in eliminating clutter and enhancing S/N that improves the performance of imaging.

REFERENCES

- [1].Collins et al, "Design Construction and Testing of a Ground Penetrating Radar System for Use in Landmine Detection", Thesis, University of Manitoba, Canada, March 2002.
- [2].Balanis C A, 1997. Antenna Theory: Analysis and Design (John Wiley & Sons, New York) 950 pp.
- [3].Daniels D J, 1996. Surface penetrating radar (The Inst. Electrical Eng., London) 320 pp.
- [4].J.G. Proakis & D.G. Manolakis: Digital Signal Processing, New Jersey: Prentice Hall, 3rd edition, 1996.
- [5].ATMEL, "Manual and Data sheet of ATMEL AT89C51"
- [6].Innovative Electronics, "DT51 I2C ADDA DRIVER REV3", April 2002

A Simple Inversion Technique of Cross-Hole Data for Location of Buried Pipes

Kazunori Takahashi, and Motoyuki Sato

Center for Northeast Asian Studies, Tohoku University, Japan

Abstract – A new inversion technique to locate buried pipes has been developed. The inversion algorithm estimates the location by searching the minimum prediction error for the first arrival time. Thus, the technique is a kind of parameter optimization techniques and does not image anything, but it can indicate the location obviously. The comparison of the predictions with measurements is performed focusing on the arrival curve shape unlike conventional ray tomography. Thus, the arrival time picking does not affect the estimation, and the arrival curve can easily be selected by maximum amplitudes or thresholding, for instance. The technique can explicitly and efficiently use *a priori* information on the target in the forward modeling. Therefore, the inversion calculation can be done very quickly and is stable. The inversion technique is verified with field data for a metallic pipe. The inversion result can estimate the location successfully. Therefore, the inversion technique is suitable for this purpose and to use on site. It can provide useful information also to non-specialists of radar and geological technologies who are involved with civil engineering.

1. Introduction

GPR operated on the ground surface is commonly used to locate buried pipes and subsurface cavities non-destructively, because it can achieve high resolution and possesses visualization capabilities. Surface GPR, however, cannot be used for deeply buried pipes because of strong attenuation of the electromagnetic wave in the subsurface medium. For such cases, borehole radar is generally used because its antennas can approach to a target via drilled boreholes. Nevertheless, the antennas can only be scanned along the wells, and range resolution (horizontal resolution for vertical boreholes) yields relatively poor. One can achieve higher resolution by using higher frequencies at the expense of the detectable range. Thus, localization of pipes and other objects with high accuracy is still a challenging problem.

Numerous imaging, tomography, and inversion techniques have been studied for borehole measurements using two or more wells, i.e., cross-hole measurements. Most of these techniques are computationally expensive to calculate very complex scattering mechanisms in order to achieve accurate results. Moreover, they do not directly and efficiently use *a priori* information and number of parameters to be estimated is too much, yielding that they are unstable and requires much time to compute.

A new inversion technique has been developed to locate deeply buried pipes precisely by borehole radar measurements [1], [2]. The inversion is based on a parameter optimization technique, thus it only estimates the location of the targets and it does not image anything unlike conventional inversion and tomographic techniques. Moreover, the inversion can implement *a priori* information on the target, yielding stable and fast computation.

This paper describes the inversion algorithm and demonstrates it with field datasets to show the performance and effectiveness.

2. Inversion Algorithm

2.1 Procedure

In most cases, some information on a target is available prior to measurements and investigations, for example, the target material and the dimension. Moreover, a separation of boreholes and properties of subsurface medium must be known when the boreholes are drilled. The inversion technique firstly assumes the information available. For a metallic pipe, the cross section of the pipe may be a circle, thus the approximated first arrival times can be calculated very easily, for example by geometrical optics for a homogeneous subsurface space, when a pipe location is fixed at a particular location. The approximated arrival time varies for various transmitter and receiver positions and the pipe location. The inversion technique compares the approximated arrival times with times selected from measured datasets, and the comparison is repeatedly performed for all the possible locations of the pipe, i.e., the technique uses a parametric approach. Then the technique determines the pipe location as the location that yields arrival

times most similar to those of measured data. To compare the approximated with selected arrival times, a new scheme is proposed to avoid errors of arrival time pickings from measured data.

2.2 Comparison of Arrival Time Curves

It is very easy to select a time $t_{meas}(z_t, z_r)$ at the maximum amplitude in a measured time trace for a transmitter at a depth of z_t and a receiver at z_r for instance. The selected time by this manner is no longer true for the first arrival. However, it can be assumed that the curves connecting the times are parallel to the true first arrival curve, meaning the medium has less anisotropy and dispersion, and the directivity effect of an antenna is small. This situation is illustrated in Figure 1. The similarity between the measured maximum-amplitude curve $t_{meas}(z_t, z_r)$ and the approximated first arrival curve $t_{cal}(z, x, z_t, z_r)$ with an assumed pipe at (z, x) can be evaluated by taking an error $e(z, x, z_t)$ of the curve gradients with respect to the receiver depth z_r and the integration.

$$e(z, x, z_t) = \frac{1}{N_r} \int \left| \frac{\partial}{\partial z_r} t_{meas}(z_t, z_r) - \frac{\partial}{\partial z_r} t_{cal}(z, x, z_t, z_r) \right| dz_r \quad (1)$$

where N_r is the number of receivers for a transmitter. The error can be calculated for each transmitter depth. The lower error indicates higher similarity between the two curves, meaning the higher probability of the object location. Then a total error for a series of all transmitter depths $e_{total}(z, x)$ is defined by integrating $e(z, x, z_t)$ along the transmitter depth z_t as

$$e_{total}(z, x) = \frac{1}{N_t} \int e(z, x, z_t) dz_t \quad (2)$$

where N_t is the number of transmitters. In the distribution of the $e_{total}(z, x)$, a low value region has a high probability of the pipe location.

3. Experimental Result

Field measurements were carried out in an urban area in the city of Sendai, Japan. The target is a metallic pipe for water supply having a diameter of 0.9 m. It is known prior to the cross-hole fan measurements that the pipe is buried about 12 m. Two boreholes were drilled with a separation of 3.3 m on both sides of the pipe as shown in Figure 2. The measurements were conducted using a borehole radar system developed by Center for Northeast Asian Studies, Tohoku University [3]. The system is based on a vector network analyzer and is stepped-frequency radar system. A frequency range from 2 to 402 was used with dipole antennas whose length is 900 mm. The dominant frequency of the measured data is about 80 MHz, which corresponds a wavelength of 1-2 m in subsurface medium. Figure 3 shows the obtained radar profiles for the transmitter at depths of 11.0, 11.5, 12.0, 12.5, and 13.0 m and the receiver

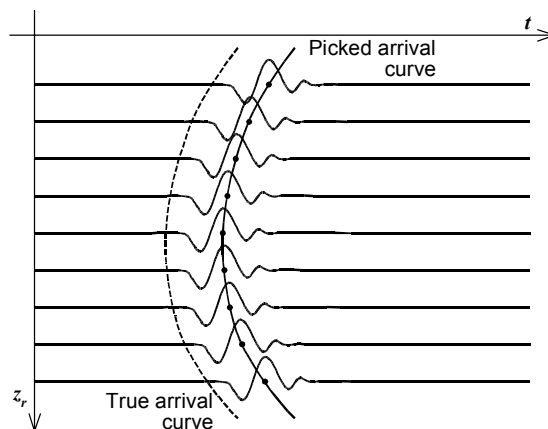


Figure 1: An example of a true arrival curve and an arrival curve selected by maximum-amplitude.

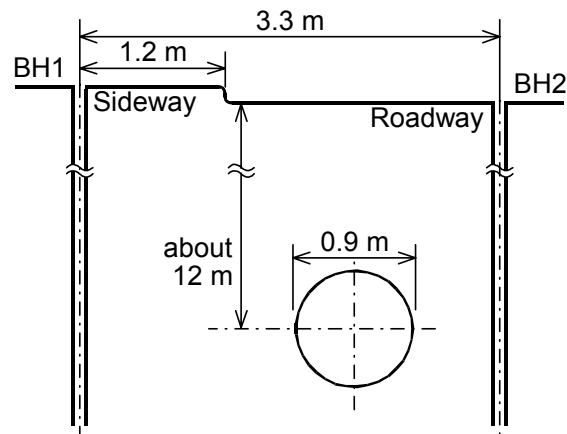


Figure 2: Configuration of the measurements in Sendai, Japan.

scanned at 10.0-14.0 m.

Since we can find discontinuities in the radar profiles, the subsurface may be layered with two kinds of media. As the forward modeling, a two-layer model shown in Figure 4 is constructed for a two-dimensional TE finite difference time domain (FDTD) method, in order to obtain approximated arrival times. The model has a layering interface at a depth of 12.5 m, and the relative permittivities are set to $25 \epsilon_0$ and $20 \epsilon_0$ for the upper and lower media, respectively. The cell size is 0.1×0.1 m, and the time step is 0.1 ns. An absorbing boundary condition (ABC) is not implemented in the model, and the calculation is terminated when a first arrival is observed. The pipe locations are assumed every 0.1 m in both horizontal and vertical directions.

For the inversion, an approximated arrival time is selected by a threshold at 40 % of maximum amplitude in a measured trace. The threshold value is determined just as it gives smooth curves. The result is shown in Figure 5. A low error region is localized and the minimum error is located at a depth of 12.4 m and 2.0 m apart from the borehole BH1. The estimated location agrees well with the known information that the pipe is close to the borehole BH2 rather than BH1.

4. Conclusion

The new inversion technique has been developed to locate buried pipes. As demonstrated in this paper, the inversion can retrieve the location of a buried pipe from field data even it has strong influences of the geological structure. It shows that the inversion is very stable and robust. Since only simple calculation is employed in this inversion, the computation requires very low costs. Moreover, the inversion explicitly indicates the location of a target unlike the conventional imaging techniques and the detailed interpretations of the results are unnecessary. The features can be rather important advantages to use onsite and to provide useful information to non-specialists. The technique can easily be applied to various targets by slightly modifying the forward modeling. Therefore, the inversion has very high usability and potential.

Acknowledgement

We acknowledge Dr. Tadao Haryu from Hokko Georesearch, Japan for providing the opportunity to carry out the field experiment in Sendai, Japan. Part of this work was supported by JSPS Grant-in-Aid for Scientific Research (S) 14102024.

References

1. Takahashi, K., and Sato, M., "Estimation of a buried pipe location by borehole radar," in *Proc. IEEE IGARSS 2005*, Seoul Korea, in DVD, 2005.
2. Takahashi, K., "Detection and localization of subsurface objects by ground penetrating radar," Ph.D. thesis, Tohoku University, Japan, 2006.
3. Takahashi, K., Liu, S., and Sato, M., "Interferometric borehole radar system," in *Proc. 9th Int. Conf. GPR*, Santa Barbara, CA USA, Proceedings of SPIE vol. 4758, pp. 19-24, 2002.

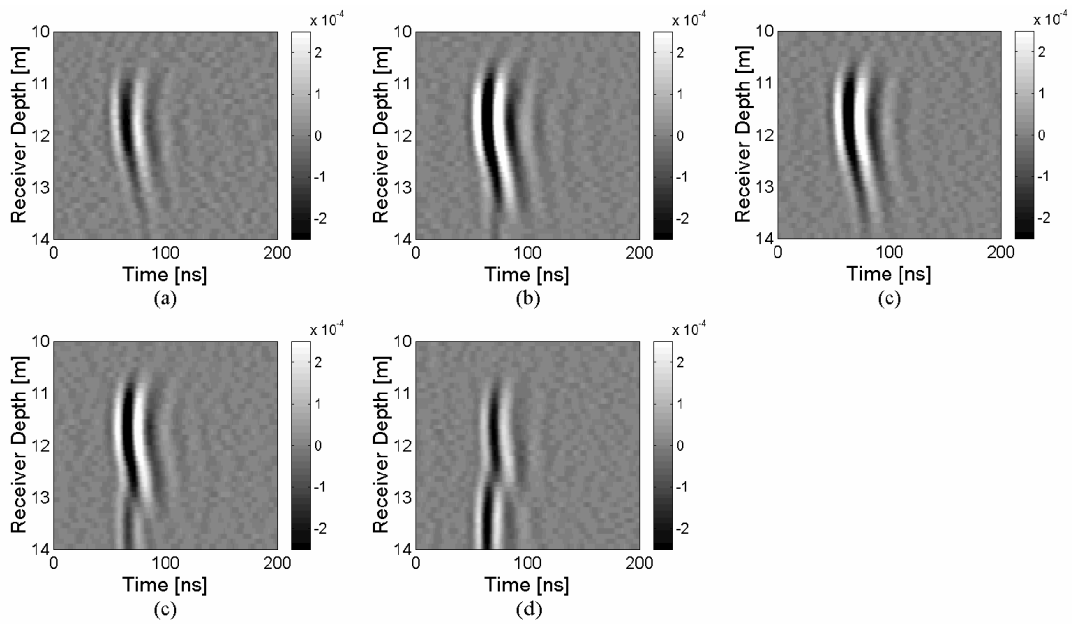


Figure 3: Radar profiles measured by the transmitter at 11.0 m (a), 11.5 m (b), 12.0 (c), 12.5 (c), and 13.0 m (d).

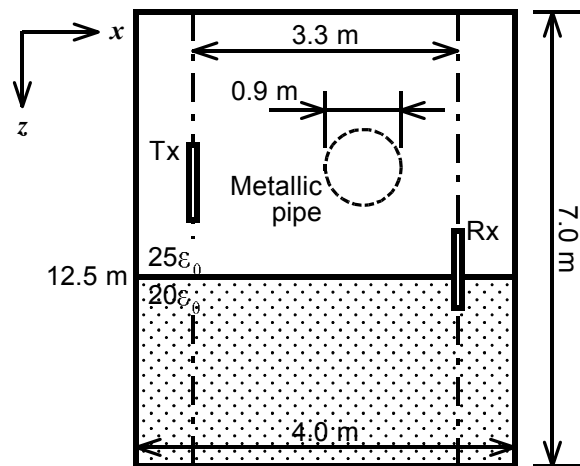


Figure 4: Model of 2D TE FDTD employed as the forward model of the inversion.

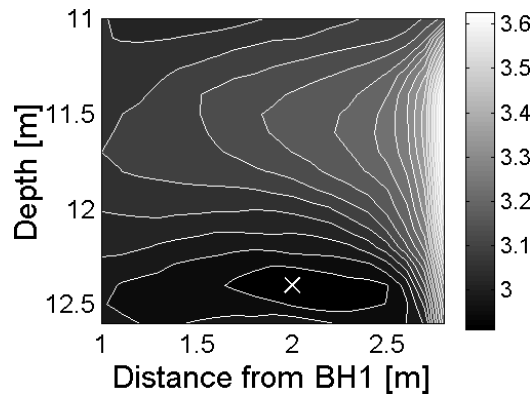


Figure 5: Total error distribution calculated for the metallic pipe. The white cross indicates the minimum error at a depth of 12.4 m and 2.0 m apart from the borehole BH1.

Construction of Rain Attenuation predictive model at FWA and Ka band Satellite Communications

R. Saotome, T. Miyazato, and S. Tamaki
University of the Ryukyus, Japan

Abstract—The technology of compensating degradation of the communication quality by rain attenuation is studied for many years. However, in the field of satellite communication, the research has been actively at Ku band. So, there are still few research examples of the rain attenuation characteristic in terrestrial communication and satellite communication at Ka band. The actual proof experiment using the 18GHz band FWA was conducted by North-South Daito island of Okinawa Prefecture from September, 2003. As a result of this experiment, we could obtain precious data sets. Furthermore, the propagation experiment using a 18GHz and 26GHz band FWA is due to be started between Tsuken island and University of the Ryukyus (about 17km) in April, 2006.

In this research we examine about the rain attenuation model based on a time series analysis technique and we do the molding of the rain attenuation characteristic in a short-term.

1. Introduction

Recently, demands for high speed and large capacity of the wireless communication have been increased. Okinawa Prefecture is the island area of subtropical climate. The islands is scattered over a large area of North, south, east and west. Therefore, there are many areas where the high-speed Internet network is not provided with basic services. In order to remedy the area, It is necessary to use the easy sub-millimeter wave band radio communications of high bandwidth called Ka band satellite communication (WIDNS: Wideband InterNetworking engineering test and Demonstration Satellite) and FWA (Fixed Wireless Access) as remedy.

However, this frequency band is weak in rain. An attenuation of radio wave by the rain is called 'Rain Attenuation'. It is very important problem for the communication using high frequency band in the subtropical region. There have been researches to find an effective technique to compensate the loss of the rain attenuation. Those researches, however, were mainly discussed for the use of the satellite communication, and there have been quite few case for the terrestrial communication. Furthermore, there is also a need for obtaining the transmission characteristics in Okinawa, where the transmission path is built mostly on the ocean in the archipelago.

In general, although a statistics approach has been a mainstream method that clarify the relationship between the rain attenuation time (disconnection time) and the cumulative time distribution of rain, it is quite difficult to apply to a short-term rain attenuation made by the typhoon or rain squall.

In this paper, to model the rain attenuation characteristic for a short-term such as rainstorm, we propose new type of method based on time-series analysis.

2. Experiment procedure

Minamidaito Island and Kitadaito Island are the detached island of Okinawa Pref. The distance of them are about 11Km. Fig.1 shows the propagation path.

The experiment has been started since October, 2003. Rain rate, Rx level and BER (Bit Error Rate) are measured in each base station in this experiment. The experiment data is shown in Fig.2. In Fig2, the data which the typhoon passes is included in this period. It is recognized that the difference was seen in rain rate by the measurement point when the heavy rain attenuation cause. Generally, when the rain attenuation exceeds 30dB, it is assumed that phenomenon such as disconnection occurs. With the latest analysis, using the part above attenuation 30dB, it draws up the model.

3. Modeling of Rain Attenuation Characteristics

As for rain attenuation problem research is advanced from the time before in satellite communications field. When designing the circuit, there is many a thing which uses the accumulation time distribution of rain rate. Mostly, accumulation time distribution of rain rate is used for communication circuit design. Communication



Figure 1: Daito islands

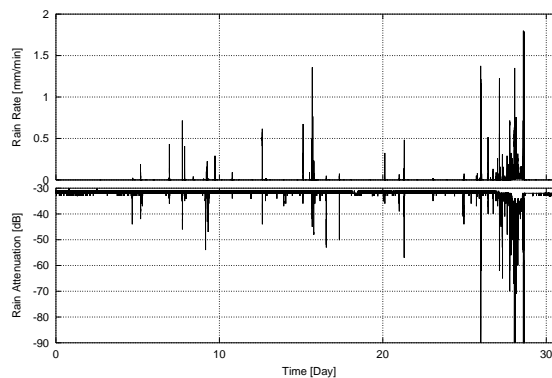


Figure 2: Rain-rate, Rain-attenuation

circuit design uses "an accumulation time distribution of rain intensity" in many cases. However, strong rain have a brief duration. In this study we investigate "Characteristics of the attenuation by especially intense Rains". Therefore, it examines concerning the technique where short duration the modeling does the characteristic of variation not only accumulation time distribution.

3.1 Statistical method

Generally, the satellite communications circuit designs that disconnection time is less than 0.01% of year at Ku band. Cumulative time distribution of rain for one year with the antenna installation position is measured. Rain-rate of 0.01% of the circuit design place is calculated from the result. The value is fitted in formula of the rain attenuation quality which is advised with ITU-R, value of cumulative time 0.01% of the rain attenuation is estimated. Fig.3 shows the cumulative time distributions of rain attenuation and rain rate. That data has displayed the north and south Daito islands and the Minamidaito island due to Meteorological Agency. When example is increased from this figure, cumulative time rate 0.01% of the Kitadaito island is rain rate 51mm/h. This value is introduced into ITU-R advice system and estimator of rain attenuation is calculated.

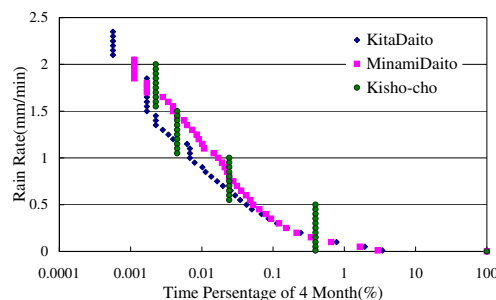


Figure 3: Cumulative time distributions of rain rate

This method, using cumulative time, estimates the rain attenuation. It becomes estimate with the long span such as some minute during 1 years. Main cause of circuit cutting is the typhoon or heavy rain. It is difficult to model a characteristics of short continuous duration. This paper presents the rain attenuation model which uses the time series model.

3.2 Proposal Method

It applies rain attenuation phenomenon making use of the time series model which is used well putting to the field of control and statistical modeling, sets.

The time series model is classified broadly into the short memory model and the long-term memory model. As time interval becomes large, the characteristics of coefficient of correlation which is while observation quickly becoming 0 is called short-term memory characteristic. Conversely, long-term memory nature is the character which cannot disregard the correlation coefficient between observation values even if a time interval becomes large.(Fig.4) In this paper, the attenuation is presumed making use of three models of the 1)ARMA model, 2)the ARMAX model, and 3)the ARFIMA model which are used generally with time series analysis.

1) and 2) are the stationary linear model and it belongs to the "short-term memory". In contrast, 3) belongs to the "long-term memory". That recently is observed in various fields such as traffic and economic issue and weather phenomenon of Internet.

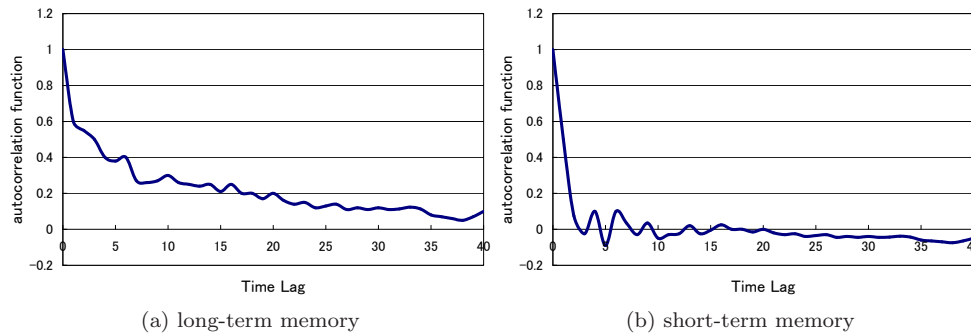


Figure 4: autocorrelation function of long-term and short-term memory

3.3 short-term memory model

In this research, the rainfall attenuation model is expressed by the ARMA model known well by the time series analysis. In addition, the ARMAX model from whom an exogenous input is added to the ARMA model is examined too.

Until recently the thing which measures the rain phenomenon in propagation path regarding law, is equal to the impossibility.

Therefore, a rain gauge on the strength is installed near a transceiver antenna, and rain intensity of the measured base station is made into typical rain intensity.

In this research, rain rate at both bureaus is measured in the opposition system of 11Km, and the attenuation is estimated from that data as an input.

Let $y(t)$ and $u(t)$ be a output and a input, and q expresses path-delay operator. The important thing is how to treat a disturbance signal denoted by $e(t)$. Let nk be a number of time delay at output, three equations are described as follows.

$$A(q) = 1 + a_1q^{-1} + \dots + a_{na}q^{-na} \tag{1}$$

$$B(q) = b_1 + b_2q^{-1} + \dots + b_{nb}q^{-nb} \tag{2}$$

$$C(q) = 1 + c_1q^{-1} + \dots + c_{nc}q^{-nc} \tag{3}$$

By using of these polynomials, following model is derived.

3.3.1 ARMA(AutoRegressive Moving-Average) model

It is the auto-regressive moving-average model which have two large features of "linearity" and "short-term memory characteristic". By using of these characteristics, the equation is simplified as follows.

$$A(q)y(t) = C(q)e(t) \tag{4}$$

When $C(q)$ is equal to 1, it becomes AR (Auto-regressive model).

3.3.2 ARMAX(AutoRegressive Moving Average eXogenous)model

The ARMAX model is the model which considers exogenous input u positively. Where $y(t)$ is output, $u(t)$ is input, $e(t)$ is disturbance(modeling error and noise). nk is time delay.

$$A(q)y(t) = B(q)u(t - nk) + C(q)e(t) \tag{5}$$

When $C(q) = 1$ is, the ARMAX model is equal to the ARX model. It becomes an ARX model when an ARMAX model is $C(q)=1$. It verified also about the ARX model. The input section of the ARX model and the ARMAX model rain rate, the rain attenuation applied the output section.

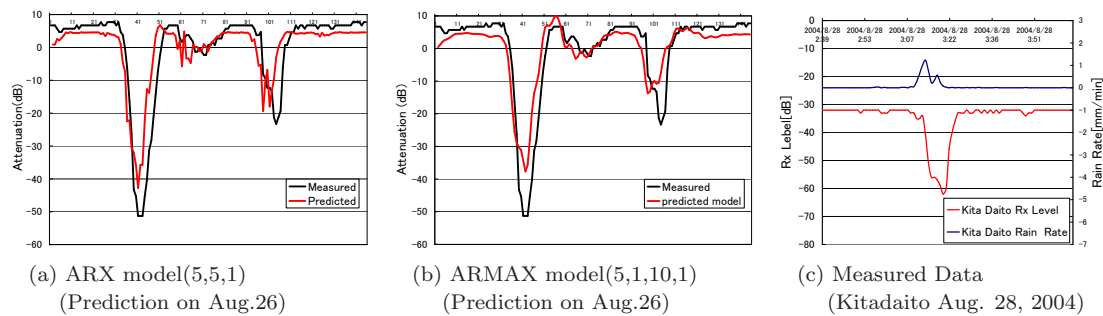


Figure 5: Examples of short-term memory model

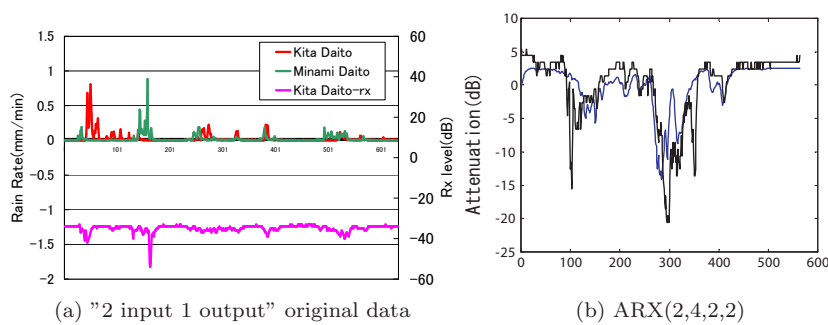
There were six sections where typical data was included in the all observational input/output data sets. Then, six models are first derived by using the six data sets. Next, five data sets other than the data used to decide the model respectively in that are applied, and a qualitatively excellent parameter is decided.

The degree of the parameter was decided based on both AIC criteria and trial and error. Here, example as an observation data, concerning sampling time 1 minute is expressed. A Model is calculated from the data 2004 August 28th. Fig.5(a), Fig.5(b) the event of the Kitadaito island August 26th of the same year to the formula is the example which it tries fitting with the ARX model and the ARMAX model.

Both the ARX model and the ARMAX model relatively it is the satisfactory result, but, there was a problem where it cannot follow the attenuation when influence of the rain of the Minamidaito island is large in another event.

Then, also the rain rate data of the Kitadaito island and the model of 2 input 1 outputs which input both of rain rate of the Minamidaito island constituted concerning the above-mentioned ARX model. The result is shown in the Fig.6.

But, when either one between both base station rain phenomenon occurs with one side regarding a certain event, precision deteriorated even from 1 input time.



(a) "2 input 1 output" original data (b) ARX(2,4,2,2)
Figure 6: Example of "2 input 1 output" ARX 2 Model"

It could cancel the problematical point of single input model, but, when either one between both base station rain phenomenon occurs with only one side, precision deteriorated even from single input model.

3.4 long-term memory model

The ARX model and the ARMAX model are the model which estimates linear stationary process. So when modeling at nonlinear or non-stationary process, those mathematical models can not be suitable for estimating.

Moreover, because ARX and the ARMAX model are models by whom the short-term memory process is shown, these cannot be used for the modeling of the long-term memory process.

Then, we examine whether the characteristic of the rain attenuation and rain rate belongs to the long-term memory process.

Hurst Analysis

There is a decision index of long time memory process so called "Hurst parameter". Hurst parameter is the important parameter which characterizes long-term memory process.

The influence that a present event exerts on the event in the future is given by the next expression.

$$C = 2^{(2H - 1)} \quad (6)$$

where C is a scale of correlation and H is Hurst parameter. The values of Hurst parameter range between 0 and 1. A value of 0.5 indicates a true random walk. In the random walk there is no correlation between any element and a future element. A Hurst parameter H , $0.5 < H < 1$ indicates long-term memory process. A Hurst parameter H , $0 < H < 0.5$ indicates short-term memory process.

But, because various techniques are lifted in decisive method of Hurst parameter, this time it tried with typical seven methods.

Furthermore, in order to inspect simultaneously whether there is the influence with the sampling time of the data, 5 minutes, 10 minutes, 30 minutes, dividing into 60 minutes and 4 stages, it tried. The result is shown in the figure.

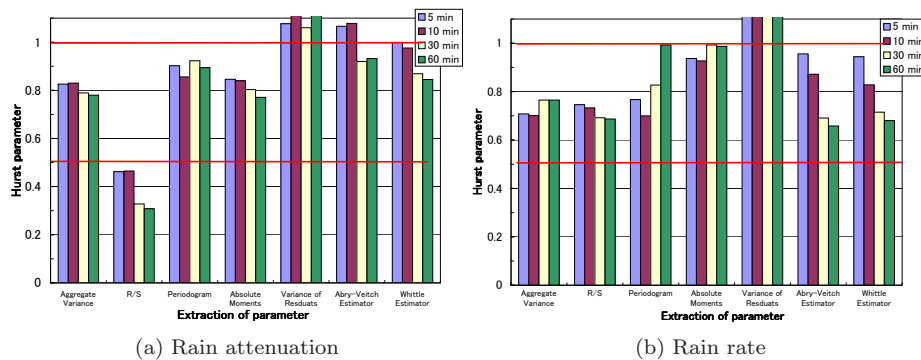


Figure 7: Hurst parameter of Oct.2003 - Mar.2004

It can presume that it is the data where rain rate, both attenuation as for Hurst parameter those of the 1 or less of 0.5 or more are more than the figure, have long-term memory characteristic.

4. Conclusion

In this research, rain attenuation characteristics was modeled by using of time series analysis method. The experimental results, as for the rain rate and the rain attenuation both could verify that it possesses the character which is called the long-term memory dependency. Future work makes the model by whom the long-term storage dependency is positively considered.

Additionally, we recorded six times of disconnection in total by an invasion of a typhoon all over the experiment period. The data at the time of the typhoon is very valuable, not only the side which this time was examined, it is necessary to examine from various angles.

Acknowledgment

The authors would like to thank NEC, Okinawa Pref., Kitadaito Village Office and NTT WEST for provision of experiment data.

REFERENCES

1. J.Beran, *Statistics for Long-Memory Process*, Chapman & Hall, New York, 1994.
2. R.Saotome, T.Miyazato, S.Tamaki, "Construction of Rain Attenuation predictive model at 18GHz band FWA," *SITA2005*, Vol. 2, No. 40.5, 761-764, Okinawa, Japan, Nov. 2005.

Propagation Characteristics of FM Broadcasting Waves at the Mid Niigata Prefecture Earthquake

Shigeru Takahashi, Masakazu Kobayashi, Akiyuki Kaneda,
Masahiro Nishi and Teruaki Yoshida
Faculty of Information Sciences, Hiroshima City University, Japan

Abstract - We have been conducting 24 hours monitoring observations of FM broadcasting waves using PLL synthesized tuners at the Hitachi, Yokosuka and Nobeyama observational sites. All the three sites are monitoring FM Sendai (77.1 MHz), and the Nobeyama site is also monitoring FM Niigata (82.3 MHz). These systems were working at the Mid Niigata Prefecture Earthquake (MEQ) on Oct. 23, 2004, and we have obtained the data to discuss whether seismic propagation anomalies caused by the MEQ exist. In this paper, we report the propagation characteristics of these broadcasting waves by comparison of the data on usual days and the MEQ day. We have confirmed that the ordinary propagation state in the frequency 77.1 MHz is subject to tropospheric propagations. In order to check the peculiarities of EM, we have verified all the data during Oct. 17-25, 2004. The results are that no anomalies could be seen at the three sites, and the received level variations during this period were dominated by tropospheric propagation as usual. In addition, the results of 82.3 MHz observations were also the same as those of 77.1 MHz. We conclude that in 77.1 MHz and 82.3 MHz, any EM phenomena related with the reflection or disturbance of the ionosphere were not detected before and after the MEQ.

1. Introduction

Since the coming of the 1995 Hyogoken-Nanbu earthquake, eyes in some people have turned towards seismic electromagnetic (EM) phenomena. Some researchers insisted that they had received the 77.1 MHz FM broadcasting wave that had been reflected by the ionosphere before this earthquake¹, and such concerns about the relationship between earthquakes and EM phenomena have spawned a number of vigorous studies with diverse frequencies covering DC, ULF, ELF, VLF, LF, MF, HF and VHF bands². Despite these efforts there is not always consensus on this issue because the phenomena would be quite subtle and only sensitive instruments installed under the EM-noiseless environments are required for detection.

Besides broadcasting waves, modern society has numerous artificial sources of EMs from electrical appliance. In addition, natural phenomena such as solar flare and radiations from Milky Way, thunderstorm, snow clouds etc. can be the sources of EM noises. Both the artificial and natural contaminations should be identified and segregated from observational data in order to discuss whether the radiations of EMs can be a candidate for the precursor of earthquake.

From 1997, we have been conducting 24 hours monitoring observations of EM phenomena in VHF bands, especially 76-90 MHz, which are assigned for FM broadcastings in Japan. The observational sites have been installed over the east part to west in Japan, and the number amounts to 13. We show the data before and after the Mid Niigata Prefecture Earthquake (MEQ) obtained at the Hitachi, Yokosuka and Nobeyama sites. All the three sites are monitoring FM Sendai (77.1 MHz), and the Nobeyama site is also monitoring FM Niigata (82.3 MHz). These systems were working at the MEQ on Oct. 23, 2004, and we obtained the observational data to discuss whether seismic propagation anomalies caused by the MEQ exist. It is noteworthy that at the Nobeyama site, we observed the 82.3 MHz broadcasting waves which had passed above the epicenter of the MEQ.

In this paper, we show instruments setting and observational methods which are used at the Hitachi,

Yokosuka, and Nobeyama sites in chapter 2, and then results and discussions are described in chapter 3 and 4.

2. Observations

We have selected the VHF bands (30 MHz ~ 300 MHz) for observations, especially monitored the FM broadcasting wave, which are allocated over the range 76 MHz ~ 90 MHz and well controlled in Japan. A PLL synthesized FM tuner which has the detection limit of -120 dBm was used as a receiver^{3,4,5}. The 4 antennas typically directed towards the NSEW are installed on the roof of the building. Observed received levels were recorded every two seconds with PCs. We also recorded demodulated sounds in the PCs to confirm and discern the arrival of extraneous FM broadcasting waves. The observational system is illustrated in Figure 1, and observational sites, Hitachi, Yokosuka and Nobeyama, and the epicenter of the MEQ, are marked in Figure 2.

The instruments were shielded to eliminate noises coming from surroundings and instruments themselves. The struggle with these artificial noises, such as selecting noiseless location and shielding of instruments, always has much difficulty in doing, can attain the detection of the radiation from the Milky Way (~ -115 dBm). We regard the Milky Way as a useful indicator of the EM noise level in the VHF bands.

3. Propagation characteristics of 82.3 MHz

We show the 82.3 MHz data before and after the MEQ occurred at 17h 56m 00, Oct 23, (Local time) in 2004, and those of the same day but different year (2005) for comparison. As shown in Figure 2, the 82.3 MHz broadcasting waves passed above the epicenter of the MEQ, and it must be an interesting topic to see if any anomaly can be found in the data on adjacent days. The Figure 3(a) and Figure 3(b) illustrate the received level variations in 82.3 MHz at the Nobeyama site on Oct. 17-25 in 2004 and 2005, and Figure 4(a) and Figure 4(b) do cumulative probabilities, respectively. The time MEQ occurred is also marked. The 2004 data indicate that around -110 dBm, the received levels have fluctuation $\pm 2 \sim 10$ dBm after and before the MEQ, and the Oct. 18 data show a remarkable increase; the received level had a peak -97 dBm at midnight. One would think that this anomaly may be the precursor of the MEQ, at least have any relation with the MEQ, but we never hasten to draw a conclusion from these results. We compared the 2004 and 2005 data to investigate whether such anomaly could be seen in other days. From Figure 3(b), the 2005 data also have the similar variations; e.g. on Oct 20, the peak level reached ~ -90 dBm, so that the variation seen in Oct. 18 would not be extraordinary. To confirm the ordinal variability in 2004 and 2005, we verified daily cumulative probabilities in the received levels (Figure 4(a) and 4(b)). While the 2004 data have the range $-106 \sim -97$ dBm of 1% value, the 2005 the range $-107 \sim -86$ dBm, which means the fluctuation in 2005 have 10 dB larger than those in 2004. It is well known that the state of atmosphere, whose refractive index is described as a function of temperature, wind velocity, pressure etc. along propagating paths, often affects the received levels of EMs, and increase of the received level is frequently

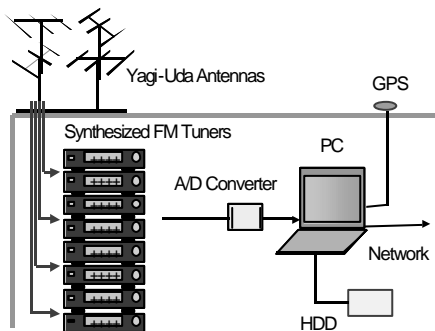


Figure 1: Observation system.

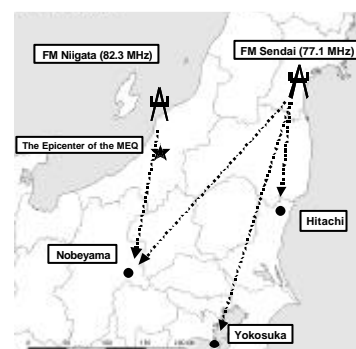


Figure 2: Loci of observational sites, FM radio stations and the epicenter of the MEQ

observed in a place where high atmospheric pressure overlies^{6,7}. Actually, on Oct. 18, the Nobeyama site and its propagation paths were under high-pressure area, and therefore it is valid to consider that the variation was due to the duct propagation. On the other hand, on Oct. 19, 20 and 21, the received levels were almost constant because atmosphere was stirred by the typhoon No. 23 passing across Japan on these days, and the refractive index of the atmosphere became homogeneous.

According to these results, we assert that the usual received level variations at the Nobeyama site in 82.3 MHz are subject to the tropospheric propagation, and then the variation on the Oct. 18 was ordinary rather than precursory.

4. Propagation characteristics of 77.1 MHz

We also monitor the 77.1 MHz (FM Sendai) because the propagation anomalies in this frequency were reported when 1995 Hyogoken-Nanbu earthquake occurred. The observations have been carried out at the three different sites, Hitachi, Yokosuka and Nobeyama. Figure 5 illustrates the received level variations at the three sites from Aug to Nov in 2004. Since in the frequency 77.1 MHz, received levels at each site have interferences by the radio station that has the same frequency in Tokyo (Housou-Daigaku: The University of the Air), we sampled the data only when the broadcasting of the Housou-Daigaku stopped at midnight. From the Figure 5, we found that there are differences in the received levels among the three sites. The received levels at the Hitachi and Yokosuka sites wander around -105 dBm ~ -95 dBm, whereas the Nobeyama site -115 dBm ~ -120 dBm; i.e. the received levels at the two former sites exhibit about 20 dB higher than those at the Nobeyama site.

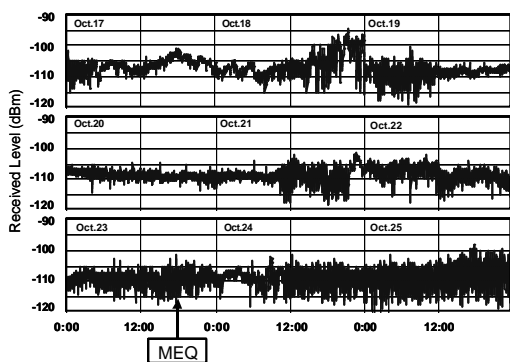


Figure 3(a): Received level variations in 82.3 MHz at the Nobeyama site on Oct. 17-25, 2004

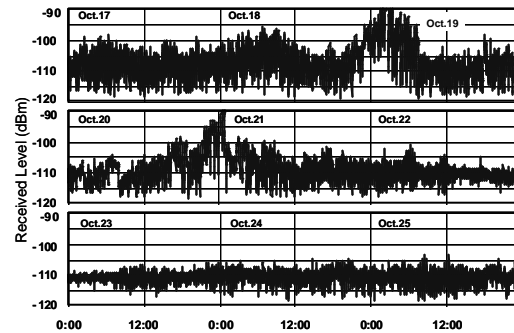


Figure 3(b): Received level variations in 82.3 MHz at the Nobeyama site on Oct. 17-25, 2005

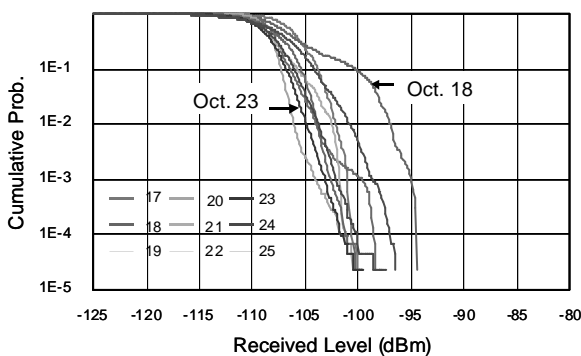


Figure 4(a): Cumulative probabilities of received levels in 82.3 MHz at the Nobeyama site on Oct. 17-25, 2004

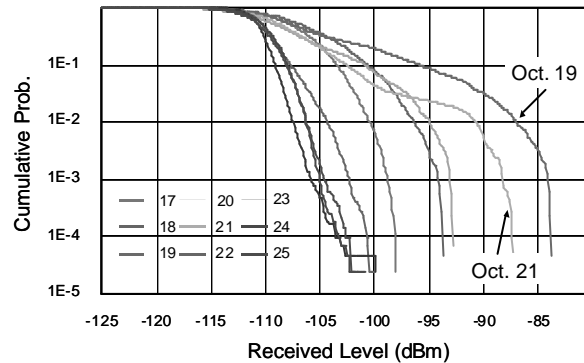


Figure 4(b): Cumulative probabilities of received levels in 82.3 MHz at the Nobeyama site on Oct. 17-25, 2005

This is due to the terrain differences in propagation paths from the FM Sendai broadcast station to each site. As indicated in Figure 6, there is no line of sight for each site, and thus the received levels are most affected by terrain features. The mountains, Abukuma-Highlands, which are located along the paths of the Hitachi and Yokosuka sites and are several hundred meters in height in average. In contrast, the mountains along the path of the Nobeyama site are as much as 2000 m in height, and thus the pass loss in 77.1 MHz becomes larger compared with those of the Hitachi and Yokosuka. If the ionosphere reflected the 77.1 MHz EM waves, the received levels would be similar at the three sites because all the sites are within the lines of sights from the ionosphere. Accordingly, we insist that the explanation that observed differences were induced by the reflections of the ionosphere is implausible from the reasons mentioned above, and such differences are caused in chief by the terrain features.

In order to see the widths of the variations around the MEQ day, we verified the received levels at the Nobeyama site in 2004 and the same day/month in 2005 for comparison. Figure 7(a) and Figure 7(b) denote the cumulative probabilities in 77.1 MHz on Oct 17-25 in 2004 and 2005, respectively. We should note that the range of variations in 2004 is the same as that in 2005; both are about -119 dBm ~ -117 dBm, which indicates that none of peculiar things were found in the data, even on the MEQ day. We conclude that no phenomenon was found in the 77.1 MHz before and after the MEQ at the Nobeyama site, and the same conclusion has been obtained in the case of 82.3 MHz.

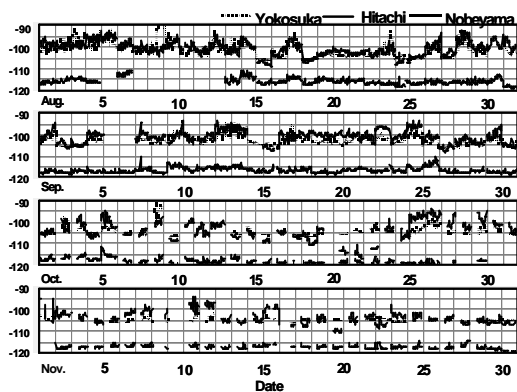


Figure 5: Received level variations in 77.1 MHz at the Hitachi, Yokosuka and Nobeyama sites on Oct. 17-25, 2004

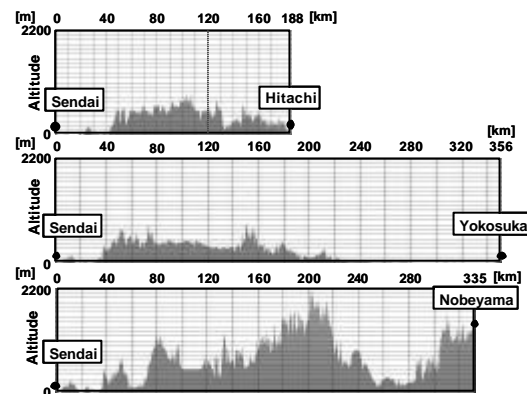


Figure 6: Propagation Paths from FM Sendai to the Hitachi, Yokosuka and Nobeyama Observational sites

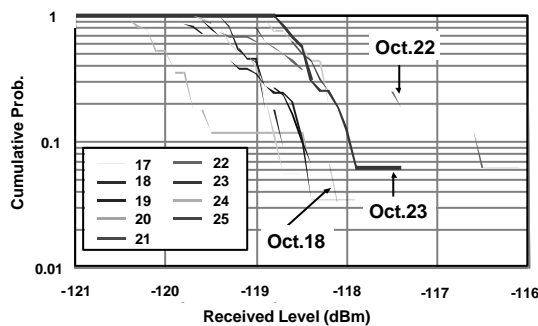


Figure 7(a): Cumulative probabilities of received levels in 77.1 MHz at the Nobeyama site on Oct. 17-25, 2004

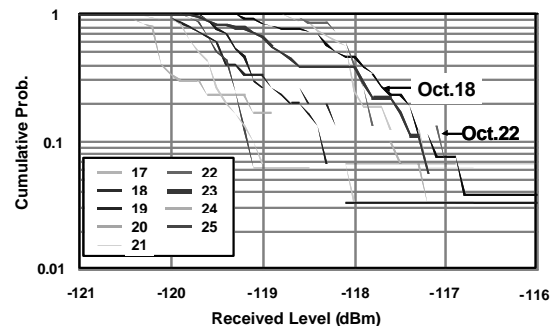


Figure 7(b): Cumulative probabilities of received levels in 77.1 MHz at the Nobeyama site on Oct. 17-25, 2005

5. Conclusions

- (1) We have been conducting 24 hours monitoring observations of FM broadcasting waves using PLL synthesized tuners at the Hitachi, Yokosuka and Nobeyama observational sites. The used frequency is 77.1 MHz at the Hitachi, Yokosuka and Nobeyama sites, and 82.3 MHz at the Nobeyama site.
- (2) At the Nobeyama site, we could observe the 82.3 MHz broadcasting wave that had passed above the epicenter of the MEQ, however we could not detect any anomalies in the data, moreover, no precursor was found before/after the MEQ.
- (3) The Hitachi, Yokosuka and Nobeyama observational sites are monitoring the 77.1 MHz broadcasting wave from FM Sendai. The propagation properties were characterized by the terrain features along the paths. In this case also, we could not find any phenomenon related to the precursor of the MEQ.

Acknowledgements

We thank Nobeyama radio observatory, Department of Media and Telecommunications Engineering, Ibaraki University, and the Yokosuka Electrical Communications Laboratory of Nippon Telegraph and Telephone public co-operation for help on the observations. This study was supported by Grants-in-Aid for Scientific Research, JSPS and Hiroshima-city University research funding.

References

1. Kushida, Y. and R. Kushida, "On a Possibility of Earthquake Forecast by Radio Observation in the VHF Band", *Riken Review*, Vol. 19, 1-13, 1998.
2. Hayakawa, M. and Y. Fujinawa (ed.), *Electromagnetic Phenomena Related to Earthquake Prediction*, Terra Science Publishing Company, Tokyo, 1994.
3. Yoshida, T., "Observations of Seismic Electromagnetic Phenomena in VHF band by Dual Frequency Method", *Electrical Engineering in Japan*, Vol. 155, No.4, 36-44, 2006.
4. Yoshida, T. and M. Nishi, "The Observation of Broadband Co-seismic Electromagnetic Waves in VHF Band", *IEEE APS-2001*, 184-187, 2001.
5. Yoshida, T., Patent No. 2956685 (1999).
6. Bremmer, H., *Terrestrial Radio Waves*, Elsevier Publish, 1949.
7. ITU-R, *Recommendations Radio Wave Propagation*, Vol. P Series, 1998.

Study on the propagation environment evaluation for the land mobile satellite link using GPS

W. A. W. Z. Abidin, K. Fujisaki, and M. Tateiba

Department of Computer Science and Communication Engineering,
Kyushu University, Japan

Abstract—The proper planning of the Earth-space Mobile Satellite systems requires propagation data from different regions in the world to fit into the Land Mobile Satellite (LMS) propagation models. This report investigates a cheaper, simpler but efficient measurement technique using the Global Positioning System (GPS) receiver to study the LMS link. The commercially available GPS receivers are able to provide the related signal strength intensity data which has a big potential for the study of the LMS link. In this report, the measurement method used to obtain propagation data for different LMS propagation environments is explained and discussed. In addition, results obtained from the measured data are presented.

1. Introduction

In the LMS system, two main sources of signal degradation are shadowing effect and multipath fading. The shadowing is caused by the presence of obstacles that impedes the line-of-sight (LOS) signal such as building and trees. Multipath effect is due to the arrival of the reflected LOS signals of different amplitude and phase which can cause signal fluctuations. These reflections are due to the surrounding environment such as buildings, trees and electric poles. The fading statistical characterization requires data from large quantity of measurements to fit the parameters of the mathematical models used to represent the land mobile satellite link.

The LMS system designers require information regarding signal degradation effects for various environmental or geographical areas. Many investigations have been performed at different frequency bands [1] - [5] and have addressed issues such as the effect of shadowing and multipath on the land mobile satellite signal.

Over the last two decades, the investigations were done using the existing geo-satellite system or airborne platform [1] - [5]. These methods are complex and costly which prevent more data representing different parts of the world to be obtained easily. Some researchers have been using the GPS in their research as an alternative to the common method of existing geo-satellite system or airborne platform [8], [9].

The GPS system which has a constellation of 21 Medium-Earth-Orbit (MEO) satellites transmitting at L-band (1575.42MHz) provides a cheaper and simpler alternative. Since GPS receivers are readily available and also able to provide information about signal strength intensity of many satellites at the same time, the current work concentrates on the signal intensity measurement using the GPS receiver. This measurement technique allows a lot of data to be recorded simultaneously from different satellite at any instant of time for different number of propagation environments (urban, suburban, rural) with different elevations.

Due to these advantages, we will develop an LMS propagation environment evaluation system based on the raw propagation data obtained from the portable and commercially available GPS receivers. This LMS evaluation system would be able to predict propagation signal performance of mobile users when moving in any geographical environment.

By using the portable GPS receiver, measurements were carried out for the open space and the tree-shadowed environments under fine weather conditions with clear open sky. Raw GPS data was automatically recorded for later analysis. This paper is organized in the following way. Section 2 describes the experimental aspect of the propagation measurement at L-band. In Section 3, the experimental results are discussed followed by the conclusion in Section 4.

2. Propagation Measurement

2.1 Measurement Methodology

In this measurement, a commercially available, portable handheld Garmin eTrex GPS receiver is used which can track up to 12 satellites at the same time, providing data such as signal-to-noise-ratio (SNR), elevation angle and azimuth. These data are automatically recorded on a notebook computer for later analysis. For the purpose of this preliminary study, data has been measured within the vicinity of the Hakozaki Campus in

Kyushu University. This location has been chosen since it has the geographical environment that represents the mobile satellite environment; i.e. open space, shadowed and multipath.

Figure 1 shows a sample of the output data obtained from the GPS receiver by a computer. This data have the National Marine Electronic Association (NMEA) data format, a specification that defines the common data structure between various pieces of marine electronic equipment. GPS receiver communication belongs to this specification. The idea of NMEA is to send a line of data called a sentence that is totally self contained and independent from other sentences. For this study, the sentence of interest is the GPGSV (Satellite in view) sentence which contains the information about the SNR together with the elevation and azimuth information.

```

$GPRMC,152926,V,6027.8259,N,02225.6713,E,10.8,0.0,190803,5.9,E,S*22
$GPRMB,V,,,,,,,,,A,S*0E
$GPGGA,152926,6027.8259,N,02225.6713,E,8.09,2.0,44.7,M,20.6,M,,*79
$GPGSA,A,3,07,08,09,11,18,23,26,28,29,,,,,6.6,2.0,3.0*38
$GPGSV,3,1,09,07,29,138,44,08,22,099,42,09,30,273,44,11,07,057,35*75
$GPGSV,3,2,09,18,28,305,43,23,14,340,39,26,64,222,49,28,60,084,49*7E
$GPGSV,3,3,09,29,52,187,48*4E
$GPGLL,6027.8259,N,02225.6713,E,152926,V,S*48
$GPBOD,T,M,,*47
$SPGRME,15.0,M,22.5,M,15.0,M*1B
$SPGRMZ,147,f,3*19
$GPRTE,1,1,c,*37
$GPRMC,152928,V,6027.8319,N,02225.6713,E,10.8,0.0,190803,5.9,E,S*29
    
```

Figure 1: GPS receiver output.

The value of the undisturbed SNR given by Butsch [8] to be in the order of 45dBHz to 50dBHz while the loss of lock threshold is between 28dBHz and 30dBHz. We have chosen the 45dBHz as the reference SNR and this value is consistent with the raw data that has been measured under the open space environment. In this study, signal with values below the 45dBHz are considered as experiencing attenuation. For this portable receiver, the lost of signal lock occur when the SNR is less than 30dBHz. The receiver will give 0 dBHz when signal lock is lost. Therefore, the attenuation of up to 15dBHz can be observed with this one.

To show the feasibility of this method, data have been recorded for different geographical environments such as open space and shadowed environments. The same measurements have been repeated to validate the previously obtained data. For all measurement, the GPS receiver has been placed flat facing the sky in order to make it behaves like an omnidirectional antenna. The receiver also has the ability to reject signals arriving from behind and this removes the effect of multipath signals due to the ground. From this set up, data for a number of satellites for different elevation and azimuth can be measured simultaneously.

2.2 Open Space Set Up

Figure 2(a) shows the experimental set up for the open space environment. The GPS receiver was placed at the very top of a building directly facing the sky with no obstacles within the 30m radius of the receivers. Measurements were taken under the sunny, clear sky conditions.

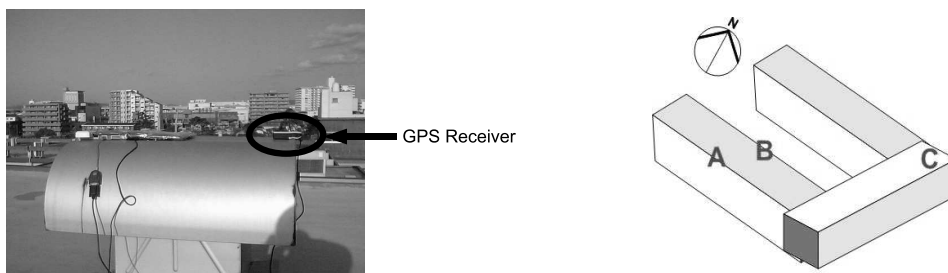


Figure 2: (a) Open space set up (b) Measurement locations for Table 1.

Table 1 shows a number of visible satellites when the GPS receiver was placed facing the sky. During the measurement, SNR for the open space environment was measured for a period of about 30 minutes at 3 different locations and at different times. These observation points correspond to locations A, B and C in Figure 2(b). From Table 1, the number of satellites visible for each measurement are shown in the second column from left and the number of satellites having SNR equal or greater than 45dBHz are shown in the third column. It can be observed that there are a lot of satellites giving SNR of equal or greater than 45dBHz for this experimental set up out of the total satellites visible during the measurement.

Table 1: A Number of Visible Satellites under the Open Space Environment.

Measurement	Total Visibled Satellite	No. of Satellite with SNR \geq 45dBHz
Location A	9	7
Location B	10	6
Location C	10	6

As expected, for this set up, we obtained more satellites giving SNR of equal or greater than 45dBHz for elevation angle as low as 15°. In this experiment, those satellites with SNR less than 45dBHz are due to signal arriving from low elevation angles. These low elevation angles are outside the receiver’s 3-dB beamwidth and thus the SNR experienced drop in gain. By having many satellite SNRs from the same measurement, we can utilize the data to study the attenuation effect on the signal arriving from different positions; by referring to the values of the azimuth and elevation angle.

3. Results and Discussion

3.1 Open Space Results

Other measurements were carried out to validate the SNR result obtained from the same satellite at different times. Data was measured over a single day period and compared with that measured in a five-day period (Figure 3). These figure shows the value of SNR against elevation and azimuth of Satellite ID 3 (SID3). The actual value of the azimuth can be obtained by multiplying the value of azimuth in Fig. 3 by a factor of 4.

It can be observed that the SNRs for the single-day and the five-day show similarity in their respective SNR pattern over the same elevation and azimuth angles. This validated that data obtained from the receiver is consistent regardless on which day it is measured. The missing data from Fig.3(b) was due to the data partially measured over the period of five days. For low elevation, less than 15°, the SNR is given as 0dBHz because the receiver will only provide SNR of equal or greater than 30dBHz. The SNR of equal or greater than 45dBHz was obtained for elevation of about 15°.

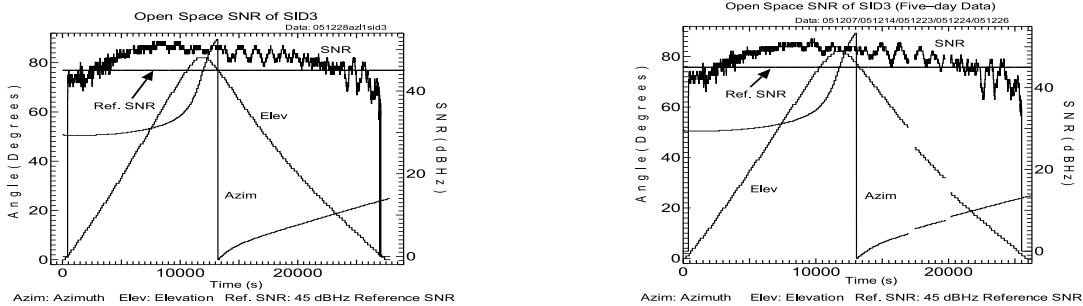


Figure 3: (a) SNR of SID3 (Single-day data)

(b) SNR of SID3 (Five-day data).

In Figure 4, the result obtained for SID9 and SID22 are depicted. These results have been obtained from the same set of data as that of Fig.3(a). The small fluctuations on the SNR are due to the effect of multipath fading. Under the open space environment, the received SNR will still experience peak-to-peak power variations of less than 5dB due to multipath fading [5].

From Fig. 4, it can be observed that for a long period of time over a wide range of elevation and azimuth the measured SNR was equal or greater than 45 dBHz. These value can be measured for elevation angle as low as 15° and as high as 90°.

The difference in the elevation and azimuth of the SID9 and SID22 is because the two satellites orbiting the earth along their own orbit. They will be visible from the point of view of the GPS receiver at different time of the day. For the purpose of the analysis, the time axis has been set from 0s.

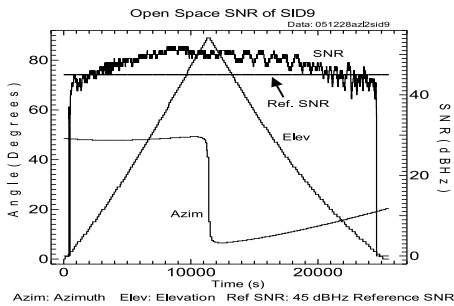
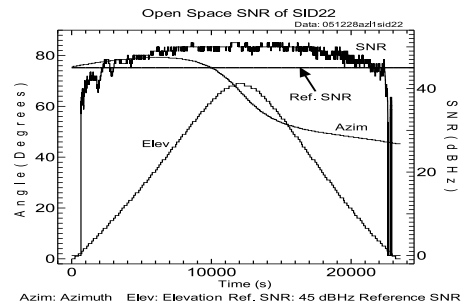


Figure 4: (a) SNR of SID9



(b) SNR of SID22.

On the other hand, the roadside shadowing model given in the Rec. ITU-R P.681-6 only covers elevation angle from 20° to 80° . By using the GPS receiver, it is possible to obtain data for elevation angle lower than 20° and greater than 80° .

3.2 Tree-shadowed

Figure 5 shows the set up for a tree shadowed environment. During this measurement, the GPS receiver was placed on top of a circular table on the ground. From the GPS receiver point of view, it is receiving satellite signals which experience shadowing effect due to the presence of trees. Since the GPS receiver is receiving satellite signals from different directions, results for heavily-shadowed and moderately-shadowed are given in this report to show the effect of shadowing.

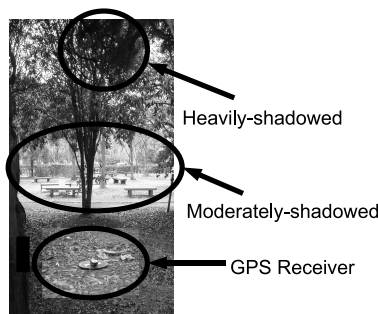


Figure 5: Tree-shadowed environment

Figure 6 shows the SNR of SID3 and SID19 for this set up. The SNR for SID3 and SID19 were obtained from the same set of data. This data was measured for about 1 hour 10 minutes under fine weather condition. In Fig. 6, there are two SNR values plotted on the graphs; the SNR for the open space environment and the SNR for the tree-shadowed environment.

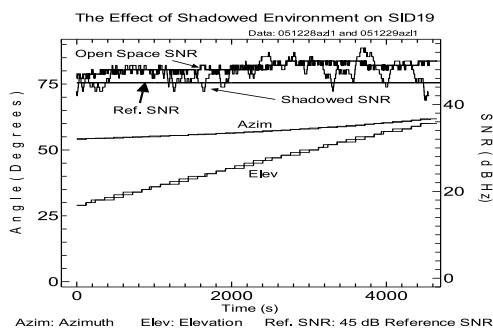
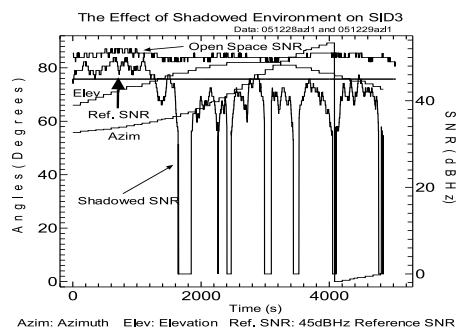


Figure 6: (a) SNR of moderately-shadowed environment



(b) SNR of the heavily-shadowed environment

It can be observed from Fig. 6(a) that the SNR for the tree-shadowed environment follows the same pattern as that of the open space environment but experienced slight fluctuations. This is due to the effect of tree leaves and woody parts that give rise to the multipath component of the arriving signal. High SNR (about 45dBHz) was obtained because the GPS receiver was receiving signal from the position where there were less dense tree leaves and also due to the presence of a space between the ground and the tree leaves during this period of measurement. This corresponds to the moderately-shadowed area shown in Fig. 5.

In Fig. 6(b), the SNR dropped below the 45dBHz line after about 1200s. This is due to the presence of tree leaves as well as woody part of the tree which attenuated the received signal (Heavily-shadowed area in Fig. 5). As the satellite moves along the orbit, the increase in the elevation together with the change in position from where the signal arrive (azimuth) caused the GPS receiver to experience line-of-sight (LOS) environment to the tree-shadowed environment. Under the shadowing condition, the value of SNR is below the 45dBHz line and in some cases, the lost of signal lock happened. For the period between 0s to 1200s, the SNR exceeded the 45dBHz line but experienced more fluctuation compared to the SNR under the open space environment. This is expected due to the presence of more multipath components for the tree-shadowed environment.

From Fig. 6, we have shown that the effect of shadowing due to trees could be studied by using this portable GPS receiver with signal attenuation of up to 15dBHz can be observed.

4. Conclusion

This preliminary study has been carried out to show the feasibility of using the commercially available portable GPS receivers to study the quality of the LMS link. The ability of GPS receivers to provide SNR of many satellites at any instant of time allows comparison to be made for any geographical environment of interest. With this simple and cheap technique, more propagation data representing land mobile satellite system for different part of the world can be obtained easily.

The results can be summarized as follows:

- a) under the open space environment, the SNRs received from different number of satellites are consistent over a wide range of elevation angle and azimuth.
- b) under the shadowed environment, the SNR experiences fluctuations due to the presence of tree leaves, branches as well as the woody part of the tree.
- c) the ability of the portable GPS receiver to measure signal strength intensity up to the 90° elevation angle enables data to be measured for all range of elevation angles.
- d) with this method, the cost of doing research and data measurement time can be greatly reduced due to the low-cost of the receiver and also it is readily available and easy to manage.

REFERENCES

1. Vogel, W. J. and Goldhirsh, J., "Fade measurements at L-band and UHF in mountainous terrain for land mobile satellite systems," *IEEE Trans. Antennas Propagation*, Vol 36, Jan. 1998.
2. Yamamoto, S., Okamoto, E., Aboudebra, A. A., and Ikegami, T., "Propagation measurements for land mobile satellite communications at S-band with Nongeo ETS-VI satellite," *Proc. Int. Mobile Satellite Conf.*, 1997.
3. Goldhirsh, J. and Vogel, W. J., "Mobile satellite system fade statistics for shadowing and multipath from roadside trees at UHF and L-band," *IEEE Trans. Antennas Propagation*, Vol 37, Apr. 1989.
4. Hase, Y., Vogel, W. J. and Goldhirsh, J., "Fade-durations derived from land-mobile-satellite measurements in Australia," *IEEE Trans. on Communications*, Vol 39, 1991.
5. Goldhirsh, J. and Vogel, W. J., "Handbook of propagation effects for vehicular and personal mobile satellite systems: Overview of experimental and modeling results," <http://www.utexas.edu/research/mopro/papercopy/handbook.pdf>, 1998.
6. Smith, H., Gardiner, J. G., and Barton, S. K., "Measurements on satellite-mobile channel at L and S bands," *Proc. Third Int. Mobile Satellite Conf.*, IMSC'93, 1993.
7. Sheriff, R. E. and Hu, Y. F., *Mobile Satellite Communication Networks*, John Wiley and Sons Ltd, 2001.
8. Butsch, F., "GPS and GLONASS Radio Interference in Germany", *Proceeding of ION*, 1999.
9. Kirchner, M. and Becker, M., "The Use of Signal Strength Measurements for Quality Assessments of GPS Observations," Reports on Geodesy No. 2. (73), http://www.fomi.hu/cegrn/public/Kirchner_Becker_05.pdf, 2005.

Electromagnetic Fields Due to a Vertical Electric Dipole above an Electrically Large Stratified Spherical Earth

Ting Fei, Le-Wei Li, and Tat-Soon Yeo

Department of Electrical and Computer Engineering
National University of Singapore, Kent Ridge, Singapore

Abstract—The electromagnetic fields due to a vertical dipole radiating in the presence of a stratified sphere (used to model the earth) is represented by infinite summation in spherical systems. It is known that the series usually has slow convergence when both the source and the observation point are on or close to the same surface. For an electrically large sphere, the field is more difficult to calculate because the number of the series terms is about $10ka$ (where a is the radius of the sphere and k is the wave number). In this paper, a convergence acceleration method is used to compute the fields generated by a vertical electric dipole over a stratified large sphere. As a practical and interesting application, the simulation results are given for the fields near the surface of the earth. The convergence property is analyzed. The results are also computed and compared with those by asymptotic methods based on Watson transformation.

1. Introduction

The radiation of an electric dipole over an electrically large sphere has been the subject of numerous investigations. It is fairly straightforward to obtain exact series solutions for the fields where the associated dyadic Green's functions (DGFs) are given in terms of double infinite series. However, for the wavelength in the air being much smaller than the radius of the sphere, the series converges very slowly. Therefore, most of the research works focused on asymptotic methods such as steepest descents, stationary phase [3, 2], and uniform asymptotic expansions [1]. The kernel of these methods is the Watson's transformation by which the slowly converging eigenfunction expansion in partial waves was converted into an integral which in turn generated a rapidly converging series. However, those methods are not universally accurate or even valid regardless of the positions of the source and observation points. The series representation of the radiated electromagnetic field due to a dipole still serves as a good and especially an exact solution form for the problem.

In this paper an accurate and efficient method is obtained for all positions of source and observation points. The series of the scattered field is then accelerated by using Kummer's transformation. Numerical results are presented to compare with asymptotic solution. Also, the convergence property with respect to an angle θ from 0 to π is discussed.

2. Formulations and Equations

The problem defined here is a vertical electric dipole (VED) radiating in the presence of a three-layered sphere. The center of the sphere is the origin of the spherical coordinate system (r, θ, ϕ) . The sphere is a perfect conducting sphere coated with a dielectric shell, and surrounded by air ($r > a$). The air and the dielectric medium are characterized by wave number k_1 , and k_2 , respectively. The radius of the sphere from the surface of the dielectric coating to the center of the sphere is a . The height of the VED from the dielectric surface is z_s . The dipole is located at a distance $b = a + z_s$ from the center of the sphere. The current distribution under the spherical coordinates is expressed by

$$\mathbf{J}(\mathbf{r}') = I_0 \frac{\delta(r' - b)\delta(\theta')\delta(\phi')}{b^2 \sin \theta'} \hat{\mathbf{r}},$$

where I_0 denotes the amplitude of the current distribution while $\delta(\bullet)$ stands for the Dirac delta function.

2.1 Exact Series Solutions

The electric field in the outer space is expressed by use of the dyadic Green's functions [5]. The total field can be split into direct wave and scattered wave as follows:

$$\mathbf{E}_{\text{total}}(\mathbf{r}) = \mathbf{E}_{\text{direct}}(\mathbf{r}) + \mathbf{E}_{\text{scat}}(\mathbf{r}) \quad (1a)$$

Furthermore, the direct wave have the analytic expressions [4]

$$\mathbf{E}_{\text{direct}}(\mathbf{r}) = -\frac{\omega\mu_0 I_0}{4\pi b} \frac{1}{k_1} \nabla \times \nabla \times \left[\frac{e^{ik_1 R}}{ik_1 R} \mathbf{r} \right], \quad (2a)$$

$$\mathbf{E}_{\text{scat}}(\mathbf{r}) = -\frac{\omega\mu_0 I_0}{4\pi b} \sum_{n=0}^{\infty} (2n+1) \mathcal{B}_N^{11} h_n^{(1)}(k_1 b) \left[\frac{n(n+1)}{k_1 r} h_n^{(1)}(k_1 r) P_n(\cos \theta) \hat{\mathbf{r}} + \partial \hbar(k_1 r) \frac{\partial P_n(\cos \theta)}{\partial \theta} \hat{\boldsymbol{\theta}} \right] \quad (2b)$$

where \mathcal{B}_N^{11} is the reflection coefficient defined by

$$\mathcal{B}_N^{11} = \frac{k_1 j_n(k_1 r_1) (\partial \hbar_{22} \partial \mathfrak{S}_{21} - \partial \hbar_{21} \partial \mathfrak{S}_{22}) + k_2 \partial \mathfrak{S}_{11} (\partial \mathfrak{S}_{22} h_n^{(1)}(k_2 r_1) - \partial \hbar_{22} j_n(k_2 r_1))}{k_1 h_n^{(1)}(k_1 r_1) (\partial \hbar_{21} \partial \mathfrak{S}_{22} - \partial \hbar_{22} \partial \mathfrak{S}_{21}) - k_2 \partial \hbar_{11} (\partial \mathfrak{S}_{22} h_n^{(1)}(k_2 r_1) - \partial \hbar_{22} j_n(k_2 r_1))}, \quad (3a)$$

$$\partial \hbar_{ij}(z) = \frac{1}{z} \frac{d[z h_n^{(1)}(z)]}{dz} \Big|_{z=k_i r_j}, \quad \partial \mathfrak{S}_{ij}(z) = \frac{1}{z} \frac{d[z j_n(z)]}{dz} \Big|_{z=k_i r_j}, \quad R = \sqrt{b^2 + r^2 - 2br \cos \theta} \quad (3b)$$

while $j_n(z)$ and $h_n^{(1)}(z)$ denote the spherical Bessel functions of the first kind and the third kind, respectively, $P_n(\cos \theta)$ is the Legendre function of the first kind, and an $e^{-i\omega t}$ time dependence is assumed and suppressed in the expression of the above and subsequent fields.

In order to accelerate the convergence of the series in equation (2b), we propose to extract the contribution of the electric field due to an image dipole of the real dipole in the presence of a large-radius sphere. The image location of a real source at $r = b$ can be approximated as at $r = 2a - b$. Employing the expression in Eq. (2a), for $r \gtrsim 2a - b$, we have the electric field radiated from the image source if the surface is planar given as

$$\mathbf{E}_{\text{image}}(\mathbf{r}) = -\frac{\omega\mu_0 I_0}{4\pi b} \frac{1}{k_1} \nabla \times \nabla \times \left[\frac{e^{ik_1 R'}}{ik_1 R'} \mathbf{r} \right], \quad \text{where } R' = \sqrt{r^2 - 2r(2a - b) \cos \theta + (2a - b)^2}. \quad (4)$$

Further, we can derive the following asymptotic expression:

$$\frac{j_n[k_1(2a - b)]}{\mathcal{B}_N^{11} h_n^{(1)}(k_1 b)} \approx -\left(\frac{2a - b}{b}\right)^n \frac{k_1^2 + k_2^2}{k_1^2 - k_2^2} \quad \text{as } n \rightarrow \infty. \quad (5)$$

The series term in (2b) at $n = 0$ is zero and therefore it is equivalent to start from $n = 1$. Further, the scattered field can be rewritten as

$$\mathbf{E}_{\text{scat}}(\mathbf{r}) = -\frac{b}{2a - b} \frac{k_1^2 - k_2^2}{k_1^2 + k_2^2} \mathbf{E}_{\text{image}}(\mathbf{r}) + \mathbf{E}_{\text{corr}}(\mathbf{r}), \quad (6a)$$

$$\mathbf{E}_{\text{corr}}(\mathbf{r}) = -\frac{\omega\mu_0 I_0}{4\pi b} \sum_{n=1}^{\infty} (2n+1) \left[\mathcal{B}_N^{11} h_n^{(1)}(k_1 b) + \frac{b}{2a - b} \frac{k_1^2 - k_2^2}{k_1^2 + k_2^2} j_n[k_1(2a - b)] \right] \left[\frac{n(n+1)}{k_1 r} h_n^{(1)}(k_1 r) P_n(\cos \theta) \hat{\mathbf{r}} + \partial \hbar(k_1 r) \frac{\partial P_n(\cos \theta)}{\partial \theta} \hat{\boldsymbol{\theta}} \right]. \quad (6b)$$

Since $\mathbf{E}_{\text{image}}$ has the analytic expression, computation efforts are focused on the term \mathbf{E}_{corr} . For a large order of n , it is time-consuming to computer Hankel functions and the Legendre functions which are obtained by an iteration method. Therefore, Debye's formulas for Hankel functions [8] and the following asymptotic expression of Legendre functions [9] are employed to avoid the iteration and thus greatly reduce the computational time

$$P_n(\cos \theta) = \sqrt{\frac{2}{\pi n \sin \theta}} \cos [(n + 0.5)\theta - \pi/4]. \quad (7)$$

Numerical results show that \mathbf{E}_{corr} converges much faster than $\mathbf{E}_{\text{image}}$.

2.2 Asymptotic Residue Solutions

The height of the dipole is z_s from the surface of the earth and the height of the observation point is z_r from the surface of the earth. Based on Watson's transformation, the electric field is given by Fock [6] and Wait [7]

$$E_r = E_0 \cdot e^{i\pi/4} \cdot \sqrt{\pi x} \cdot \sum_{s=1}^{\infty} \frac{1}{t_s - q^2} \frac{w_1(t_s - y_s)}{w_1(t_s)} \frac{w_1(t_s - y_r)}{w_1(t_s)} e^{it_s x}, \quad (8)$$

where

$$E_0 = \frac{iI d s k_1}{2\pi} \frac{\eta e^{ik_1 a \theta}}{a \sqrt{\theta \sin \theta}}, \quad (9a)$$

$$y_s = \left(\frac{2}{k_1 a}\right)^{1/3} k_1 z_s, \quad (9b)$$

$$y_r = \left(\frac{2}{k_1 a}\right)^{1/3} k_1 z_r, \quad (9c)$$

$$x = \left(\frac{k_1 a}{a}\right)^{1/3} \theta, \quad (9d)$$

$$q = \frac{k_1 \sqrt{k_2^2 - k_1^2}}{k_2^2} \cdot \tan\left(\sqrt{k_2^2 - k_1^2} l\right) \cdot \left(\frac{k_1 a}{2}\right)^{1/3}, \quad (9e)$$

while $w_1(t)$ is the Fock notation of the Airy function and the t_s are the solutions to the following equation

$$w_1'(t) - q w_1(t) = 0. \quad (10)$$

3. Numerical Results

In this section, we consider the example of the radio waves on the spherical earth. The earth radius is taken to be 6370 km. The numerical results by convergence acceleration method are given and compared with those from asymptotic expression. Investigation of the series shows that the oscillation of the series gets faster with the increase of the observation angle θ . Also, the series converges much slowly when $\theta \rightarrow 0$ or $\theta \rightarrow \pi$ while for θ not in the neighborhood of 0 or π , the convergence speed is not much different.

Figure 1 shows the series solution of the correction part E_{corr} computed from $n = 1$ to $n = 16000$ with a truncation error 10^{-4} . The thickness of the dielectric layer is taken to be $l = 100$ m and $\epsilon_r = 15$ at a frequency of 100 kHz. The dipole is placed at 10 m above the earth surface. The observation point is taken to be at $z_r = 500$ and the arc distance is 200 km.

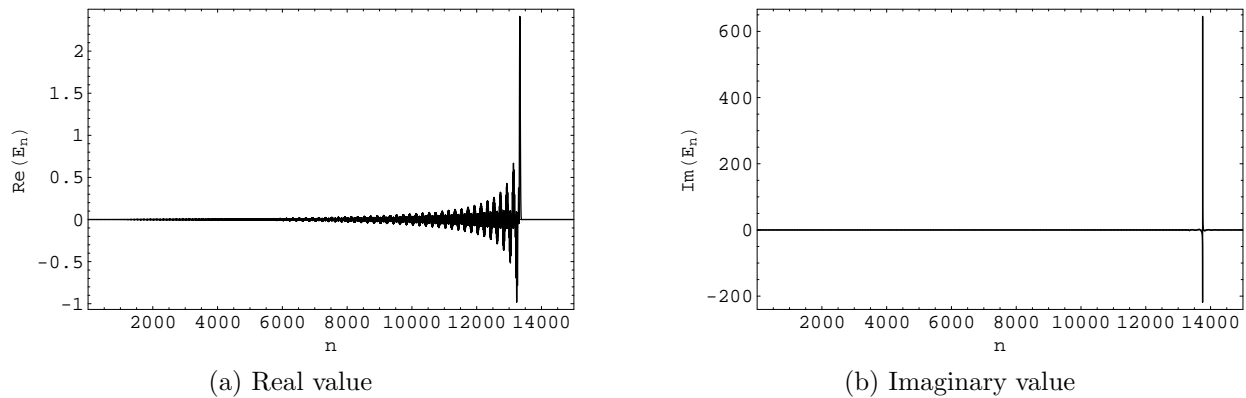


Figure 1: Convergence pattern of E_{corr}^r

From Figure 1 we can see that the magnitudes of the first 10000 terms are very small. The main contribution is from the terms near $k_1 r$ which is coincident with the analysis of Fock [6]. Figure 2 shows that the real and imaginary part of these terms. The summation of the first 10000 terms are $0.397905 - i0.33541$, while the summation of the first 16000 terms are $57.2283 + i107.29$.

Figure 3 shows the simulation results based on series and asymptotic solutions. The curve by series computation oscillates drastically, but the curve by asymptotic residue methods is very smooth and passes through the middle of the oscillating curve. Therefore, the residue method is verified to be a good approximation while the series solution is still an exact one.

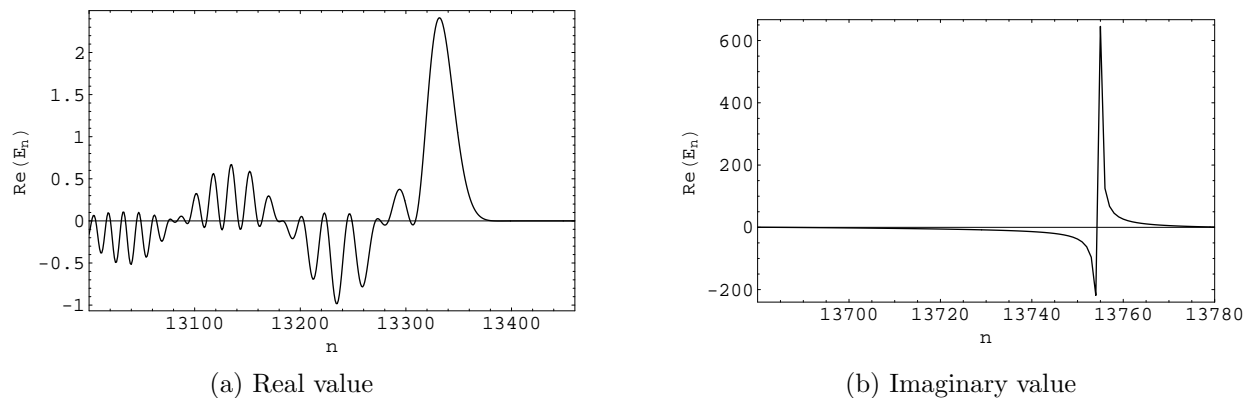
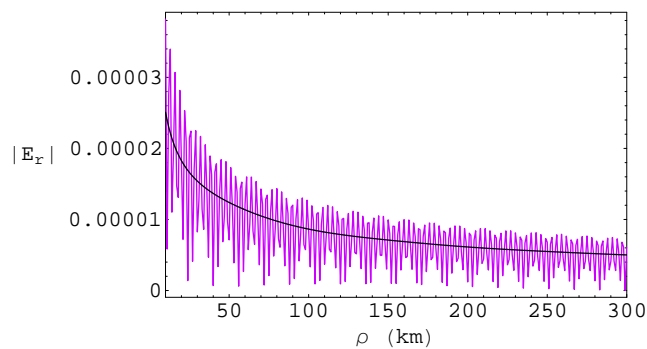
Figure 2: Convergence pattern of E_{corr}^r 

Figure 3: The comparison of field strengths between series solution (dash line) and residue solution (continuous curve).

4. Conclusion

The slow convergence problem of the radiation of a vertical dipole in the presence of a three-layered sphere is resolved in this paper. The total field is split into two parts and the analytical representation of the direct field and the convergence acceleration method for the scattered field are combined to give an efficient and accurate solution. The convergence property is analyzed. The computational results based on two methods are also compared.

REFERENCES

1. Chew, W. C., *Waves and Fields in Inhomogeneous Media*, Van Nostrand, New York, 1990.
2. Ishimaru, A., *Electromagnetic Wave Propagation, Radiation, and Scattering*, Prentice Hall, Englewood Cliffs, New Jersey, 1991.
3. Felsen, L. B., and Marcuvitz, N., *Radiation and Scattering of Waves*, Prentice-Hall, New Jersey, 1973.
4. Li, L. W., Fei, T., Wu, Q., Yeo, T. S, "Convergence acceleration for calculating radiated fields by a vertical electric dipole in the presence of a large sphere," *Antennas and Propagation Society International Symposium, 2005 IEEE*, Vol. 2B, 117–120, 2005.
5. Tai, C. T., *Dyadic Green's Functions in Electromagnetic Theory*, IEEE Press, Piscataway, New Jersey, 1994.
6. Fock, V. A., *Electromagnetic Diffraction and Propagation Problems*, Pergamon, Oxford, 1965.
7. Wait, J. R., *Electromagnetic Waves in Stratified Media*, IEEE Press, New York, 1996.
8. Sommerfeld, A. J. W., *Partial Differential Equations in Physics*, Academic Press, New York, 1949.
9. Abramowitz, M., Stegun, I., *Handbook of Mathematical Functions with Formulas, Graphs and Mathematical Tables*, Dover, New York, 1970.

Derivation of a conditional distribution of fade-slope by the analysis of absolute slope

F. F. Fondjo, K. Fujisaki, and M. Tateiba

Department of Computer Science and Communication Engineering
Kyushu University, Japan

T. Matsuoka

Department of Electrical Engineering
Kyushu Sangyo University, Japan

Abstract—Using a simple approach for data analysis, we present and discuss the derivation of fade slope conditional probability distribution based on its symmetry. From our analysis, we found that a more accurate distribution function is obtained by modeling the fade slope distribution based on its symmetry property rather than carrying the modeling process on the whole fade slope data set. Therefore, we proposed that the analysis process should be carried out using the absolute value of the fade slope in order to obtain more accurate results.

1. Introduction

With the congestion of lower frequency bands and the permanent demand by commercial satellite traffic for high data rate transfer capability, satellite designers tend to move to Ka (30/20 GHz) and above frequency bands which provide a prompt response to their need. Unfortunately, these frequencies are subject to severe climatic effects, especially rainfall, which generally constrain available bandwidth, thereby making the satellite link inefficient. This happens because link models used for estimation and control of satellite systems during the fading period, combined or not, refer to long-term and yearly averaged statistics. Therefore, real-time estimation and statistics of fades through the fade slope could be an alternative to efficiently understand the time to time behavior of satellite channels.

Many programs have been achieved by the European Space Agency and the NASA in order to efficiently characterize the satellite link for reliable services [1]. The data and results from these experiments are now used for link fade dynamics modeling and validation. Recently, these results have been adopted by the ITU-R community under the reference ITU-R P.1623 [2]. However, most of the measurements stored in databases during these campaigns had been made in temperate zones of the Northern Hemisphere [3][4] where rainfall outages seem to be minimal and reveal less fade dynamics than tropical and subtropical areas. Hence, the ITU-R results do not agree mostly with data from experiments carried out in latter areas. It therefore seems important to make worldwide measurements and build more reliable models that may agree with experiment from most rain regions.

Since the real-time estimation of fades turns out to be difficult due to the randomness of various physical phenomena affecting the satellite link, it is essential to use an important database of receive signal level in order to guarantee that the derived fade slope model should be close to the reality of the link. Due to the lack of enough data and in order to reduce the error between the model and the data, we exploited the symmetric of the fade slope that has been observed and confirmed by other researchers. In the paper, instead of deriving the fade slope distribution from the complete data set, we used the absolute value of the slope to increase the data set and capture all variations of the distribution. Then, based on the obtained conditional probability density of the absolute fade-slope, we derived the conditional fade slope distribution.

2. Experimental System and Fade Distribution

Kyushu University is situated between the ITU-R rain regions M and K. Since Kyushu is located in southern Japan, typhoons frequently cross this area, bringing a lot of rain. Our experimental system used for the data acquisition operates in Ku-band(14/12 GHz) and consists of 2 rainfall intensity sensors and 4 Very Small Aperture Terminals (VSATs) of 1.8 m diameter directed toward JCSAT-1B communication satellite at the geostationary orbit of longitude 150°E. The elevation angle is 45.6° for these stations. These VSATs are located as shown in Fig.1. The experimental system observes the received signal level and the rainfall intensity every

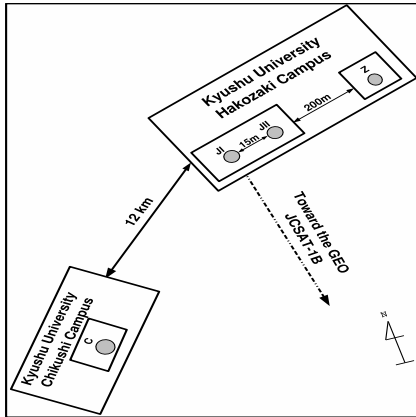


Figure 1: The location of Kyushu University VSATs experimental stations.

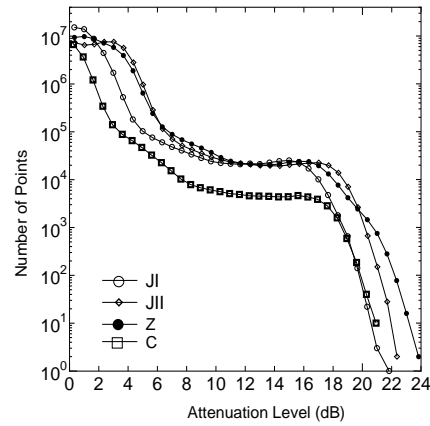


Figure 2: Number of data points collected for each VSAT station.

0.2 second and 1.0 second respectively. The modulation type is the QPSK with coding rate $r = 1/2$. During experiments, one of these VSATs is used for data transmission to the satellite and all of them receive the returned signal. This experimental stations are being used to conduct several experiments for earth-satellite link clarification in Ku-band since 1997. In this paper, these stations are called: Station JI, Station JII, Station Z, and Station C.

The analyzed data are the received signal levels. In order to contain as much rain events as possible, based on rainfall data, occurred attenuation data have been collected in 3 years (2000-2002) from June to September for stations JI, JII, and Z while for station C the data have been collected in 2000 from June to September. We can see from the distribution of rain attenuation presented in Fig. 2 that, although the number of faded points decrease with attenuation within the chosen period, the attenuation characteristic is almost the same as those observed in some tropical region [5].

3. Evaluation approach of the absolute fade slope conditional probability distribution

By definition, the fade slope is the measurement of the attenuation rate with respect to time [1]. If we suppose that we have a continuous time random received signal $Sl(t) = Sl_0(t) + m(t)$, where $m(t)$ is a zero-mean random process. Although the received signal level is continuous, it is always collected after a certain period of time and therefore the collected data are not often continuous. It is then important to define the discrete fade slope as follows:

$$\zeta_{\Delta t}(t_i) = \left(Sl_0\left(t_i + \frac{\Delta t}{2}\right) - Sl_0\left(t_i - \frac{\Delta t}{2}\right) \right) / \Delta t \quad (1)$$

This difference process is perfectly defined for any fixed $\Delta t > 0$ and $\zeta_{\Delta t}$ should converge to the desired continue time fade slope ζ as $\Delta t \rightarrow 0$. Many methods have been developed for the fade slope estimation [6]-[9].

Although the fade slope measures the slow varying rain attenuation rather than the fast-varying scintillation, we believe that it is reasonable to apply a strict filtering process rather than to use a long sampling period and differential step for suppressing scintillation effects. Long steps could lead to a reduction of the fade slope's range and therefore could give a false fade slope estimation as shown in Ref. [10]. In this reference, we showed that by applying a sampling period of 0.2 s and for the worst case 0.4 s could be used without aliasing the real variation of the received signal. In the following analysis, the raw data collected at 0.2 second period (i.e. differential step $\Delta t = 0.4$ s) is filtered by applying a 30 s moving average filter.

Let $p_A(\zeta)$ and $\tilde{p}_A(|\zeta|)$ be the fade slope and the absolute fade slope conditional probability distribution respectively. For the most general case, $p_A(\zeta)$ and $\tilde{p}_A(|\zeta|)$ are related by Eq. (2).

$$\tilde{p}_A(|\zeta|) = \begin{cases} p_A(-\zeta) + p_A(\zeta) & \text{if } \zeta \neq 0 \\ p_A(\zeta) & \text{if } \zeta = 0 \end{cases} \quad (2)$$

Previous studies on fade slope have shown that the fade slope conditional probability distribution has a symmetric shape along the p axis with a maximum at $\zeta \cong 0$ [2][3][10]. This characteristic implies that $p_A(-\zeta) \cong p_A(\zeta)$.

Since the $|\zeta| \in \mathbb{R}^+$ and that $|\zeta| = 0$ is binned together with $|\zeta| \rightarrow 0$, $p_A(\zeta)$ will be calculated as follows:

$$p_A(\zeta) = \frac{1}{2} \tilde{p}_A(|\zeta|) \quad \text{if } \zeta \neq 0 \tag{3}$$

and $p(\zeta = 0)$ will be obtained by extrapolating $\tilde{p}_A(|\zeta|)$ to $\zeta = 0$.

4. Data Analysis and Results

By using the absolute value of the slope, we can increase the number of data points while reducing the fluctuation and then allow an accurate derivation of the probability distribution model. Figure 3 presents the variation of conditional probability distribution of the absolute fade slope for each experimental station.

In order to model the variation of the conditional probability distribution of absolute fade slope, we evaluated the standard deviation and the normalized absolute fade slope as follows:

$$\sigma_{|\zeta|}(A) = \sqrt{\frac{1}{N} \sum_{i=1}^N (|\zeta|_i - |\zeta|_{\text{ave}})^2} \tag{4}$$

$$\hat{\sigma}_{|\zeta|} = \frac{\sigma_{|\zeta|}}{A \cdot F(f_{3\text{dB}}, \Delta t)} \tag{5}$$

where $|\zeta|$ is the absolute fade slope set calculated at the attenuation threshold A and $|\zeta|_{\text{ave}}$ the average of $|\zeta|$,

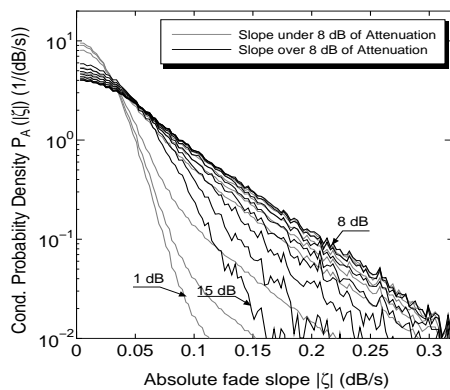


Figure 3: Absolute fade slope conditional probability distribution as observed in all VSAT stations.

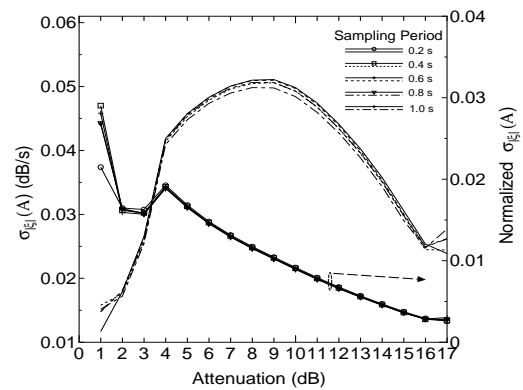


Figure 4: Absolute fade slope and normalized absolute fade slope standard deviation as observed in all VSAT stations for different sampling rate.

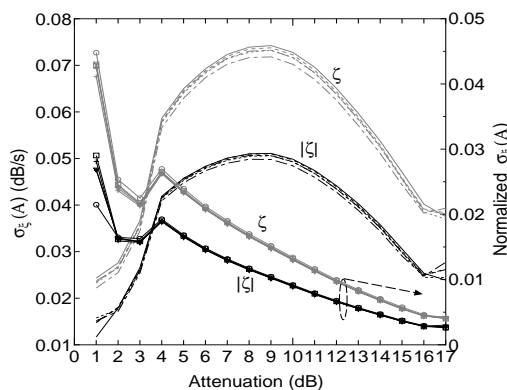


Figure 5: Impact of the absolute value of fade slope on the standard deviation. Similar results were obtained in all stations.

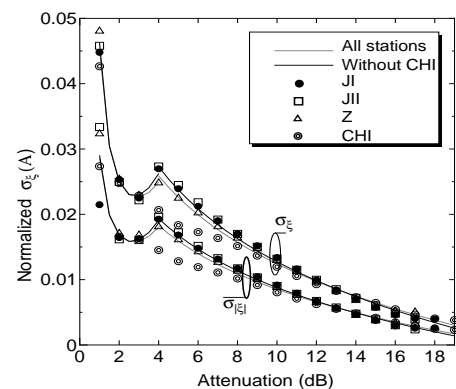


Figure 6: Fitted curve of the normalized standard deviation of absolute fade slope.

Table 1: Parameters obtained in Eq. (7)

Stations	α	β	γ	α'	β'
Standard deviation of ζ (σ_ζ)					
With C	2.53×10^{-2}	1.79	-1.69	4.62×10^{-2}	-31.76×10^{-2}
Without C	2.37×10^{-2}	1.95	-1.86	4.92×10^{-2}	-32.19×10^{-2}
Standard deviation of $ \zeta $ ($\sigma_{ \zeta }$)					
With C	1.58×10^{-2}	1.81	-1.61	3.30×10^{-2}	-32.22×10^{-2}
Without C	1.47×10^{-2}	1.97	-1.77	3.53×10^{-2}	-32.62×10^{-2}

$$F(f_{3\text{dB}}, \Delta t) = \pi\sqrt{2} \left[f_{3\text{dB}}^{-b} + (2\Delta t)^b \right]^{-1/2b}$$

is given in ITU-R P.1623 with $b = 2.3$.

$f_{3\text{dB}}$ is the 3 dB cut-off frequency of the 30 s moving average filter. $f_{3\text{dB}} = 1.47 \times 10^{-2}$, 1.46×10^{-2} , 1.45×10^{-2} , 1.44×10^{-2} , and 1.43×10^{-2} Hz for sampling rate 0.2, 0.4, 0.6, 0.8 and 1.0 s respectively (i.e. $\Delta t = 0.4, 0.6, 1.2, 1.6$ and 2.0 s respectively).

Figure 4 shows the variation of the standard deviation and the normalized standard deviation of the absolute fade slope. From this graph we can still observe as mentioned in [10] that the standard deviation of the fade slope has a maximum around 8 dB and that its normalization depends only on the attenuation threshold. Figure 5 presents the impact of the absolute value on the standard deviation. We can observe that the absolute value reduces considerably the variations observed around the mean value of the fade slope i.e. reduces the standard deviation of the slope. With an optimal curve search software and according to the fact that $p_A(-\zeta) \cong p_A(\zeta)$, we observed that the distribution presented in Fig. 3 can be modeled by Eq. (6) for most rain regions [5].

$$p_A(|\zeta|; \nu, \sigma_{|\zeta|}) = \frac{\nu}{\pi\sigma_{|\zeta|} \left(1 + \left(\frac{|\zeta|}{\sigma_{|\zeta|}} \right)^2 \right)^n} \Rightarrow p_A(\zeta; \nu, \sigma_\zeta) = \frac{\nu/2}{\pi\sigma_\zeta \left(1 + \left(\frac{\zeta}{\sigma_\zeta} \right)^2 \right)^n} \quad (\text{dB/s})^{-1} \quad (6)$$

where $\nu, \sigma_{|\zeta|}$ are positive and real parameters that vary according to the rain region and $n \in \mathbb{N}^*$. ν is derived by fitting the curves in Fig. 3 for all stations. From the fitted data and for all stations the best fit for all stations is obtained for $\nu = 1$ and $n = 2$. We assumed that the normalized standard deviation does not depend on the geographical position of the station. By fitting $\hat{\sigma}_{|\zeta|}$ and σ_ζ as shown in Fig. 6 for all stations with and without the station C and considering the Eq. (5), we derived $\sigma_{|\zeta|}$ as described by Eq. (7). We note that similar function was also obtained for σ_ζ .

$$\sigma_{|\zeta|}(A) = A F(f_{3\text{dB}}, \Delta t) \times \begin{cases} \alpha\beta^A A^\gamma & \text{for } A \leq 4 \text{ dB} \\ \alpha'(1 + \beta' \ln(A)) & \text{for } A \geq 4 \text{ dB} \end{cases} \quad (7)$$

where $\alpha, \beta, \gamma, \alpha'$ and β' are given in Table 1 for $\sigma_{|\zeta|}$ and σ_ζ .

To evaluate the model performance, we defined the Root Mean-Square Error (RMSE) as follows:

$$RMSE_A = \sqrt{\frac{1}{N+1} \sum_{i=-\frac{N}{2}}^{\frac{N}{2}} \left(p_A(\zeta_i; \nu, \sigma_\zeta) - \tilde{p}_A(\zeta_i) \right)^2} \quad (8a)$$

$$RMSE = \frac{1}{17} \sum_{A=1}^{A=17} RMSE_A \quad (8b)$$

where A is a given attenuation threshold in dB, $p_A(\zeta_i; \nu, \sigma_\zeta)$ the modeled function and $\tilde{p}_A(\zeta_i)$ the distribution obtained from experimental data. By applying Eq. (8) to experimental data using σ_ζ without C, we obtained for the proposed analysis approach a RMSE $\approx 0.0011, 0.0010, 0.0013$ and 0.0017 for stations JI, JII, Z and C

respectively while using the distribution function proposed in Ref. [10], we obtained the $RMSE \approx 0.7, 0.75, 0.73$ and 0.8 for stations stations JI, JII, Z and C respectively. We can see from these results that the proposed approach can help in an efficient derivation of the fade slope conditional probability distribution. We note that the fade slope obtained in studied rain region does not agree with the model proposed in Refs. [2][4] as mentioned in Ref. [10]. Therefore comparisons are carried out only for improved fade slope model from our stations.

5. Conclusion

This paper evaluated the conditional probability distribution of absolute the fade slope and derived the conditional probability of the fade slope. From the analyses carried out in this paper, we found that the fade slope probability distribution function could be derived from data with high accuracy ($RMSE \approx 0.002$) if the symmetry of the fade distribution is exploited. Therefore, we would like to recommend the estimation steps used in this paper to be the fade slope distribution modeling process.

REFERENCES

1. Julie F., Louis J. I. et al., "Fade Slope Analysis for Alaska, Florida, and New Mexico ACTS Propagation Data at 20 and 27.5 GHz," Proc. of The IEEE, Vol.85, No.6, pp.926-035, June 1997.
2. Rec. ITU-R P.1632, Prediction method of fade dynamics on Earth-space paths, 2003.
3. Max M. J. L. van de Kamp, "Statistical Analysis of Rain Slope," IEEE Trans. on Ant. and Prop., Vol. 51, No.8 August 2003.
4. Max M. J. L. van de Kamp, "Climatic Radiowave Propagation Models for satellite Communication systems," Ph.D dissertation, Eindhoven Univ. Tech., 1999.
5. Harry E. Green, "Propagation Impairment on Ka-Band SATCOM Links in Tropical and Equatorial Regions," IEEE Ant. and Prop. Magazine, Vol.46, No.2, pp. 31-45, April 2004.
6. M.M.J.L. van de Kamp and L. Castanet, "Propagation Impairment Mitigation for Millimeter Wave Radio Systems: Fade dynamics Review," PM3018, 1st International Workshop, July 2002.
7. Baxter P. D., Upton G. J. G. and Eden D., "Revised method for calculation of rain-fade-slope", Electronics Letters, 37(10), 658-660,2001.
8. Steven W. Smith, The Scientist and Engineer's Guide to Digital Signal Processing, Second Edition, Chap.15, California Technical Publishing, San Diego, California,1999.
9. J. S. Simonoff, Smoothing Methods in statistics, Springer Series, Springer, 1996.
10. F. F. Fondjo, K. Fujisaki, and M. Tateiba, "Fade Dynamics on Earth-Space Paths at Ku-Band in Fukuoka, Japan Fade-Slope Evaluation, Comparison, and Model", IEEE Ant. and Wireless Prop. Letters, Vol. 5, pp.80-83, 2006

The Two-Sample Model: Short-term Prediction of Rain Attenuation

M.M.J.L. van de Kamp

University of Bath, UK

Abstract—The ‘Two-Sample Model’ predicts the probability distribution of rain attenuation a short time after a measured value, dependent on the values of two previous samples of rain attenuation. This model can be used in the design of FMT systems, to determine the required tracking speed, and can also be implemented in the FMTs themselves, to predict the probability of fades in the very near future. Furthermore, it can be used for data simulation models of rain attenuation, useful for channel modelling, to test FMTs.

A theoretical model has been developed to calculate the three parameters of the Two-Sample-Model from rain rate measurements. This model depends on wind speed, wind direction, vertical air velocity and rain height, and on the elevation and azimuth angles and the frequency of the link. The model is compared to measurements of attenuation on a satellite link in the UK, and gives good results on the long term. The verification of the dependence on meteorological parameters is limited by the resolution of the meteorological data used.

With this addition, the Two-Sample-Model parameters can be derived for different configurations using only rain rate measurements and other meteorological data. This will provide a great opportunity for the assessment of the parameters on many sites on earth where expensive satellite link measurements have not been performed, which will facilitate the design of FMTs for these sites.

1. Introduction

Rain attenuation is one of the most fundamental limitations to the performance of satellite communication links in the microwave region, causing large variations in the received signal power, with little predictability and many sudden changes. In the Ka- and V-bands, the attenuation caused by rain is too severe to be accounted for by a fixed margin in the link budget. This is why Fade Mitigation Techniques (‘FMTs’) are developed, which compensate for rain attenuation by adaptively improving the quality of the link only when the signals are degraded.

To aid the design of FMT systems, the ‘Two-Sample Model’ [1] [2] has been developed, which predicts the probability distribution of rain attenuation a short time after a measured value, dependent on the values of two previous samples of rain attenuation. This model can be used in the design of FMT systems, to determine the fade slope to be expected with a certain attenuation, and determine the required tracking speed. It can also be implemented in the FMTs themselves, to predict the probability of fades in the very near future. Furthermore, it can be used for data simulation models of rain attenuation, which are useful for channel modelling, to test FMTs.

The Two-Sample Model is described as follows. The probability distribution $p(A)$ of attenuation A at time $t+\Delta t$ is dependent on the two previous attenuation values A_0 at time t , and A_{-1} at time $t-\Delta t$, as:

$$p(A) = \frac{m_A}{2A\sigma_A} \operatorname{sech}\left(\frac{\pi m_A \ln(A/m_A)}{2\sigma_A}\right) \quad (1)$$

$$m_A = A_0 (A_0/A_{-1})^{\alpha_2} \quad (2)$$

$$\sigma_A = A_0 \sqrt{\beta_2 \Delta t} + A_0 \gamma_2 \left(1 - e^{-|\ln(A_0/A_{-1})|}\right) \quad (3)$$

where $\Delta t = 10$ s. The parameters α_2 , β_2 and γ_2 are site dependent; recommended values obtained from averages over western Europe are: $\alpha_2 = 0.4$, $\beta_2 = 2 \times 10^{-4} \text{ s}^{-1}$, and $\gamma_2 = 0.4$. For a given link, the parameters can be calculated from three dynamic quantities of rain attenuation: the autocorrelation \mathcal{A}_ζ of fade slope for a time lag of 10 s, and the variance $\sigma_{\zeta_r}^2$ and kurtosis K_{ζ_r} of relative fade slope. The fade slope ζ and relative fade slope ζ_r are defined as

$$\zeta(t) = \{A(t+\Delta t) - A(t)\} / \Delta t \quad (\text{dB/s}) \quad (4)$$

$$\zeta_r(t) = \{A(t+\Delta t) - A(t)\} / A(t) \Delta t \quad (\text{s}^{-1}) \quad (5)$$

The autocorrelation \mathcal{A}_ζ of fade slope and the variance $\sigma_{\zeta_r}^2$ and kurtosis K_{ζ_r} of the relative fade slope are related to the model parameters α_2 , β_2 and γ_2 as follows:

$$\mathcal{A}_\zeta = \alpha_2 \quad (6)$$

$$\sigma_{\zeta_r}^2 = \frac{\beta_2}{\Delta t} (1 - \alpha_2^2)^{-(0.9+2.0\gamma_2)} (1 - \gamma_2)^{-1.4} \quad (7)$$

K_{ζ_r} is related to α_2 and γ_2 as shown in Figure 1 [1].

Because the Two-Sample Model uses two previous samples, when used for short-term prediction of rain attenuation it predicts the attenuation distribution more accurately than similar models which use only one previous sample value. When used in simulation of time-series data, the result of the Two-Sample Model represents better the dynamic behaviour of a rain attenuation event [1].

2. Theory of the dynamics of rain attenuation

Because the input parameters of the Two-Sample Model are dependent on location and on meteorological parameters [3], these have to be determined for every link separately. It would be useful if these could be estimated from rain rate measurements instead of attenuation measurements.

According to the ITU-R recommendation [4], rain attenuation A is related to the rainfall intensity, or ‘rain rate’ R (mm/hr) as $L_E a R^b$, with L_E is the effective path length through rain, and a and b are frequency-, elevation- and polarisation-dependent coefficients [5]. However, rain rate is not uniform along the propagation path, so the path length L_E should be expressed as an integral along the path. In Figure 2, the situation is depicted seen from above. The integral is performed along the line S_1 - P_1 , with S_1 the ground station. The orientation of this line is defined by the azimuth angle θ_l of the link.

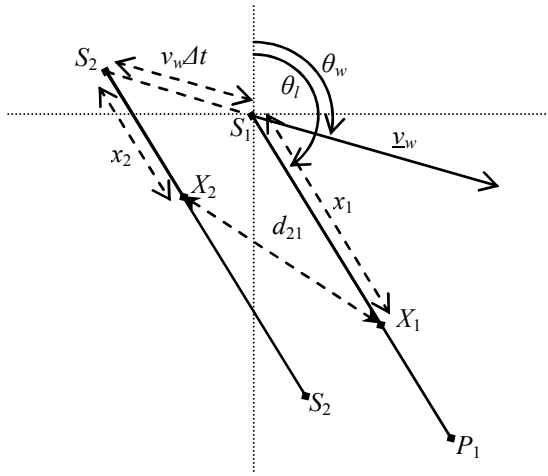


Figure 2: Configuration (seen from above) with the wind moving a rainstorm across the measurement site.

with \mathcal{A}_A^* is the autocorrelation of attenuation, and \mathcal{A}_A its correlation coefficient (normalised); these are given by [3]:

$$\mathcal{A}_A^*(\Delta t) = \frac{a^2}{\cos^2 \varepsilon} \int_0^{h_r/\tan \varepsilon} \int_0^{h_r/\tan \varepsilon} \mathcal{A}_{R^b}^*(d_{12}) dx_1 dx_2 \quad (11)$$

$$\mathcal{A}_A(\Delta t) = \frac{\int_0^{h_r/\tan \varepsilon} \int_0^{h_r/\tan \varepsilon} \mathcal{A}_{R^b}(d_{12}) dx_1 dx_2}{\int_0^{h_r/\tan \varepsilon} \int_0^{h_r/\tan \varepsilon} \mathcal{A}_{R^b}(|x_1 - x_2|) dx_1 dx_2} \quad (12)$$

with h_r is the rain height and ε is the elevation angle, and $\mathcal{A}_{R^b}^*$ the *spatial* autocorrelation of R^b , for a distance of d_{12} , and \mathcal{A}_{R^b} is its autocorrelation coefficient. From Figure 2 can be derived that the distance d_{12} is equal to:

$$d_{12} = \sqrt{v_w^2 \tau^2 + (x_1 - x_2)^2 + 2(x_1 - x_2)v_w \tau \cos(\theta_w - \theta_l)} \quad (13)$$

Furthermore, in (10) $\mathcal{A}_A^*(0, \Delta t, \Delta t)$, etc., is the integral of the product of *four* samples of attenuation separated by three time shifts. These can be found similarly as (11) [3].

The spatial autocorrelation of rain rate $\mathcal{A}_{R^b}^*$ can be found from the dynamic model of rain attenuation derived by Maseng and Bakken [7] using stochastic theory. Since in the derivation of their model, they did not take into account any path integration effect, the model may be expected to describe the temporal dynamic behaviour of rain rate. This can be converted to a spatial model using the ‘frozen storm’ hypothesis: the dependence on time τ can be converted to

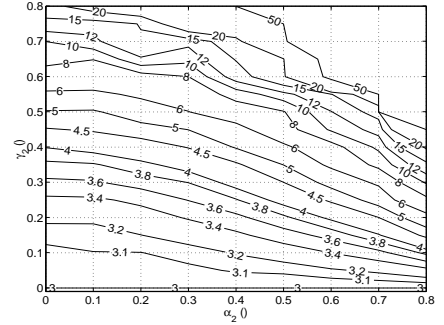


Figure 1: Contour plot of K_{ζ_r} as a function of α_2 and γ_2 .

dependence on distance d along the wind direction by substituting $\tau = d/v_w$, where v_w is the magnitude of the wind speed. Using this model, the spatial autocorrelation $\mathcal{A}_{R^b}^*$ and autocorrelation coefficient \mathcal{A}_{R^b} of R^b are found as [7]:

$$\mathcal{A}_{R^b}^*(d) = m_R^{2b} e^{b^2 \sigma_{\ln R}^2 (1 + e^{-B_x d})} \quad \mathcal{A}_{R^b}(d) = e^{b^2 \sigma_{\ln R}^2 (e^{-B_x d} - 1)} \quad (14)$$

where m_R is the long-term median value of R , $\sigma_{\ln R}$ is the long-term standard deviation of $\ln R$ and B_x is a parameter describing the spatial dynamics of rain rate.

In order to derive the parameters B_x and $\sigma_{\ln R}$, the autocorrelation was derived from rain rate data measured by Rutherford Appleton Laboratory (RAL), in Sparsholt and Chilbolton (8 km apart), UK, consisting together of 85 months of data measured in April 1997 - July 2005. To study the relation with meteorological information, meteorological data were obtained from the European Centre for Medium-range Weather Forecasts (ECMWF), from their 'ERA-40' database and its continuation 'Operational Data' [8]. These global data have a resolution of 6 hours and of 2.5° in longitude and latitude. From this database, the absolute value of wind speed v_w (m/s) at the pressure level 850 mbar was obtained, which is on average approximately 1.5 km high, the approximate height where the rain clouds are. Furthermore, the vertical air velocity v_{ver} (Pa/s) at the same height was obtained. This parameter is an indicator for the type of rain, since convective rain is associated with the updraft of air. The values were bilinearly interpolated to obtain the values in Sparsholt and Chilbolton.

The values of the parameters B_x and $\sigma_{\ln R}$ were derived by fitting the Maseng-Bakken model to the autocorrelation derived from the rain rate measurements, dependent on vertical velocity v_{ver} and wind speed v_w . The result of this is

$$B_x = 1.05 \times 10^{-3} \text{ m}^{-1} \quad \sigma_{\ln R} = 0.748 e^{1.495 v_{ver}} \quad (15)$$

3. Comparison with measurements

The theoretical model for the three dynamic quantities of rain attenuation, presented in the previous section, was tested by comparison to the parameters calculated from Italsat rain attenuation data, which were measured in Sparsholt, UK, by RAL during 44 months in April 1997 - January 2001, at 19, 40 and 50 GHz. The system parameters of this link are: $\theta_l = 161.7^\circ$, $\varepsilon = 29.9^\circ$, $\Delta t = 10$ s, and $b = 1.08$, 0.93 and 0.87 for 19, 40 and 50 GHz respectively. The input parameters v_w , θ_w , v_{ver} and h_r for the model of the dynamic parameters of rain attenuation, meteorological parameters were obtained from ECMWF.

First, the model for the autocorrelation coefficient of fade slope for a time length Δt , given in (8), was tested. The data from the three frequencies were put together to increase statistical significance, because the autocorrelation of fade slope is very similar for these three frequencies. Figure 3 (left) shows the autocorrelation of fade slope as a function of v_w and for $\theta_w = 30^\circ$, 60° and 90° ($\pm 15^\circ$), and for $h_r > 1600$ (because it was found that the model does not depend significantly on h_r in this range). Also included is the model for $\theta_w = 30^\circ$ and 60° (the latter of which is very close to the result for $\theta_w = 90^\circ$), and using the long-term average values of $h_r = 2550$ m and $v_{ver} = -0.131$ Pa/s (the average values during the attenuation measurements in Sparsholt). This figure shows in general a good agreement between the model and the measurements. Only for v_w decreasing below about 12 m/s, the measurements and the model start deviating, suggesting

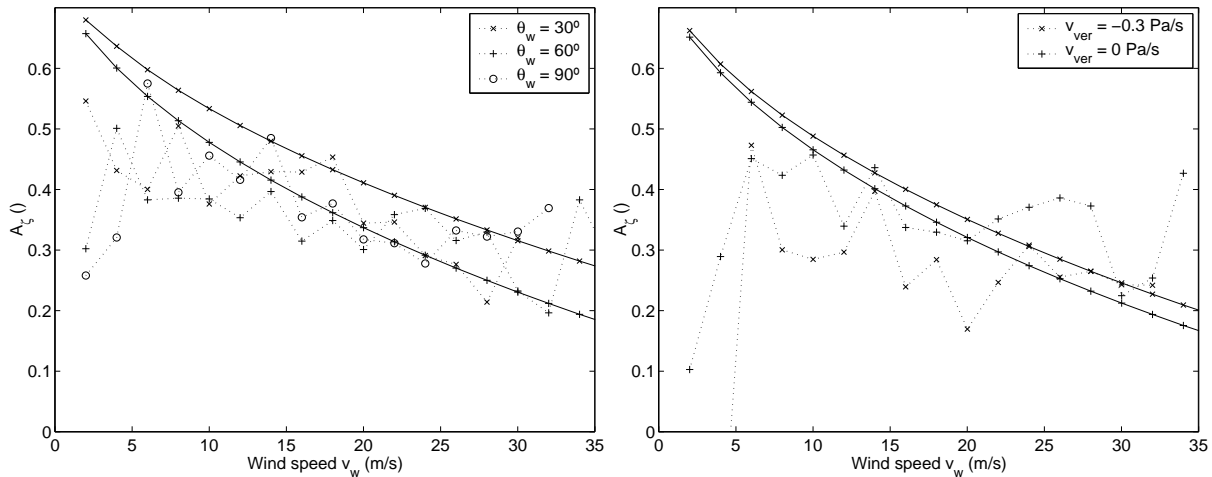


Figure 3: The measured autocorrelation coefficient of fade slope, as functions of v_w : (left) dependent on θ_w , with $h_r > 1600$ m, and the model for $h_r = 2550$ m and $v_{ver} = -0.131$ Pa/s; and (right) dependent on v_{ver} , with $h_r > 1600$ m and $50^\circ < \theta_w < 90^\circ$; and the model for $h_r = 2550$ m and $\theta_w = 60^\circ$.

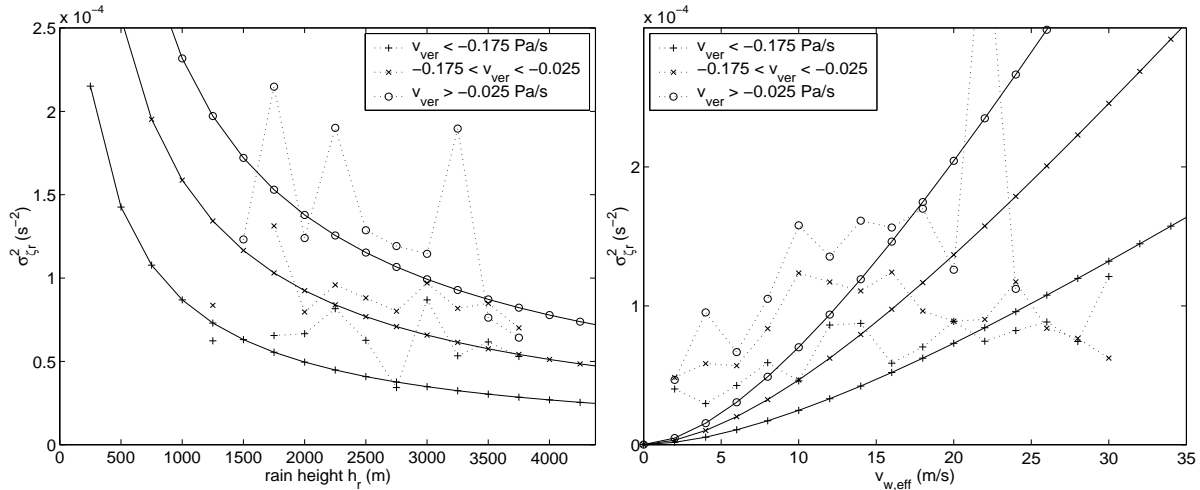


Figure 4: The measured variance of relative fade slope for three ranges of v_{ver} (.....): (left) as a function of h_r , and the theoretical expression with $v_{w,eff} = 13.6$ m/s (—); (right) as a function of $v_{w,eff}$, and the model with $h_r = 2550$ m (—).

that for low wind speeds, the assumption of the frozen storm hypothesis is not entirely correct, and some of the dynamic behaviour of rain is caused by the development of rain storms.

Figure 3 (right) shows the autocorrelation of fade slope as a function of v_w for $v_{ver} = -0.3$ Pa/s and 0 Pa/s (± 0.15), and using $h_r > 1600$ m and $50^\circ < \theta_w < 90^\circ$ (the model does not depend significantly on θ_w in this range). Also included are the results of the model, with $h_r = 2550$ m and $\theta_w = 60^\circ$ (average values in Sparsholt). This figure shows that the theoretical dependence on v_{ver} is not observed in the measurements, but on the other hand, this dependence is so weak that this is not very surprising.

Because the model for the variance $\sigma_{\zeta_r}^2$ of relative fade slope, given in (9), depends significantly on frequency, this was compared to measurements at 50 GHz only. For the purpose of comparing to measurements, the 'effective wind speed' $v_{w,eff}$ is used, which is equivalent to the wind speed for $\theta_w = \theta_l + 90^\circ$, and takes into account the dependence on both v_w and θ_w .

Figure 4 (left) shows $\sigma_{\zeta_r}^2$ as a function of h_r for different values of v_{ver} , and the model, with $v_{w,eff} = 13.6$ m/s (average value in Sparsholt). This figure shows that the model increases with v_{ver} similarly to the measurements. The variation with h_r is only slightly recognised in the measurements. However, it should be noted that the fact that the values are in the right order of magnitude is already an indication that the dependence of the model on rain height is in agreement with the measurements. If the model would be based on attenuation calculated from point rain rate, its result for the relative fade slope would be much larger, as can be seen in Figure 4 for $h_r = 0$ m (equivalent to a zero path length). It is the integrating effect along the path length which reduces the variance of relative fade slope to the order of magnitude observed. The results in this figure therefore show that the incorporation of the rain height in the model is well in agreement with measurements.

Figure 4 (right) shows $\sigma_{\zeta_r}^2$ as a function of $v_{w,eff}$ for different values of v_{ver} , and compared to the model, with $h_r = 2550$ m. This figure shows again that the average values of the model are in agreement with the measured values, but the model increases with $v_{w,eff}$ stronger than the measurements. Especially for small wind speeds, the measured $\sigma_{\zeta_r}^2$ is larger than the model. This is possibly due to the frozen-storm hypothesis. Furthermore, it was found that the use of a long-term average effective wind speed of 13.6 m/s (as in the left hand graph) gives a good agreement with measurements. This suggests that the wind speed used, with a resolution of 2.5° and 6 hours, may not be a good representative of the instantaneous wind speed on the propagation path during the measured rain event. Given the generally strong variability of wind, it seems likely that meteorological data with a higher temporal and spatial resolution would improve the correlation between the variance of relative fade slope and wind speed.

The model for the kurtosis of relative fade slope K_{ζ_r} , given in (10), was compared to measurements at 40 and 50 GHz. Figure 5 (left) shows K_{ζ_r} as a function of h_r , and the results of the theoretical expression, with $v_w = 16.3$ m/s and $v_{ver} = -0.131$ Pa/s (average values in Sparsholt). This figure shows that the model agrees reasonably with the measurements only for rain heights above about 2500 m. Below this, the model increases with decreasing rain height while the measured values decrease.

Figure 5 (right) shows K_{ζ_r} as a function of v_w , and compared to the model, with $h_r = 2550$ m and $v_{ver} = -0.131$ Pa/s. This figure shows that for the dependence on wind speed, the model agrees with the measurements: neither show any significant dependence on wind speed, and their values agree well for both frequencies.

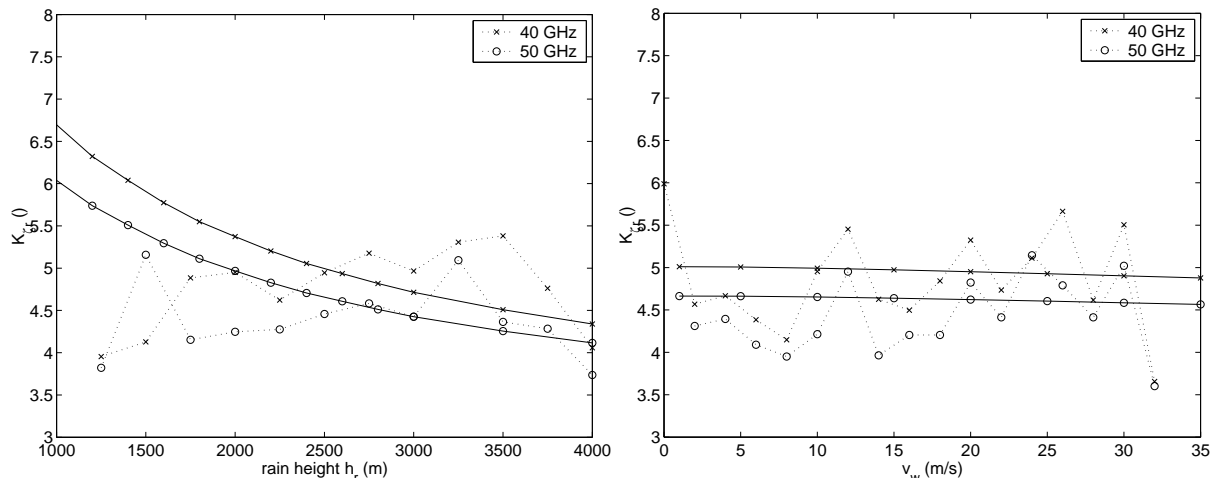


Figure 5: The measured kurtosis of relative fade slope (\cdots): (left) as a function of h_r , and the model with $v_w = 16.3$ m/s (—); (right) as a function of v_w , and the model with $h_r = 2550$ m (—). $v_{ver} = -0.131$ Pa/s.

4. Conclusions

The Two-Sample Model is a useful tool in the design for FMT systems. A model has been developed to predict the parameters of the Two-Sample Model from rain rate measurements. This model uses the frozen-storm hypothesis, and the property that the attenuation is a result of the integrated effect of rain along the propagation path.

The models for all three dynamical quantities agree well with the measurements for long-term average values of the meteorological parameters, and also in correlation with some meteorological parameters, but not with all parameters. This may be partly due to the frozen-storm hypothesis being not correct for small wind speeds, and partly due to the limited resolution of the meteorological data. At least, the results suggest that the expressions can be used to derive static climate-dependent values of the dynamical quantities of attenuation for a particular site from rain measurements and other meteorological data.

After these expressions are further validated with other measurements, they will allow to assess the long-term values of the parameters of the Two-Sample Model from rain gauge data, without the use of rain attenuation data. This can prove very useful to obtain the parameter values for sites where satellite measurements have not been performed, but rain rate measurements, which are much cheaper and easier to do, have.

Acknowledgment

This study has been performed as an External Research Fellowship for the European Space Agency (ESA). I would like to thank ESA for providing this Fellowship, the University of Bath for hosting me, and Rutherford Appleton Laboratory, Chilton, UK, for providing the attenuation and rain rate data.

REFERENCES

1. van de Kamp, M., "Dynamic Modelling of Rain Attenuation", POSTDOC Research Report, ONERA, Toulouse, France, RT 1/06733.04 DEMR, March 2003.
2. van de Kamp, M.M.J.L., "Short-term prediction of rain attenuation using two samples", *Electron. Lett.*, Vol. 38, 1476–1477, 2002.
3. van de Kamp, M., "Theoretical and empirical studies of the dynamic parameters of rain attenuation", External Fellowship Report, European Space Agency, September 2005.
4. ITU-R, "Propagation data and prediction methods required for the design of Earth-space telecommunication systems", Recommendations of the ITU-R, Rec.P.618-8, 2003.
5. ITU-R, "Specific attenuation model for rain for use in prediction methods", Recommendations of the ITU-R, Rec.P.838-2, 2003.
6. Taylor, G. I., "Statistical theory of turbulence", *Proc. Roy. Soc. London*, A164, 1938, pp. 476-490.
7. Maseng, T. and P. M. Bakken, "A Stochastic Dynamic Model of Rain Attenuation", *IEEE Transactions on Communications*, Vol. 29, 660–669, 1981.
8. European Centre for Medium-Range Weather Forecasts, <http://www.ecmwf.int/>

Rain Attenuation Characteristics of Up and Down Link Radio Waves of Ku-band Satellite Communications Observed in Japan and Indonesia

Yasuyuki Maekawa, Shinichi Tsujino, and Yoshiaki Shibagaki

Dept. of Telecommunications & computer networks Osaka Electro-Communication University, Japan

Toru Sato

Dept. of Communications & Computer Engineering, Kyoto University, Japan

Mamoru Yamamoto, Hiroyuki Hashiguchi, and Shoichiro Fukao

Research Institute for Sustainable Humanosphere, Kyoto University, Japan

Abstract - Rain attenuation characteristics of up- and down-link radio waves of Ku-band satellite communications in both Japan and Indonesia are presented for the past three years of 2003-2005, using Japan's domestic communication satellite Superbird C (144 ° E in orbit) that connects Research Institute for Sustainable Humanosphere of Kyoto University (RISH) to Equatorial Atmosphere Radar Observatory (EAR; 0.2 ° S, 100.3 ° E). The yearly cumulative time percentages of the observed rain attenuation are in good agreement with the ITU-R (International Telecommunication Union – Radiocommunication Sector) predictions for both locations in Japan and Indonesia. At EAR in Indonesia, however, the time percentages of both up- and down-link attenuation become much smaller than the ITU-R predictions in the range of larger than 10 dB. This indicates the reduction of equivalent path length down to about 2 km, as also revealed by the X-band radar observations along the same propagating path. This equivalent path length seems rather short compared with those obtained in other tropical observation sites, being attributed to unique features of the EAR site that is located in a highland basin and has a comparatively low elevation angle of 39 ° even in the tropics.

Key words: *Rain attenuation, Ku-band, Satellite Communication, Tropics*

1. Introduction.

Rain attenuation of the radio wave used in satellite communications is a significant problem for frequency bands of higher than 10 GHz such as Ku band (14/12GHz) and Ka (30/20) GHz [1-3]. The rain attenuation problem becomes quite severe even for Ku-band radio waves in heavy rain regions like tropics [4-5]. Demand for high capacity satellite communications using the Ku band, however, is rapidly increasing in new developing areas such as the South-East Asia, which is included in one of the world heaviest rain regions [6-7]. Therefore, it is urgent to investigate the Ku-band rain attenuation characteristics in more detail in the tropics.

In this study, signal levels of Ku-band satellite radio waves are received at both VSAT (Very Small Aperture Terminal) stations of Superbird C that connect Research Institute of for Sustainable Humanosphere of Kyoto University (RISH) in Japan to Equatorial Atmosphere Radar Observatory (EAR) in Indonesia [8]. The measurements of the signal levels have been continuously conducted since January 2003 at both stations. The up-link attenuation at each station in rainy condition, which is usually difficult to obtain, is estimated from the down-link signal level simultaneously measured at its opposite station in clear sky condition. The measurements of up-link attenuation are thus made possible by the property of SCPC (Single Channel Per Carrier) signals used in this experiment, which are linearly amplified without saturation of the satellite transponders [9].

This paper presents the rain attenuation characteristics of the Ku-band satellite communications in the tropics for the past three years from January 2003 to December 2005. Some differences are pointed out in their characteristics between the temperate and tropical regions. Specifically, their statistics are compared with the recent ITU-R (International Telecommunication Union – Radiocommunication Sector) predictions [10], and discrepancies in time percentages in a high attenuation range are discussed in light of the reduction of equivalent path length through the tropical convective precipitating clouds. The discussion is partly verified by simultaneous X band radar observations conducted at the EAR Observatory. Also, observational results on Ku-band satellite signal measurements in other nearby tropical sites are introduced for the comparison.

2. Observational Results

The EAR observatory of Kyoto University is located in West Sumatra Prefecture, Indonesia (EAR; 0.2° S, 100.3° E). The VSAT station here uses the up-link transmission frequency of 14.4651 GHz and the down-link receive frequency of 12.3992 GHz. The elevation angle is 39° , which is rather low for the equatorial region, since it is connected to Japan's domestic communication satellite (144° E in orbit) launched around the longitude of Japan. At RISH, in Uji, Japan, the up-link transmission frequency is 14.1292 GHz, and the down-link receive frequency is 12.7351 GHz. The elevation angle is 49° . At both stations, the up-link radio waves use the vertical linear polarization, while the down-link radio waves use the horizontal linear polarization. Also, both VSAT systems have an off-set Gregorian parabola dish with diameter of 1.8 m and a data transmission rate of 128 kbps.

In our previous study [11], some remarkable features are already obtained for the tropical rain attenuation statistics, which are largely different from those of the temperate regions. First, at EAR in Indonesia, the attenuation ratio is larger than that observed at RISH in Japan even in the severe attenuation range of more than 10 dB. The simultaneous X-band radar observations suggest that this larger ratio is primarily caused by simple convective clouds with one single cell possibly carrying smaller raindrop size distributions (DSD). On the other hand, the difference between worst month and yearly average statistics is rather smaller due to the lack of seasonal temperature variation in the tropics, while the yearly time percentages are, in general, larger than those at RISH in Japan. Also, the yearly average attenuation statistics are, as a whole, in good agreement with the ITU-R predictions (2003) for both up- and down-link attenuation at both stations in Japan and Indonesia, using their local 0.01% values of rainfall rate. In the attenuation range of more than 10 dB, however, the time percentages at EAR become much smaller than the predictions, indicating the remarkable reduction of the equivalent path length down to about 2 km. The radar observations also reveal that intense echo cores of the convective clouds are confined to 2 km along the same propagation path.

Figure 1 depicts qui-probability values of the down-link attenuation against the rainfall rates obtained at (a) RISH and (b) EAR, respectively. The observational periods are the two years of 2004-2005 for (a) RISH and the three years of 2003-2005 for (b) EAR, respectively, since the rainfall rate measurement started at the end of 2003 at RISH. Solid and dashed lines indicate theoretical relationships between attenuation and rainfall rate for equivalent path lengths of 2-6 km. In this calculation, the raindrop size distribution (DSD) is based on the Marshall-Palmer type [12]. At RISH in Japan, the equivalent path length is estimated to be around 4 km from these theoretical lines in Fig.1(a). It slightly decreases down to 3 km as the rainfall rate exceeds 60 mm/h or so. This equivalent path length of about 4 km agrees with that obtained by the CS propagation experiments for Ka-band beacon signal (19.5GHz) with elevation angle of 48° at Kashima, Ibaraki, in Japan [13].

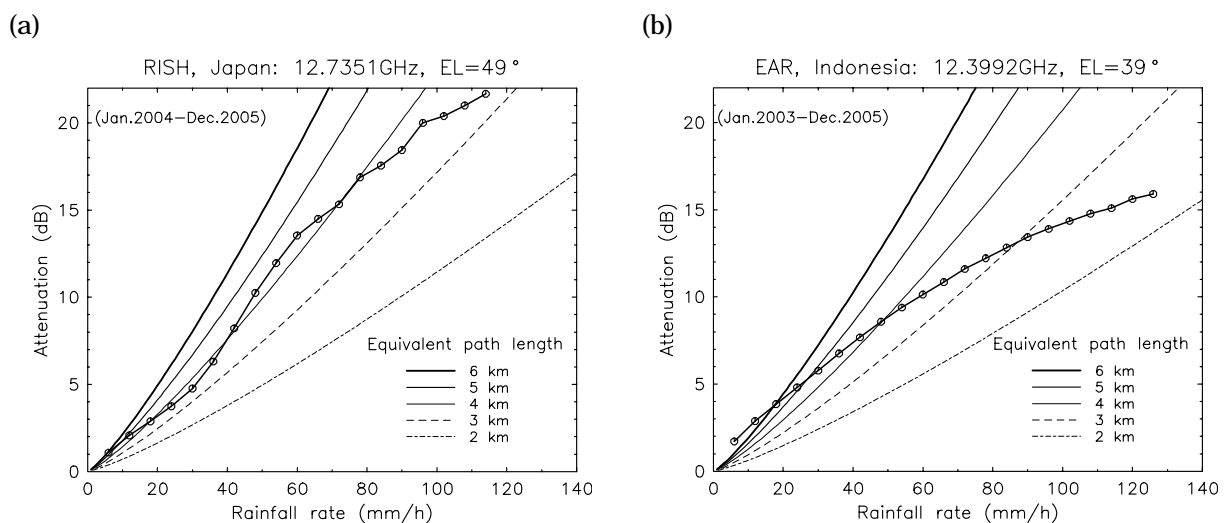


Figure 1: Equi-probability values of down-link attenuation against the rainfall rate obtained at (a) RISH and (b) EAR.

At EAR in Indonesia, however, the equivalent path length similarly estimated in Fig.1(b) rapidly decreases down to 2 km as the rainfall rate approaches 130 mm/h, whereas it is kept more than 3 km below about 60 mm/h. These characteristics of the equivalent path lengths are found in the up-link attenuation at both stations in a similar manner. Also, the simultaneous radar observations demonstrate that the size of intense rain cells along the propagation path is reduced down to about 2 km as the rainfall rate extremely increases [11].

Next, Fig.2 shows equi-probability values of the Ku-band down-link satellite radio wave attenuation against the rainfall rates obtained at other nearby locations in the tropical region. Fig.2(a) is taken from the observations conducted at Bandung in Indonesia for two years from January 1999 to July 2000 [7], while Fig.2(b) from those at Lae in Papua New Guinea for four years from February 1991 to January 1995 [4]. These equi-probability relationships in Figs.2(a) and (b) are inferred from their cumulative time percentages of rainfall rate and attenuation that originally appeared in their literatures [4],[7]. Solid and dashed lines similarly indicate theoretical relationships between attenuation and rainfall rates for equivalent path lengths of 2-6 km using the relevant radio wave frequencies, polarizations, and elevation angles at each site.

The radio wave frequency at Bandung in Indonesia is 12.247 GHz with elevation angle of 64.7° , and it is 12.75 GHz with elevation angle of 73° at Lae in Papua New Guinea. Both stations receive horizontal linear polarization radio waves. Bandung is located in a high land about 700 m above the mean sea level (MSL), similar to EAR which is 865 m above the MSL, while Lae is situated in a low land near the MSL. It should be noted in Figs.2(a) and (b) that the equivalent path lengths estimated from their equi-probability relationships are still kept around 3 km up to the attenuation of 20 dB at both locations even in the tropical region.

From the comparison of the observations at EAR with those of other tropical locations, the very short equivalent path length obtained from the equi-probability relationships between attenuation and rainfall rate in Fig.1(b) is, thus, attributed to the unique features of the location that lies in a high land basin and propagation path condition at the EAR site, rather than a general property of the tropical convective precipitating clouds.

As was mentioned in our earlier study [11], the X-band radar observations revealed a comparatively simple structure of convective precipitating clouds over the EAR site and their relatively low cloud tops since it is located in a highland basin. Also, compared with the other tropical locations, the relatively low elevation angle (39°) at the EAR site may yield a rather short propagation path length through isolated convective clouds with one single cell, in contrast to widespread stratiform clouds in the temperate region.

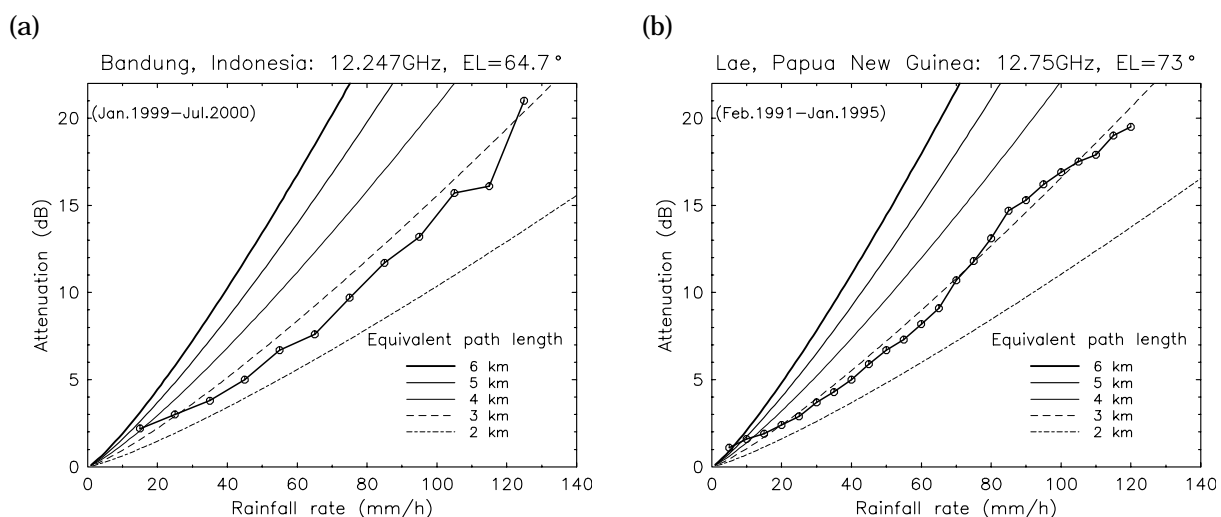


Figure 2: Equi-probability values of down-link attenuation against the rainfall rate obtained at (a) Bandung in Indonesia [7] and (b) Lae in Papua New Guinea [4].

3. Conclusions

This study has presented the three year statistics of rain attenuation characteristics obtained from the Ku-band satellite communications links at the EAR site in Indonesia, which is just located on the equator. The statistical results are compared with those observed at the Japan side of the same satellite communications link and those previously collected in other tropical locations near the EAR site. The yearly time percentages of the observed rain attenuation are, as a whole, in good agreement with the ITU-R predictions (2003) for both locations in Japan and Indonesia. At EAR in Indonesia, however, the time percentages become much smaller than the ITU-R predictions in the attenuation range of larger than 10 dB. Consequently, the equivalent path length is estimated to decrease down to about 2 km through the heavy rain area with rainfall rates of more than 100 mm/h,. This result is found to be even shorter compared with those obtained in the other nearby sites in the tropics. These unique features of the EAR site seem to be caused by its location in a highland basin and a comparatively low elevation angle of 39 ° even in the tropics.

Acknowledgements

The authors deeply thank the staff of Equatorial Atmosphere Radar Observatory for assisting our study. This work is supported by Grant-in-Aid for Scientific Research on Priority Area-764 of the Ministry of Education, Culture, Sports, Science and Technology of Japan (Grant No.14213201).

REFERENCES

1. Arbesser-Rastburg, B. R. and G.Brussaard, "Propagation research in Europe using the OPYMPUS satellite," *Proc. IEEE*, Vol.81, 865-875, 1993.
2. Bauer, R., "Ka-band propagation measurement: An opportunity with advanced communication technology satellite (ACTS)," *Proc. IEEE*, Vol.85, 853-862, 1997.
3. Karasawa, Y. and Y. Maekawa, "Ka-band earth-space propagation research in Japan," *Proc. IEEE*, Vol.85, 821-842, 1997.
4. Pan, Q. W., G. H. Bryant, J.McMahon, J. E. Allnutt, and F. Haidara, "High elevation angle satellite-to-earth 12 GHz propagation measurements in the tropics," *International Journal of Satellite Communications*, Vol.19, 363-384, 2001.
5. Pan, Q. W. and J. E. Allnutt, "12-GHz fade durations and intervals in the tropics," *IEEE Trans. Antennas and Propagat.*, Vol.52, 693-701, 2004.
6. Minakoshi, H., K.Igarashi, T.Boonchauk, N.Hemmakorn, A.Yagasena, S.I.Hassan, J.Suryana, U.Sastrokusumo, S.C.N.Monje, and R.Reyes, "Rain attenuation measurements in Ku-band satellite communication in the East-Asian region under the POST-PARTNERS project," *2001 Asia-Pacific Radio Science Conference, Digest*, Vol.1, 153, F1-2-01, 2001.
7. Sastrokusumo, U., H. Wundarto, J. Suryana, K.Igarashi, and H. Minakoshi, "Two years rainfall rate andrain attenuation measurements in Indonesia under the POST-PARTNERS Project," *2001 Asia-Pacific Radio Science Conference, Digest*, Vol.1, 153, F2-3-05, 2001.
8. Fukao, S., H. Hashiguchi, M. Yamamoto, T. Tsuda, T. Nakamura, M.K. Yamamoto, T. Sato, M. Hagio, and Y. Yabugaki, "The Equatorial Atmosphere Radar (EAR): System description and first results," *Radio Sci.*, Vol.38, 1053, doi:10.1029/2002RS002767, 2003.
9. Hatsuda, K., Y.Aoki, H.Echigo, F.Takahata, Y.Maekawa and K.Fujisaki, "Ku-band long distance site-diversity (SD) characteristics by using new measuring system," *IEEE Trans. Antennas and Propagat.*, Vol.52, 1481-1491, 2004.
10. ITU-R, P837-1, "Characteristics of precipitations for propagation modeling," *ITU-R Recommendations*, 2003.
11. Maekawa, Y., T. Fujiwara, Y. Shibagaki, T. Sato, M. Yamamoto, H. Hashiguchi, and S. Fukao, "Effects of tropical rainfall to the Ku-band satellite communications links at the Equatorial Atmosphere Radar Observatory," *J. Meteor. Soc. Japan*, Vol.84C. in press, 2006.
12. Iida, T., *Satellite Communications (in Japanese)*, Ohmusha, 427p., 1997.
13. Fukuchi, H., T. Kozu, K. Nakamura, J. Awaka, H. Inomata, and Y.Otsu, "Centimeter wave propagation experiments using the beacon signals of CS and BSE satellite," *IEEE Trans. Antennas and Propagat.*, Vol.31, 603-613, 1983.

Diurnal and Seasonal Variations of Cloud and Water Vapor in Troposphere

Qing Wei Pan¹, Jeremy E. Allnut², and Charles Tsui¹

(1) Manukau Institute of Technology, Department of Electrical & Computer Engineering, New Zealand

(2) George Mason University, Department of Electrical and Computer Engineering, USA

Abstract

Long-term satellite beacon measurements have been extensively used to establish ground truth data for prediction procedures. Initially, attenuation and depolarization were the key parameters sought, supplemented more recently with secondary data on fade duration and intervals, site diversity, and fade rates. An analysis of four years worth of data from an experiment in Papua New Guinea has shown evidence of diurnal, seasonal, and annual variations in the clear-sky level that appear to show evidence of atmospheric tidal effects of cloud water-droplet concentration and tropospheric water-vapor content that have implications in the design of satellite systems.

1. Introduction

A 12.75 GHz beacon receiver located in Lae, Papua New Guinea (PNG) – approximate coordinates 7° S, 147° E – received transmissions from OPTUS satellites located at 160° E longitude. The elevation angle was close to 73°. The main experimental results have been documented [1, 2, 3]. In the design of satellite communications links, account has to be taken of the likely impairment levels to be experienced for those time intervals when specified performance and availability criteria have to be met. These criteria are normally specified for average annual periods or worst months. Propagation data acquired from experiments such as the one conducted at Lae, PNG, permit the validity of propagation prediction procedures to be verified, or if necessary, changed. Since propagation measurements are key to verifying modeling accuracy, great care is taken to ensure the accuracy of the results.

Many factors can affect the accuracy of measured beacon data. The principal causes for variations in received beacon level in essentially clear sky are thought to be due to:

- Thermal effects on the spacecraft
- Satellite antenna beam pointing changes
- Satellite orbit perturbations
- Earth station equipment instabilities
- Variations in atmospheric water vapor and liquid content
- Variations in scintillation activity

Most of the above can be compensated for with a good knowledge of the satellite transmission and beam pointing variations and the use of a co-located radiometer to provide a baseline clear sky level. However, after removing as far as possible satellite and earth station-induced effects, there still remained a significant variation in the perceived clear-sky level over daily, seasonal, and annual periods within the Lae data. These variations in clear sky level – essentially changes in the transmission level in the absence of rain – were investigated further. Fig. 1 shows a typical Hot Season 4-day period of clear-sky beacon level and sky-noise temperature diurnal variations. The average received beacon level was -67 dBm (shown as 0 dB reference). A Cool Season example is shown in Fig. 2.

2. Analysis of Variations

Initial inspection of the radiometric data showed, as expected, the lowest sky-noise levels in the coolest part of the pre-dawn period between 2 to 6 a.m. local time (around 38 K) and the highest sky-noise levels just after the midday period between 11 a.m. and 1 p.m. local time (around 52 K). These are also confirmed by analyzing the beacon signal data, which show a maximum at 5 to 7 a.m. and minimum at 1 to 3 p.m. (Fig. 3). On top of these changes in simple absorption levels due to water vapor and droplets, there was a marked variation over the diurnal period in the tropospheric scintillation activity. Scintillation amplitudes for the cooler and hotter periods of the day were ± 0.5 dB and ± 1.5 dB, respectively. However, the sky-noise temperature variations in both seasons were similar, i.e. ± 7 K. This phenomenon may be explained by the fact that the 12.75 GHz beacon receiver will detect scintillations due to

humidity and turbulence effects, while the 11.4 GHz radiometer will only detect enhanced sky noise emissions from the humidity component.

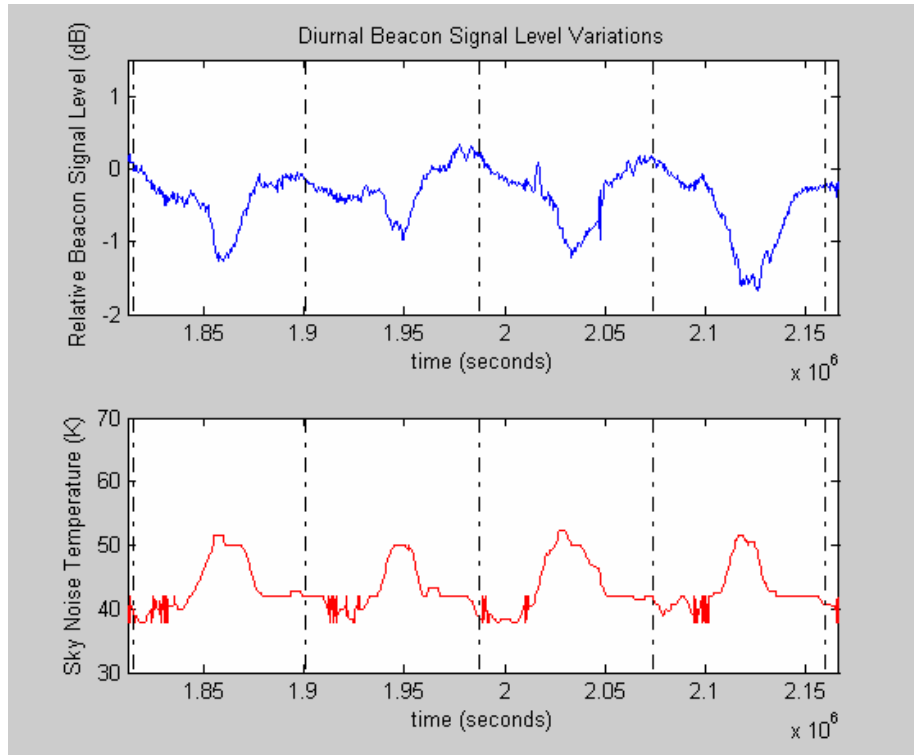


Figure 1: Diurnal beacon signal and sky-noise temperature variations from 24/02/93 to 27/02/93 (Hot Season)

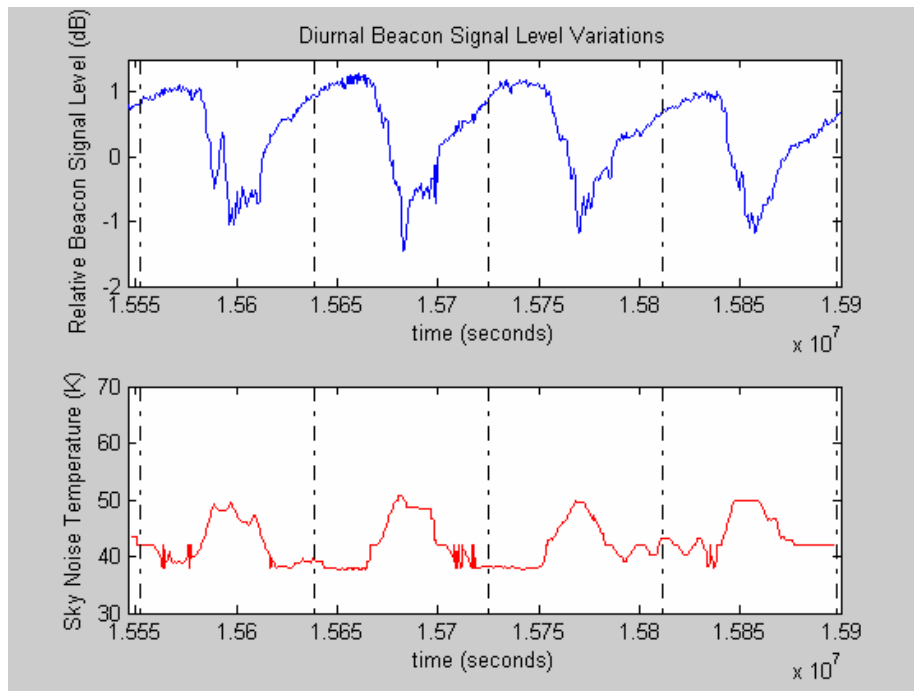


Figure 2: Diurnal beacon signal and sky-noise temperature variations from 03/08/93 to 06/08/93 (Cool Season)

Overall, the variation in the clear-sky level due to changes in water vapor content and scintillation activity could be as much as 3 dB peak-to-peak. For a Ku-band VSAT system that is designed to operate with a 7 dB margin, a change of 3 dB of signal level (and hence C/N) in just clear-sky conditions is significant.

Changes in signal level in clear-sky that are due to satellite-induced effects will have a periodicity of one sidereal day (23 h 56 m 4 s), reflecting one rotation in geostationary orbit. Those that are due to atmospheric changes driven by solar heating will have a periodicity of one solar day (24 h). To establish what the overall long-term variations were and their periodicity, an analysis was conducted to find the spectrum of the signal variations. These are shown in Figs. 3 and 4.

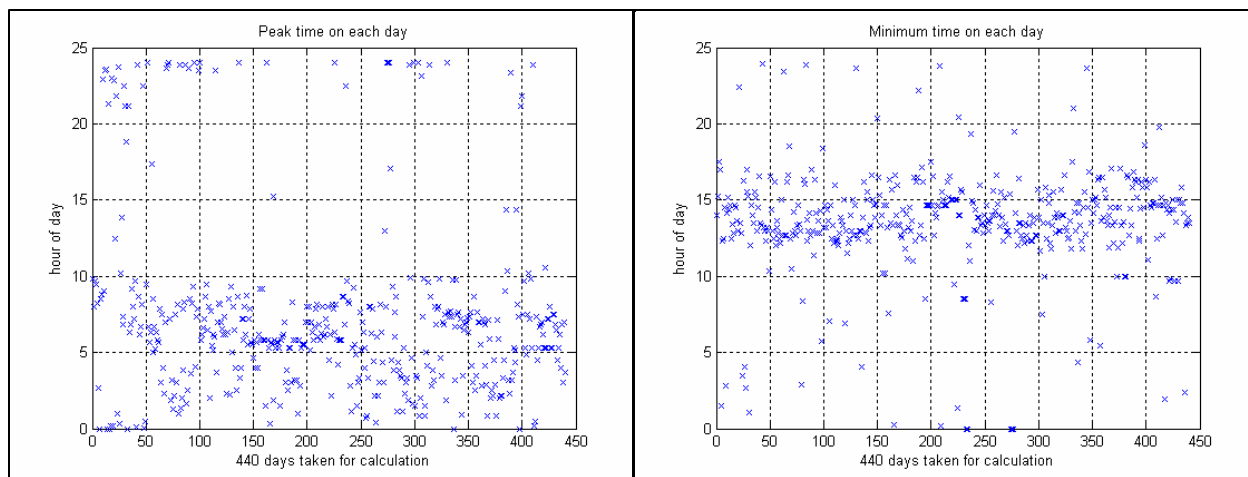


Figure 3: Scatter plots indicate peak beacon level occurs at 6:00 a.m. and minimum occurs at 1:00 p.m.

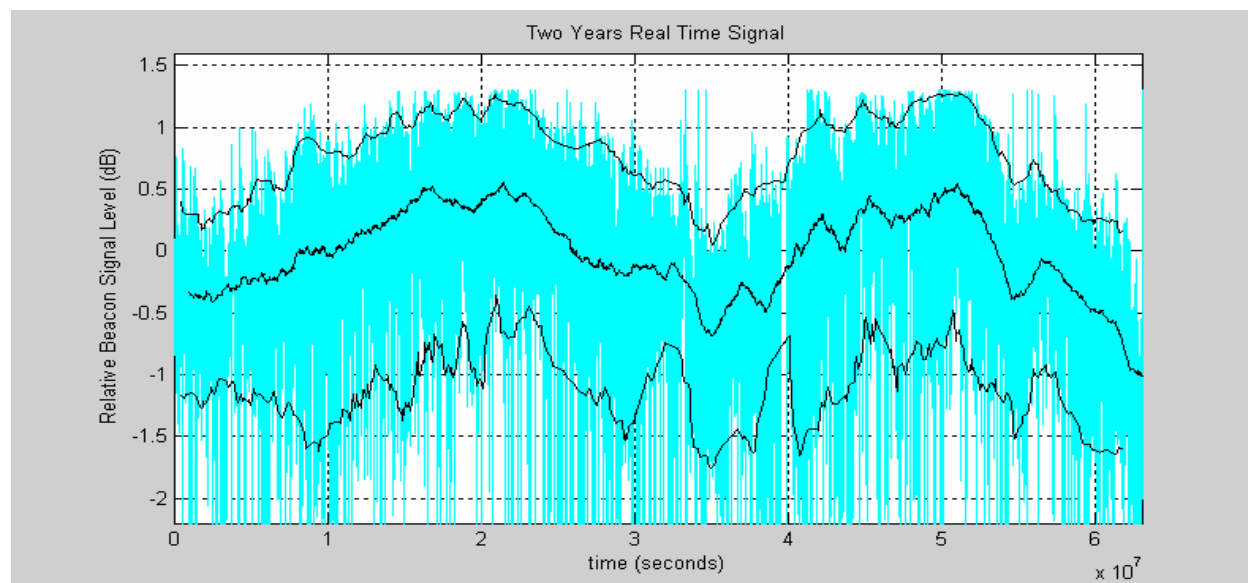


Figure 4: Variations in the received beacon level from 01/02/93 to 31/01/95

Fig. 4 shows changes in the received beacon level in a two-year period. The central and outer solid lines correspond to the average level and the envelope of the diurnal variations, respectively. The large negative level changes are due to rain attenuation, while the enhancements are due to scintillation activity. The average signal level in the hotter convective season (October to March) is about 0.5 dB lower than that in the cooler stratiform season (April to September). This indicates that the convective cloud (≥ 10 km) is much thicker than the stratiform cloud (≤ 5 km).

The diurnal peak-to-peak level differences during the convective and the stratiform season are about 1.5 dB and 2.5 dB, respectively. One of the reasons for these differences is the seasonal humidity – 85 to 95 % in convective season and 90 to 100 % in stratiform season. The other reason is the diurnal temperature variations – from 30 to 35 °C in the convective season and from 20 to 30 °C in the stratiform season. Water content in clouds and air is proportional to humidity and temperature.

In Fig. 5, the major spectral component corresponds to a solar day, with harmonics of the line having lesser intensity. The other significant component is a solar year, which indicates the seasonal variations.

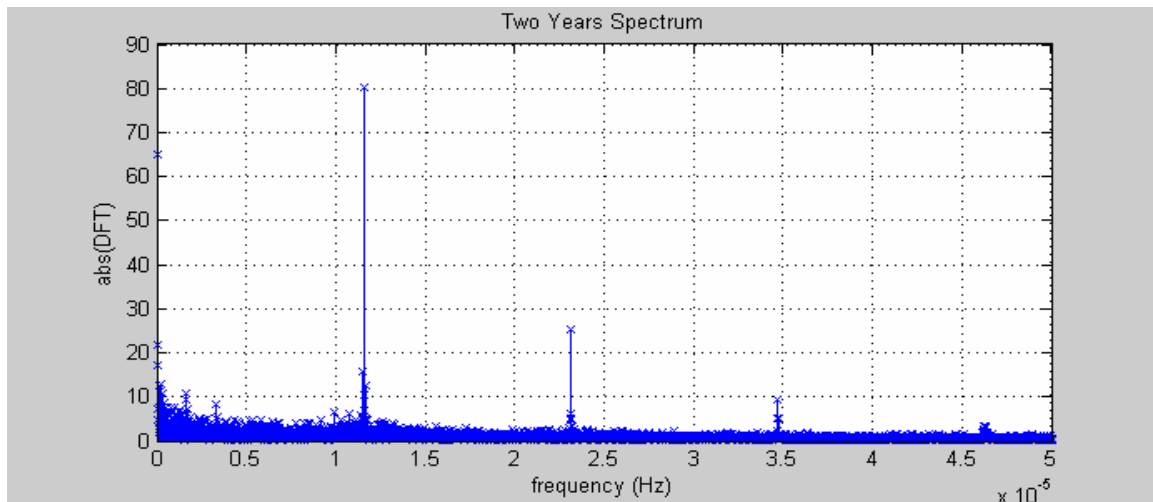


Figure 5: DFT analysis of the spectrum of the signal variations

3. Conclusion

The variations in the received clear-sky level of the satellite beacon show evidence of a diurnal variation that is a solar day, not a sidereal day, and so the cause of the variations would appear to be the variation in the incident solar energy [4]. This was somewhat expected as scintillation activity, the main cause for the variations, is driven by a combination of heat (the driving force of convection) and moisture content: the larger both of these parameters become, the greater is the scintillation activity. What was not anticipated was the clear annual periodicity in the variation of the mean clear sky level that can be seen in Fig. 4. Evidence for annual periodicity in absorption levels through the atmosphere has been observed before in experiments that were aimed at detecting pollutants [5], but it is believed that the results shown here are the first to indicate the same apparent atmospheric tidal effects on the mean clear-sky level with an annual periodicity. In rain-fade countermeasure design for a Ku/Ka-band VSAT system in the tropics, the compensation for signal impairment due to tropospheric/atmospheric thermal tide should also be included.

REFERENCES

1. Pan, Q. W., Bryant, G. H., McMahon, J., Allnutt, J.E., and Haidara, F., "High elevation angle satellite-to-earth 12 GHz propagation measurements in the tropics", *Int. J. Satell. Commun.*, Vol. 19, 363-384, 2001.
2. Pan, Q. W. and Allnutt, J. E., "12 GHz fade durations and intervals in the tropics", *IEEE Trans. Antennas Propagat.*, Vol. 32, No. 3, 693-701, 2004.
3. Pan, Q. W., Allnutt, J. E., and Haidara, F., "Seasonal and diurnal rain effects on Ku-band link designs in rainy tropical regions", *Electron. Lett.*, Vol. 36, No. 9, 841-842, 2000.
4. Sheaffer, J. D., and Gray, W. M., "Effects of Diurnal Variations of Outgoing Longwave Radiation Over the Tropical Oceans", *9th ARM Sci. Team Meeting Proc.*, San Antonio Texas, 1999.
5. Pérez-Munuzuri, V., "Forecasting of Chaotic Cloud Absorption Time series for Meteorological and Plume Dispersion Modeling", *J. Appl. Meteor.*, Vol. 37, 1430-1443, 1998.

Characterization of Rainfall Rate , Ku-band Rain Attenuation and Tropospheric Scintillation at Indonesian Tropical Cities

Joko Suryana U Sastrokusumo Sugihartono
STEI ITB, Indonesia

Kenji Tanaka K Igarashi
NiCT Japan

Mitsuyoshi Iida
ARIB Japan

e-mail: joko@ltrgm.ee.itb.ac.id

Abstract— In this paper, we present our contribution of Rainfall rate and Ku-band rain attenuation measurements at Bandung. This measured data is an important complement to several of previous recorded data from other tropical cities in Indonesia for characterizing the Ku-band Satellite Propagation in Tropical area. The two years of our experiment results indicate that the measured $R_{0.01}$ rainfall rate at Bandung is 120 mm/h and the measured $A_{0.01}$ rain attenuation is 17 dB. Therefore, the P region of ITU-R model is over estimated for Bandung, and we suggest that Q-region of ITU-R model is more suitable for Bandung. Another previous measurements which had performed in Indonesia confirmed with our conclusions that some cities in Indonesia have not only P-region of ITU-R model (such as Padang, Bengkulu an Makassar), but also N (Jayapura) and Q-region (Surabaya). And on their Rec. 837-3 2001 , ITU-R has confirmed that almost Indonesian cities have rainfall rate 100-120 mm/h. Based on 10 samples rainfall rate in Indonesian Archipelago, we have developed New Prediction Model of $R_{0.01}$ value for Indonesian cities. Relating to the rain attenuation statistics, we have found out, that the DAH Model is valid for Indonesia. We also have found out that if Bandung is modelled by Q-region of ITU-R, we should include the wetting antenna effects as the correction factor to the the ITU-R model for confirming with the measured $A_{0.01}$ rain attenuation. Concerning to the tropospheric scintillation , we have noted that in a tropical region such as Indonesia, the magnitude of the Ku-band scintillation is seasonal dependence, reaching variance 0.4 dB (maximum) in rainy season and 0.2 dB (minimum) in dry season.

1. Ku-band Propagation Measurement System at Bandung

The Ku-band propagation measurement system uses a small antenna and a front end shared by the beacon receiver and the Earth Station IDU [1] is shown as in figure 1.

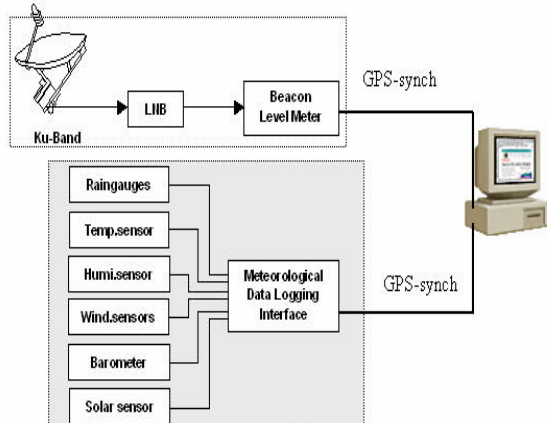


Figure 1. Ku-band Propagation Measurement at Bandung

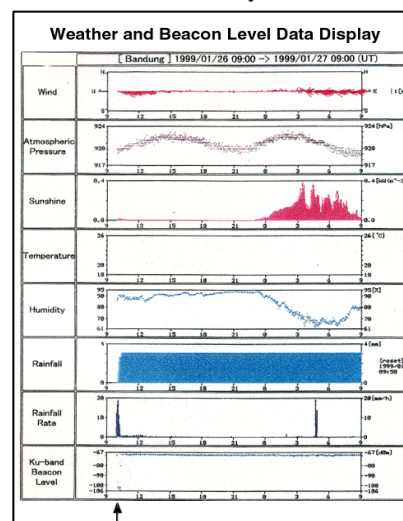


Figure 2. Display of Weather and Beacon level Data

The meteorological data recorded from the sensors (such as : Raingauges, Temperature, Wind speed and direction, Humidity, Barometer and Solar sensors) is GPS-synchronized with beacon level measurement. The PC-based data acquisition system consists of eight channels for measuring the seven meteorological parameters of six sensors and one propagation parameter, i.e beacon level. The PC hardware and software for data collection receives all data transmitted from data acquisition board, logs the data to disk, and displays the collected data for user viewing which implemented with LabView. This graph is example of weather and Beacon level display at Bandung on 24 January 1999 as figure 2 [1]:

2. Rainfall Rate Measurement Results of Indonesian Cities

2.1. Bandung

The two years of our experiment results [1] indicate that the measured $R_{0.01}$ rainfall rate at Bandung is 120 mm/h. The International Telecommunication Union, ITU, has categorized Indonesia as Region P, countries with very high rain precipitation. According to ITU-R' version, rain intensity that will cause the interruption of a communication link for 0.01% per year is 145 mm/hour. Therefore, the P region of ITU-R model is over estimate for Bandung, so we suggest that Q-region of ITU-R model is more suitable for Bandung.

2.2. Other Indonesian Cities

Another previous measurements which had performed in other tropical Indonesian cities confirmed with our conclusion that some cities in Indonesia have not only P-region of ITU-R model (such as Padang, Bengkulu and Makassar), but also N (such as Jayapura) and Q-region (such as Surabaya) [3][4][5]. The following figure 3 shows us about the rainfall characteristics at Bandung, Padang, Surabaya and Jayapura compared with P, Q, N zones of ITU-R Model.

Table 1. Rainfall rate profiles of 24 Indonesian Cities

No.	Kota	Altitude (m)	Latitude	Longitude	R _{0.01}
1	Jatibuhur	604	-6.58	107.33	109.2
2	Bandung	700	-6.95	107.57	120
3	Dempasar	25	-8.98	115.23	109
4	Jayapura	210	-2.37	140.69	113.9
5	Yogyakarta	133	-7.78	110.4	121.3
6	Surabaya	15	-7.23	112.75	119.6
7	Jakarta	5	-6.15	106.8	120.4
8	Medan	49	3.57	98.6	126.2
9	Bandar Lampung	0	-5.27	105.1	123.3
10	Jambi	22	-1.63	103.6	124.4
11	Manado	25	-1.53	124.9	129.9
12	Banjarmasin	0	-3.43	114.7	125.5
13	Tana hmerah	19	-6.13	140.3	138
14	Semarang	21	-6.98	110.3	134
15	Pekabaru	15	0.47	101.4	130.9
16	Palembang	2	-2.9	104.7	132.1
17	Balipapan	0	-1.27	116.9	127.7
18	Bengkulu	8	-3.88	102.3	142.7
19	Padang	200	-1	100.2	146
20	Makassar	6	-5.07	119.5	141.3
21	Maros	40	-4.98	119.58	148
22	Pontianak	30	0.15	109.4	137.1
23	Cibinong	33	-6.57	106.75	159
24	Putussibau	10	0.83	112.93	152

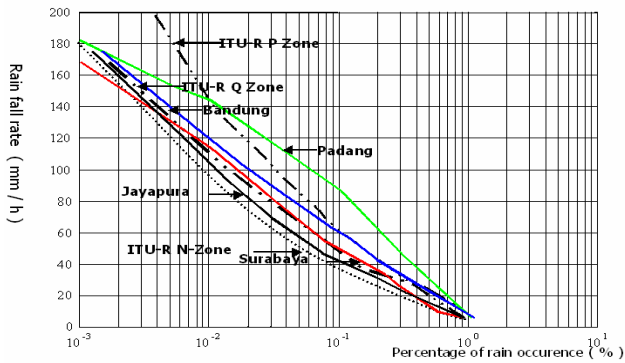


Figure 3. Rainfall Characteristics at Several cities in Indonesia compared with ITU-R Model

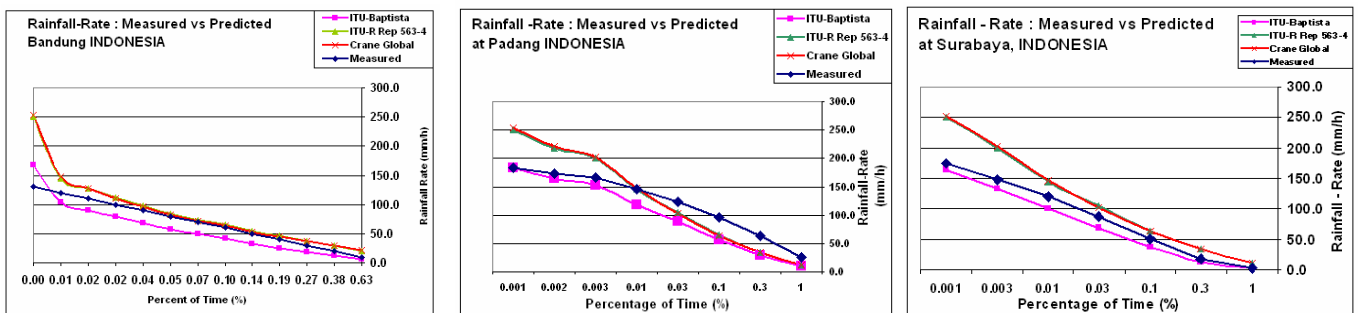


Figure 4. Measured vs Predicted Rainfall Rate at Bandung, Padang and Surabaya

3. Measured vs Predicted Rainfall Rate for Indonesian Cities

Prediction methods is another way to determine the rainfall rate but with some limitations. The rainfall rate prediction such as the ITU-R Rep. 563-4 and the Global Crane model can be used to do this. Some experts consider these models are not accurate enough, because there were too few samples used when developing the models. The following graphs give the comparison of measured and predicted value of rainfall rate at Bandung [1], Padang [4] and Surabaya [3] as figure 4.

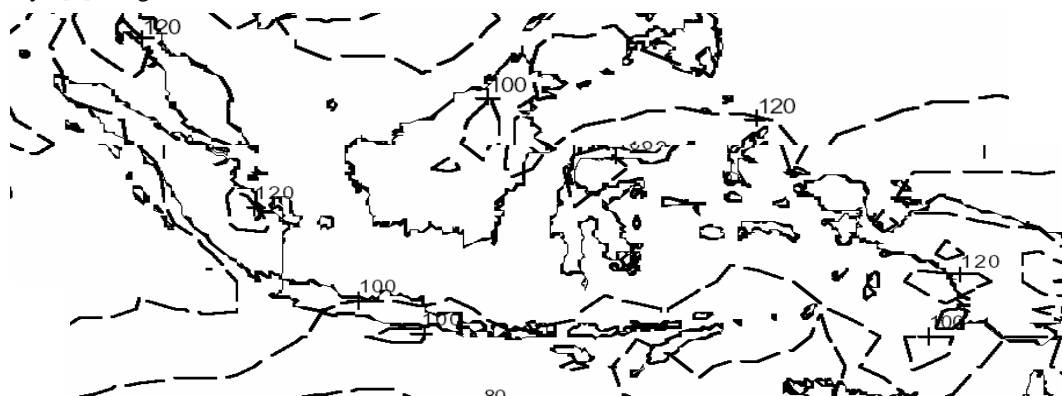


Figure 5. Rainfall rate profile of Indonesian Cities according to ITU-R P.837-3

3.1 ITU-R Recommendation P.837-3 for Rainfall rate profile of Indonesian Cities

ITU-R Assembly, had published their recommendation P.837-3 [7], which present the model to derive the rainfall rate exceeded for a given probability of the average year and a given location. This model is to be applied to the data supplied in the digital files ESARAIN which derived from 15 years of data of the European Centre of Medium-range Weather Forecast (ECMWF). And for easy reference, ITU-R Assembly also provides the figure of rainfall rate exceeded for 0.01% of the average year. Figure 5 above illustrate the rainfall rate model for Indonesian cities. From these figure we can see, that most of Indonesian cities has R0.01 between 100 -120 mm/h.

3.2 Our new model of Rainfall Rate for Indonesian Cities

The rainfall rate prediction model which applicable especially for Indonesia, can be developed more accurate and convincingly with the availability of field measurements as presented above. By using the data, and added to it (other) data concerning rain and thunderstorm days from the Indonesian Meteorological and Geophysical Institute, the Rainfall Rate Prediction Model for the Indonesia archipelago becomes [7]:

Table 2 Measured vs New Model Rainfall Rate

City	R _{0.01} Measured	R _{0.01} New Model	Error
Bandung	120	118.4	1.33%
Cibinong	159	155.8	2.02%
Denpasar	109	109.5	0.50%
Jatiluhur	109.2	113	3.45%
Maros	148	146.1	1.29%
Padang	146	153.7	5.27%
Putussibau	152	144.7	4.82%
Surabaya	119.6	116.1	2.95%
Tanahmerah	138	142.2	3.02%

$$R_{0.01} = f(\text{Lat, Long, M, Mm}) = 128.192 - 0.037 * \text{Lat} -$$

$$0.393 * \text{Long} + 0.012 * \text{M} + 0.017 * \text{Mm} \quad (1)$$

with: R_{0.01} = rainfall-rate 0.01% of time in a year (mm/h)

M = average rainfall a year (mm)

Mm= maximum rainfall (monthly) in 30 years

Lat = latitude

Long = longitude

The above table 2 shows us the comparisons of measured and new model of rainfall rate for Indonesian cities using equation 1.

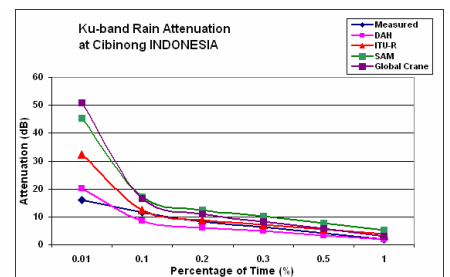
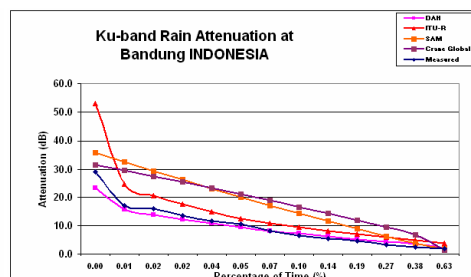
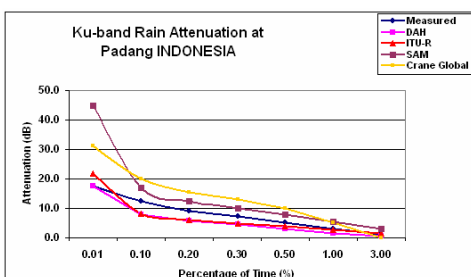
4. Ku-band Rain Attenuation Measurement Results

The International Telecommunication Union, ITU, has categorized Indonesia as Region P, a country with very high rain precipitation. According to ITU's version, rain intensity that will cause the interruption of a communication link for 0.01% per year is 145 mm/hour. Such rain intensity can cause 28 db rain attenuation for a link working in the 14 GHz band; that is pretty high. Such attenuation should be compensated with powerful RF at the transmit side. The rain attenuation for satellite links can be calculated using following models:

- ITU – R (formerly CCIR Model)
- SAM (Simple Attenuation Model)
- Global Crane Model
- Model DAH (Dissanayake, Allnutt, Haidara Model) [2]

To confirm which is the preferred model to be used in Indonesia, field measurements should also be carried out. Measurements of rain attenuation in Indonesia have been done for satellite communication links in Padang, Cibinong [4] and Bandung [1]. The two years of our experiment results indicate that the measured A_{0.01} rain attenuation is 17 dB . It also has been found out, after analysis, that the DAH Model [6] for rain attenuation prediction is valid for Indonesia, besides the ITU Model.

a. Measured vs Predicted at Bandung b. Measured vs Predicted at Padang c. Measured vs Predicted at Cibinong



4.1. Wetting Antenna as correction factor

The two years of our experiment results indicate that the measured $A_{0.01}$ rain attenuation is 17 dB, this value is about 3 dB greater than computed $A_{0.01}$ using Q-region of ITU-R model. This suggests that there could be another significant attenuation mechanism present. The effects of water on the antenna radome and reflector wetting are the possible cause of the higher attenuation measured [8].

So, we also have performed experimentally the magnitude of the signal loss when the antenna reflector and the antenna feed horn radome surfaces are wet and its correlation to rain rates which is simulated by using the water sprayer during clear sky condition [8]. The wetting antenna test results introduced about 2.5 dB losses at 40 mm/h simulated rain rate which is close with our simple theoretical approach (2.7 dB). So we can make the correction of the measured rain attenuation at Bandung by using wetting antenna factor which will shift the measured rain attenuation graph 3 dB such illustrated in figure 5 below :

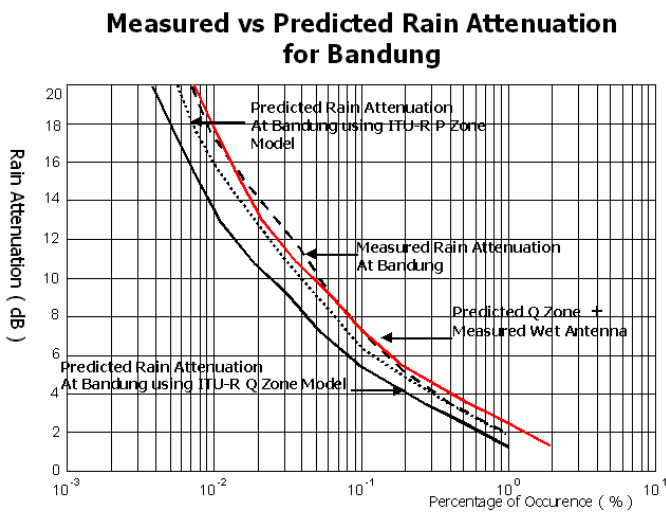


Figure 6 Measured vs ITU-R Prediction with wetting antenna correction

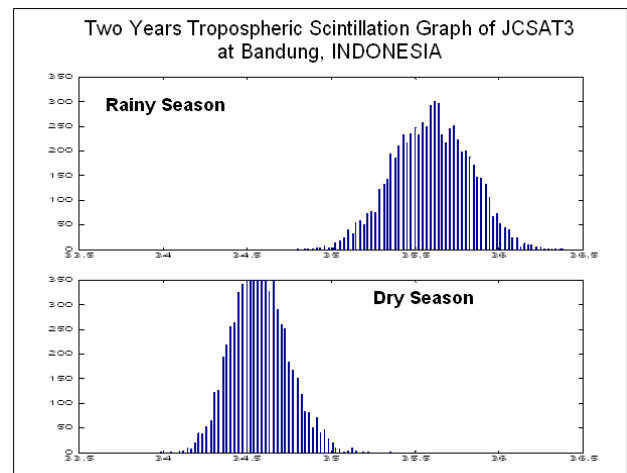


Figure 7. Two Years Tropospheric Scintillation graph of JCSAT3 during Rainy season Months and Dry Season at Bandung Indonesia

5. Measured Ku-band Tropospheric Scintillation Data Processing for Bandung

From the experiment results [10], we find out that the scintillation in tropical region is seasonal dependence, reaching variance 0.4 dB (maximum) in rainy season and 0.2 dB (minimum) in dry season. This results are depicted as in figure 6. We also noted that the long term PDF and its spectrum shape using Savitzky-Golay LPF is very closely with the conventional moving average LPF [9] as illustrated in figure 7 and 8 below [10] :

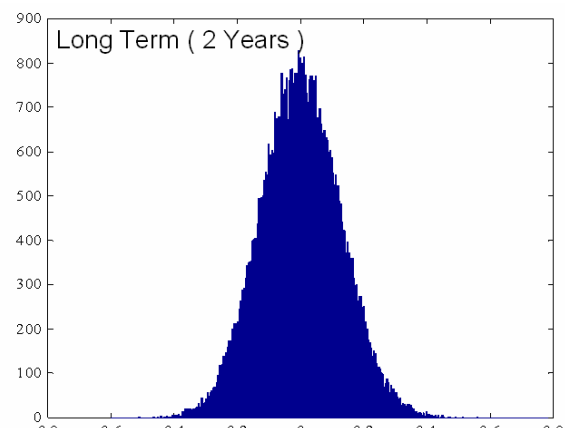


Figure 8. Long term pdf of Tropospheric Scintillation at Bandung Indonesia

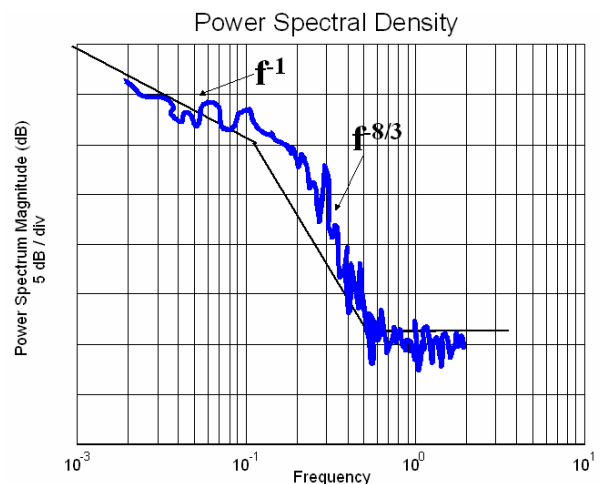


Figure 9. Corresponding Power Spectral Density of Tropospheric Scintillation at Bandung Indonesia

6.Summary

The two years of our experiment results indicate that the measured $R_{0.01}$ rainfall rate at Bandung is 120 mm/h. Therefore, the P region of ITU-R model is over estimate for Bandung, so we suggest that Q-region of ITU-R model is more suitable for Bandung. Another previous measurements which had performed in other tropical Indonesian cities confirmed with our conclusion that some cities in Indonesia have not only P-region of ITU-R model (such as Padang, Bengkulu and Makassar), but also N (such as Jayapura) and Q-region (such as Surabaya). From the comparisons of predicted rainfall rate well known models with measured rainfall rate of tropical cities in Indonesia, we can see that there are significant differences. So the new model of rainfall rate should be developed which has small deviation.

It also has been found out, after analysis, that the DAH Model for rain attenuation prediction is valid for Indonesia, besides the ITU Model. The wetting antenna test results introduced about 2.5 dB losses at 40 mm/h simulated rain rate which is close with our simple theoretical approach (2.7 dB). So we can make the correction of the measured rain attenuation at Bandung by using wetting antenna factor. We also find out that the tropospheric scintillation in tropical region is seasonal dependence, reaching variance 0.4 dB (maximum) in rainy season and 0.2 dB (minimum) in dry season.

REFERENCES

- [1]. Suryana et al., Two Years Rainfall Rate and Rain Attenuation Measurements in Indonesia under Post-PARTNERS Project, Asia-Pacific Radio Science Conference, Japan, 2001
- [2]. Prima Setiyanto, Prediction Models of Rain Rate ($R_{0.01}$) and Rain Attenuation in Ku-band Satellite Communications System for Indonesian Archipelago, Master Thesis, Electrical Engineering Department, ITB, 2003.
- [3]. Adji et al., Rain Attenuation Characteristics for the Indonesian Domestic Satellite in the Ku-band, Eindhoven University of Technology, Netherlands, 1995
- [4]. Juy, M. et al., Measurement Of 11 GHz Attenuation Using The Intelsat V Beacon In Indonesia, International Journal Of Satellite Communications, Vol.8, 251-256, 1990
- [5]. Maagt, P.J.I. et al., Results of 11.2 GHz. Propagation Experiments in Indonesia, Electronics Letters, 28th.October 1993, Vol.29, No.22
- [6]. Dissanayake et al., A Prediction Model that Combines Rain Attenuation and Other Propagation Impairments Along Earth – Satellite, IEEE Transactions On Antennas and Propagation, Vol.45, No.10, October, 1997.
- [7]. RECOMMENDATION ITU-R P.837-3, "Characteristics of precipitation for propagation modelling :Question ITU-R 201/3", 2001
- [8]. Suryana et al., Study on Wet Antenna at Ku-band for Further Considerations of Propagation Measurement and Antenna Design, Asia-Pacific Radio Science Conference, Japan, 2001
- [9]. Karasawa Y et al., Tropospheric scintillation in the 14/11-GHz bands on earth-space paths with low elevation angles, IEEE Trans. Antennas Propagation 36, 563-569
- [10] Lenni Yulianti et al., Seasonal Dependence of Clear Air Tropospheric Scintillation from Ku-band Propagation Using JCSAT3 in Indonesia, Proceeding of APRASC'01, Chuo University

Preliminary Assessment of Electromagnetic Absorption in the Breast for Cylindrical Microwave Breast Cancer Detection Systems

J. E. Johnson, T. Takenaka
Nagasaki University, Japan

Abstract—In this work, electromagnetic absorption in the breast is analyzed for a cylindrically arranged breast cancer detection system. An FDTD-based electromagnetic simulator is utilized to characterize the response of a hemispherical breast model to microwave radiation from dipole and Vivaldi antennas at both 3 and 6 GHz. Peak specific absorption rates (SARs) are calculated and power absorption patterns are analyzed. Results of the study provide evidence that typical breast cancer detection systems should remain well within prescribed peak SAR limits. Advantages for breast imaging when utilizing a more directional (Vivaldi) antenna are also demonstrated.

Introduction

Microwave based systems for the detection of breast cancer have been under development for several years and are progressing towards practical use in a clinical environment. As these systems reach the clinical phase, it will be important to accurately assess potential safety hazards to patients. A common technique for assessing safety levels for microwave exposure is by characterizing specific absorption rates (SARs) inside the body and comparing them to prescribed maximum limits, such as those described by the IEEE [1] and the ICNIRP [2]. Demonstrating that local SARs occurring in microwave imaging systems fall below these prescribed guidelines will provide solid evidence that these systems are safe for use on human patients. Establishing such evidence is an important aspect in the development of these systems, as they are being explored as a safer imaging modality than X-ray mammography, which utilizes ionizing radiation. In this paper, a preliminary assessment of expected SAR levels for the microwave breast imaging system currently being developed at Nagasaki University [3–5] is conducted.

Methods

For preliminary assessment of SAR levels in the breast, a simple hemispherical breast model was formed as shown in Fig. 1. The electrical properties of the breast model, summarized in Table 1, were derived using the four-term Cole-Cole parameters [6,7] for infiltrated fat (normal breast tissue), muscle (chest wall), and wet skin, and the corresponding tissue densities were adapted from Gandhi et. al. [8]. The breast model is surrounded by a loss-less immersion liquid which improves the coupling of the microwave signal into the breast.

Table 1: Characteristics of hemispherical breast model.

Tissue	Freq.=3GHz		Freq.=6GHz		$\rho(kg/m^3)$
	ϵ_r	$\sigma(S/m)$	ϵ_r	$\sigma(S/m)$	
Breast Tissue	10.66	0.34	9.80	0.87	920
Chest-wall	52.06	2.14	48.22	5.20	1050
Skin	42.11	1.95	38.38	4.54	1100

Microwave signals were radiated into the breast model utilizing both a simple half-wavelength dipole antenna and a broad-band, antipodal Vivaldi antenna. SAR calculations were conducted for frequencies of 3 and 6 GHz, and for immersion liquids with dielectric constants (ϵ_{imm}) of 10 and 2.5. The antenna dimensions were designed for favorable performance with each immersion liquid and at each frequency utilizing a commercial, FDTD/FIT-based electromagnetic simulator (CST Microwave Studio version 2006.0.0). Pertinent properties of the antennas

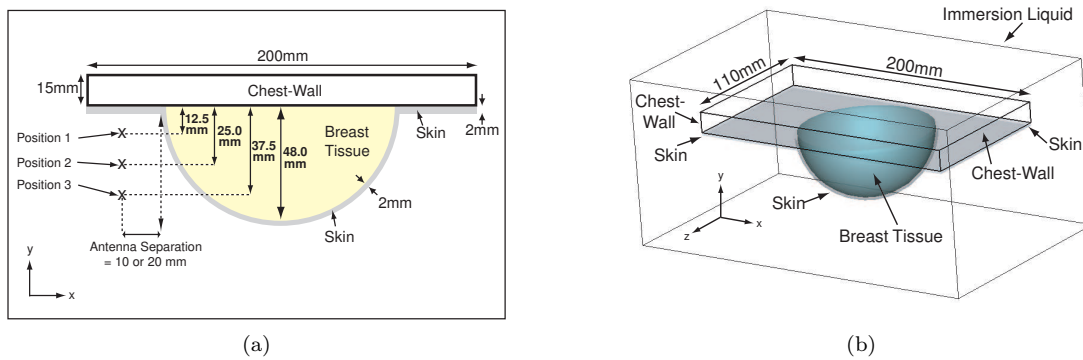


Figure 1: Configuration of hemispherical breast model utilized for SAR calculations: (a) Side view showing cross section of model, as well as center positions of antennas; (b) Perspective view of model.

Table 2: Characteristics of antennas utilized in this study.

	Dipole Antenna				Vivaldi Antenna			
	$\epsilon_{imm}=10.0$		$\epsilon_{imm}=2.5$		$\epsilon_{imm}=10.0$		$\epsilon_{imm}=2.5$	
Frequency	3 GHz	6GHz	3 GHz	6GHz	3 GHz	6GHz	3 GHz	6GHz
Return Loss (dB)	-10.1	-10.6	-23.5	-29.5	-13.0	-20.5	-8.6	-15.9
Gain (dB)	2.3	2.4	2.1	2.1	6.6	10.7	5.5	6.5
E-Plane BW	76.1°	76.3°	78.4°	79.4°	43.3°	25.0°	69.7°	89.7°
H-Plane BW	Omnidir	Omnidir	Omnidir	Omnidir	109.8°	67.1°	101.8°	80.2°
Max. Phys. Dimension	15.3mm	7.5mm	27.7mm	13.0mm	30.0mm	40.0mm	30.0mm	30.0mm

are summarized in Table 2. Microwaves were transmitted at either 3 or 6 GHz from the positions shown in Fig. 1(a). The dipole antenna was centered at each position, with the arms of the dipole aligned with the y-axis. The radiating face of the Vivaldi antenna was also centered at each position, however the Vivaldi was utilized in both a vertical (E-field aligned with the y-axis) and horizontal (E-field aligned with the z-axis) alignment. The antennas were positioned at a distance of 10mm from the outermost point of the breast for the $\epsilon_{imm}=10$ immersion liquid and a distance of 20mm for $\epsilon_{imm}=2.5$.

CST Microwave Studio was utilized to calculate the electromagnetic fields and resulting SARs within the breast model. Subgridding was utilized for the FDTD grid, with a grid size of ≤ 1 mm in critical regions (i.e. skin and normal breast tissue) and no larger than 3.5 mm in less vital regions (i.e. the outer areas of the immersion liquid). The localized 10g average SAR values (SAR_{10g}) were calculated for an input power level (P_{in}) of 500 mW. Utilizing the peak SAR values and the value of the total power radiated from the antenna, the maximum antenna radiated power limit (P_{lim}) allowable to remain within the peak SAR safety limit of $SAR_{10g}=2.0$ W/kg [1, 2] was calculated.

Results and Discussion

The results of the SAR calculations conducted with the $\epsilon_{imm}=10$ immersion liquid and at 3 GHz are summarized in Table 3, which includes the following: each antenna type and position; the minimum distances from the antenna to the breast (D_{BR}) and to the chest-wall (D_{CW}); the percentage of the radiated power absorbed in the breast, including the skin surrounding the breast (P_{BR}); the percentage of the radiated power absorbed in the chest-wall, including the skin covering the chest area (P_{CW}); the peak SAR_{10g} value; and finally, the maximum radiated power limit (P_{lim}) calculated as described above. Observing Table 3, it is clear that as the antenna is moved upwards toward the chest wall (from position 3 to 1), the decreased distance to the body causes an expected general increase in peak SAR. The table also indicates problems that begin to occur as the

antennas are brought physically closer to the chest-wall. When utilizing the dipole in position 1, for example, 42.6% of the radiated power is absorbed in the chest-wall (P_{CW}) compared with only 17.9% in the breast (P_{BR}). The Vivaldi is more efficient at directing energy into the breast from position 1, with $P_{BR}=24.4\%$, although it also leads to higher absorption in the chest-wall (28.9%). At position 2, P_{CW} is much lower for all three antennas. The horizontally aligned Vivaldi gives the highest SAR_{10g} from position 2 ($SAR_{10g}=5.5$ W/kg), with a corresponding radiated power limit of $P_{lim}=164.6$ mW. Fig. 2 shows the SAR_{10g} deposition patterns for all three antennas at position 2, with parts (a)-(c) showing a cross-section (xy plane) through the breast and parts (d)-(f) showing the SAR profile over the skin surface. Parts (a)-(c) of Fig. 2 demonstrate that the peak absorption area occurs mostly in the skin and superficial areas of normal tissue just beneath the skin, a trend generally observed for all cases analyzed in this study. Comparison of the responses in Fig. 2 reveals a relative similarity in the absorption pattern among the three antennas. However, the dipole antenna creates an area of significant absorption towards the edge (left side) of the chest wall that can be attributed to the omnidirectional radiation characteristic of the dipole in the H-plane. The horizontally aligned Vivaldi shows a greater vertically dispersed deposition pattern than the Vivaldi with vertical alignment. This is evident from comparison of Fig. 2(b) and (e) with Fig. 2(c) and (f), which shows higher SARs upward towards the chest wall as well as downward towards the lower part of the breast with the horizontally aligned Vivaldi. The differences between the horizontally and vertically aligned Vivaldi antennas reflect the significantly larger H-plane beamwidth of the Vivaldi compared with the E-plane beamwidth (Table 2). Overall, the vertically aligned Vivaldi deposits the highest percentage of power in the breast $P_{BR}=31.0\%$ and the lowest percentage in the chest-wall $P_{CW}=15.5\%$.

Table 3: Summary of SAR simulation results: $\epsilon_{imm}=10.0$, $Freq=3GHz$, $P_{in}=500mW$

Position	Antenna	D_{BR} (mm)	D_{CW} (mm)	P_{BR} (%)	P_{CW} (%)	SAR_{10g} (W/kg)	P_{lim} (mW)
1	Dipole	10.2	2.9	17.9	42.6	7.2*	133.1
	Vivaldi (Horiz)	11.4	9.9	24.4	28.9	5.2*	177.7
2	Dipole	13.1	15.4	21.2	16.6	3.6	257.5
	Vivaldi (Vert)	11.0	8.0	31.0	15.5	4.5	197.6
	Vivaldi (Horiz)	16.3	22.4	29.9	19.4	5.5	164.6
3	Dipole	19.9	27.9	17.1	8.9	2.2	409.9
	Vivaldi (Vert)	15.3	20.5	27.1	8.6	3.2	282.1
	Vivaldi (Horiz)	26.2	34.9	25.9	12.4	3.5	256.0

*maximum occurs in the skin of the chest-wall, rather than the skin of the breast

Table 4 summarizes the results obtained with $\epsilon_{imm}=10$ and at 6 GHz (note that results from position 3 are not shown for the remainder of this study). Comparison of Table 4 and Table 3 reveals considerable increases in peak SAR values occurring as the frequency is increased. This can be largely attributed to the significant increase in the conductivity of the skin when the frequency rises from 3 to 6 GHz. The peak SAR_{10g} values occurring with the dipole and horizontal Vivaldi at position 1 are the largest obtained of all cases examined in this study, reaching 8.3 and 9.9 W/kg respectively (with corresponding P_{lim} values of 113.0 and 93.5 mW). For 6 GHz, energy is more efficiently directed into the breast itself, demonstrated by higher P_{BR} and lower P_{CW} values. This effect is more significant for the Vivaldi antenna (in both alignments), and can be attributed in part to the narrowing beamwidth of the Vivaldi in both the E- and H-planes with increased frequency.

Table 5 gives a summary of the results obtained when utilizing an immersion liquid of $\epsilon_{imm}=2.5$ at both 3 and 6 GHz. When utilizing a lower ϵ_{imm} , the dimensions of the antennas generally need to be increased to maintain favorable radiation characteristics (Table 2). As a result, the dipole and (vertical) Vivaldi antennas are physically closer in proximity to the chest wall (D_{CW} is small) in many instances. Furthermore, reduction of ϵ_{imm} results in a longer equivalent wavelength, bringing the antennas electrically closer to the chest wall. Due to these factors, the dipole and vertically aligned Vivaldi antennas tend to radiate poorly into the breast, with large coupling to the chest wall. However, the horizontally aligned Vivaldi remains reasonably well separated from the chest wall and generally deposits a large portion of energy into the breast itself. The most stringent antenna radiated power limitation that occurs with the $\epsilon_{imm}=2.5$ immersion liquid is $P_{lim}=131.1$ mW when utilizing the horizontally aligned Vivaldi antenna in position 1 at 6 GHz.

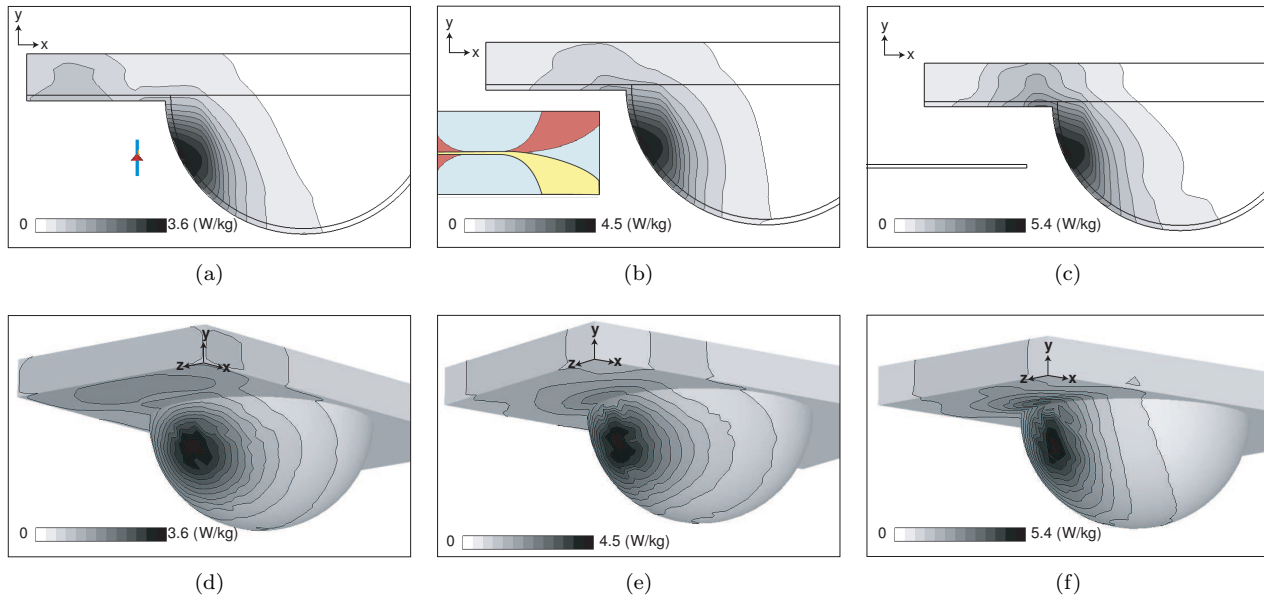


Figure 2: SAR_{10g} deposition profiles with $\epsilon_{imm}=10$, frequency=3GHz, and at position 2. Parts (a)-(c) show a cross-section through the breast (xy plane) for the Dipole, vertically aligned Vivaldi, and horizontally aligned Vivaldi, respectively. Parts (d)-(f) show the corresponding profiles over the skin surface.

Table 4: Summary of SAR simulation results: $\epsilon_{imm}=10.0$, $Freq=6GHz$, $P_{in}=500mW$

Position	Antenna	D_{BR} (mm)	D_{CW} (mm)	P_{BR} (%)	P_{CW} (%)	SAR_{10g} (W/kg)	P_{lim} (mW)
1	Dipole	10.8	6.8	19.3	31.9	8.3	113.0
	Vivaldi (Horiz)	11.4	9.9	32.4	26.4	9.9	93.5
2	Dipole	14.7	19.3	18.8	15.2	5.2	183.0
	Vivaldi (Vert)	11.0	8.0	36.0	10.1	8.2	111.9
	Vivaldi (Horiz)	16.3	22.4	34.2	14.3	8.1	111.0

Conclusion

Results of this preliminary study indicate that a large margin of safety can be expected for a typical, cylindrically configured breast cancer detection system. The most stringent radiated power limitation of $P_{lim}=93.5$ mW is well below radiated power levels utilized in ongoing imaging experiments at Nagasaki University [3-5], which utilizes standard network analyzer measurements with input power levels that never exceed 10 mW and are typically lower than 1 mW. Other research groups developing breast cancer detection techniques are utilizing similar measurement systems [7, 9, 10] which more than likely utilize similar power levels. However, electromagnetic absorption patterns and peak SAR limits in breast cancer detection systems will depend on system specific variables such as the antenna type, immersion liquid, frequency range, and distance from the antenna to the body. Further system-specific studies utilizing simulation of realistic MRI-derived models, or measurement of human tissue phantoms will provide more accurate estimations of expected SAR values in these systems. Nevertheless, the very low SAR levels obtained in this study hint that peak SAR limits are unlikely to be exceeded in typical systems and provide reassurance that these systems represent a safe modality for the detection of breast cancer.

Another conclusion that can be reached from this study is that utilizing a directional antenna (Vivaldi) has distinct advantages over an omni-directional antenna. The Vivaldi antenna deposited a greater percentage of power into the breast in all cases, while generally depositing much less power into the chest wall. Depositing a majority of energy into the breast itself is an important aspect of the antenna which should lead to greater

Table 5: Summary of SAR simulation results: $\epsilon_{imm}=2.5$, $P_{in}=500mW$

Freq (GHz)	Position	Antenna	D_{BR} (mm)	D_{CW} (mm)	P_{BR} (%)	P_{CW} (%)	SAR_{10g} (W/kg)	P_{lim} (mW)
3	1	Vivaldi(Horiz)	21.4	9.9	18.5	31.1	4.6*	191.6
3	2	Dipole	21.3	9.2	10.0	21.5	1.6	580.4
		Vivaldi(Vert)	20.3	3.0	16.3	31.5	3.5*	229.1
		Vivaldi(Horiz)	26.3	22.4	26.8	19.3	4.3	208.4
6	1	Dipole	20.4	4.0	8.8	45.7	5.9*	155.1
		Vivaldi(Horiz)	21.4	9.9	26.2	27.9	7.0	131.1
6	2	Dipole	23.5	16.5	9.7	16.0	1.9	492.6
		Vivaldi(Vert)	21.0	8.0	22.9	15.4	4.3	219.0
		Vivaldi(Horiz)	26.3	22.4	28.6	16.3	6.2	145.6

*maximum occurs in the skin of the chest-wall, rather than the skin of the breast

system efficiency and dynamic range. Furthermore, the horizontally aligned Vivaldi was advantageous because it could be centered at the same vertical position as the other antennas with a much larger physical separation from the chest wall, although in some cases the large H-plane beamwidth led to a higher chest wall absorption (P_{CW}).

Overall, this study has given preliminary evidence that cylindrical breast cancer detection systems can be designed to easily meet standard SAR safety requirements, with a maximum allowable radiated power level of 93.5 mW. A directional antenna (Vivaldi) has shown potential advantages over a lower gain, omnidirectional (dipole) antenna for breast imaging applications.

REFERENCES

1. "IEEE standard for safety with respect to human exposure to radiofrequency electromagnetic fields, 3kHz to 300GHz," IEEE Standard C95.1-2005, April 2006.
2. "Guidelines for limiting exposure to time-varying electric, magnetic, and electromagnetic fields (up to 300 GHz)," *Health Phys.*, vol. 74, no. 4, pp. 494–522, 1998.
3. J. Johnson, H. Zhou, and T. Takenaka, "Experimental three-dimensional time-domain reconstruction of dielectric objects for breast cancer detection," *Mediterranean Microwave Symposium*, Sept. 2006, (Forthcoming).
4. T. Takenaka, T. Tanaka, and H. Zhou, "Reconstruction of 3-D dielectric objects from experimental data in the time domain," *PIERS, Boston, MA, USA - Abstracts*, p. 546, March 2006.
5. H. Zhou, T. Takenaka, and T. Tanaka, "Time-domain reconstruction of lossy objects using dipole antennas," *Microwave & Optical Technology Letters*, vol. 44, pp. 238–243, 2005.
6. S. Gabriel, R. W. Lau, and C. Gabriel, "The dielectric properties of biological tissues: III. Parametric models for the dielectric spectrum of tissues." *Phys Med Biol*, vol. 41, no. 11, pp. 2271–2293, Nov 1996.
7. X. Li, S. Davis, S. Hagness, D. van der Weide, and B. VanVeen, "Microwave imaging via space-time beamforming: experimental investigation of tumor detection in multilayer breast phantoms," *IEEE Trans. Microw. Theory Tech.*, vol. 52, pp. 1856–1865, 2004.
8. O. Gandhi, Q. Li, and G. Kang, "Temperature rise for the human head for cellular telephones and for peak SARs prescribed in safety guidelines," *IEEE Trans. Microw. Theory Tech.*, vol. 49, no. 9, pp. 1607–1613, 2001.
9. J. Sill and E. Fear, "Tissue sensing adaptive radar for breast cancer detection – experimental investigation of simple tumor models," *IEEE Trans. Microw. Theory Tech.*, vol. 53, pp. 3312–19, 2005.
10. D. Li, P. Meaney, T. Reynolds, S. Pendergrass, M. Fanning, and K. Paulsen, "Parallel-detection microwave spectroscopy system for breast imaging," *Review of Scientific Instruments*, vol. 75, no. 7, pp. 2305–2313, 2004.

Experimental test system to assess the EMI from RFID reader/writer on implantable cardiac pacemaker

Shunichi FUTATSUMORI, Taichi KONO, Takashi HIKAGE, Toshio NOJIMA
Graduate School of Information Science and Technology, Hokkaido University, Japan

Ben KOIKE
Japan Automatic Identification Systems Association, Japan

Abstract—In this paper, a newly developed experimental test system for electromagnetic interference (EMI) due to Radio Frequency Identification (RFID) reader/writers on medical devices is introduced and the basic design concept is discussed. The aim of this research is to establish an EMI estimation method using FDTD analysis and a measurement system to obtain precise and detailed EMI characteristics regarding RFID EMI on medical devices. Practical situations of EMI due to existing RFID reader/writers on medical devices is investigated and ways to prevent this EMI are currently discussed by some organizations. In addition, more detailed investigations need to be carried out such as the effects of the three-dimensional electromagnetic fields (EMF) containing human body of actual environments. Furthermore, it is required to design an experiment system with minimum measurement errors. The EMI test experiments on 13 types of implantable pacemakers and defibrillators were carried out to validate the fundamental performance of the test system.

1. Introduction

Radio Frequency Identification (RFID) technologies have been expected to become essential technologies for creating an IT oriented and automated future society. Applications of RFID technologies are not only for product management and identification instead of conventional barcode technology. In addition to existing frequency bands for RFID systems, newly assigned UHF bands for long-range communication have been available in most parts of the world since 2006 [1]. RFID systems are assumed to achieve wide spread applications along with development of legal systems and market's demands.

Recently, many wireless communication devices are introduced to our daily lives. Electromagnetic interference (EMI) on medical devices due to wireless communication devices is serious concerned and a lot of research has been studied [2]-[8]. In particular, EMI on medical devices from mobile phone systems are examined precisely. This research investigates the effect of the electromagnetic fields due to mobile phones and also base stations [2]-[6]. Guidelines to prevent the EMI is provided and operated based on technical report [6]. EMI due to RFID reader/writers on medical devices is investigated with the same experimental method. In addition, guidelines to prevent this EMI are currently discussed by some organizations [7]. Detailed investigations need to be carried out such as the effects of the three dimensional electromagnetic fields (EMF) containing human body of actual environments. Furthermore, it is required to design an experiment system with minimum measurement errors. The aim of this research is to establish an EMI estimation method using FDTD analysis. To develop the estimation method, it is very important to investigate detailed and precise EMI test experiments. The test experiments make clear the relations between EMI effect and electromagnetic field distribution as well as occurrence mechanism of EMI.

In this paper, experimental test system to assess the EMI due to RFID reader/writers on implantable cardiac pacemakers and implantable cardioverter-defibrillators (ICD) are discussed. First, test experiments to acquire a fundamental EMI data and characteristics of RFID reader/writer antennas are explained. The experiments employ newly developed test system and existing procedure. Second, to obtain fundamental data for quantitative assessment of EMI as well as validation of numerical analysis results, field distributions of RFID reader/writers and standard dipole antennas are measured. In addition, a constructed analytical models of the test system and a human torso phantom are shown.

2. Experiments

To obtain a fundamental EMI data and characteristics of RFID reader/writer antennas, test experiments are carried out. The experiments on 26 types of antennas and 13 types of pacemakers and ICDs are conducted.

Exposure antennas include 10 types of commercially available RFID reader/writers and 16 types of standard dipole antennas. Each signal power and modulation method of input signal is defined as 1 type when standard dipole antennas are employed. Tested pacemakers and antennas are shown in Table 1 and Table 2. Pacemakers and ICDs have many operating modes and functions - pacing/sensing polarity, single/dual chamber mode, and antitachycardia functions. The total test mode is 1888 modes at different function modes, frequency bands and RFID reader/writer antennas.

2.1 Experimental test system

RFID systems are typically operated at the frequency bands - 125 kHz, HF (13.56 MHz), UHF (950 MHz) and 2.45 GHz, as shown in Table 2. Furthermore, these antennas usually have different shapes, locations and radiating fields depending on their purpose, operating frequency bands and their manufacturers. Moreover, positions between a human torso phantom and RFID reader/writer antennas must be determined precisely and movable. It is required to measure the EMI due to various antennas with accuracy and repeatability. A new test system consists of a flat human torso phantom based up on Irnich's model, a function generator, a chart recorder and a measurement platform [2] was developed. An overall view of the experimental test system is shown in Fig.1. The two-axis sliding measurement platform shown in Fig.2 enables us to measure RFID antennas moving parallel to the torso phantom (y -axis direction), while maintaining same distance between the phantom and antennas (x -axis direction). All parts of this platform are made of dry wood. This system has advantages of high efficiency and reliable assessment.

2.2 Electromagnetic interference test experiments

Conditions of test experiments such as configurations of the equipment, procedures, determination of interference levels are same as reference [7]. In addition, a breakdown of the test modes are shown in Table 3. The pacemakers and ICDs are programmed to VVI mode (the Ventricle chamber is paced, the Ventricle chamber is sensed, and the response to sensing is Inhibited) and AAI mode (the Atrium chamber is paced, the Atrium chamber is sensed, and the response to sensing is Inhibited).

Table 1:
Pacemakers and implantable cardioverter-defibrillators

Tested devices	Type of chambers	Number of devices
Pacemaker	Single chamber	5
	Dual chamber	5
Implantable Cardioverter-Defibrillator	Single chamber	1
	Dual chamber	2
Total		13

Table 2:
Antennas in each frequency bands

Frequency bands	Type of antennas	Number of antennas
125 kHz	RFID reader/writer	4
HF (13.56 MHz)	RFID reader/writer	2
	Standard dipole	10
UHF (950 MHz)	RFID reader/writer	2
	Standard dipole	6
2.45 GHz	RFID reader/writer	2
	Total	26

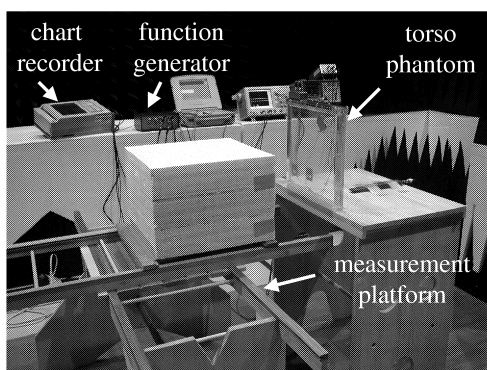


Figure 1: The experimental test system.

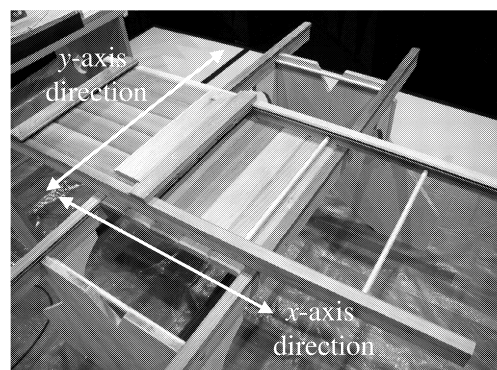


Figure 2: The two-axis sliding measurement platform.

Table 3: The total test modes

Frequency bands	Types of antennas	VVI Inhibit		VVI Asynchronous		AAI Inhibit		AAI Asynchronous		False Positive	False Negative	Total modes
		UNI	BI	UNI	BI	UNI	BI	UNI	BI	BI	BI	
		125KHz	RFID reader/writer	28	40	28	40	32	40	32	40	
HF(13.56MHz)	RFID reader/writer	14	20	14	20	16	20	16	20	10	10	160
UHF (950MHz)	Standard dipole	56	80	56	80	64	80	64	80	40	40	640
	RFID reader/writer	16	20	16	20	12	12	12	12	4	4	128
2.45GHz	Standard dipole	42	60	42	60	48	60	48	60	30	30	480
	RFID reader/writer	14	20	14	20	16	20	16	20	10	10	160
Total modes		170	240	170	240	188	232	188	232	114	114	1888

For each of the two pacemaker modes (AAI and VVI), there are two types of tests which are conducted - one with an injected Electrocardiogram (ECG) signal (typical inhibition), and one with no injected ECG signal (typical asynchronous pacing). In particular with ICDs, there are an additional two test modes, False Positive mode (one with no injected ECG signal and false detection of fibrillation (False Positive mode)), and False Negative mode (one with injected ECG signal and false non-detection of fibrillation).

3. Measurement of field distributions

To obtain fundamental data to validate results of numerical analysis, field distributions of RFID reader/writers antennas and standard dipole antennas are measured. The obtained distributions are both electric and magnetic fields. The reason for this is near fields of the antennas are not proportioned to each other. Figure 3 shows one of the probe positioners, which is made of styrene foam. This positioner enables reliable measurement taking the advantages of low reflection or absorption of electromagnetic fields. Figure 4 is an example of three-dimensional measured magnetic field distributions. The total number of measured antennas is same as Table 2.

4. Analytical models

We will carry out more detailed EMI investigation using FDTD analysis [8] such as the effects of the three-dimensional EMF containing human body of actual environments. The end goal of this research is to establish an EMI assessment employing numerical analysis regarding RFID EMI on medical devices. To obtain detailed analytical model, modeling of test system and the human torso phantom are conducted. The proposed test system composed of the two-axis sliding measurement platform and others are designed with the premise of numerical analysis. In addition, material constant of saline solution (NaCl 1.8g/L) and acryl amide for the torso phantom are measured using an open-ended coaxial probe method. Both relative dielectric constants ϵ_r and loss tangent $\tan\delta$ for each RFID operated frequency band are measured and applied for the model. Figure 5 shows an example of calculated electric fields on the torso phantom exposed by radio waves from a UHF band standard dipole antenna.

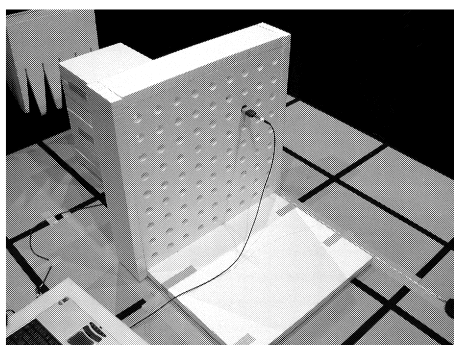


Figure 3: The probe positioner.

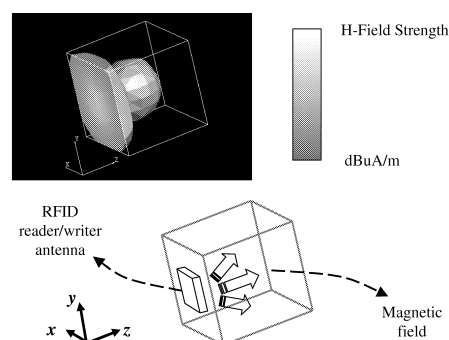


Figure 4: Measured magnetic field distributions.

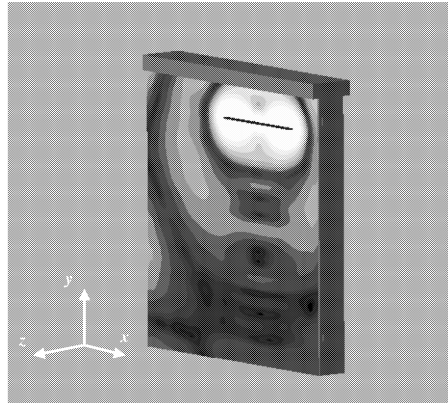


Figure 5: An example of calculated electric fields.

5. Conclusion

In this paper, EMI test system to assess the EMI due to RFID reader/writer on implantable cardiac pacemakers and ICDs were discussed. First, the new test systems for measuring the EMI were developed and test experiments were explained. Second, to obtain fundamental data for quantitative assessment of EMI as well as validation of numerical analysis results, field distributions of RFID reader/writers and standard dipole antennas were measured. Finally, constructing analytical model of test system and human torso phantom are shown. Next step of this research is to establish a quantitative EMI estimation method using numerical analysis. In addition, more detailed investigations such as how to estimate the effects of the human body's absorption/reflection and other lossy materials existing in actual environments will be conducted.

Acknowledgment

The authors would like to thank the members of the Pacemaker Committee of Japan and Japan Automatic Identification Systems Association for their cooperation and support, Mr. T. Toyoshima and Mr. H. Fujimoto, Medtronic Japan Co., Ltd. for thier help in construction of the experimental test system.

REFERENCES

1. *Class 1 Generation 2 UHF Air Interface Protocol Standard Version 1.0.9*, EPCglobal, Inc., 2005.
2. W. Irnich, L. Batz, R. Muller, and R. Tobisch, "Electromagnetic interference of pacemaker by mobile phones," *PACE*, vol. 19, pp.1431-1446, Nov. 1996.
3. T. Toyoshima, M. Tsumura, T. Nojima, and Y. Tarusawa, "Electromagnetic interference of implantable cardiac pacemakers by portable telephones," *Japanese journal of cardiac pacing and electrophysiology*, vol. 12, no.5, pp. 488-497, 1996.
4. Y. Tarusawa, K. Ohshita, Y. Suzuki, T. Nojima, and T. Toyoshima, "Experimental estimation of EMI from cellular base-station antennas on implantable cardiac pacemakers," *IEEE Trans. Electromagn. Compat.*, vol. 47, no. 4, pp.938-950, Nov. 2005.
5. T. Nojima, and Y. Tarusawa, "A new EMI test method for electronic medical devices exposed to mobile radio wave," *IEICE trans. Commun.*, vol.E88-B, no.1, pp. 11-18, Jan. 2001.
6. *Guidelines on the use of radio communication equipment such as cellular telephones - Safeguards for electric medical equipment*, presented at the EMC Conf. Japan, Electromagnetic Medical Equipment Study Group, 1997.
7. *Investigation and research report of electromagnetic interference on medical devices (in Japanese)*, Ministry of Internal Affairs and Communications (MIC) of Japan, Mar. 2005.
8. J. Wang, O. Fujiwara, and T. Nojima, "A model for predicting electromagnetic interference of implanted cardiac pacemakers by mobile telephones," *IEEE Trans. Microwave Theory Tech.*, vol. 48, no. 11, pp.2121-2125, Nov. 2000.

APPLICATION OF WAVELETS TO THE STUDY OF THE HUMAN SLEEP SLOW OSCILLATION

Sami Barmada[#], Elisa Biagi[#], Laura Brotini[#], Angelo Gemignani^{*}, Alberto Landi[#], Danilo Menicucci^{*},

^{}Department of Physiology and Biochemistry "G. Moruzzi," University
of Pisa, via San Zeno 31, 56127, Pisa, Italy
phone: +39 050 2213484 – fax: +39 050 2213527 - e-mail: gemignani@dfb.unipi.it*

*[#]Department of Electrical Systems and Automation, University
of Pisa, via Diotisalvi 2, 56126, Pisa, Italy
phone: +39 050 2217300 – fax: +39 050 2217333 - e-mail: sami.barmada@dsea.unipi.it*

Abstract: The slow oscillation represents a fundamental basic phenomenon of the sleep; it is characterized by typical frequencies less than 1 Hz. We have applied on human sleep EEG the wavelet expansion method to automatically detect the slow oscillation. According to literature, obtained results are consistent with typical frequency of slow oscillation, and they have been confirmed in this paper also by applying the Hilbert Huang transform. The study of sleep slow oscillation is still at an early stage, although it seems to be extremely promising for neurophysiology and for neurophysiopatlogy. To our knowledge, the tools used in this paper were not previously applied to the study of human sleep

Keywords: Sleep, Slow oscillation, Wavelet method, Hilbert Huang method, Monitoring, Human.

1. INTRODUCTION

During slow wave sleep, the electroencephalographic pattern is characterized by a succession of K-complexes, sleep spindles, and delta waves [1]. Despite this hypersynchronization of the electrical cortical activity, which is negatively correlated to the cerebral metabolism [2], the electrophysiological and molecular mechanisms of the brain remain intensely active ([3], [4]).

In fact, intracellular recordings in animals have revealed that during K-complexes and delta waves, the membrane potentials of cortical neurons oscillate between states of deep hyperpolarization (down state) and states of wake-like depolarization (up state) [5]. Each down-and-up-state lasts a fraction of second (700 ms circa). During the down state the electrical cortical activity is silent, whereas during the up state, an intense neural discharge is present [6]. This cellular behaviour was called "slow oscillation" and represents the fundamental cellular phenomenon underlying neural activity in slow wave sleep (NREM sleep stage 3 and 4 or delta sleep).

This cellular phenomenon is detectable also in sleep EEG pattern of humans [7] and recently [8] described that "sleep slow oscillations are travelling waves that sweep the human cerebral cortex up to once per second". Further, the authors pointed out that each slow oscillation has a definite site of origin, originating more frequently at anterior cortical regions and propagating to posterior cortical areas with a higher reproducibility across nights and across subject.

A primary goal of our research is the definition of an automatic method for detecting instantaneous frequencies typical of the sleep slow oscillations in human EEG data: they have characteristic frequencies less than 1 Hz.

In order to detect and classify such phenomenon, a wavelet based approach has been implemented [9]. The choice of a wavelet basis as a tool comes from the authors experience on wavelet based signal processing: the ability of wavelets to isolate and discriminate compact support patterns in a complex and noisy signal (as the EEG signal) has been proven in the recent years; furthermore the wavelet expansion can be easily performed with a set of filters. Generally signal processing engineers are used to choosing more conventional methods, such as the ones based on the Fourier analysis. Unfortunately the Fourier transform is based on the assumption of stationarity of the signal to be analysed. Furthermore the standard Fourier analysis gives only an indication of the general frequency content of a signal, while completely loosing any local time information. Sometimes the Short Time Fourier Transform is used, but it requires the proper choice of a time window, conditioning the whole analysis.

In order to validate our results a comparison with the Hilbert-Huang transform has been performed [10].

2. DESCRIPTION OF THE SIGNAL PROCESSING TECHNIQUES

In this section we describe the two methods we used for the detection of the slow oscillation, together with the first description [8] of its characteristic, the Massimini Criteria.

2.1 *Massimini criteria*

According to [8], each channel was scanned with a sliding window in order to identify all signal shapes with the following features:

- (a) a negative zero crossing and a subsequent positive zero crossing separated by 0.3–1.0 sec,
- (b) a negative peak between the two zero crossings with voltage less than $-80 \mu\text{V}$,
- (c) a negative-to-positive peak-to-peak amplitude $>140 \mu\text{V}$.

In Fig.1, an example of sleep slow oscillation, according to Massimini criteria, is shown.

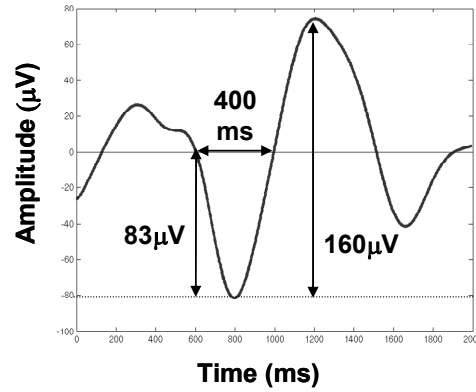


Fig. 1. Sleep slow oscillation waveform and its characteristic parameters.

2.2 Wavelet based decomposition

The main feature that makes wavelets attractive is that the Wavelet Transform (WT) of a function $f(t)$ gives a function of two parameters: time t and scale s , the latter being the key point of WT. Unlike the Short Time Fourier Transform (the signal is filtered through a time window and then Fourier Transform is performed), which works with a fixed window, WT works with a scaled window allowing the visibility of the whole frequency content.

Like the Short Time Fourier Transform (STFT) the wavelet analysis is based on the introduction of a window function $\Psi(u)$ (which is in general a complex function), called mother wavelet. It is scaled and translated according to the expression:

$$\Psi_{s,t}(u) = |s|^{-p} \Psi\left(\frac{u-t}{s}\right) \quad (1)$$

where the parameter s ($s \neq 0$) is the scaling factor, while p ($p \geq 0$) can be chosen in order to let all the wavelets have the same energy. As the Fourier transform is the combination of complex exponential functions, the WT of a signal $x(u)$ is the combination of scaled and translated versions of the mother wavelet Ψ multiplied by the signal $x(u)$. Hence the continuous WT is defined as:

$$\bar{x}(s,t) = \int_{-\infty}^{+\infty} \overline{\Psi}_{s,t}(u) x(u) du = \langle \Psi_{s,t}, x \rangle \quad (2)$$

where $\overline{\Psi}_{s,t}(u)$ is the complex conjugate of $\Psi(u)$. If the value of the WT of the signal x is high for a determined scale and time, the scaled wavelet at the time t and the signal are strictly correlated.

The importance of the WT, if compared to the STFT can be roughly explained as follows: let us suppose that the mother wavelet is centred on t_0 and has time width T . Then $\Psi_{s,t}$ is centred on st_0+t and has time width sT ; consequently the WT gives information about the signal in the interval $[st_0+t-sT, st_0+t+sT]$. With the increase of s , the width of the window increases, while the resolution decreases. If we define ν_0 and Ω respectively as the centre and the bandwidth of $\hat{\Psi}(\Omega)$ (the Fourier transform of the mother wavelet), we obtain that the WT gives information about the frequency spectrum of the signal inside the interval $[(\nu_0-\Omega)/s, (\nu_0+\Omega)/s]$. Therefore for small s , we have a wide frequency band, high frequency spectrum centre value and a narrow time window; while high values of s give narrow bandwidth, small frequency spectrum centre value and at the same time a wide time window. This is in accordance with the fact that low frequency components are better revealed by the use of wide time windows, while high frequency components need a narrow time window.

As a matter of fact, the WT studies the signal via a window characterised by a continuous variation of width avoiding the limit of the STFT, which is based on the use of a fixed window.

Furthermore it is possible to define a multi-resolution scheme, on bases of wavelet functions at different scales, that acts on a signal like a sub band filtering procedure. This leads to the possibility of decomposing a signal into a sum between a blurred version of the signal itself (f^M) and a series of details (d^i). It is evident that this property is useful in pattern recognition applications, since the different details can enhance and/or show characteristics not visible in the original signal.

2.3 Hilbert Huang method

The Hilbert transform $Y(t)$ of a signal $X(t)$ is defined by the integral:

$$Y(t) = \frac{1}{\pi} P \int_{-\infty}^{\infty} \frac{X(\tau)}{t-\tau} d\tau \quad (3)$$

Where P stands for the Cauchy principal value.

Consider $X(t)$ and $Y(t)$ as the real and imaginary parts of the analytic signal $Z(t)$:

$$Z(t) = X(t) + iY(t) = a(t)e^{i\theta(t)} \quad (4)$$

where

$$a(t) = [X^2(t) + Y^2(t)]^{1/2} \text{ and } \theta(t) = \text{atan}\left(\frac{Y(t)}{X(t)}\right) \quad (5)$$

It is convenient to define the Hilbert instantaneous frequency as the time derivative of the phase of the analytic signal $Z(t)$:

$$\omega = \frac{d\theta(t)}{dt} \quad (6)$$

It represents a mono-component definition, i.e., data must be consistent with (6) and at each time one and only one instantaneous frequency exists.

Unfortunately signals are usually multicomponent, and the instantaneous frequency definition (6) cannot be extensively applied.

To make the instantaneous frequency (6) applicable, [10] presented a signal decomposition method, able to decompose a signal into intrinsic mode functions (IMF) to which (6) can be applied.

An IMF is a function that satisfies the two following properties:

- (1) the number of extrema and the number of zero crossings is equal (or differing at most by one)
- (2) the mean value of the envelope defined by the local maxima and the envelope defined by the local minima is equal to zero at any point.

Since most data do not satisfy above properties, in the hypothesis that any signal consists of different simple IMFs, the EMD method is developed to extract IMF components.

The EMD method operates through six steps [14]: at the end of the procedure we have a residue r and a collection of n IMFs, named h_i ($i=1, \dots, n$). The h_i are generated being sorted in descending order of frequency and therefore h_1 is the first IMF and it is associated with the locally highest frequency. Furthermore the original X can be exactly reconstructed by a linear superposition.

After IMF decomposition, the Hilbert transform can be applied to each IMF, and the Hilbert instantaneous frequency can be extracted. After performing the Hilbert transform on each IMF component, the signal can be expressed as:

$$X(t) = \sum_{j=1}^n a_j(t) \exp\left(i \int \omega_j(t) dt\right) \quad (7)$$

The frequency-time distribution of the amplitude is designated as the Hilbert–Huang spectrum.

3. SLOW OSCILLATION DETECTION

10-20 Jasper EEG recordings were performed in a representative male subject (age 35 years) during the first sleep episode of the night. The subject was placed in a shielded, soundproof room and allowed to sleep at his customary bedtime. All signals were band-pass filtered (0.1 – 4 Hz) and digitized at 250 Hz. All signals were monopolar and re-referenced to the average of the signals recorded from the two earlobes. Sleep stages were scored according to [13].

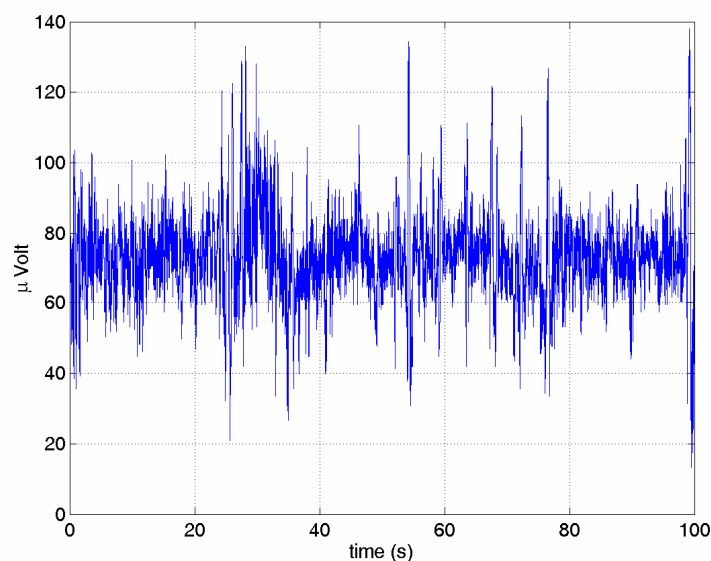


Figure 2 EEG recorded signal

Figure 3 shows part of the wavelet expansion, performed with a Daubechies Wavelet Basis with 10 vanishing moments. Based on the author’s experience, Daubechies wavelets are the family that best performs for such analysis, and the choice of a high number of vanishing moments (the order of the polynomials that such basis can represent without any approximation error) is due to the characteristic of the waveform we are looking for.

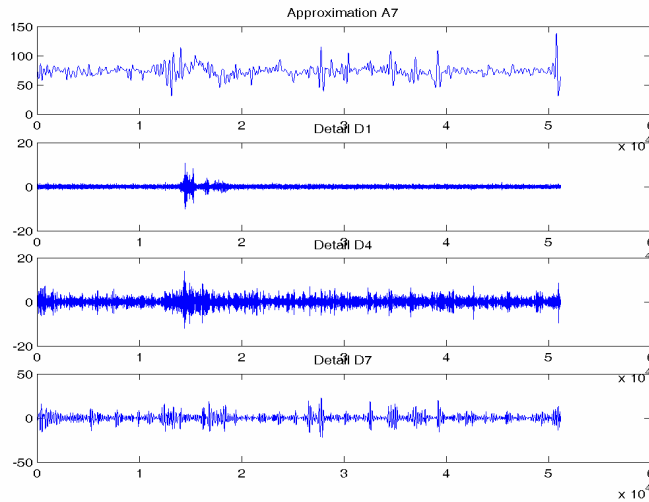


Figure 3 Approximation at level 7 and three details of the wavelet expansion

From Figure 3 it is evident that the wavelet expansion automatically performs the signal denoising, removing the noise (higher frequency components) of the signal, which is comprised in the details. The approximation can be seen as the original signal where all the details have been removed, and due to the above mentioned characteristics of the wavelet expansion with Daubechies wavelets, the typical waveform of the slow oscillation should be evident now.

Figure 4 shows a part of the signal (in particular around time 54 s) where the pattern of the slow oscillation is present and the same part of the signal before the wavelet expansion was performed. It is evident that the application of the wavelet expansion is fundamental for the location of the pattern reported in Fig. 1.

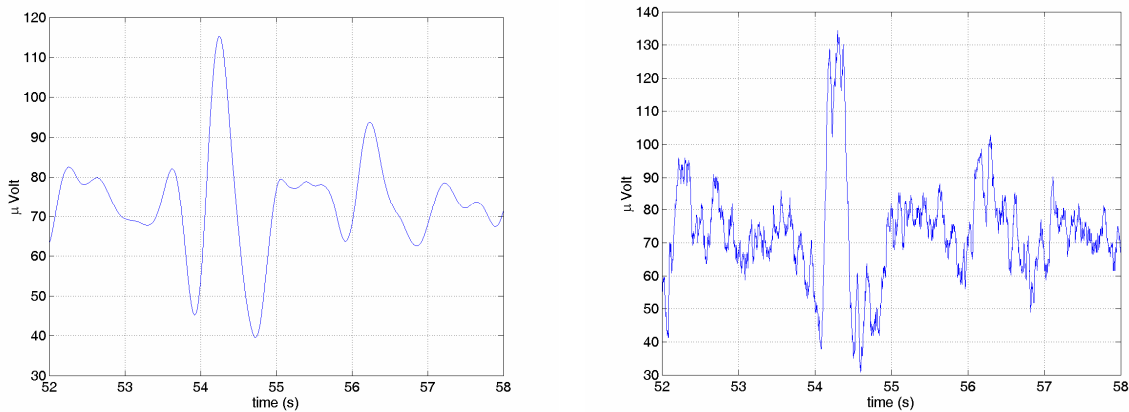


Fig. 4 The signal around time 54 s where the slow oscillation is present.

In order to verify if the slow oscillation has been properly detected, we can perform a Hilbert-Huang transform in order to calculate the local frequency content, and verify if it is lower than 1 Hz. Figure 5 shows the IMF decomposition as obtained according to the description of Section II.

To extract the instantaneous frequency, our analysis was limited to the second IMF of Fig. 5, which shows the best correlation with the recorded EEG signal. In order to obtain the instantaneous frequency of the slow oscillation, we have multiplied the sampling rate by the mean value of the instantaneous frequencies computed from the second IMF using the Hilbert transform. In this case the mean value is 1.7×10^{-3} and the sampling rate is 512 Hz, so that the slow oscillation instantaneous frequency is 0.8 Hz. This result is consistent with a typical frequency of slow oscillation that is centred around 0.8 Hz [5]. Furthermore we have verified our approach on EEG slow waves not corresponding to Massimini criteria.

4. CONCLUDING REMARKS

The results of the study indicate the effectiveness of the Hilbert Huang method to detect the sleep slow oscillation in the human EEG. Our data are in a good agreement with the criteria applied by Massimini *et al.* (2004) for recognizing slow oscillation.

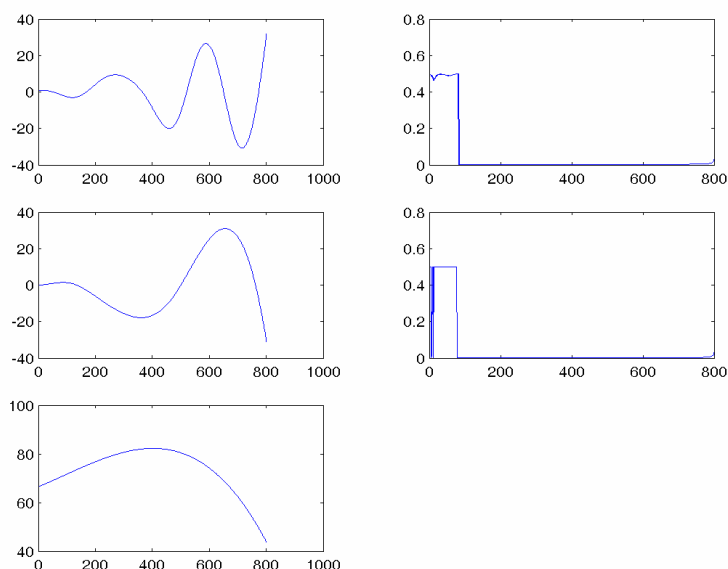


Fig. 5 Hilbert Huang transform: the resulting IMF

Our approach differs from the usual study of the slow oscillation mainly based on the shape of the waveform, providing a method for an automatic detection of this bioelectrical phenomenon. The study of sleep slow oscillation is still at an early stage, although it seems to be extremely promising. From a physiological point of view, the slow oscillation is associated to molecular and synaptic remodelling of cortical neurons occurring during sleep. Therefore it may be correlated to the beneficial effects of sleep on cognitive and emotional functions. From a pathophysiological point of view, in [8] is shown that slow oscillation is a wave that travels on the cortex and therefore it may be considered as a good index of anatomical and functional connectivity. Several neurological and psychiatric disorders could be sustained by alterations of the cortical connectivity ([15], [16]).

REFERENCES

- [1] Steriade, M, "Corticothalamic resonance, states of vigilance and mentation. *Neuroscience*" 101, 2000, 243–276.
- [2] Maquet P. "Functional neuroimaging of normal human sleep by positron emission tomography" *J Sleep Res.* 9, 2000, 207-31.
- [3] Frank M.G., Issa N.P., Stryker M.P. "Sleep enhances plasticity in the developing visual cortex". *Neuron*, 30, 2001, 275-287.
- [4] Tononi G, Cirelli C. "Sleep and synaptic homeostasis: a hypothesis" *Brain Res Bull*, 62, 2003, 143-50.
- [5] Steriade M, Timofeev I. "Neuronal plasticity in thalamocortical networks during sleep and waking oscillations" *Neuron*, 37, 2003, 563-76.
- [6] Steriade M, Timofeev I, Grenier F "Natural waking and sleep states: a view from inside neocortical neurons". *J Neurophysiol* 85, 2001, 1969-1985.
- [7] Achermann P., Borbély A. "Low-frequency (<1 Hz) oscillations in the human sleep EEG", *Neuroscience* 81, 1997, 213–222.
- [8] Massimini M, Huber R, Ferrarelli F, Hill S, Tononi G. "The sleep slow oscillation as a traveling wave" *J Neurosci*, 24, 2004, 6862-6870.
- [9] Mallat S. "A Wavelet tour of signal processing", Academic Press
- [10] Huang N. E., Shen Z, Long SR, et al. "The empirical mode decomposition and the Hilbert spectrum for nonlinear and non-stationary time series analysis". *Proc R. Soc, London A454*, 1998, 903–995.
- [11] Amzica F., Steriade M. "Electrophysiological correlates of sleep delta waves". *Electroencephalogr Clin Neurophysiol.* 107, 1998, 69-83.
- [12] Amzica F., Steriade M. "The functional significance of K-complexes" *Sleep Med Rev.* 6, 2002, 139-149.
- [13] Rechtschaffen A., Kales A. "A Manual of Standardized Terminology, Techniques and Scoring System for Sleep Stages of Human Subject". Washington, DC: US Government Printing Office, US Public Health Service, 1968
- [14] Balocchi, R., et al. "Deriving the respiratory sinus arrhythmia from the heartbeat time series using empirical mode decomposition". *Chaos, Solitons and Fractals* 20, 2004, 171-177.
- [15] Gemignani, A. et al. "Slow wave and REM sleep mechanisms are differently altered in hereditary pick disease associated with the TAU G389R mutation" *Arch Ital Biol* 143, 2005, 65-79.
- [16] Harrison, P.J. "The neuropathology of schizophrenia. A critical review of the data and their interpretation" *Brain*, 122, 1999, 593-624.

Position and Attitude Determination for Bistatic SAR Experiments – Basic Considerations

S. Knedlik, P. Uboldosold, O. Loffeld

University of Siegen, Center for Sensorsystems (ZESS), Germany

Abstract—Challenging bistatic SAR experiments are under way [1]. Among them is a hybrid experiment where the carrier platforms will be an aircraft and Germany's national remote sensing satellite TerraSAR-X. Because of the different trajectories of the involved platforms, the overlapping of transmitter and receiver antenna footprints is an issue. In this paper we illuminate some basics, namely on the proposed geometric modeling of the antenna pointing, and the position and attitude covariance analysis and interpretation.

1. Introduction

Starting with suggestions of constellations of passive micro-satellites for synthetic aperture radar (SAR) Interferometry (e.g., Cartwheel [2], Pendulum [3]), which simultaneously receive signals transmitted from an existing spaceborne radar, bi- and multi-static SAR has become of rapidly increasing interest to the science community in recent years. The involved platforms carrying transmitter and/or receiver antennas can for instance be satellites, airplanes, unmanned aerial vehicles (UAVs), or even towers. Among the advantages of bi- and multi-static configurations in comparison to usual mono-static SAR are [1, 4]:

- additional information due to the bistatic reflectivity of targets can be exploited
- di- and polyhedral effects that outshines image details can be reduced yielding further improved classification results
- SAR imaging in along-track direction will be possible
- cost reduction, as well as reduced size, weight, energy consumption is possible
- reduced vulnerability in case of appropriate military systems

Despite remarkable progress in the derivation of proper processing algorithms (e.g., [5, 6]) and in the development of the required technology, bistatic SAR imaging is far away from being operational. There are several research challenges, among them accurate positioning and attitude determination.

Bistatic airborne/airborne as well as hybrid (satellite/airborne) experiments are in preparation in a large coordinated joint package project between ZESS and FGAN, funded by the German Science Foundation (DFG). They are based on FGAN's PAMIR (Phased Array Multifunctional Imaging Radar) system and TerraSAR-X (Germany's national remote sensing satellite which will be launched in October 2006 and whose scientific utilization is coordinated by the German Aerospace Center (DLR)) [1]. Both systems are operating in X-band.

In case of the planned hybrid experiment, where the satellite has an orbit velocity of about 7.6 km/s compared to only 0.1 km/s of the airborne platform, there will be a difference in the velocities of both antenna footprints in the order of 70. The overlap of the antenna footprints will be just a few seconds in maximum [7]. Hence, positioning and attitude determination is an important issue to guarantee an overlapping of transmitter and receiver antenna footprints (by appropriate antenna steering) during the mission. So, in bistatic SAR we have in summary stringent requirements on attitude and position determination with respect to the following steps: footprint chasing, motion compensation, geo-referencing, processing of raw data (estimation of time difference parameter a_1 and slant range ratio parameter a_2), and SAR Interferometry.

In SAR Interferometry, the sensitivity of the generated Digital Elevation Models (DEMs) to crucial interferometric parameters like the interferometric baseline (the vectorial distance between the both antenna phase centers) depends on the parameters (e.g., wavelength, orbit) of illuminator and passive receive-only carriers. An appropriate analysis with respect to passive micro-satellites is given in [8]. Here, a maximum height error of 1 m would (in case of X-band) require the knowledge of baseline length and baseline roll angle with errors smaller than a few mm or arcsec, respectively. Concerning footprint chasing, attitude perturbations of about 0.01° in heading, elevation, and bank angle could cause a maximum displacement of the antenna pointing of about 220 m (north-east plane) in case of TerraSAR-X. And in case of the aircraft, $\pm 0.5^\circ$ errors (in the three Euler angles) yield maximum tie point errors of about 120 m [9]. Baseline estimation and footprint chasing are examples where accurate *relative* position and attitude determination is required – relative with respect to the carrier platforms and not to the positioning method.

In this paper we will consider the geometric modeling of the antenna pointing and how position and attitude accuracy can be analyzed.

2. Geometric Modeling of the Antenna Pointing

Let us first consider coordinate frames that will be needed. The applied coordinate frames are usually Cartesian, and all are right handed: The *Origin* is Earth’s center of mass if not stated otherwise.

The *Orbital Plane System (OS; o)* is used to describe and calculate the orbit: *X-Axis*: points towards the perigee; *Z-Axis*: orthogonal to the orbital plane; *Y-Axis*: completes the right-handed orthogonal system. Keplerian parameters are used to specify the orbit (right ascension of the ascending node (RAAN) Ω , inclination i , argument of perigee ω_{per} , semi major axis, numerical eccentricity, time of perigee passage).

The *Earth-Centered Inertial Coordinate System (ECI; i)* is ‘fixed’ in space (it does not rotate with the Earth) and hypothetically time invariant. Because it is inertial with respect to rotation, but non-inertial with respect to translation it is called a quasi-inertial system. *X-Axis*: points towards the vernal equinox; *Z-Axis*: parallel to the rotation axis of the Earth (north polar axis); *Y-Axis*: completes the right-handed orthogonal system.

A *trajectory system (TS)* (and/or the Tangential-Cross-Normal (TCN) system) will be used: *Origin*: fixed at satellite, *X-Axis*: orthogonal to the plane spanned by satellite-1 s velocity vector and zenith, *Z-Axis*: pointing to inverse nadir, *Y-Axis*: completes the right-handed orthogonal coordinate system. In case of the satellite, the normalized antenna pointing vector will be described with respect to the nadir: $\vec{n}_{AP} = [\sin(\text{off} - \text{nadir}) \ 0 \ -\cos(\text{off} - \text{nadir})]^T$.

As terrestrial equatorial system the *WGS 84 Earth-Centered Earth-Fixed (ECEF; e)* System will be used. It includes an Earth model which is defined by a set of primary and secondary parameters and which is well described in literature. *X-axis*: Pointing to the intersection of zero meridian plane and equatorial plane; *Z-axis*: Pointing to North Pole; *Y-axis*: Completes the right-handed orthogonal coordinate system (from origin in the equatorial plane 90° east of the x-axis). Note that there are geocentric latitude, geodetic latitude and parametric latitude. Ellipsoidal coordinates (latitude, longitude, height) or Cartesian coordinates can be used.

Considering a flat earth approximation, a local tangent plane and appropriate right-handed local-level coordinate systems (index: l) like *north-east-down (NED)* and *east-north-up (ENU)* are used.

Several body coordinate frames (index: b) are used. The carrier fixed *Carrier Body Coordinate system (CBC)* has the *Origin* somewhere at the carrier of interest. The *X-axis* is along the carrier longitudinal axis (positive to the front), the positive *Y-axis* out of the right hand side, and the *Z-axis* such that turning to the right is positive. Other body coordinate systems are fixed at an Inertial Measurement Unit (IMU; I) (or at gyroscopes and accelerometers). Moreover, there is the *Antenna (Body) Coordinate System (ACS; a)* with its *Origin* at the phase center of the antenna. The positive *X-axis* points forward the antenna longitudinal axis, the positive *Y-axis* is directed to the right side of the antenna and the positive *Z-axis* is normal to the x and y axes, pointing downward. In case of no electronic beam steering via phase shifts, the z-axis would be in direction of the antenna pointing vector.

In Fig. 1 a simplified modeling of the antenna pointing is shown.

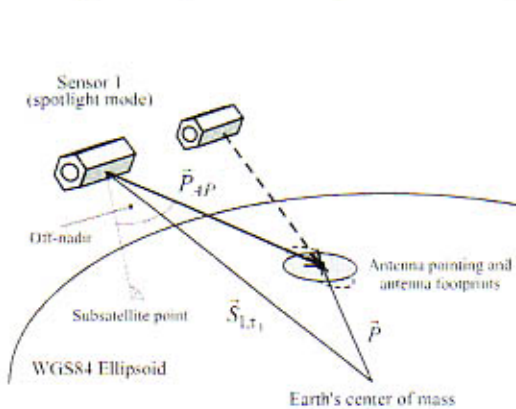


Fig. 1a): Geometric Modeling (WGS84 Earth Model)

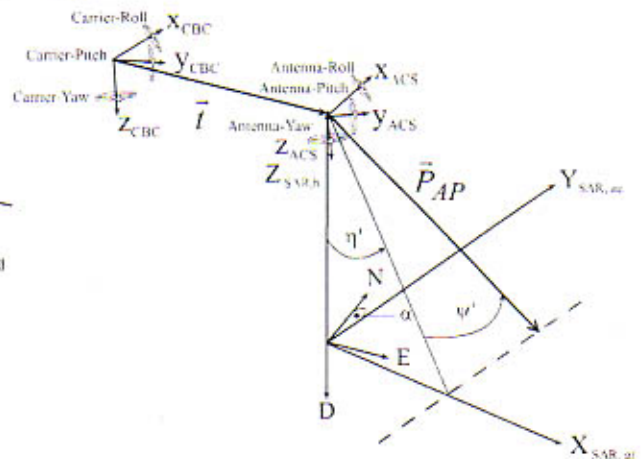


Fig. 1b): Geometric Modeling (Local Tangent Plane)

The coordinate system which is used in SAR (ground range, azimuth) and which is established after motion compensation is usually neither in alignment with the x-axis of the ACS nor necessarily with the velocity vector of the carrier. Therefore, the incidence and squint angles η' and ψ' differ from the angles of antenna steering in azimuth or elevation.

The transformation between local-level and body coordinate frames becomes easy if we commit ourselves to use always the same rotation sequence. Hence, we use the *body Euler angles sequence* $R_{l,f}^b = R_{1,f}(\phi)R_{2,f}(\theta)R_{3,f}(\psi)$. That is, frame rotation from NED to BCS is obtained by a first rotation about

the z-axis (third axis) of the reference system (down) through *heading* ψ , is followed by a rotation about the new y-axis through the *elevation angle* θ , and a rotation about the newest x-axis through the *bank angle* ϕ . See fig. 2.

Incremental perturbations about each of the body-axes are called *yaw*, *pitch*, and *roll*, respectively [10].

The rotation matrix which takes the local-level frame into the body coordinate frame is therefore

$$R_{l,f}^b = \begin{bmatrix} 1 & 0 & 0 \\ 0 & \cos \phi & \sin \phi \\ 0 & -\sin \phi & \cos \phi \end{bmatrix} \begin{bmatrix} \cos \theta & 0 & -\sin \theta \\ 0 & 1 & 0 \\ \sin \theta & 0 & \cos \theta \end{bmatrix} \begin{bmatrix} \cos \psi & \sin \psi & 0 \\ -\sin \psi & \cos \psi & 0 \\ 0 & 0 & 1 \end{bmatrix} = \begin{bmatrix} c\psi c\theta & s\psi c\theta & -s\theta \\ c\psi s\theta \sin \phi - s\psi c\phi & s\psi s\theta \sin \phi + c\psi c\phi & c\theta \sin \phi \\ c\psi s\theta \cos \phi + s\psi s\phi & s\psi s\theta \cos \phi - c\psi s\phi & c\theta \cos \phi \end{bmatrix} \quad (1)$$

with $c = \cos$ and $s = \sin$.

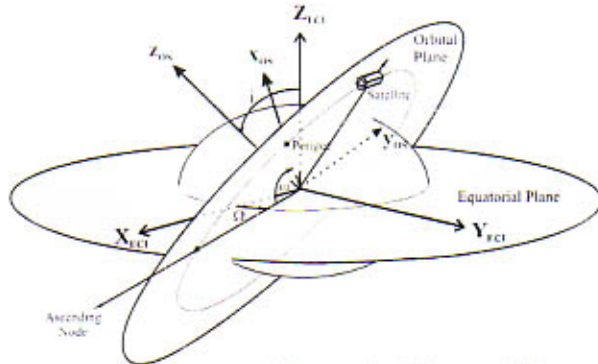


Fig. 2a) ZXZ Euler sequence which rotates inertial frame to orbit frame

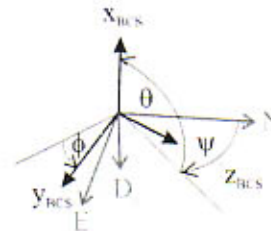


Fig. 2b) ZYX Euler sequence which rotates local-level frame to body coordinate frame

The transformation from ECEF to ECI and vice versa is done by considering Greenwich sidereal time (Earth rotation rate of approx. 15 °/h). The frame transformation from ECI to OS is given by the *orbit Euler angle sequence* $R_{INS,f}^{OS} = R_{3,f}(\omega_{per})R_{1,f}(i)R_{3,f}(\Omega)$. The matrix that rotates ENU to NED (and vice versa) is

$R_{ENU,f}^{NED} = \begin{bmatrix} 0 & 1 & 0 \\ 1 & 0 & 0 \\ 0 & 0 & -1 \end{bmatrix}^T$. Positions given in ECEF frame (e.g., GPS satellites) can for instance be transformed into a local-level frame by using the unit vectors of ECEF-axes in ENU coordinates:

$$R_{ECEF,f}^{ENU} = \begin{bmatrix} \mathbf{1}_X & \mathbf{1}_Y & \mathbf{1}_Z \end{bmatrix}_{ENU} = \begin{bmatrix} -\sin \theta & \cos \theta & 0 \\ -\sin \phi \cos \theta & -\sin \phi \sin \theta & \cos \phi \\ \cos \phi \cos \theta & \cos \phi \sin \theta & \sin \phi \end{bmatrix}$$

with $\theta =$ local reference longitude and $\phi =$ local geodetic latitude. For the transformation from TS to ECI the matrix will consist of the following unit vectors:

$$R_{TS,f}^{ECI} = \begin{bmatrix} \mathbf{1}_{X_{TS}} & \mathbf{1}_{Y_{TS}} & \mathbf{1}_{Z_{TS}} \end{bmatrix}_i = \begin{bmatrix} \|\vec{n}_{S_i} \times \vec{e}_{v_i}\| & \|(\vec{n}_{S_i} \times \vec{e}_{v_i}) \times \vec{n}_{S_i}\| & \|\vec{n}_{S_i}\| \end{bmatrix}$$

In case of a rotation of the two considered coordinate frames with respect to each other with time, the appropriate transformation matrix is of course also time dependent. The time derivative of a rotation matrix consists of the original matrix and the angular rate matrix (angular rate of the original frame with respect to the target frame in the original frame).

There are some disadvantages inherent of Euler angle sequences such as at least one singularity which leads to the recommendation of *quaternions* to represent coordinate transformations. So, considering a 3-D rotation matrix Q , the rotation angle can be calculated as $\varphi = \arccos((Tr(Q)-1)/2)$ and the components of the quaternion

$u = u_0 + iu_1 + ju_2 + ku_3$ representing the rotation are $u_0 = 0.5 \cdot \sqrt{q_{11} + q_{22} + q_{33} + 1}$; $u_1 = (q_{23} - q_{32})/(4u_0)$; $u_2 = (q_{31} - q_{13})/(4u_0)$; $u_3 = (q_{12} - q_{21})/(4u_0)$. A vector \underline{v} will be rotated through an angle 2θ about the axis of rotation \underline{q} of the unit quaternion $q = q_0 + \underline{q} = \cos\theta + \underline{u} \sin\theta$ by the operation $q\underline{v}q^*$. Frame rotation is described by $\underline{w} = q^*\underline{v}q$ (cf. [10]).

The effect of *incremental rotations about each of the body-axes* can be described by exploiting that in case of small angles α one may write $\sin \alpha \approx \alpha$ and $\cos \alpha \approx 1$. In case of incremental rotations about the body-axes Eq. (1) becomes

$$W_{\Delta} = \begin{bmatrix} 1 & \Delta yaw & -\Delta pitch \\ -\Delta yaw & 1 & \Delta roll \\ \Delta pitch & -\Delta roll & 1 \end{bmatrix} = I + \Omega \quad (2)$$

which can be used to approximately relate the sensed body rates and Euler angle rates. Again, the use of quaternions would be recommended as it is shown in [10].

3. On Positioning and Attitude Determination Accuracy Measures and Covariance Visualization

Errors in position measurements will directly yield antenna pointing errors in local north, east, or down. Errors in the knowledge of the appropriate Euler angles cause differences between the assumed antenna pointing vector (and the related tie point in the north, east-plane) and the true antenna pointing vector \vec{P}_{AP} .

Positioning errors can be described by ellipses or ellipsoids. Measures of accuracy and precision, like CEP (circular error probable), SEP (spherical error probable), MSPE (mean square positional error), MRSE (mean radial spherical error), 95% confidence level and 3-sigma, can be defined and represent a certain scaling of the ellipse or ellipsoid. If the real distribution of the error sources is not known, it is according to the Central Limit Theorem useful to assume *Gaussian distribution* of the position errors in each dimension.

Considering horizontal (2-D) positioning errors, and assuming the most general case, we have the joint probability density function

$$f_{x,y}(\xi, \zeta) = \frac{1}{2\pi\sigma_x\sigma_y\sqrt{1-\rho_{xy}^2}} \cdot \exp\left\{-\frac{1}{2(1-\rho_{xy}^2)}\left[\frac{(\xi-m_x)^2}{\sigma_x^2} - \frac{2\rho_{xy}(\xi-m_x)(\zeta-m_y)}{\sigma_x\sigma_y} + \frac{(\zeta-m_y)^2}{\sigma_y^2}\right]\right\}$$

with the correlation coefficient $\rho_{xy} = \frac{E\{xy\}}{\sigma_x\sigma_y}$.

The probability that realizations are within a radius R is then (zero mean random variables for convenience)

$$F_\rho(R) = \frac{1}{2\pi\sigma_x\sigma_y\sqrt{1-\rho_{xy}^2}} \cdot \int_0^R \int_0^{2\pi} \exp\left\{-\frac{1}{2(1-\rho_{xy}^2)}\left[\frac{r^2\cos^2\theta}{\sigma_x^2} - \frac{2\rho_{xy}r^2\cos\theta\sin\theta}{\sigma_x\sigma_y} + \frac{r^2\sin^2\theta}{\sigma_y^2}\right]\right\} dr d\theta$$

After some mathematics we have

$$F_\rho(R) = \frac{1}{\sigma_x\sigma_y\sqrt{1-\rho_{xy}^2}} \cdot \int_0^R r \cdot \exp\left\{\frac{-r^2(\sigma_x^2 + \sigma_y^2)}{4(1-\rho_{xy}^2)\sigma_x^2\sigma_y^2}\right\} \cdot I_0\left[\frac{-r^2[(\sigma_x^2 - \sigma_y^2)^2 + 4\rho_{xy}^2\sigma_x^2\sigma_y^2]}{4(1-\rho_{xy}^2)\sigma_x^2\sigma_y^2(\sigma_x^2 - \sigma_y^2)}\right] dr \quad (3)$$

with the modified Bessel function of the first kind of order zero $I_0(z) = \frac{1}{2\pi} \int_0^{2\pi} \exp\{\pm z \cos 2\theta\} d\theta$. Setting (3)

equal to a certain value (e.g., $F_\rho(R) = 0.5$) defines a measure of accuracy (or precision in case of biases). A solution of this equation does not exist in a closed form. More or less efficient ways to evaluate this circular error probability integral can be found in the literature (e.g., [11, 12]). The same holds for the 3-D position error and the calculation of the appropriate spherical error probability integral (e.g., [13, 14]). In case of independent position errors with the same standard deviation the horizontal error is *Rayleigh* distributed, and the 3-D radial error is described by the well-known *Maxwell-Boltzmann* distribution.

The visualization of the hyperellipsoid related to the position error covariance matrix is straightforward, that its scale and orientation will be found by decomposing the matrix into a diagonal matrix Λ containing all eigenvalues (yielding finally the radiuses along the main axes) and an orthogonal transformation matrix Q composed of all normalized eigenvectors (yielding orientation).

In the following it is shown how pointing uncertainty is affected by attitude uncertainties (cf. [15]): Let us consider incremental, stochastic attitude perturbations $\underline{\Delta}_{att} = [\Delta roll \quad \Delta pitch \quad \Delta yaw]^T$ which are assumed to be Gaussian with respect to its mean estimate. Eq. (2) is valid and the attitude covariance matrix is $P_{\Delta\Delta} = E\{\underline{\Delta\Delta}^T\}$. The appropriate ellipsoid has no direct connection to the position space. Now, let us assume a relative position measurement vector given in a known reference system

$$\underline{b} = \bar{\underline{b}} + \Delta\underline{b} = [\bar{b}_x \quad \bar{b}_y \quad \bar{b}_z]^T + [\Delta b_x \quad \Delta b_y \quad \Delta b_z]^T$$

with $\Delta\underline{b}$ = zero mean Gaussian and uncorrelated with attitude. This vector can be mapped into the frame BCS_0 defined by the mean attitude estimate (nominal attitude). Mapping into the perturbed attitude frame yields

$$\underline{b}_{BCS} = W_\Delta \cdot \underline{b}_{BCS_0} = W_\Delta \cdot \bar{\underline{b}}_{BCS_0} + W_\Delta \cdot \Delta\underline{b}_{BCS_0} = \bar{\underline{b}}_{BCS_0} + \Omega \cdot \bar{\underline{b}}_{BCS_0} + \Delta\underline{b}_{BCS_0} + \Omega \cdot \Delta\underline{b}_{BCS_0}$$

with mean $E\{\underline{b}_{BCS}\} = \bar{\underline{b}}_{BCS_0}$ and noise (that defines the covariance)

$$\Delta\underline{b}_{BCS} = \underline{b}_{BCS} - \bar{\underline{b}}_{BCS} = \Omega \cdot \bar{\underline{b}}_{BCS_0} + \Delta\underline{b}_{BCS_0} + \Omega \cdot \Delta\underline{b}_{BCS_0} \approx \Delta\underline{b}_{BCS_0} + \Omega \cdot \bar{\underline{b}}_{BCS_0}$$

Relating this stochastic vector to the mean yields:

$$\Delta \underline{b}_{BCS,r} = \frac{\Delta \underline{b}_{BCS}}{\|\underline{b}_{BCS}\|} \approx \frac{\Delta \underline{b}_{BCS_0}}{\|\underline{b}_{BCS_0}\|} + \frac{\Omega \cdot \underline{b}_{BCS_0}}{\|\underline{b}_{BCS_0}\|} = \Delta \underline{b}_{BCS_0,r} + Z \cdot \underline{\Delta}_{att}$$

with

$$\frac{\Omega \cdot \underline{b}_{BCS_0}}{\|\underline{b}_{BCS_0}\|} = \frac{1}{\|\underline{b}_{BCS_0}\|} \cdot \Omega \cdot \begin{bmatrix} \underline{b}_{BCS_0,x} \\ \underline{b}_{BCS_0,y} \\ \underline{b}_{BCS_0,z} \end{bmatrix} = -\frac{1}{\|\underline{b}_{BCS_0}\|} \cdot \begin{bmatrix} 0 & \underline{b}_{BCS_0,z} & -\underline{b}_{BCS_0,y} \\ -\underline{b}_{BCS_0,z} & 0 & \underline{b}_{BCS_0,x} \\ \underline{b}_{BCS_0,y} & -\underline{b}_{BCS_0,x} & 0 \end{bmatrix} \cdot \begin{bmatrix} \Delta roll \\ \Delta pitch \\ \Delta yaw \end{bmatrix} = Z \cdot \underline{\Delta}_{att}$$

Obviously, we have for the covariance with consideration that $\Delta \underline{b}_{BCS_0}$ and $\underline{\Delta}_{att}$ are uncorrelated:

$$P_{bb} \approx P_{b_0,b_0} + Z \cdot P_{\Delta\Delta} \cdot Z^T \quad (4)$$

with $P_{bb} = E\{\Delta \underline{b}_{BCS,r} \cdot \Delta \underline{b}_{BCS,r}^T\}$, and $P_{b_0,b_0} = E\{\Delta \underline{b}_{BCS_0,r} \cdot \Delta \underline{b}_{BCS_0,r}^T\}$. The resulting covariance P_{bb} consists of an additional term due to attitude uncertainty which may not only cause an enlargement of the ellipsoid dimensions but also a change of orientation of the ellipsoid. That is, with (4) we know how to augment expected uncertainty of a relative position measurement when it is considered for a sensor in a body frame, the attitude of which is subject to attitude determination.

4. Conclusion

In this paper some fundamentals regarding position and attitude determination for future bistatic SAR experiments are presented. The geometric modeling of the antenna pointing as well as the description of pointing uncertainty affected by position and attitude errors is considered.

Behind the scope of this paper is the modeling of aircraft and satellite dynamics, which is an important issue to enable accurate and near real-time position and attitude determination by optimal fusion of all available position and attitude information. This redundant information can be obtained from a network of GPS receivers, gyroscopes, accelerometers and other sensors like magnetometer. Appropriate suboptimal data fusion approaches of the raw data are under research. The aim is to meet the high requirements regarding position and attitude knowledge at comparatively low cost.

Acknowledgement

Part of the work reported herein has been funded by the German Science Foundation (DFG), grant number KN 876/1-1, which is gratefully acknowledged.

REFERENCES

- [1] J. H. G. Ender, O. Loffeld, A. R. Brenner, W. Wiechert, J. Klare, U. Gebhardt, I. Walterscheid, S. Knedlik, M. Weiss, H. Nies, C. Kirchner, M. Kalkuhl, H. Wilden, K. Natroshvili, A. Medrano-Ortiz, A. Amankwah, A. Kolb, and S. Ige, "Bistatic exploration using spaceborne and airborne SAR sensors - A close collaboration between FGAN, ZESS and FOMAAS," *IGARSS'06 (IEEE 2006 Geoscience and Remote Sensing Symposium)*, Denver, Colorado, USA, 2006, in print.
- [2] D. Massonnet, "Capabilities and limitations of the interferometric cartwheel," *IEEE Transactions on Geoscience and Remote Sensing*, vol. 39, pp. 506-520, 2001.
- [3] A. Moreira, G. Krieger, and J. Mittermayer, "Comparison of several bistatic SAR configurations for spaceborne SAR Interferometry," *IGARSS'01 (IEEE 2001 Geoscience and Remote Sensing Symposium)*, Sydney Australia, 2001.
- [4] G. Krieger, H. Fiedler, and A. Moreira, "Bi- and multistatic SAR: potentials and challenges," *EUSAR 2004 (5th European Conference on Synthetic Aperture Radar)*, Ulm, Germany, 2004.
- [5] O. Loffeld, H. Nies, V. Peters, and S. Knedlik, "Models and useful relations for bistatic SAR processing," *IEEE Transactions on Geoscience and Remote Sensing*, vol. 42, pp. 2031-2038, 2004.
- [6] K. Natroshvili, O. Loffeld, H. Nies, A. Medrano-Ortiz, and S. Knedlik, "Focusing of general bistatic SAR configuration data with 2D inverse scaled FFT," *IEEE Transactions on Geoscience and Remote Sensing*, 2006, in print.
- [7] U. Gebhardt, O. Loffeld, H. Nies, S. Knedlik, and J. Ender, "Bistatic airborne/spaceborne hybrid experiment: basic considerations," *Proceedings of SPIE: Sensors, Systems, and Next-Generation Satellites IX*, vol. 5978, pp. 479-488, 2005.
- [8] S. Knedlik, O. Loffeld, and H. Nies, "Sensitivity of DEMs generated from interferometric cartwheel configurations," *IGARSS'03 (IEEE 2003 Geoscience and Remote Sensing Symposium)*, Toulouse, France, 2003.
- [9] S. Knedlik, O. Loffeld, and U. Gebhardt, "On position and attitude determination requirements for future bistatic SAR experiments," *IGARSS'06 (IEEE 2006 Geoscience and Remote Sensing Symposium)*, Denver, USA, 2006, in print.
- [10] J. B. Kuipers, *Quaternions and Rotation Sequences*. Princeton: Princeton University Press, 2002.
- [11] I. A. Gura and R. H. Gersten, "Interpretation of n-dimensional covariance matrices," *AIAA Journal*, vol. 9, pp. 740-742, 1971.
- [12] D. A. Shnidman, "Efficient computation of the circular error probability (CEP) integral," *IEEE Transactions on Automatic Control*, vol. 40, pp. 1472-1474, 1995.
- [13] S. Del Marco, "A series representation of the spherical error probability integral," *IEEE Transactions on Aerospace and Electronic Systems*, vol. 29, pp. 1349-1356, 1993.
- [14] A. B. Chatfield, *Fundamentals of high accuracy inertial navigation (Progress in Astronautics and Aeronautics)*, vol. 174. Cambridge, Massachusetts: AIAA, 1997.
- [15] S. Tanygin and J. Woodburn, "Attitude Covariance Visualization," *AIAA/AAS Astrodynamics Specialist Conference and Exhibit*, Monterey, California: AIAA, 2002.

Transmission Characteristics of UART-CSMA/CD Control Network with One-chip Microcontroller and RS-485 Driver IC

C. Ninagawa, K. Yokohama, F. Aoi, H. Otake

Mitsubishi Heavy Industries, Ltd.

Y. Miyazaki

Aichi University of Technology

Abstract — In a control network for a building air-conditioning system, signal waveforms in the transmission line without terminators were calculated and compared with experiments. The bit rate was decided by an analysis for distortion of the signal waveform due to line end reflections. At the bit rate decided by the analysis, performance of a special type of CSMA/CD (Carrier Sense Multiple Access with Collision Detection) communication firmware has been evaluated.

1. Introduction

Cost is one of the most important factors in control networks for building facilities such as air-conditioning or lighting systems. A typical control network consists of hundreds of controllers, and the total length of the line is approximately a thousand meters. Therefore, reducing parts of each controller and the network line has been required.

We proposed a media access control method of CSMA/CD (Carrier Sense Multiple Access with Collision Detection) using only UART (Universal Asynchronous Receiver Transmitter) in a microcontroller[1]. We study a possibility of omitting network line terminators. As well-known, depending on relationship between line length and signal bit rate, the transmission has to be treated as a distributed constant circuit. However, there have been not so many researches on calculation for signal waveforms of a control network line without terminators [2]. In this research, we show a simple calculation method for predicting affection of signal reflections in order to decide a transmission bit rate for a terminator-less network.

At the bite rate restricted by impedance mismatching, communication performance of our UART-CAMA/CD method has been evaluated. We have confirmed our UART-CSMA/CD control network's practical performance.

2. UART-CSMA/CD Control Network

(2.1) Control Networks for Building Facilities

Fig. 1 shows concept of a control network for air-conditioning facility. In a typical building air-conditioning system, there are tens or hundreds of controllers distributed throughout the building. These controllers exchange communication packets of several bytes. The total line length often reaches as long as approximately 1000 m. To reduce the cost of control networks, both the costs of each controller and network installation should be decreased.

Firstly for each controller, circuit parts should be as few as possible. Both application and communication firmware should be implemented in the same microcontroller chip. Since most modern microcontrollers have a built-in UART, development of original communication firmware using only the built-in UART greatly reduces parts of each controller. For the physical layer, the RS-485 driver IC has been chosen. The RS-485 standard is a differential voltage signal data-transmission scheme that offers robust solutions for transmitting data over long distances and noisy environments.

Secondly, cost of the network installation is important. As regard to network cabling, mandatory conditions are low cost of generic cables and the maximum length of one kilometer without repeaters. Since mechanical strength is required in rough areas, heavy duty polyvinyl chloride cables should be used. Moreover, the network impedance termination is neglected because of installation cost.

(2.2) UART-CSMA/CD method

From the above-mentioned requirements, we have developed an extremely low-cost CSMA/CD network, which greatly reduces communication circuit parts. By adopting the connection shown in Fig. 2, the ReceiveShiftRegister of the UART reads the bit string sent by its SendShiftRegister simultaneously. Then, when it has received the whole one-byte data, the internal logic of the UART generates an

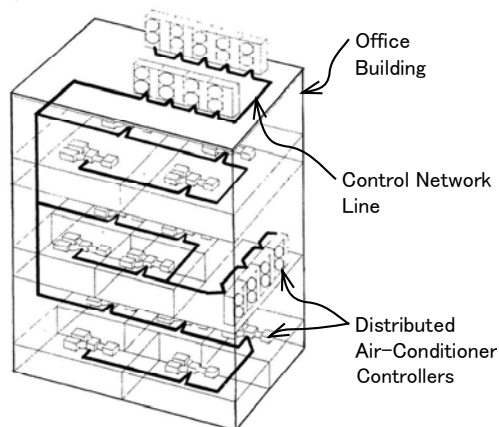


Fig.1 Air-conditioner control network

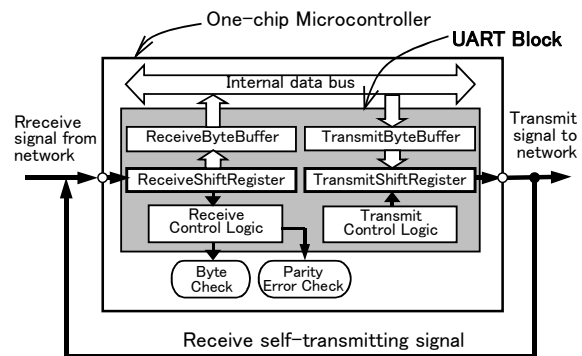


Fig.2 UART-CSMA/CD method

interrupt signal. If a collision has occurred during sending one-byte data, the original byte is destroyed and consequently the received bit string becomes different from the original one. At this point, our CSMA/CD firmware uses two mechanisms for judging if the byte data has been destroyed. One is using a ParityErrorCheck mechanism built in the UART logic, and the other is ByteCheck with the original byte kept in our CSMA/CD software.

Some conventional methods judge a packet collision by impedance change of the line such as Ethernet 10BASE5. In these methods, a sending controller is not required to read every bit of the self-sending signal. However, since our UART method judges a collision only by firmware, every bit of the sending data must be read at the sending point as well as the receiving points. Therefore, in our UART-CSMA/CD method, the signal waveform of every bit of data is very important.

(2.3) Transmission line without terminators

Since this network has to be installed in the most inexpensive way, any network wiring devices such as line terminators are neglected. It is well-known that impedance mismatching at the terminal points adversely affects on the signal waveform in the case of a significantly long line. As the length of a control network for building facility is very long, influence of the signal reflection at the line terminal should be investigated in order to make an engineering decision of omitting terminators and still maintaining correct digital data transmission.

Since input and output impedance of an RS-485 driver IC is typically about 12 k Ω and 20 Ω , respectively. As the characteristic impedance of a typical cable is about 100 Ω , impedance mismatch at the load and source points is significantly large. In other words, the reflection coefficients at the source points are large as well as the load point.

It is well-known that a "kink" shape is seen on the rising part of the signal pulse at the source point in the case of severe impedance mismatching at the far end of the line. This kink shape is made by the leading edge of the returning wave reflected at the far end. The width of the kink shape corresponds to the round trip time. We denote the width of this kink shape as "kink width" W_k . It is important to retain this kink area out of the receive sampling point of the pulse. Otherwise, the receiver might read the signal level within the kink part of the pulse, and judges the bit as wrong digital level.

3. Signal Transmission Waveforms

(3.1) Analysis Model

We have studied reflections of signal pulse waveforms by a simple transient analysis of a finite length distributed constant circuit. The fundamental equations of signal voltage $v(x, t)$ and current $i(x, t)$ for a distributed constant circuit are

$$\begin{cases} -\frac{\partial v(x,t)}{\partial x} = L_0 \frac{\partial i(x,t)}{\partial t} + R_0 i(x,t) \\ -\frac{\partial i(x,t)}{\partial x} = C_0 \frac{\partial v(x,t)}{\partial t} + G_0 v(x,t) \end{cases} \quad (1)$$

where L_0, R_0, C_0 , and G_0 , are first order circuit constants of the transmission line. As our network cable is very thick such as 2 mm^2 wire, the line is treated as lossless for simplicity. Assuming $R_0 = G_0 = 0$, the following wave equations are obtained:

$$\begin{cases} \frac{\partial^2 v(x,t)}{\partial x^2} = L_0 C_0 \frac{\partial^2 v(x,t)}{\partial t^2} \\ \frac{\partial^2 i(x,t)}{\partial x^2} = L_0 C_0 \frac{\partial^2 i(x,t)}{\partial t^2} \end{cases} \quad (2)$$

Taking Laplace transformation of the voltage part of the wave equations, the following is obtained.

$$\frac{d^2 V(x,s)}{dx^2} = \gamma^2 V(x,s) \quad (3)$$

A general solution of the Laplace transformed wave equation is as follows,

$$V(x, s) = A_1(s) e^{-\gamma x} + A_2(s) e^{\gamma x} \quad (4)$$

where $\gamma = s(L_0 C_0)^{1/2}$ is a propagation constant. We denote propagation velocity as $w = (L_0 C_0)^{-1/2}$. By giving boundary conditions, initial conditions, and a source voltage function as a step function of constant voltage $E(s) = (1/s)E_l$, the Laplace transformed function is given by

$$V(x, s) = [E_l Z_l / (Z_l + Z_0)] \{ (1/s)e^{-\gamma x} + I_2 (1/s)e^{-\gamma(2l-x)} + I_1 I_2 (1/s)e^{-\gamma(2l+x)} + I_1 I_2^2 (1/s)e^{-\gamma(4l-x)} + I_1^2 I_2^2 (1/s)e^{-\gamma(4l+x)} + \dots \} \quad (5)$$

By taking inverse Laplace transformation using a unit step function $u[t]$, we get a solution of $v(x, t)$ as

$$v(x, t) = [E_l Z_l / (Z_l + Z_0)] \{ u[t - x/w] + I_2 u[t - (2T_{OW} - x/w)] + I_1 I_2 u[t - (2T_{OW} + x/w)] + I_1 I_2^2 u[t - (4T_{OW} - x/w)] + I_1^2 I_2^2 u[t - (4T_{OW} + x/w)] + \dots \} \quad (6)$$

where $Z_0 = (L_0/C_0)^{1/2}$ is the characteristic impedance of the line, Z_l is the source impedance, Z_2 is the load impedance, l is the line length, $T_{OW} = l/w = l(L_0 C_0)^{1/2}$ is the one way trip time, $I_1 = (Z_l - Z_0) / (Z_l + Z_0)$ is the source reflective coefficient, and $I_2 = (Z_2 - Z_0) / (Z_2 + Z_0)$ is the load reflective coefficient. Both Z_l and Z_2 are assumed to be pure resistance.

(3.2) Numerical Calculations and Observations

We have compared step response calculations by the above analysis and signal waveforms observed by an oscilloscope. The bit rate has been chosen, as a trial, $R_{BIT} = 19.6 \text{ kbps}$ ($W_{BIT} = 52 \mu \text{ s}$). The line length has been fixed as $l = 1000 \text{ m}$. The voltage source $E_l = 3.0 \text{ V}$ and the source impedance $Z_l = 28 \Omega$ were deduced from the RS-485 driver IC data book. The type of the cable was a polyvinyl chloride (PVC) twisted cable with 2 mm^2 (AWG14) wires. The theoretical values of cable parameters have been calculated by the following analytical expressions for a pair of two wires placed close together[3],

$$C_0 = \pi \epsilon / \ln [d_w + (d_w^2 - 4r_w^2)^{1/2}] \quad (7)$$

$$L_0 = (\mu / \pi) \ln [d_w + (d_w^2 - 4r_w^2)^{1/2}] \quad (8)$$

$$Z_0 = 120 (\mu_r / \epsilon_r)^{1/2} \ln [d_w + (d_w^2 - 4r_w^2)^{1/2}] \quad (9)$$

where d_w and r_w are cable dimensions shown in Fig. 3, then, $\epsilon, \epsilon_r, \mu$, and μ_r are dielectric constants and permeabilities, respectively. Using typical values of $\epsilon_r = 4.0$ and $\mu_r = 1.0$ for PVC and dimensions shown in Fig. 3, we have obtained the theoretical values of C_0, L_0 , and Z_0 as shown in Table 2. The cable parameters have been also measured as shown in Table 2.

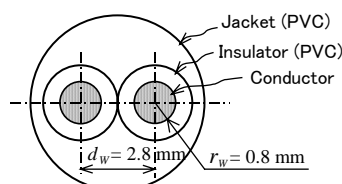


Fig. 3 Cross section of the cable

Table. 2 Cable parameters

Parameter	Calculated	Measured
C_0	0.096 [$\mu\text{F}/\text{km}$]	0.12 [$\mu\text{F}/\text{km}$]
L_0	0.46 [mH/km]	0.59 [mH/km]
$Z_0 = (L_0/C_0)^{1/2}$	69 [Ω]	70 [Ω]

Fig. 4 shows calculations and observations of the signal waveforms for the case without terminators. We set conditions that only two controllers were connected directly by the above mentioned type of cable. At the source point, $x = 0$ m, a typical kink shape is seen on the rising part of every bit pulse. We have obtained the calculated kink width $W_{KC} = 13 \mu\text{s}$ at the source point as seen in Fig. 4(a). The kink width W_{KC} corresponds to the round trip time of the signal propagation, i.e., $W_{KC} = 2T_{OW} = 2l/w = 2l(L_0 C_0)^{1/2}$.

Severe affection of reflections are predicted at the half-way point of $x = 500$ m and the load point of $x = 1000$ m in the Fig 4(a). The kink width at the source point, i.e. at a sending controller, is the largest as compared with other points. In the case of actual waveform observation, the kink width at the source point was observed as $W_{KO} = 13 \mu\text{s}$, which is the same result of the above mentioned calculation. The percentage width of the kink $\xi = W_{KC} / W_{BIT} = W_{KO} / W_{BIT} = 13 \mu\text{s} / 52 \mu\text{s} = 25 \%$. The reflected signal level ratio $L_R = V_1 / V_2$ at the source point was 1.7 by the calculation, and 2.0 by the observation in the case without terminator as shown in Fig. 4.

Fig. 5 is for the case with terminators. The impedance of the load point terminator Z_2 was chosen to be pure resistance of 120Ω . This terminator impedance is the manufacturer's recommendation value. In this case, the distortions of waveform have been greatly reduced at all of the source, midway, and load points. The kink width is not changed because the propagation velocity $w = (L_0 C_0)^{-1/2}$ is not affected by the terminator impedance. The signal waveforms by the calculations are similar to those observed in the actual transmission line. We have confirmed our simple calculation of waveform is useful to predict the kink width.

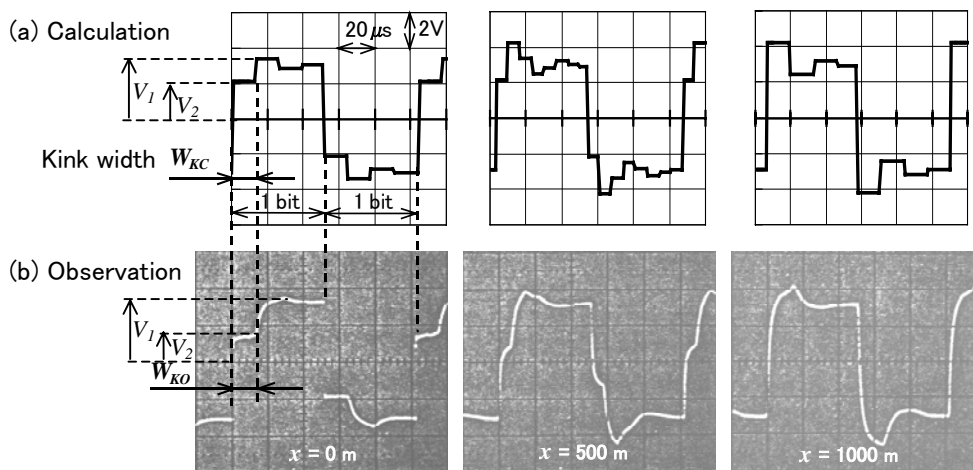


Fig.4 Transmission waveforms : without terminator

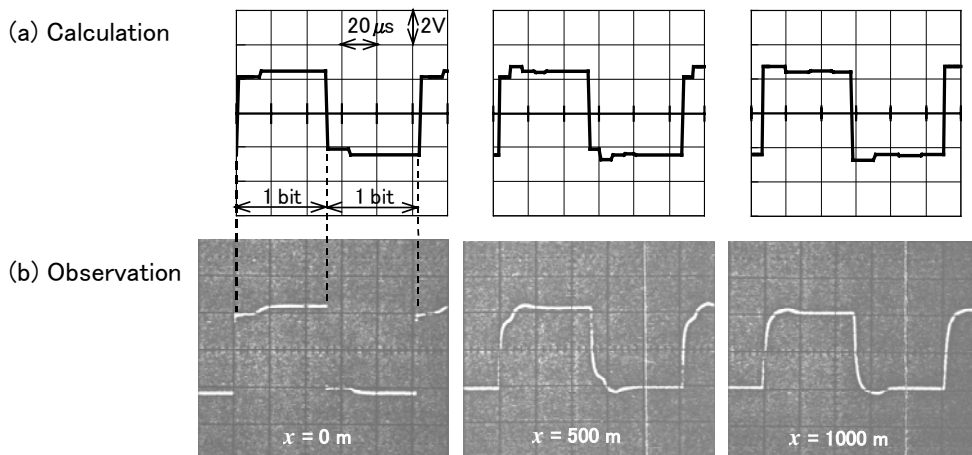


Fig.5 Transmission waveforms : 120 Ω terminator

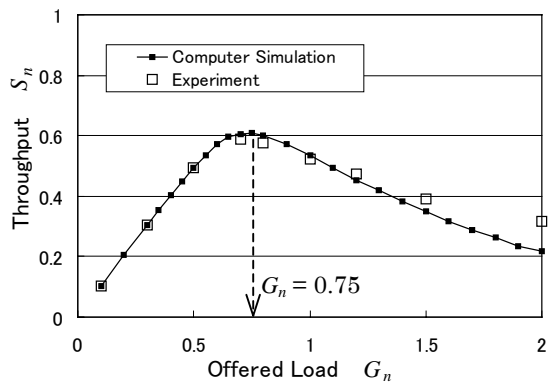


Fig. 6 Performance (Throughput)

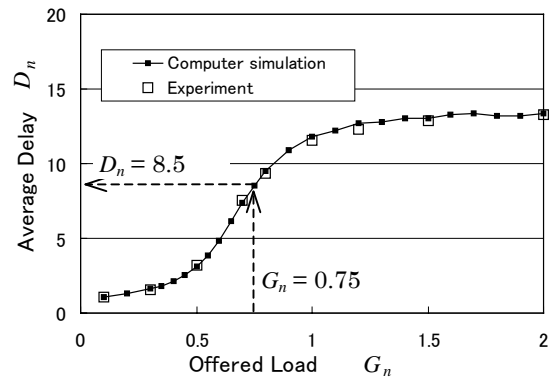


Fig. 7 Performance (Average delay)

4. Transmission Characteristics

In cases without terminators, both the calculated and measured percentage width of the kink was $\xi = 25\%$ at 19.2 kbps. Branches, stubs, or loop connections of the line may widen the percentage in practical use. Therefore, from an engineering judgement, we have chosen the next lower available bit rate $R_{BIT} = 9.6$ Kbps. In this case, the expected percentage kink width becomes $\xi = W_{KC} / W_{BIT} = 13 \mu s / 104 \mu s = 13\%$, which supposed to have a enough margin.

Since the bit rate has been set as a slow speed of 9.6 kbps from the investigation in the above sections, evaluation of communication performance has become necessary in order to confirm our UART-CSMA/CD system has enough performance. The number of controllers and the packet length have been chosen to be $M = 48$, $T_p = 16$ bytes (that is 0.0183 s at 9.6 kbps), respectively.

Communication performance has been evaluated by computer simulations and experiments in terms of throughput S_n and average delay D_n . Here, S_n means the expected number of successful transmissions per the packet length time, and D_n means the expected delay relative to the packet length time. We assumed offered communication load is aggregation of packets generated from all controllers as Poisson process[4].

The maximum throughput was $S_n = 0.6$, when the offered load is $G_n = 0.75$ (i.e. the sum of the offered packets occupies 75% of the time axis) as shown in Fig. 6. The actual number of successful packets per second is 33 packets/s at 9.6 kbps and 16 byte-packet. The average delay was $D_n = 8.5$ at the load point of $G_n = 0.75$ as shown in Fig. 7. At this load point, the actual average transmission delay is 0.15 s. This means our design allows 33 controllers to send a packet with the average delay of 0.15 s during every second. This sending rate is enough for building facility controls, and relative utilization of 60% (i.e. $S_n = 0.6$) of transmission line is quite satisfactory as a random access protocol firmware.

5. Conclusion

In this paper, we have shown our simple calculation of signal waveform is effective to predict distortions due to reflections in the case of impedance mismatching at the line end. By deciding the bite rate under the condition of omitting line terminators, communication performance of our proposed UART-CSMA/CD firmware was evaluated, and confirmed to be satisfactory for control networks for building facilities.

References

- [1] Ninagawa,C., Yokohama,K., Aoi,F., and Miyazaki,Y., "Performance analysis on air-conditioner control CSMA/CD protocol by embedded microcontroller UART collision detection," *IEEJ Trans. IA*, Vol. 126, No.5, pp.665-672, 2006 (in Japanese).
- [2] Canright,R., "Simulating and controlling the effects of transmission line impedance mismatches," *IEEE 23rd Conf. on Design Automation*, pp.778-785, 1986.
- [3] Matick, M., "Transmission lines for digital and communication networks," An IEEE PRESS Classic Reissue, Picataway, NJ, 1995.
- [4] Li,S., and Miyazaki,Y., "A performance analysis of buffered DQDB network with request arrival process depending on its counter value and its location on the bus," *IEICE Trans. Commun.*, Vol.E81-B, No.3, pp.493-502, 1998.

Code Recognition Characteristics in Optical Label Matching with Integrated-Optic Collinear Acoustooptic Devices

Nobuo Goto¹, Yasumitsu Miyazaki²

¹ Toyohashi University of Technology, ² Aichi University of Technology

Abstract Optical processing with efficient coding is expected in photonic label routing network. We consider optical codes encoded in the time and spectral domains. In this study, collinear acoustooptic (AO) switches are investigated as a constituent elements of a wavelength selective correlator for optical BPSK codes. Crosstalk in code recognition is discussed with numerical analysis considering AO filtering characteristics for optical processing with collinear AO devices.

1 Introduction

Optical label switching technology has been considered to be a potential candidate for near-future networks. [1, 2] The label can be represented as optical signals in various formats such as in a pulse train in the time domain, in a single pulse with multiple wavelengths, or in combined signals in the time and spectral domains. To interpret the codes representing the label information, various optical methods with passive devices have been investigated, where correlation is performed between the incident optical codes and codes stored in the optical system. [2, 3]

The authors have studied recognition of optical codes encoded in the time and spectral domains with acoustooptic (AO) processors. [3, 4] We have proved that the orthogonal Hadamard codes in binary phase shift keying (BPSK) or on-off keying (OOK) formats can be recognized by using code matching between the optical incident code and stored reference codes represented by surface acoustic waves (SAWs). For optical codes encoded in the time domain at a single wavelength, a combination of optical delay lines and parallel AO switches can be used for code matching. [4] To increase the number of distinguishable codes, effective use of optical interference is indispensable. Therefore, optical codes in BPSK format are considered in this report. The code matching characteristics are theoretically discussed.

2 Code Matching with Parallel Collinear AO Switches

A proposed code matching system consists of collinear AO switches and electric gates. As for collinear AO switches, two kinds of mode conversion have been employed, that is, mode conversion between different order modes in the same polarization or between different polarizations. The authors have investigated the former type of devices. [5, 6] The device consists of an asymmetric directional coupler. Mode coupling between the fundamental two modes is induced by collinear AO interaction.

A proposed device structure for code matching is illustrated in Fig. 1(a). The device consists of N_t parallel AO switches, delay lines, dividers and combiners. Optical switching through collinear AO

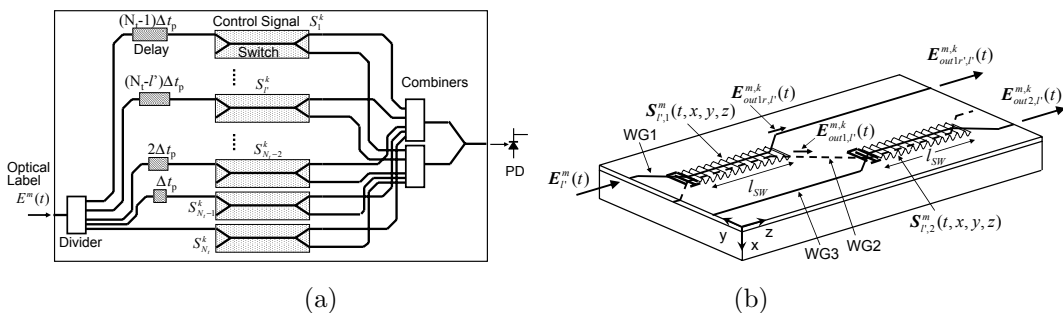
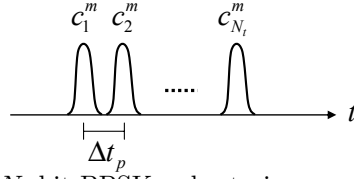


Figure 1: Proposed device structure for code matching in the time domain. (a) A schematic structure of the whole device and (b) double-stage switch for suppressing optical frequency shift.

Figure 2: N_t -bit BPSK pulse train as a coded label.

interaction is accompanied by frequency shift of an amount equal to the surface acoustic wave (SAW) frequency. The frequency shift is not desirable for optical processing using interference in this device. Therefore, we consider a double-stage switching as shown in Fig. 1(b). The frequency shift is compensated since the frequency shift through the second switching has the opposite sign with the same amount as the first switching. In the AO switching, the SAW which satisfies a switching condition can switch an optical signal from one output port to the other. The SAWs in the parallel AO switches can represent a code $\tilde{c}^k = (\tilde{c}_1^k, \tilde{c}_2^k, \dots, \tilde{c}_{N_t}^k)$, where $\tilde{c}_i^k = 0$ or 1 corresponding to "0" or "1", respectively.

We consider a SAW strain at the two l' -th AO switches as given by

$$\mathbf{S}_{l',1}^k(t, x, y, z) = \mathbf{S}_{l',2}^k(t, x, y, z) = \tilde{c}_l^k \mathbf{s}_0(x, y) \cos(\Omega_0 t - K_0 z) \quad (1)$$

where $\mathbf{s}_0(x, y)$ is the amplitude distribution of the strain related to complete switching, K_0 is the propagation constant of the SAW at angular frequency Ω_0 . The origin of z is assumed to be at the entrance of the interaction region of each AO switches. We consider optical codes $\mathbf{c}^m = (c_1^m, c_2^m, \dots, c_{N_t}^m)$ consisting of a N_t -bit BPSK pulse train as shown in Fig. 2. The incident electric field of the encoded optical pulse train in the input waveguide of the device shown in Fig. 1(a) is written as

$$\mathbf{E}^m(t, x, y, z) = \mathbf{E}_0(x, y) \sum_{l=1}^{N_t} c_l^m g_{in,0}(t - (l-1)\Delta t_p) \exp\{-j\beta z + j\omega_0[t - (l-1)\Delta t_p]\} \quad (2)$$

where $g_{in,0}(t)$ is the envelope of each pulse, Δt_p is the pulse period, ω_0 is the optical angular frequency, β is the propagation constant of the fundamental mode in the input waveguide. Since we consider BPSK codes, each bit of the codes is $c_i^m = e^{j0} (= 1)$ or $e^{j\pi} (= -1)$. We denote elements of these codes as "1" or "0" corresponding to e^{j0} or $e^{j\pi}$, respectively. In the following description, we omit the spatial distribution of optical signals for convenience. The switched output due to the first AO interaction is given by

$$\begin{aligned} \mathbf{E}_{out1,l'}^{m,k}(t) = & \frac{\mathbf{E}_0}{N_t} \sum_{l=1}^{N_t} \tilde{c}_l^k c_l^m g_{out,0}(t - (l-l')\Delta t_p - t_1 - l_{SW}/v) \\ & \times \exp\{j\{(\omega_0 - \Omega_0)[t - (l-l')\Delta t_p - t_1 - l_{SW}/v] - (\beta - K_0)(l_{SW} - (N_t - l')\Delta t_p v)\}\} \end{aligned} \quad (3)$$

where $t_1 = (N_t - 1)\Delta t_p$, $g_{out,0}(t)$ is the envelope of the switched pulse, l_{SW} is AO interaction length, and v is the velocity of optical wave in the waveguides. The output from the unswitched port is written as

$$\begin{aligned} \mathbf{E}_{out1r,l'}^{m,k}(t) = & \frac{\mathbf{E}_0}{N_t} \sum_{l=1}^{N_t} [\tilde{c}_l^k c_l^m g_{in,0}(t - (l-l')\Delta t_p - t_1 - l_{SW}/v) \\ & + \tilde{c}_l^k c_l^m g_{out,0}^{res}(t - (l-l')\Delta t_p - t_1 - l_{SW}/v)] \\ & \times \exp\{j\{\omega_0[t - (l-l')\Delta t_p - t_1 - l_{SW}/v] - \beta(l_{SW} - (N_t - l')\Delta t_p v)\}\} \end{aligned} \quad (4)$$

where the envelopes of the switched and unswitched output pulses, $g_{out,0}(t)$ and $g_{out,0}^{res}(t)$, respectively, are defined by

$$\hat{g}_{out,0}(\omega) = \hat{g}_{in,0}(\omega) \hat{f}_{AO1}(\omega), \quad \hat{g}_{out,0}^{res}(\omega) = \hat{g}_{in,0}(\omega) \hat{f}_{AO1}^{res}(\omega) \quad (5)$$

where $\hat{g}_{in,0}(\omega)$, $\hat{g}_{out,0}(\omega)$ and $\hat{g}_{out,0}^{res}(\omega)$ mean the Fourier transform of $g_{in,0}(t)$, $g_{out,0}(t)$ and $g_{out,0}^{res}(t)$, respectively; $\hat{f}_{AO1}(\omega)$ and $\hat{f}_{AO1}^{res}(\omega)$ are AO switching characteristics for switched and unswitched output port, respectively.

The switched output $\mathbf{E}_{out1,l'}^{m,k}(t)$ is switched again with the second AO switch, resulting in the switched output $\mathbf{E}_{out2,l'}^{m,k}(t)$ as given by

$$\begin{aligned} \mathbf{E}_{out2,l'}^{m,k}(t) &= \frac{\mathbf{E}_0}{N_t} \sum_{l=1}^{N_t} \tilde{c}_l^k \tilde{c}_l^m g_{out2,0}(t - (l-l')\Delta t_p - t_2) \\ &\times \exp\{j\{\omega_0[t - (l-l')\Delta t_p - t_2] - \beta(2l_{SW} - (N_t - l')\Delta t_p v)\}\} \end{aligned} \quad (6)$$

where $t_2 = t_1 + 2l_{SW}/v$, and Fourier transform of $g_{out2,0}(t)$ is defined as

$$\hat{g}_{out2,0}(\omega) = \hat{g}_{out,0}(\omega) \hat{f}_{AO2}(\omega) \quad (7)$$

where $\hat{f}_{AO2}(\omega)$ is the AO switching characteristics of the second AO switch, where the mode conversion is reversed compared to the first AO switching. The unswitched output from the first AO switch propagates along the waveguide of the length l_{SW} , and the output is written as

$$\begin{aligned} \mathbf{E}_{out1r',l'}^{m,k}(t) &= \frac{\mathbf{E}_0}{N_t} \sum_{l=1}^{N_t} [\tilde{c}_l^k \tilde{c}_l^m g_{in,0}(t - (l-l')\Delta t_p - t_2) + \tilde{c}_l^k \tilde{c}_l^m g_{out,0}^{res}(t - (l-l')\Delta t_p - t_2)] \\ &\times \exp\{j\{\omega_0[t - (l-l')\Delta t_p - t_2] - \beta(2l_{SW} - (N_t - l')\Delta t_p v)\}\} \end{aligned} \quad (8)$$

The switched and unswitched outputs are added with optical combiners separately as

$$\mathbf{E}_{out2,total}^{m,k}(t) = \sum_{l'=1}^{N_t} \mathbf{E}_{out2,l'}^{m,k}(t), \quad \mathbf{E}_{out1r',total}^{m,k}(t) = \sum_{l'=1}^{N_t} \mathbf{E}_{out1r',l'}^{m,k}(t) \quad (9)$$

We assume that the pulse period Δt_p is chosen so that the following conditions are satisfied,

$$\omega_0(l-l')\Delta t_p = 2n\pi, \quad \beta(N_t - l')\Delta t_p v = 2n'\pi \quad (n, n' : \text{integer}) \quad (10)$$

We also assume the AO switching to have ideal switching characteristics, that is

$$g_{out2,0}(t) = -g_{in,0}(t), \quad g_{out,0}^{res}(t) = 0 \quad (11)$$

These two outputs are optically added with the combiner and the output is given by

$$\begin{aligned} \mathbf{E}_{add}^{m,k}(t) &= \mathbf{E}_{out2,total}^{m,k}(t) + \mathbf{E}_{out1r',total}^{m,k}(t) \\ &= -\frac{\mathbf{E}_0}{N_t} \sum_{l'=1}^{N_t} \sum_{l=1}^{N_t} (\tilde{c}_l^k \tilde{c}_l^m - \tilde{c}_l^k \tilde{c}_l^m) g_{in,0}(t - (l-l')\Delta t_p - t_2) \exp\{j[\omega_0(t - t_2) - 2\beta l_{SW}]\} \end{aligned} \quad (12)$$

This optical output is converted to electric signal with a photodiode (PD), resulting in the current

$$I^{m,k}(t) = I_0 \left| \mathbf{E}_{add}^{m,k}(t) \right|^2 = \frac{I_0}{N_t^2} \left| \sum_{l'=1}^{N_t} \sum_{l=1}^{N_t} (\tilde{c}_l^k \tilde{c}_l^m - \tilde{c}_l^k \tilde{c}_l^m) g_{in,0}(t - (l-l')\Delta t_p - t_2) \right|^2 \quad (13)$$

The correlation signal appears at the time $t = t_2$. Therefore, the current of eq. (13) is processed with a gate to select the pulse at $t = t_2$. The gated output current is written as

$$I_{gated}^{m,k}(t) = \frac{I_0}{N_t^2} \left| \sum_{l'=1}^{N_t} \sum_{l=1}^{N_t} (\tilde{c}_l^k \tilde{c}_l^m - \tilde{c}_l^k \tilde{c}_l^m) \right|^2 g_{in,0}^2(t) \quad (14)$$

In the case of $N_t = 4$, the largest value equal to 16 appears at $t = t_2$ for the input \mathbf{c}^1 and \mathbf{c}^{16} . These two codes cannot be distinguished. It is found that a half of the binary codes can be distinguished. In general, the number of the codes that can be distinguished with N_t parallel AO switches is $N_{code} = 2^{N_t-1}$. The output power $P_{gated}^{m,k}$ for the N_t -bit codes is given by

$$P_{gated}^{m,k} = \begin{cases} N_t^2 & (m = k) \\ (N_t - 2)^2 & (\text{Maximum for } m \neq k) \end{cases} \quad (15)$$

The output intensity is plotted in Fig. 3.

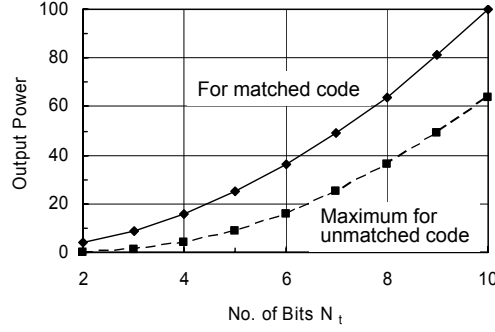


Figure 3: Output intensities and the crosstalk of the unmatched output.

3 Evaluation of Code Matching Considering AO Switching Characteristics

In the previous section, ideal switching characteristics were assumed in the AO switches. When we consider high-bit-rate pulses, the wavelength dependence of the AO switches cannot be ignored. Therefore, we evaluate code matching characteristics by taking the frequency-dependence into consideration.

We consider a bandwidth-limited optical pulse train. The envelope of normalized encoded pulses is

$$g_{in,c}^m(t) = \sum_{l=1}^{N_t} c_l^m g_{in,0}(t - (l-1)\Delta t_p), \quad (16)$$

where the single pulse shape $g_{in,0}(t)$ is generated from a rectangular pulse with a pulse width τ by limiting the bandwidth B . Here, we assume $\Delta t_p = 11.7$ ps, $\tau = \Delta t_p/2$ and $B = 160$ GHz.

Next, we consider the filtering characteristics in the AO switching. The half-width of the main lobe in the filtering characteristics is given by $\Delta K l_{SW} = \sqrt{3}\pi$ [5, 6], where ΔK is a shift of the propagation constant from the phase matching condition given by $K_0 = \Omega_0/v = \omega_0 \Delta N/c$, where c is the optical velocity in free space, ΔN is the difference of the effective indices of the optical two modes concerned in the AO mode conversion. As a numerical example, we assume $\Delta N = 0.08$, which corresponds to SAW of frequency $\Omega_0/(2\pi) = 200$ MHz, velocity $v_a = 3770$ m/s and optical wavelength $\lambda = 1.5$ μm . The half bandwidth of the main lobe B_{AO} is found to be $B_{AO} = \sqrt{3}c/2\Delta N l_{SW}$. When the AO interaction length l_{SW} is 5 mm, B_{AO} is found to be 650 GHz.

The outputs from a single-stage AO switch for the pulse train are given by

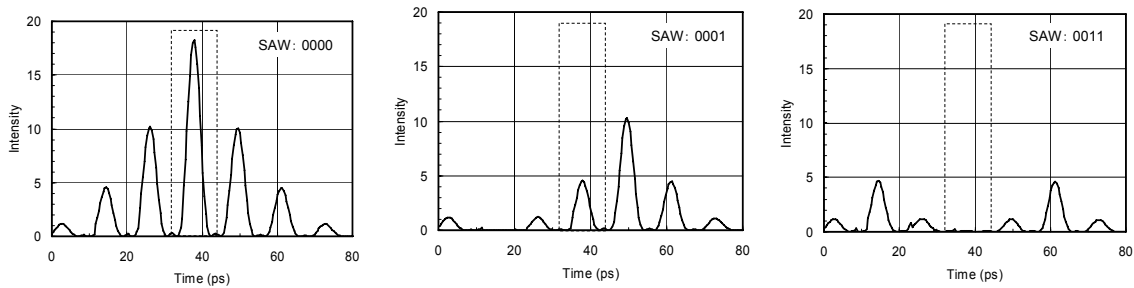
$$g_{out1,c}^m(t) = \mathcal{F}^{-1}[\hat{g}_{out1,c}^m(\omega)] = \mathcal{F}^{-1}[\hat{g}_{in,c}^m(\omega)\hat{f}_{AO1}(\omega)] \quad (17)$$

$$g_{out1,c}^{res\ m}(t) = \mathcal{F}^{-1}[\hat{g}_{out1,c}^{res\ m}(\omega)] = \mathcal{F}^{-1}[\hat{g}_{in,c}^m(\omega)\hat{f}_{AO1}^{res}(\omega)] \quad (18)$$

When the output $g_{out1,c}^m(t)$ from the first AO switch is switched with the second AO switch, the switched output $g_{out2,c}^m(t)$ is written as

$$g_{out2,c}^m(t) = \mathcal{F}^{-1}[\hat{g}_{out1,c}^m(\omega)\hat{f}_{AO2}(\omega)] \quad \text{and} \quad g_{out2,c}^{res\ m}(t) = \mathcal{F}^{-1}[\hat{g}_{out1,c}^m(\omega)\hat{f}_{AO2}^{res}(\omega)] \quad (19)$$

Next, we calculate the optical addition of the parallel AO switches. An optical code $\mathbf{c}^{m=1} = "0000"$ is assumed for the incident pulse train. Since the double-stage switched intensity is reduced by about 5 %, the unswitched output $g_{out1,c}^{res\ m}(t)$ is reduced by multiplying a coefficient 0.95. Some examples of the output intensity corresponding to $|E_{add}^{m,k}(t)|^2$ are shown in Fig. 4, where the codes represented by SAW are $\mathbf{c}^{k=1} = "0000"$, $\mathbf{c}^{k=2} = "0001"$ and $\mathbf{c}^{k=4} = "0011"$ are considered. The gated output power, that is, the optical signal enclosed with the dashed rectangle in Fig. 4, are summarized in Fig. 5, where the power is normalized so that the power for $\mathbf{c}^{k=1} = "0000"$ is 16.



(a) For SAW of code "0000" (b) For SAW of code "0001" (c) For SAW of code "0011"

Figure 4: Output pulse trains from code matching device in the case of optical incident code of "0000"

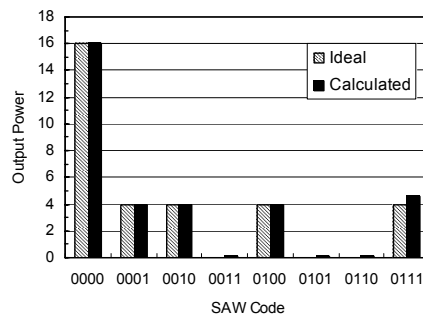


Figure 5: Matched output intensity and maximum of unmatched output intensity for 4-bit codes.

4 Conclusion

We investigated code matching with collinear AO switching elements. The number of N_t -bit BPSK codes distinguishable with parallel AO elements is found to be 2^{N_t-1} . A maximum crosstalk for unmatched code is $20 \log(1 - 2/N_t)$. The code matching is numerically analyzed by considering the AO switching characteristics. The system can be developed to code matching for codes encoded in the spectral and time domains. When the number of codes in the time domain is reduced to $2^{N_t-1} - 1$, WDM code can be processed with parallel N_λ processors and electrical post-processing. We will further investigate the system architecture of the router with control protocol for routing.

References

- [1] D.J. Blumenthal, B. E. Olsson, G. Rossi, T. E. Dimmick, L. Rau, M. Masanovic, O. Lavrova, R. Doshi, O. Jerphagnon, J. E. Bowers, V. Kaman, L. a. Coldren and J. Barton, "All-optical label swapping networks and technologies", *J. Lightwave Technol.*, vol.18, no.12, pp.2058-2075, 2000.
- [2] K. Kitayama, N. Wada and H. Sotobayashi, "Architectural considerations for photonic IP router based upon optical code correlation", *J. Lightwave Technol.*, vol.18, no.12, pp.1834-1844, 2000.
- [3] N. Goto and Y. Miyazaki, "Label recognition with wavelength-selective collinear acousto-optic switches for photonic label routers", *Jpn. J. Appl. Phys.*, vol.44, no.6B, pp.4449-4454, 2005.
- [4] N. Goto and Y. Miyazaki, "Label recognition using collinear acousto-optic devices in WDM photonic router", *IEEEJ Trans. EIS*, vol.125, no.12, pp.1784-1789, 2005.
- [5] T. Kondo, Y. Miyazaki and Y. Akao, "Optical tunable switched directional couplers consisting of two thin-film waveguides using surface acoustic waves", *Jpn. J. Appl. Phys.*, vol.17, no.7, pp.1231-1243, 1978.
- [6] N. Goto and Y. Miyazaki, "FDTD analysis of wavelength-selective optical switch using collinear acousto-optic interaction for WDM routing", *Trans. IEICE Electron.*, vol.J86-C, no.12, pp.1272-1281, 2003.

Theoretical Analysis of Propagation characteristics in Medium Waves Transmission from the Top of the Mountain

Y.Norimatsu

Nankai Broadcasting Ltd., Japan

K.Ono, M.Matsunaga

Ehime University, Japan

Abstract—The propagation characteristic of the medium wave band from transmitting station on the top of mountain has been analyzed by the two methods. Furutsu's method as an analytical solution and the beam propagation method as a convenient numerical method are applied to the problem. The results obtained by the methods predict that, if the medium waves are transmitted from the top of the mountain, the receiving field strength on the plain are not so small rather large compared with those from the transmitter in the plain.

1. Introduction

The transmitting station of the medium wave band is usually set up in the plains where the electric conductivity is essentially high and a very large site to lay a radial ground is easily available. As the area around the transmitting station becomes a residential area, compatibility of high power transmitter with living environment has become difficult. When we update an antenna with deterioration of facilities, this causes it difficult to update an antenna in the same sites or to secure a new site on plains area.

Another reason to set the transmitting station on the mountain areas comes from Japanese geographical features, which have complex terrains including many mountain areas. However, the researches on transmitting radio waves from the top of mountain are very few as far as the authors know, because the conductivity of mountain area is considered to be too low for efficient emission of radio wave.

Furutsu's method and the Beam Propagation method (BPM) are applied to the problem. The results obtained by the methods predict that, if the medium waves are transmitted from the top of the mountain, the receiving field strength on the plain are not so small rather large compared with those from the transmitter in the plain.

2. Propagation analysis by Furutsu's method

Furutsu had presented the theory that deal with the propagation properties of radio waves along irregular terrains which have different electric constants, dielectric constants and conductivities [1],[2]. He gave the analytical solutions. To simplify the analysis, we apply the analytical solution to the model of mountains shown in the figure 1, which has the antenna on the plateau with arbitrary height.

In this model, we set the transmitting antenna on the plateau, and the receiving antenna on the plain. The dielectric constants and conductivities of plateau are 5 and 0.001, which assume constants of the dry earth. The constants for plains are taken from the normal earth, and are 10 and 0.001. In the figure 1, k is the wavenumber and is defined by equation (1). Applying the Furutsu's method to the model in the figure 1, attenuation function A at the receiver is expressed by the following equation.

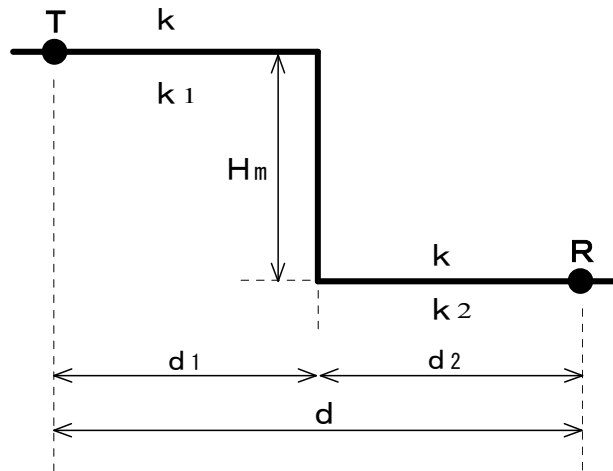


Figure 1: A transmitting station on the mountain modeled as the plateau with height H_m . T and R denote the transmitting and receiving antenna, respectively.

$$\begin{aligned}
 A = e^{-(S_1^2+S_2^2)} & \left[U(\sqrt{\Gamma_1} S_2 + \sqrt{\Gamma_2} S_1) - j\sqrt{\pi} (\sqrt{t_2/\Gamma_2} + \sqrt{t_1/\Gamma_1})^{-1} \right. \\
 & \times \left[\sqrt{t_1 t_2 / \Gamma_1 \Gamma_2} \cdot U(S_2 + j\sqrt{t_2}) \cdot U(S_1 + j\sqrt{t_1}) + \sqrt{t_2/\Gamma_2} \{ U(q_2, (\sqrt{\Gamma_1} S_2 + \sqrt{\Gamma_2} S_1) / p_2) \right. \\
 & \left. \left. - U(p_2, (S_2 + j\sqrt{t_2}) / p_2) \} + \sqrt{t_1/\Gamma_1} \{ U(q_1, (\sqrt{\Gamma_1} S_2 + \sqrt{\Gamma_2} S_1) / q_1) - U(p_1, (S_1 + j\sqrt{t_1}) / p_1) \} \right] \right] \quad (1)
 \end{aligned}$$

where

$$\left. \begin{aligned}
 k &= 2\pi/\lambda \\
 k'_1 &= k_1^2 / \sqrt{k_1^2 - k^2} \\
 k'_2 &= k_2^2 / \sqrt{k_2^2 - k^2}
 \end{aligned} \right\} \text{Vert. Pol.} \quad r_1 = d_1 / (d_1 + d_2) \quad , \quad r_2 = d_2 / (d_1 + d_2)$$

$$\begin{aligned}
 t_1 &= -j(k/k'_2)^2 k \cdot d_2 / 2 & S_1 &= (a_3 - a_1) \sqrt{k/2d_1} e^{-j\pi/4} \\
 t_2 &= -j(k/k'_1)^2 k \cdot d_1 / 2 & S_2 &= (a_3 - a_2) \sqrt{k/2d_2} e^{-j\pi/4}
 \end{aligned}$$

$$U(z) = \frac{2}{\sqrt{\pi}} e^z \int_z^\infty e^{-x^2} dx$$

$$U(z, n/z) = \left(\frac{2}{\sqrt{\pi}} \right)^2 e^{z^2 + n^2} \int_z^\infty dx \cdot e^{-x^2} \int_{(n/z)x}^\infty e^{-y^2} dy$$

The figure 2 shows the field strength at receiver as a function of distance from antenna set at the edge of plateau. We assume that the transmitted power is 1 kW, the frequency is 1 MHz and the antenna efficiency is 100 %. Numerical results thus obtained by our model verify that the field strengths at the propagation distance are nearly the same or even higher than those from transmitters setting up in the plains.

The field strength far from the edge is not so smaller than the case of transmitting from the edge. However, the field strength near the edge, which is the shadow region, decrease drastically and gradually

recover its strength of unshaded region as we expect from wave optics. The results illustrated in the figures 2 and 3 imply that radio wave transmission from the top of mountain is not disadvantageous than that from the plain.

The results also imply that radio wave transmission from the top of mountain is not disadvantageous than that from the plain as far as wave propagation is concerned.

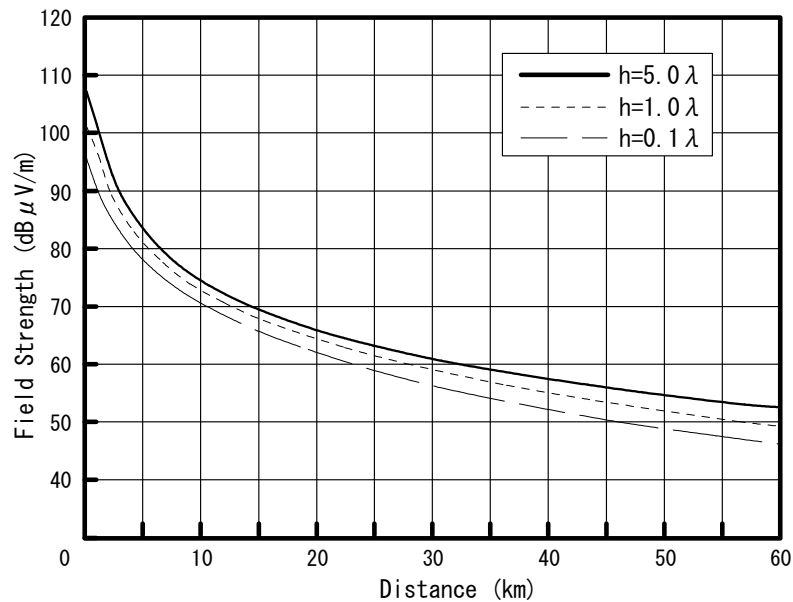


Figure 2: Field strength at the receiver in which the mountain height H_m normalized by the wavelength are 5.0, 1.0 and 0.1.

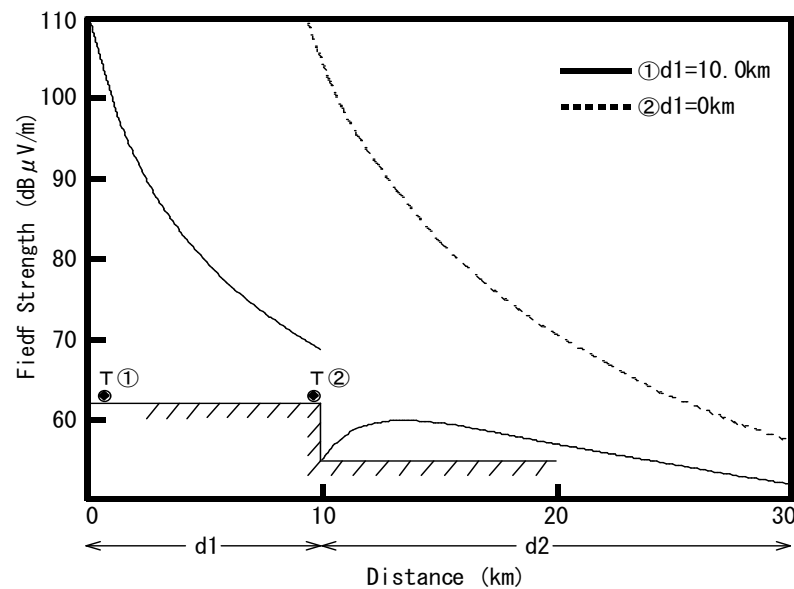


Figure 3: Field strength at the receiver. Solid and dot lines show the field strength when the antennas on the plateau are set 10km from the edge and at the edge, respectively.

3. Propagation analysis by Beam propagation method

Furutsu's method is desirable, since it gives analytical expression for receiving field strength. However, it is difficult to apply to the staircase terrain model that can approximate the gentle sidehill of real mountains. Moreover, it cannot estimate the diffraction occurred at the edge of the plateau. We employ the beam propagation method to deal with the diffraction effect on receiving field strength numerically [3]. Transmitted wave from antenna is assumed to be two-dimensional Gaussian beam with its spot size 80m and emitted parallel to the ground. Antennas are set at the edge of the plateau. The center of Gaussian beam is 300 m high from the ground level.

The figure 4 illustrates the field strength contours obtained by BPM. Antennas are set (a) on the edge of plateau and (b) on the top of mountain with gentle hillside. The figure 5 illustrates the transmission loss as a function of the distance from the antennas.

The waves reflected from earth interfere with the direct waves from antenna, when the waves are emitted at the edge of plateau. This interference causes stripe patterns in the figure 4(a) and the undulation in the figure 5. On the other hand, when the waves emitted from the top of mountain with gentle hillside, number of stripe arisen from interference is few and propagation loss is almost the same as the emission from the edge, i.e., emission from the top of mountain without gentle hillside.

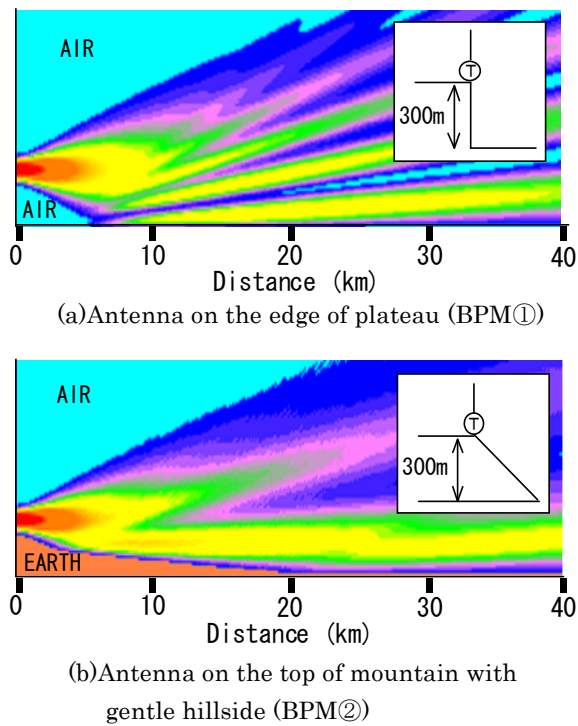


Figure 4: Field strength contours obtained by BPM.

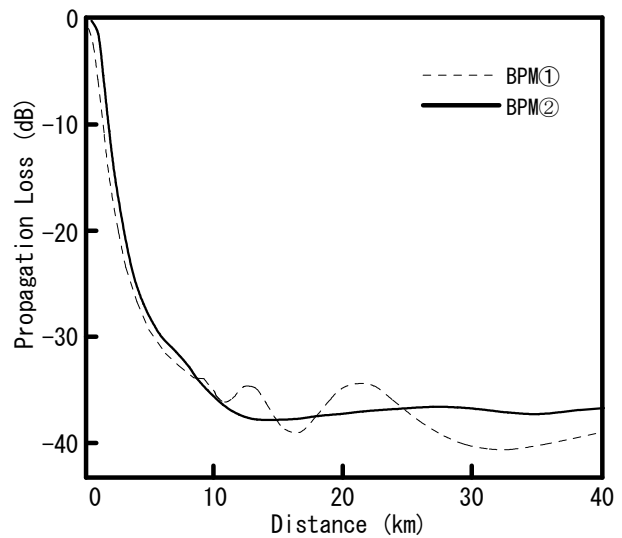


Figure5: Propagation loss as in the figure 4.

4. Conclusion

The propagation of radiowave transmitted from the top of mountain is analyzed by means of two methods, Furutsu's method and BPM. The numerical results obtained by the methods predict that, if the medium waves are transmitted from the top of the mountain, the receiving field strength on the plain are not so small rather large compared with those from the transmitter in the plain.

Since the mountain areas have lower conductivity and dielectric constant than plains have, they are considered to have poor transmission efficiency and are not suited for transmitting station. It is necessary to verify the radiation efficiency of transmitter set on the top of mountain and the propagation characteristic in medium waves transmission from the top of mountain.

An experimental verification is now being planned as a practical matter.

REFERENCES

- [1] Furutsu, K., "On the theory of Radio Wave Propagation Over Inhomogeneous Earth," *J. Radio Res. Lab.*, Vol.67, D, No.1, 1963.
- [2] Furutsu, K. and Wilkerson, R. E., "Some Numerical Results Based on the Theory of Radio Wave Propagation Over Inhomogeneous Earth," *J. Radio Res. Lab.*, Vol.68D, No.7, 1964.
- [3] Levy, M., Parabolic equation methods for electromagnetic wave propagation, *IEE Electromagnetic Wave Series 45*, 2000.

Electromagnetic Analysis of Circular Waveguides for Tera Hertz Transmission Using Conformal Mapping

Yasumitsu Miyazaki

Department of Electronics and Information Engineering, Aichi University of Technology
50-2 Manori, Nishihazama-cho, Gamagori, 443-0047 Japan

Abstract

Extremely high radio frequency technology of Tera Hertz frequency band is rapidly developed recently, particularly for electromagnetic wave generation of Tera Hertz frequency band. These frequency bands are between Giga Hertz frequency band of millimeter waves and optical band of far infrared waves. However, transmission waveguides for Tera Hertz frequency bands have not been studied. The TE₀₁ mode of circular waveguide has been enough investigated for low loss transmission of 50GHz millimeter waves. In this paper, the TE₀₁ modes in circular waveguides of over sizes are discussed for Tera Hertz electromagnetic waves by mixed method of conformal mapping and integral equation with Green's dyadics.

Introduction

Extremely high radio frequency technology of Tera Hertz frequency band is rapidly developed recently^{1,2)}, particularly for electromagnetic wave generation of Tera Hertz frequency band. However, transmission waveguides for Tera Hertz frequency bands have not been studied. The TE₀₁ mode of over-size circular waveguide has been enough investigated for low loss transmission of 50GHz millimeter waves^{3,4)}. In this paper, the TE₀₁ modes in circular waveguides with a few mm radius of over sizes compared with wavelengths are discussed for Tera Hertz electromagnetic waves of less than 300 μm wavelength⁵⁻⁸⁾.

The TE₀₁ modes have low loss characteristics for large radiuses of circular waveguides compared with wavelengths of Tera Hertz electromagnetic waves and are proportional to inverses of three powers of radiuses and roots of frequencies, when conductors of waveguide have non-dispersive conductivities. If conductivities of waveguide wall metals have dispersive characteristics in the Tera Hertz frequency bands and complex dielectric constants, attenuation characteristics are very different from those of millimeter wave cases. Particularly, in this paper, mode conversions and reflections of the TE₀₁ mode of Tera Hertz frequency band in curved circular waveguides are studied by mixed method of conformal mapping and integral equation with Green's dyadics⁸⁾.

Dispersion characteristics of conductors at Tera Hertz frequency band

Electromagnetic wave characteristics of a conductor at Tera Hertz frequency band are given by the conductivity and the dielectric constant. The electric displacement vector \mathbf{D} has the following relation to the electric field vector \mathbf{E} and the polarization vector \mathbf{P}

$$\mathbf{D} = \epsilon \mathbf{E} = \epsilon_0 \mathbf{E} + \mathbf{P} \quad (1)$$

where ϵ is the dielectric constant of the medium. For the mass m of an electron in the conductor and its position vector \mathbf{r} , we have, using motion parameters,

$$\mathbf{p} = -e\mathbf{r}, \quad m \frac{d^2 \mathbf{r}}{dt^2} + \gamma \frac{d\mathbf{r}}{dt} + c\mathbf{r} = -e\mathbf{E} \quad (2)$$

Assuming the time factor as $e^{j\omega t}$ and the density of the electron as N , the total polarization vector \mathbf{P} and the dielectric constant ϵ are given by

$$\mathbf{P} = \frac{Ne^2}{m\omega^2 - j\omega + c} \mathbf{E} \quad (3) \quad \epsilon = \epsilon_0 - \frac{Ne^2}{m\omega^2 - j\omega + c} \quad (4)$$

Also, using transport parameters τ and μ , the conductivity is given by

$$\mathbf{J} = \sigma \mathbf{E} = N \frac{d\mathbf{r}}{dt} q \quad (5) \quad \frac{d\mathbf{r}}{dt} + \boldsymbol{\alpha} = \mu \mathbf{E} \quad (6)$$

Although the dielectric constant ϵ and the conductivity σ of the conductor are given by eq.(4)-(6), the experimental data for ϵ and σ at Tera Hertz frequency band have not been shown sufficiently. However, in future, the experimental data would be found precisely. In a copper case, the conductivity σ is shown as $5,800 \times 10^7$ S/m at the frequency lower than millimeter wave frequency band. If we take the complex dielectric constant of the conductor as ϵ , ϵ is given by

$$\epsilon = \epsilon_r - j\sigma / \omega = \epsilon' - j\epsilon'' \quad (7)$$

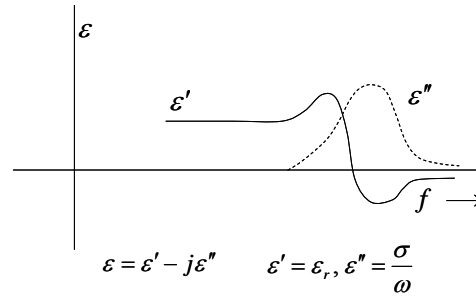


Fig. 1: Dispersion characteristics of the complex dielectric constant

Eigen electromagnetic fields in circular waveguides

When the waveguide walls of the circular waveguide with radius a is not perfect electric conductor and has finite conductivity, electromagnetic fields on the walls satisfy the impedance boundary condition

$$\mathbf{n} \times \mathbf{E} = \frac{1}{2} \delta \mu \omega (1 + j) \mathbf{H}, \quad \delta = \sqrt{\frac{2}{\omega \mu \sigma}}, \quad R_s = \sqrt{\frac{\omega \mu}{2 \sigma}} \quad (8)$$

In case of circular waveguide, the transverse components of the eigen fields for TM_{mn} and TE_{mn} modes are

$$\psi_{[mn]}(r, \theta) \psi_{[mn]}(r', \theta') = \frac{(2)_m}{\pi} \cos m(\theta - \theta') \cdot \frac{J_m(\chi_{mn} r) J_m(\chi_{mn} r')}{(x_{mn}^2 - m^2) J_m^2(x_{mn}')} \quad (9)$$

$$\varphi_{(mn)}(r, \theta) \varphi_{(mn)}(r', \theta') = \frac{(2)_m}{\pi} \cos m(\theta - \theta') \cdot \frac{J_m(\chi_{mn} r) J_m(\chi_{mn} r')}{x_{mn}^2 J_{m+1}^2(x_{mn})} \quad (10)$$

Noting that $J_m^{(0)}(x_{mn}^{(0)}) = 0$, $\chi_{mn}^{(0)} = x_{mn} / a$, $\beta^{2(r)} = \beta^2 - \chi_{mn}^{2(r)}$ and $(2)_m = 2(m=0)$, $0(m \geq 1)$, the imaginary parts of the propagation constants β_{mn} and β'_{mn} of the TM_{mn} and TE_{mn} mode, $\beta_{mn}^{(i)}$ and $\beta'_{mn}^{(i)}$ are given by

$$\beta_{mn} = \beta_{mn}^{(r)} - j\beta_{mn}^{(i)}, \quad \beta_{mn}^{(i)} = \frac{R_s}{\zeta} \frac{1}{a} \frac{\beta}{\sqrt{\beta^2 - \chi_{mn}^2}}$$

$$\beta'_{mn} = \frac{R_s}{\zeta} \frac{1}{a} \left\{ \frac{m^2}{x_{mn}^2 - m^2} + \frac{\chi_{mn}^2}{\beta^2} \right\} \frac{\beta}{\sqrt{\beta^2 - \chi_{mn}^2}} \quad (11)$$

$$J_m^{(0)}(x_{mn}^{(0)}) = 0, \quad \chi_{mn}^{(0)} = \frac{x_{mn}^{(0)}}{a}$$

where $\beta = \omega \sqrt{\epsilon \mu}$, $\zeta = \sqrt{\mu / \epsilon}$.

Here, we consider the dyadic Green's function $\Gamma(\mathbf{r}, \mathbf{r}')$ satisfying the following equations

$$\nabla \times \nabla \times \Gamma - \beta^2 \Gamma = \Gamma = \mathbf{I} \delta(\mathbf{r} - \mathbf{r}') \quad (12)$$

$$[\mathbf{n} \times \Gamma]_{r=a} = 0$$

where \mathbf{I} is the unit dyad. $\Gamma(\mathbf{r}, \mathbf{r}')$ in eq. (12) is expressed concretely, using eigen functions for the transverse cross section, $\{\psi_{mn}\}$ and $\{\varphi_{mn}\}$

$$\Gamma(\mathbf{r}, \mathbf{r}') = \left(\mathbf{i}_z \mathbf{i}_z - \frac{1}{\beta^2} \nabla \nabla' \right) G^{(1)}(\mathbf{r}, \mathbf{r}')$$

$$+ \nabla_t \nabla_t' H^{(1)}(\mathbf{r}, \mathbf{r}') + \mathbf{i}_z \times \nabla_t \mathbf{i}_z \times \nabla_t' H^{(2)} \quad (13)$$

where

$$G^{(1)} = \sum_{m,n} \frac{\chi_{mn}^2 \varphi_{(mn)}(x, y) \chi_{mn}^2 \varphi_{(mn)}(x', y')}{2j\beta_{mn}} e^{-j\beta_{mn}|z-z'|} \quad (14)$$

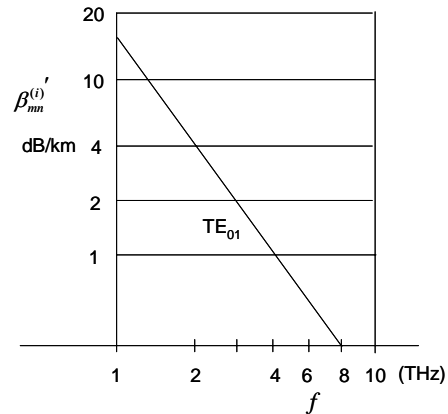


Fig.2: Attenuation characteristics of the circular waveguide with the inner radius of 5mm

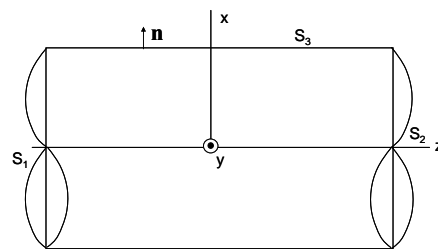


Fig. 3: Waveguide

$$H^{(1)} = \sum_{m,n} \frac{\varphi_{(mn)}(x,y)\varphi_{(mn)}(x',y')}{2j\beta_{mn}} e^{-j\beta_{mn}|z-z'|} \quad (15) \quad H^{(2)} = \sum_{m,n} \frac{\psi_{[mn]}(x,y)\psi_{[mn]}(x',y')}{2j\beta_{mn}} e^{-j\beta_{mn}|z-z'|} \quad (16)$$

$$\nabla^2 G + \beta^2 G = -\delta(\mathbf{r} - \mathbf{r}'), \quad [G^{(1)}]_{r=a} = 0, \quad \nabla_t = \nabla - \frac{\partial}{\partial z} \mathbf{i}_z$$

$\psi_{[mn]}$ and $\varphi_{(mn)}$ are the eigen functions satisfying the Neumann and Dirichlet boundary condition on the boundary of transverse cross sections and orthogonal conditions

$$\int \psi_{[mn]}\psi_{[m'n']} dS = \chi_{mn}^{-2} \delta_{mm'} \delta_{nn'}, \quad \int \varphi_{(mn)}\varphi_{(m'n')} dS = \chi_{mn}^{-2} \delta_{mm'} \delta_{nn'}$$

Here, $\beta_{mn}^{(r)02} = \beta^2 - \chi_{mn}^{02}$, $\delta_{mm'} = 1(m = m')$, $0(m \neq m')$, $m=0,1,2, \dots$, $n=1,2, \dots$.

In case of the open type waveguide for the continuous spectral transmission, $\sum_{m,n}$ may be replaced to $\iint dmdn$.

Electromagnetic fields in curved circular waveguide

We consider the electromagnetic fields in the curved circular waveguide shown in Fig. 4. The circular waveguide with the radius of curvature R , placed in the space of rectangular coordinate (X,Y,Z) is considered. The medium in the waveguide is isotropic and homogeneous. Let the dielectric constant of the medium be ϵ , the permeability of the medium be μ , the propagation constant be $\beta = \sqrt{\omega^2 \epsilon \mu}$ and the time factor be $e^{j\omega t}$, the equation for the electric field is derived from Maxwell's equations,

$$\nabla_{x,y,z} \times \nabla_{x,y,z} \times \mathbf{E} - \beta^2 \mathbf{E} = 0, \quad \nabla_{x,y,z} \cdot \mathbf{E} = 0 \quad (17)$$

As for the boundary conditions, electromagnetic fields on the wall of the waveguide satisfy $\mathbf{E} \times \mathbf{n} = 0$, $\mathbf{H} \cdot \mathbf{n} = 0$ where \mathbf{n} is the unit vector normal to the boundary. The effects from the waveguide walls are given to the perturbed propagation constants.

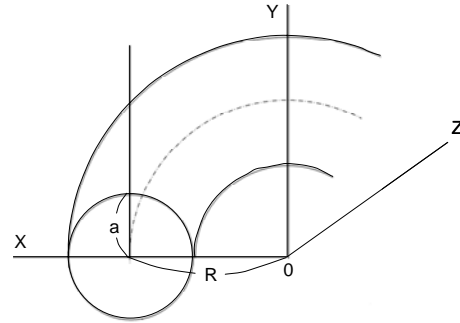


Fig. 4: Curved circular waveguide

Representation of the electromagnetic fields in the new coordinate system (x,y,z)

We consider the plane where Y is constant in the rectangular coordinate shown in Fig. 4. In the plane, we define complex planes $\dot{Z} = X + jZ$ and $\dot{z} = x + jz$. Using the mapping function $X + jZ = R(1 + x/R)e^{j\frac{z}{R}}$ and $Y=y$, the curved waveguide with radius a in Fig. 4 is transformed to the straight waveguide with radius a in the new space of rectangular coordinate (x,y,z) . Here, the line element ds^2 is given by $ds^2 = dX^2 + dY^2 + dZ^2 = dx^2 + dy^2 + h^2 dz^2$, where h is the metric coefficient and $h^2 = (1 + x/R)^2$. Also, the eq. (17) for the electric field is transformed to the following equation in the new coordinate (x,y,z) ,

$$\begin{aligned} \nabla_{x,y,z} \times \nabla_{x,y,z} \times \mathbf{E} - \beta^2 \mathbf{E} = & - \left(1 - \frac{1}{h^2}\right) \frac{\partial^2 \mathbf{E}_t}{\partial z^2} + \left(\frac{1}{h} \frac{\partial h}{\partial x}\right) \\ & \cdot \left(\frac{\partial E_y}{\partial x} - \frac{\partial E_x}{\partial y}\right) \mathbf{i}_y - \left\{ \left(1 - \frac{1}{h}\right) \cdot \frac{1}{h} \frac{\partial h}{\partial x} \frac{\partial E_x}{\partial z} - \frac{1}{h^2} \frac{\partial h}{\partial x} \frac{\partial E_x}{\partial z} \right\} \mathbf{i}_z \\ & - \left[\frac{1}{h^2} \cdot \frac{\partial}{\partial x} \left(h \frac{\partial E_z}{\partial z} \right) - \frac{\partial^2 E_z}{\partial x \partial z} \right] \mathbf{i}_x \\ & + \left\{ \left(\frac{1}{h} - 1\right) \frac{\partial^2 E_z}{\partial z \partial y} - \left(\frac{1}{h} - 1\right) \frac{1}{h} \frac{\partial^2 E_z}{\partial z^2} \right\} \mathbf{i}_y - \frac{\partial}{\partial x} \left(\frac{1}{h} \frac{\partial h}{\partial x} E_z \right) \mathbf{i}_z \\ = & F(\mathbf{E}) \end{aligned} \quad (18)$$

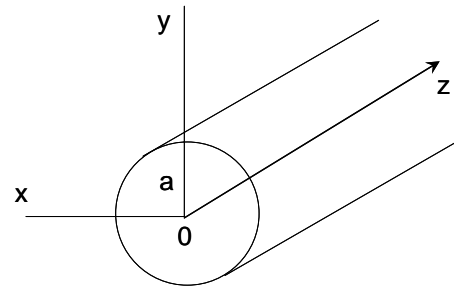


Fig. 5: Curved circular waveguide in the new coordinate system

where \mathbf{i}_x , \mathbf{i}_y , \mathbf{i}_z are the unit vectors in the rectangular direction x , y , z and $\mathbf{E}_t = E_x \mathbf{i}_x + E_y \mathbf{i}_y$ is the transverse component of the electric field. The right hand side of eq. (18), defined by $F(\mathbf{E})$ is the inhomogeneous term due to the bends of the waveguide. We can assume that a medium in the straight

circular waveguide in mapped new space (x,y,z) is homogeneous or there are equivalent sources in the waveguide, since the differential equation (18) is inhomogeneous. Also, if we use the cylindrical coordinate (r, θ, z) instead of the rectangular coordinate (x,y,z) in the mapped new space, the boundary condition of the electric field on the wall of the waveguide $\mathbf{E} \times \mathbf{n} = 0$ is expressed by $[E_\theta]_{r=a} = [E_z]_{r=a} = 0$, where a is the radius of the circular waveguide.

Formulation of the integral equations

Noting the presence of an inhomogeneous term in the wave equation (18), we apply Green's theorem to the inside of the waveguide with radius a in the new space (x,y,z) . Using the fundamental dyadic Green's function $\Gamma(\mathbf{r}, \mathbf{r}')$ given by eq. (12), the scattered electric field $\mathbf{E}_{scatt} = \mathbf{E}_{totl} - \mathbf{E}_{inc}$ satisfies

$$\int_V [\mathbf{E}_{scatt} \cdot \nabla \times \nabla \times \Gamma - \Gamma \cdot \nabla \times \nabla \times \mathbf{E}_{scatt}] dv = \int_{S_1, S_2, S_3} \mathbf{n} \cdot [\Gamma \times \mathbf{E}_{scatt}] - \mathbf{E}_{scatt} \times (\nabla \times \Gamma) dS \quad (19)$$

where \mathbf{E}_{totl} and \mathbf{E}_{inc} are the total and the incident electric field, \mathbf{n} is the unit vector normal to the surfaces of the waveguide. S_3 is the surface of the waveguide wall, S_1 and S_2 are the surfaces of the left and right side of the waveguide. In eq. (19), the operator $\nabla_{x,y,z}$ is denoted simply as ∇ . Hence, from equations (13)-(19) the total electric field vector \mathbf{E}_{totl} is

$$\mathbf{E}_{totl} = \mathbf{E}_{inc} + \int \Gamma \cdot \{\nabla \times \nabla \times \mathbf{E}_{inc} + F(\mathbf{E}_{totl})\} dv - \int_{S_1, S_2, S_3} \Gamma \cdot \beta^2 \mathbf{E}_{inc} dv + \int_{S_1, S_2, S_3} \mathbf{n} \cdot [\Gamma \times (\nabla \times \mathbf{E}_{scatt}) - \mathbf{E}_{scatt} \times (\nabla \times \Gamma)] dS \quad (20)$$

where $F(\mathbf{E}_{totl})$ is given by eq. (18). Particularly, when the incident wave \mathbf{E}_{inc} satisfies $\nabla \times \nabla \times \mathbf{E}_{inc} - \beta^2 \mathbf{E}_{inc} = 0$ and is the positive traveling wave incident at the surface S_1 ,

$$\mathbf{E}_{totl} = \mathbf{E}_{inc} - \int \Gamma \cdot \left[\left(1 - \frac{1}{h^2}\right) \frac{\partial^2 \mathbf{E}_t}{\partial z^2} - \left(\frac{1}{h} \frac{\partial h}{\partial x}\right) + \left(\frac{\partial E_y}{\partial x} - \frac{\partial E_x}{\partial y}\right) \mathbf{i}_y + \left\{ \left(1 - \frac{2}{h}\right) \frac{1}{h} \frac{\partial h}{\partial x} \frac{\partial E_x}{\partial z} \right\} \mathbf{i}_x + \left\{ \frac{1}{h^2} \cdot \frac{\partial}{\partial x} \left(h \frac{\partial E_z}{\partial z} \right) - \frac{\partial^2 E_z}{\partial x \partial z} \right\} \mathbf{i}_x \right. \\ \left. + \left\{ \left(\frac{1}{h} - 1\right) \frac{\partial^2 E_z}{\partial z \partial y} - \left(\frac{1}{h} - 1\right) \frac{1}{h} \frac{\partial^2 E_z}{\partial z^2} \right\} \mathbf{i}_y - \frac{\partial}{\partial x} \left(\frac{1}{h} \frac{\partial h}{\partial x} E_z \right) \right] \mathbf{i}_z \Big] dv + \int_{S_1, S_2} \mathbf{n} \cdot [\Gamma \times (\nabla \times \mathbf{E}_{scatt}) - \mathbf{E}_{scatt} \times (\nabla \times \Gamma)] dS \quad (21)$$

where the electric field of the second term is $\mathbf{E}_t = E_x \mathbf{i}_x + E_y \mathbf{i}_y$, E_x and E_y is the component of \mathbf{E}_{totl} . If we postulate the matching of the electric field on surfaces S_1 and S_2 , the third term of (21) can be omitted.

We change the eq. (19) to the appropriate form to obtain the TE and TM wave representation for the waveguide. Generally, using an arbitrary vector \mathbf{U} ,

$$\mathbf{E} = \int \Gamma \cdot \mathbf{U} dv = \sum_{m,n} V_{(mn)}^{(T)}(z) \frac{\mathbf{i}_z}{(\pm j \beta_{mn})} \nabla_t^2 \varphi_{(mn)} - \sum_{m,n} V_{(mn)}^{(R)}(z) \nabla_t \varphi_{(mn)} + \sum_{m,n} V_{(mn)}^{(T)} \mathbf{i}_z \times \nabla_t \psi_{[mn]} \quad (22)$$

where the upper and the lower superscripts are related to the traveling waves and the reflected waves, respectively. Here, $V_{[mn]}^{(T)}$ and $V_{(mn)}^{(R)}$ are the amplitudes of TE_{mn} and TM_{mn} waves, respectively. Let U_z denotes the component of \mathbf{U} along the waveguide axis and U_t is its transverse component, we have

$$V_{[mn]}^{(T)} = \frac{1}{2j\beta_{mn}'} \int \mathbf{i}_z \times \nabla_t \psi_{[mn]} \cdot \mathbf{U}_t e^{-j\beta_{mn}'|z-z'|} dv' \quad (23)$$

$$V_{(mn)}^{(R)} = \frac{1}{2j\beta_{mn}} \int \{ (\pm j) \chi_{mn}^2 U_z \varphi_{(mn)} - \beta_{mn} \nabla_t \varphi_{(mn)} \cdot \mathbf{U}_t \} e^{-j\beta_{mn}|z-z'|} dv' \quad (24)$$

From the above discussion, the electromagnetic fields in curved waveguide are obtained by solving the vector integral equation (21). Using the Born approximation, approximate solutions of (21) are obtained as iteration solutions.

For instance, we consider TE₀₁ wave incident on the circular waveguide with the radius a . If the incident wave is the TE₀₁ wave incident from the surface S_1 , we have

$$H_z = \chi_{01}^2 B_{01} J_0(\chi_{01}' r) e^{-j\beta_{01}' z}, \quad E_\theta = j\omega\mu\chi_{01}' B_{01} J_0'(\chi_{01}' r) e^{-j\beta_{01}' z} \quad (25)$$

From (23) and (24), the reflection and the mode conversions are obtained. Noting the order of $1/R$, it is known that the reflection TE_{1n}, TM₁₁ waves and the transmission TE_{1n}, TM₁₁ waves are generated on the first order of the bends. Also, the reflection and transmission TE_{0n}, TE_{2n}, TM_{0n} and TM_{2n} waves are gener-

ated on the second order of the bends. The other modes are generated on the higher order more than the third order. From the above discussion, it is found that these results give good accuracy when the product of phase constant $\beta_{mn}^{(v)}$ and the radius a of the waveguide becomes sufficiently larger than 1, particularly as for the reflection waves.

Next, we show the magnitudes of reflection and transmission TE and TM waves by conversion coefficient S whose dimension is the root of the power, when the incident wave is TE₀₁ wave with unit power. Using $V_{[mn]}^{(R)}$ and $V_{[mm]}^{(R)}$ of (23) and (24), the converted powers for TE_{mn} and TM_{mn} waves are given by

$$\left\{ \left(\frac{T}{R} \right) S_{[mn]}^{[01]} \right\}^2 = \frac{\beta_{mn}'}{\beta_{01}'} \frac{[V_{[mn]}^{(R)}]^2}{[j\omega\mu\sqrt{\pi}\chi_{01}'B_{01}aJ_0(x_{01}')]^2} \quad (25) \quad \left\{ \left(\frac{T}{R} \right) S_{(mm)}^{[01]} \right\}^2 = \frac{\beta^2}{\beta_{01}'\beta_{mm}} \frac{[V_{[mm]}^{(R)}]^2}{[j\omega\mu\chi_{01}'B_{01}aJ_0(x_{01}')]^2} \quad (26)$$

The transmission and the reflection coefficients $\left(\frac{T}{R} \right) S_{[1n]}^{[01]}$ and $\left(\frac{T}{R} \right) S_{(11)}^{[01]}$ of TE_{1n} and TM₁₁ waves, when the TE₀₁ wave is incident to the waveguide with slow bends, are given concretely by the above equations,

$$\left(\frac{T}{R} \right) S_{[1n]}^{[01]} = \frac{x_{01}'x_{1n}'^2}{\sqrt{2}\sqrt{\beta_{01}'\beta_{1n}'}\sqrt{x_{1n}'^2-1}} \frac{(\beta_{1n}'^2+3\beta_{01}'^2)e^{(-j\beta_{01}'\pm j\beta_{1n}')l}-1}{(x_{1n}'^2-x_{01}'^2)^2} \frac{a}{(\beta_{01}'\mp\beta_{1n}')R} \quad (27)$$

$$\left(\frac{T}{R} \right) S_{(11)}^{[01]} = j \frac{\beta}{\sqrt{2}} \frac{a}{x_{11}} \left\{ \frac{1}{\beta_{11}^2} \right\} \left\{ \frac{l}{e^{-j\beta_{01}'l-j\beta_{11}'l}-1} \right\} \frac{1}{R} \quad (28)$$

Fig. 6 and 7 show the results calculated using the following parameters: the diameter of waveguide $2a=5\text{mm}$, frequency 5THz and the radius of the curvature $R=10\text{m}$. As shown in Fig. 6 and 7, the reflection and the mode conversion with regard to TM₁₁, TE₁₁ and TE₁₂ waves become strong and as the frequency increases, the strong mode conversion is observed. Also the reflection waves are very weak on the order of 10^{-3} compared to the higher order mode conversion of transmitted waves at 5THz .

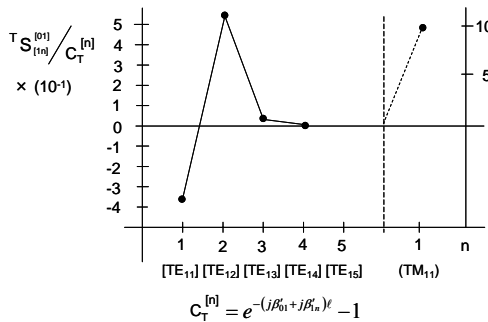


Fig. 6: Mode conversion coefficients of TE_{1n} mode and TM₁₁ mode with $f=5\text{THz}$, $2a=5\text{mm}$, $R=10\text{m}$.

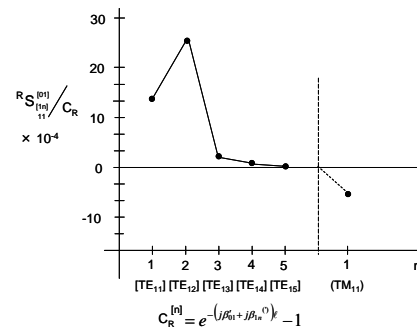


Fig. 7: Reflection coefficients of TE_{1n} mode and TM₁₁ mode with $f=5\text{THz}$, $2a=5\text{mm}$, $R=10\text{m}$.

Conclusion

We proposed the circular waveguide of over sizes as the transmission waveguide for Tera Hertz frequency band and showed the fundamental transmission characteristics for TE₀₁ mode. The transmission and reflection characteristics in the circular waveguide with homogeneous bends were studied precisely.

References

- [1] B. Ferguson and X.C. Zhang, Nature Materials, Vol.1, pp.26-33, 2002.
- [2] J. Nishizawa, Proceedings of 8th Symp. on Microwave and Optical Tech., pp.33-36, Montreal, Canada, June 2001.
- [3] S.E. Miller and A.C. Beck, Proc. IRE., **41**, 3, p.348, 1953.
- [4] A. E. Karbowiak, "Trunk waveguide communication," Chapman and Hall LTD, 1965.
- [5] K. Udagawa and Y. Miyazaki, Jour. of IECE, **47**, 8, pp.1186-1195, Aug. 1964.
- [6] K. Udagawa and Y. Miyazaki, "Theory of reflection and mode conversion through tilt of millimeter circular waveguide by conformal transformation, " I.C.M.C.I., Tokyo, M-2-2, pp.21-22, 1964.
- [7] K. Udagawa and Y. Miyazaki, Jour. of IECE, **49**, 12, pp.2407-2417, Dec. 1966.
- [8] Y. Akao and Y. Miyazaki, Trans. of IECE, **51-B**, 11, pp.553-558, Nov. 1968.